SUPRAMOLECULAR ASSEMBLY-BASED FUNCTIONAL NANOSTRUCTURES FOR BIOMEDICAL APPLICATIONS

EDITED BY: Tianjiao Ji, Huaimin Wang and Kai Han
PUBLISHED IN: Frontiers in Chemistry

frontiers Research Topics

frontiers

ISSN 1664-8714
ISBN 978-2-88966-520-4
DOI 10.3389/978-2-88966-520-4

About Frontiers

Frontiers is more than just an open-access publisher of scholarly articles: it is a pioneering approach to the world of academia, radically improving the way scholarly research is managed. The grand vision of Frontiers is a world where all people have an equal opportunity to seek, share and generate knowledge. Frontiers provides immediate and permanent online open access to all its publications, but this alone is not enough to realize our grand goals.

Frontiers Journal Series

The Frontiers Journal Series is a multi-tier and interdisciplinary set of open-access, online journals, promising a paradigm shift from the current review, selection and dissemination processes in academic publishing. All Frontiers journals are driven by researchers for researchers; therefore, they constitute a service to the scholarly community. At the same time, the Frontiers Journal Series operates on a revolutionary invention, the tiered publishing system, initially addressing specific communities of scholars, and gradually climbing up to broader public understanding, thus serving the interests of the lay society, too.

Dedication to Quality

Each Frontiers article is a landmark of the highest quality, thanks to genuinely collaborative interactions between authors and review editors, who include some of the world's best academicians. Research must be certified by peers before entering a stream of knowledge that may eventually reach the public - and shape society; therefore, Frontiers only applies the most rigorous and unbiased reviews.
Frontiers revolutionizes research publishing by freely delivering the most outstanding research, evaluated with no bias from both the academic and social point of view. By applying the most advanced information technologies, Frontiers is catapulting scholarly publishing into a new generation.

What are Frontiers Research Topics?

Frontiers Research Topics are very popular trademarks of the Frontiers Journals Series: they are collections of at least ten articles, all centered on a particular subject. With their unique mix of varied contributions from Original Research to Review Articles, Frontiers Research Topics unify the most influential researchers, the latest key findings and historical advances in a hot research area! Find out more on how to host your own Frontiers Research Topic or contribute to one as an author by contacting the Frontiers Editorial Office: frontiersin.org/about/contact

SUPRAMOLECULAR ASSEMBLY-BASED FUNCTIONAL NANOSTRUCTURES FOR BIOMEDICAL APPLICATIONS

Topic Editors:
Tianjiao Ji, Harvard Medical School, United States
Huaimin Wang, Westlake University, China
Kai Han, University of Michigan, United States

Citation: Ji, T., Wang, H., Han, K., eds. (2021). Supramolecular Assembly-Based Functional Nanostructures for Biomedical Applications. Lausanne: Frontiers Media SA. doi: 10.3389/978-2-88966-520-4

Table of Contents

frontiers in Chemistry

EDITORIAL
published: 28 January 2021
doi: 10.3389/fchem.2020.637926

Editorial: Supramolecular Assembly Based Functional Nanostructures for Biomedical Applications

Tianjiao Ji[1,2]*, *Kai Han*[3]* and *Huaimin Wang*[4]*

[1]CAS Key Laboratory for Biomedical Effects of Nanomaterials and Nanosafety, CAS Center for Excellence in Nanoscience, National Center for Nanoscience and Technology, Beijing, China, [2]Center of Materials Science and Optoelectronics Engineering, University of Chinese Academy of Sciences, Beijing, China, [3]Department of Pharmaceutical Sciences, University of Michigan, Ann Arbor, MI, United States, [4]Key Laboratory of Precise Synthesis of Functional Molecules of Zhejiang Province, School of Science, Westlake University, Westlake Institute for Advanced Study, Zhejiang, China

Keywords: supramolecular assembly, nanostructures, biomedical applications, imaging, therapy

Editorial on the Research Topic

Supramolecular Assembly Based Functional Nanostructures for Biomedical Applications

Supramolecular chemistry is an important branch of chemistry. Rationally designed molecules could spontaneously assemble to uniform nanostructures through supramolecular interactions (hydrogen bond, hydrophobic forces, Van der Waals forces, electrostatic interaction, *etc.*). For example, fatty acid–modified dexamethasone (Dex) could self-assemble to nanostructures (nanofibers or nanoparticles) through intermolecular interactions (probably through hydrophobic forces, hydrogen bond, and Van der Waals forces), and different (fatty acids) modification significantly influenced the morphologies and gelation behaviors (Liu et al.). Types of supramolecular interactions were described in the review article of Chen and his coworkers in this topic.

Taking advantages of supramolecular-based assembly, many pharmaceutical issues, such as poor solubility and short half-life of drugs under physiological conditions, can be solved. For example, poor water-soluble properties of rapamycin (RAPA, a promising drug for alleviating hepatic steatosis) limited its clinical use; however, its dispersion and bioavailability were significantly improved when encapsulated in mPEG-PLGA (through hydrophobic forces) (Zhao et al.); baicalein (BCL) is also a poor-solubility drug, but Zhang et al. prepared BCL nanocrystals (co-assembling a cationic beta-lactoglobulin with BCL) that exhibited long-term stability in physiological conditions; the half-life of nucleic acid drugs can be prolonged if they are encapsulated/absorbed in nanocarriers, which are usually obtained through electrostatic interactions, as reported by Xu et al. in this topic.

The biomedical functions of supramolecular assemblies can be determined either by the carrier molecules or by the encapsulated drugs. Zhang et al. and Jin et al. reviewed types of functional peptide-based supramolecular assemblies and their applications in cancer therapy. Li group developed an amphiphilic molecule by conjugating photosensitizer protoporphyrin IX (PpIX) and the FAM/Dabcyl-based Förster resonance energy transfer (FRET) donor–acceptor through a PEG linker, and this molecule self-assembled to nanoparticles that were able to image hypoxia environment of tumors and to achieve photodynamic therapy.

Several works (in this topic) are related to immunotherapy because immunotherapy represents a new revolution in cancer therapy and becomes a superhot topic currently. Supramolecular assembly nanostructures exhibit great potential in terms of therapeutic vaccine, immune microenvironment modulation, *etc.* The review from Chen et al. underlined the advantages of tunable, modular, and reversible supramolecular assemblies in the loading/release of adjuvant, antigen, proteins, and drugs. It highlighted different

OPEN ACCESS

Edited and reviewed by:
Tony D. James,
University of Bath, United Kingdom

***Correspondence:**
Tianjiao Ji
jitj@nanoctr.cn
Kai Han
hanka@umich.edu
Huaimin Wang
wanghuaimin@westlake.edu.cn

Specialty section:
This article was submitted to Supramolecular Chemistry, a section of the journal Frontiers in Chemistry

Received: *04 December 2020*
Accepted: *21 December 2020*
Published: *28 January 2021*

Citation:
Ji T, Han K and Wang H (2021) Editorial: Supramolecular Assembly Based Functional Nanostructures for Biomedical Applications. Front. Chem. 8:637926. doi: 10.3389/fchem.2020.637926

supramolecular assemblies for cancer immunotherapy including supramolecular peptide assembly, DNA assembly, lipid hydrophobic assembly, host–guest assembly, as well as biomolecular recognition assembly. Supramolecular hydrogels can deliver antigen to modulate immunity, and Liu et al. developed reduction-responsive co-assembled hydrogels with different surface properties *In vivo* studies demonstrated that positively charged K-vac boosted significantly higher antibody production and antitumor immune responses. Supramolecular assembly can also modulate the T-cell function, and Xie et al. described that supramolecular photothermal ICG-liposome nanoparticles with light irradiation can increase the expression of immune checkpoint biomarkers, that is, anti-program death-1 (anti-PD1) and anti–T-cell immunoglobulin and mucin domain-containing protein 3 (anti-TIM-3) monoclonal antibodies, in tumor-infiltrating CD8 T cells. Consequently, the combination with anti–PD-1 and anti–TIM-3 can inhibit both primary and distant tumor growth.

In summary, this topic reports functional nanostructures (liposome, micelle, nanofibers, *etc.*) by making full use of supramolecular self-assembly techniques. The prepared nanostructures can overcome some drawbacks (e.g., lack of targeting, low encapsulation efficiency, complex preparation procedures, *etc.*) of current nanomaterials, which can provide many feasible references for designing translational biomaterials.

AUTHOR CONTRIBUTIONS

TJ, KH, and HW discussed and wrote the manuscript.

ACKNOWLEDGMENTS

We thank all the contributors for their efforts and promising works.

Conflict of Interest: The authors declare that the research was conducted in the absence of any commercial or financial relationships that could be construed as a potential conflict of interest.

frontiers in Chemistry

ORIGINAL RESEARCH
published: 20 December 2019
doi: 10.3389/fchem.2019.00868

A Theranostic Nanoprobe for Hypoxia Imaging and Photodynamic Tumor Therapy

Jing Hao Fan[1], Gui Ling Fan[1], Ping Yuan[1], Fu An Deng[1], Ling Shan Liu[2], Xiang Zhou[2], Xi Yong Yu[1], Hong Cheng[2]* and Shi Ying Li[1]**

[1] Key Laboratory of Molecular Target & Clinical Pharmacology and The State Key Laboratory of Respiratory Disease, School of Pharmaceutical Sciences & The Fifth Affiliated Hospital, Guangzhou Medical University, Guangzhou, China, [2] Guangdong Provincial Key Laboratory of Construction and Detection in Tissue Engineering, Biomaterials Research Center, School of Biomedical Engineering, Southern Medical University, Guangzhou, China

Hypoxia is a common feature for most malignant tumors, which was also closely related to the oxygen-dependent photodynamic therapy. Based on Förster resonance energy transfer (FRET), a smart nanoprobe (designated as H-Probe) was designed in this paper for hypoxia imaging and photodynamic tumor therapy. Due to the FRET process, H-Probe could respond to hypoxia with a significant fluorescence recovery. Moreover, abundant *in vitro* investigations demonstrated that the photosensitizer of PpIX in H-Probe could generate large amounts of singlet oxygen to kill cancer cells in the presence of oxygen and light with appropriate wavelength. Also, intravenously injected H-Probe with light irradiation achieved an effective tumor inhibition *in vivo* with a reduced side effect. This original strategy of integrating hypoxia imaging and tumor therapy in one nanoplatform would promote the development of theranostic nanoplatform for tumor precision therapy.

Keywords: hypoxia, photodynamic therapy, FRET, nanoprobe, theranostic

OPEN ACCESS

Edited by:
Kai Han,
University of Michigan, United States

Reviewed by:
Xiaoding Xu,
Sun Yat-sen University, China
Jiawei Liu,
Nanyang Technological University, Singapore

****Correspondence:***
Xi Yong Yu
yuxycn@aliyun.com
Hong Cheng
chengh@smu.edu.cn
Shi Ying Li
lisy-sci@gzhmu.edu.cn

Specialty section:
This article was submitted to Supramolecular Chemistry, a section of the journal Frontiers in Chemistry

Received: *31 October 2019*
Accepted: *03 December 2019*
Published: *20 December 2019*

Citation:
Fan JH, Fan GL, Yuan P, Deng FA, Liu LS, Zhou X, Yu XY, Cheng H and Li SY (2019) A Theranostic Nanoprobe for Hypoxia Imaging and Photodynamic Tumor Therapy. Front. Chem. 7:868. doi: 10.3389/fchem.2019.00868

INTRODUCTION

The malignant tumor progression induced abnormal microenvironment would induce therapeutic resistance and poor prognosis (Dalton, 1999; Whiteside, 2008; Kessenbrock et al., 2010; Sun et al., 2012; Gajewski et al., 2013; Liang et al., 2014; Sun, 2016). Among which, the fast proliferation of cancer cells and neovascularization deficiency would cause tumor hypoxia, which is a feature of most malignant tumors (Zhou et al., 2006; Conley et al., 2011; Rankin and Giaccia, 2016; Li S. Y. et al., 2018a). Moreover, the tumor heterogeneity and individual diversity of hypoxia microenvironments could further restrict the therapeutic outcome for personalized cancer treatment. Thus, the pre-evaluation for tumor hypoxia microenvironment is of great importance for cancer precision therapy (Li S. Y. et al., 2018b). To date, a variety of fluorescent probes has been developed for tumor hypoxia imaging (Zhang et al., 2010; Cui et al., 2011; Piao et al., 2013; Liu et al., 2014, 2017; Cai et al., 2015; Zheng et al., 2015; Yu et al., 2017). However, the separate implementation of imaging and therapeutic procedures may cause report delay due to the differences in distribution of the probe and drug. Therefore, it is meaningful to design a smart platform for simultaneous tumor hypoxia imaging and therapy.

Photodynamic therapy is known to be one of the non-invasive method for highly efficient tumor treatment (Dolmans et al., 2003; Castano et al., 2006; Chatterjee et al., 2008; Lucky et al., 2015; Li et al., 2017). Under the irradiation of light with appropriate wavelength, the photosensitizer in its

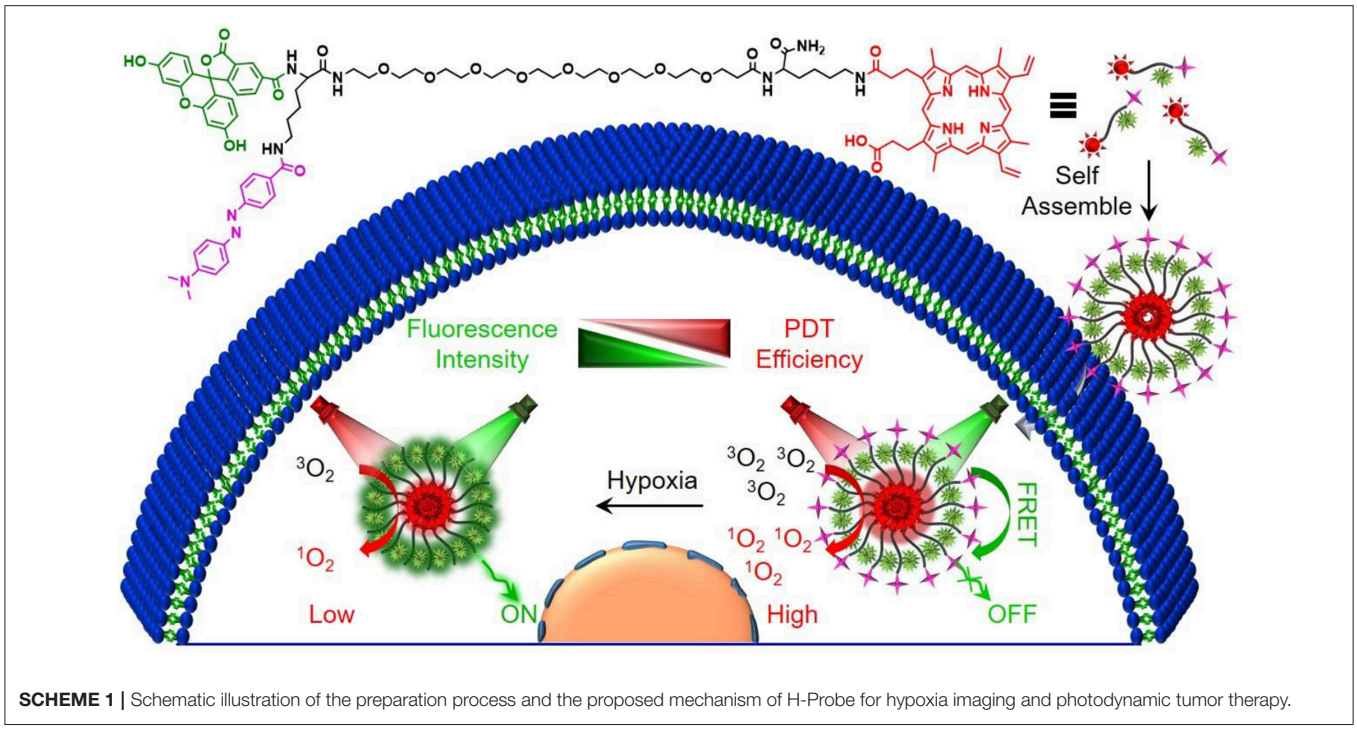

SCHEME 1 | Schematic illustration of the preparation process and the proposed mechanism of H-Probe for hypoxia imaging and photodynamic tumor therapy.

ground state translated into excited state, which could excite the triplet oxygen into singlet oxygen with the energy transfer (Celli et al., 2010; Ethirajan et al., 2011; Li X. et al., 2018; Cheng et al., 2019a). Singlet oxygen as one of the main cytotoxic substances could trigger irreversible damage of various cell constituents (Li et al., 2016; Shen et al., 2016; Cheng et al., 2019b). Significantly, oxygen is indispensable during the photodynamic therapy, which would directly impact the therapeutic efficiency (Cheng et al., 2016). Considering that most tumors were hypoxic, one platform integrating hypoxia and photodynamic therapy would be instructive for tumor theranostics.

In this work, a Förster resonance energy transfer (FRET)-based theranostic nanoprobe (designated as H-Probe) was designed for hypoxia imaging and photodynamic tumor therapy. As illustrated in **Scheme 1**, H-probe was made up of the hydrophilic PEG linker with the photosensitizer protoporphyrin IX (PpIX) and the FAM/Dabcyl-based FRET donor-acceptor fluorophores. H-Probe could self-assemble into stable nanomicelles in aqueous phase. Under normoxia, the FAM fluorescence was originally quenched by Dabcyl *via* FRET process. However, the tumor hypoxia would terminate the FRET process with the fluorescence recovery of FAM for hypoxia imaging. Moreover, in the presence of oxygen and light irradiation, H-Probe could generate the singlet oxygen for robust photodynamic therapy in incubation time- and concentration-dependent manners. After intravenous injection, H-Probe-induced photodynamic therapy could efficiently restrain the tumor growth with a minimized side effect. This FRET-based simultaneous hypoxia imaging and photodynamic therapy strategy would inspire the development of constructing theranostic nanoplatform for tumor precision therapy.

EXPERIMENT

Material

Rink amine resin (0.38 mmol/g), N-fluorenyl-9-methoxycarbonyl (Fmoc)-protected amino acid of Fmoc-Lys(Dabcyl)-OH and Fmoc-Lys(Mtt)-OH, 1-hydroxybenzotriazole (HOBt), o-benzotriazole-N,N,N′,N′-tetramethyluroniumhexaflorophosphate (HBTU) were obtained from GL Biochem (Shanghai, China) Ltd. Mito-Tracker Green, 3,3′-dioctadecyloxacarbocyanine perchlorate (DiO), singlet oxygen sensor green (SOSG), annexin V-FITC, Hoechst 33342 and 2′,7′-dichloroflorescein diacetate (DCFH-DA) were provided by Beyotime (China). Fmoc-NH-PEG_8-CH_2CH_2COOH was provided by Biomatrik Inc. Hydrazine hydrate, trifloroacetic acid (TFA), diisopropylethylamine (DIEA), Protoporphyrin IX (PpIX), 5(6)-Carboxyfluorescein (FAM) and triisopropylsilane (TIS) were purchased from Aladdin Reagent Co. Ltd. (China). LysoTracker Green, Cell Counting Kit (CCK-8) and Calcein-AM/PI Double Stain Kit were purchased from Yeasen Biotech Co. Ltd. (China). Dulbecco's modified Eagle's medium (DMEM), Dulbecco's phosphate buffered saline (PBS), fetal bovine serum (FBS), antibiotics, and penicillin-streptomycin were provided by Invitrogen Corp.

The molecular weight was measured by electrospray ionization-mass spectrometry (ESI-MS, Finnigan LCQ advantage). Particle size was analyzed by Nano-ZS ZEN 3600 (Malvern) and transmission electron microscopy (TEM, JEOL-1400 PLUS). The zeta potential was detected by NanoBrook 90Plus Zeta (Brookhaven). Inverted

microscope was applied to picture the H&E staining of tissues. Fluorescence was recorded by LS55 luminescence spectrometer (Perkin-Elmer). UV-vis absorbance was recorded by UV-vis spectrophotometry Lambda 35 (Perkin-Elmer). The intracellular fluorescence was shown by confocal laser scanning microscope (CLSM, LSM 880, Carl Zeiss). The *in vitro* and *in vivo* photodynamic therapy (PDT) was conducted using 630 nm LED light (power intensity: 29.8 mW cm^{-2}) and 630 nm He-Ne laser (power intensity: 320 mW cm^{-2}), respectively. The cell viability was measured by microplate reader (Bio-Rad) and flow cytometry (Amnis, Merck millipore).

Synthesis and Characterization of H-Probe

H-Probe was synthesized by using standard solid phase peptide synthesis (SPPS) method as pervious reports and it was stocked at −20°C in the shield of light for later use. The molecular weight of H-Probe was characterized by ESI-MS. The particle size of H-Probe in water, PBS or 10% FBS/PBS containing 0.1% DMSO was analyzed by Nano-ZS ZEN 3600. And the zeta potential was detected by NanoBrook 90Plus Zeta. The morphology of H-Probe was observed by TEM. Moreover, the UV-vis absorbance of H-Probe at the concentration of 25 μM was recorded by UV-vis spectrophotometry.

Cell Culture

Murine mammary carcinoma (4T1) cells were incubated in DMEM medium containing 10% FBS and 1% antibiotics in an atmosphere of 5% CO2 at 37°C.

Fluorescence Recovery Measurement

Above all, in the presence or absence of sodium hydrosulfite, the FAM fluorescence recovery of H-Probe in PBS (200 mM, pH 7.4) containing 1% DMSO was monitored by using LS55 luminescence spectrometer. Moreover, the cellular fluorescence recovery of H-Probe was also detected by CLSM and flow cytometry. Briefly, 4T1 cells were seeded and cultured for 24 h. Then the cells were treatment with H-Probe (50 μM) for another 24 h in normoxia (21% O_2) or hypoxia (1% O_2). On the one hand, the cells were washed with PBS for CLSM observation. On the other hand, the cells were washed and collected for flow cytometry analysis.

ROS Detection

In this work, the ROS generation was detected by using fluorescence spectrometer, CLSM and flow cytometry. For fluorescence detection, SOSG was used as the sensor of ROS. In brief, in the presence or absence of light irradiation, H-Probe (30 μM) was incubated with SOSG (5 μM) in PBS under normoxia (21% O_2) or hypoxia (1% O_2). PBS mixed with SOSG (5 μM) was used as the control. At the predetermined time, the fluorescence intensity of H-Probe was recorded. Additionally, after treatment with SOSG (5 μM), the fluorescence changes of H-Probe (30 μM) were also measured every minute under light irradiation or in the shield of light at the scheduled time.

For CLSM and flow cytometry analysis, DCFH-DA was used as the indicator of ROS. In brief, 4T1 cells were seeded and cultured for 24 h. Then the cells were treatment with H-Probe (30 μM) for another 4 h in normoxia (21% O_2) or hypoxia (1% O_2). After washed with PBS, the cells were incubated with DCFH-DA (10 μM) for 20 min. With or without light irradiation (5 min), the fluorescence in 4T1 cells was imaged by CLSM. For flow cytometry analysis, 4T1 cells were treated with H-Probe (5 μM) for 4 h in normoxia (21% O_2) or hypoxia (1% O_2). Then the cells were washed, collected and then incubated with DCFH-DA for 20 min. After that, the cells were exposed to light for 200 s or incubated in the dark. At last, the intracellular fluorescence was analyzed by flow cytometry.

Cellular Uptake and Subcellular Localization

Firstly, 4T1 cells were seeded and cultured for 24 h. Then, the cells were incubated with H-Probe (50 μM) for 4 h. After washed with PBS, the cells were stained with Hoechst 33342, LysoTracker Green and MitoTracker Green for 20, 15, 30, and 20 min, respectively. Subsequently, the cells washed and observed by CLSM.

Cytotoxicity of H-Probe

The cytotoxicity of H-Probe was evaluated by CCK-8 assay, live/dead cell staining assay, cell apoptosis assay and trypan blue staining assay. For CCK-8 assay, 4T1 cells were seeded in 96 -well plates and cultured for 24 h. Then the cells were incubated with gradient concentrations of H-Probe for 12 h under normoxia (21% O_2) or hypoxia (1% O_2). Then the cells were exposed to LED light for 200 s (630 nm, power intensity: 29.8 mW/cm^2) or incubated in the dark. After another 12 h, 10 μL of CCK-8 was added into every well. Four hours later, the absorbance at 450 nm was detected by the microplate reader. The relative cell viability was calculated as follows: cell viability (%) = OD (sample) × 100/OD (control), where OD (control) and OD (sample), respectively, represented the absorbance of samples in the absence and presence of H-Probe.

For live/dead cell staining assay, 4T1 cells were seeded and cultured for 24 h. Subsequently, the cells were treated with H-Probe (50 μM) for 4 h under normoxia (21% O_2) or hypoxia (1% O_2). After that, the cells were exposed to light for 1 min or incubated in the dark. Lastly, the cells were stained with Calcein-AM/ PI for 20 min and then observed by CLSM.

For cell apoptosis assay, 4T1 cells were seeded and cultured for 24 h. Then the cells were treated with H-Probe (10 μM) for 4 h under normoxia (21% O_2) or hypoxia (1% O_2). Subsequently, the cells were irradiated for 1 min or incubated in the dark. After that, the cells was stained with Annexin V-FITC/PI for 15 min. Then the cell apoptosis was analyzed by flow cytometry.

In vivo Tumor Therapy

All of the *in vivo* experiments were performed according to the guidelines of the Institutional Animal Care and Use

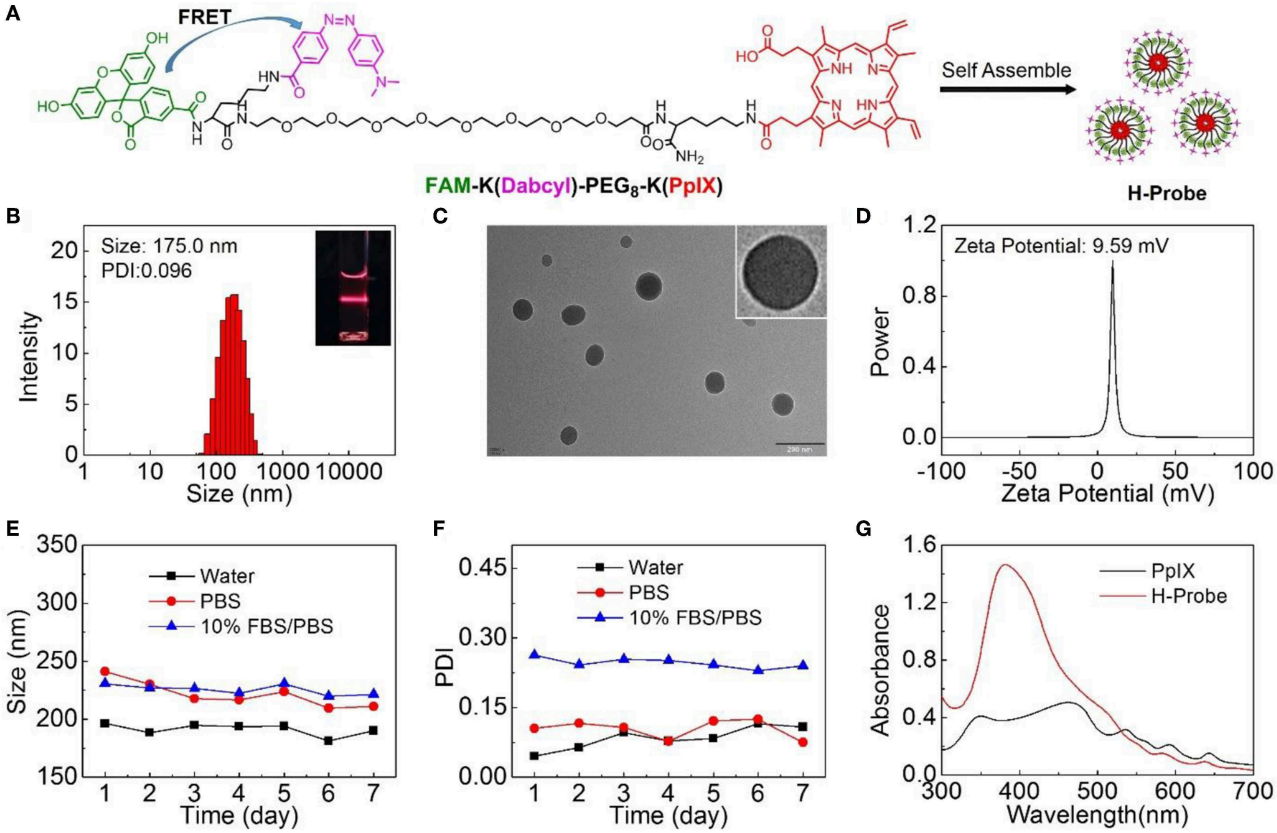

FIGURE 1 | Preparation and characterizations of H-Probe. **(A)** The chemical structure of FAM-K(Dabcyl)-PEG_8-K(PpIX) and the preparation of H-Probe. **(B)** The size distribution of H-Probe. Insert: Dindall effect of H-Probe solution. **(C)** TEM images and magnified TEM image of H-Probe. Scale bar: 200 nm. **(D)** Zeta potential of H-Probe. **(E)** The particle size and **(F)** PDI changes of H-Probe in 7 days. **(G)** The UV-vis absorbance of H-Probe and PpIX.

Committee (IACUC) of the Animal Experiment Center of Guangzhou Medical University (Guangzhou, China) as well as the Regulations for the Administration of Affairs Concerning Experimental Animals. *In vivo* tumor model was established by subcutaneously injecting 4T1 cells into the hind leg region of female BALB/c mice. 4T1 tumor-bearing mice were divided into three groups randomly (5 mice in each group), including PBS group, H-Probe group and H-Probe with light irradiation group. 4T1 tumor-bearing mice were intravenously injected with 200 μL of H-Probe for PDT at an equivalent PpIX concentration of 3 mg/kg per mouse. After administration for 12 h, the mice in light group were exposed to 630 nm He-Ne laser (power intensity: 320 mW cm^{-2}) for 5 min. The tumor volume and body weight of the mice were monitored every other day during the treatments. Tumor volume (V) was calculated as follows: V = (tumor width)^2 × (tumor length)/2. After 13 days, the mice were sacrificed and the tumors were obtained for weighing and photographing. Moreover, the tumors and the main organs (heart, liver, spleen, lung, kidney) were also analyzed through hematoxylin/eosin (H&E) staining. Besides, the blood biochemistry and blood routine of the mice were also analyzed after treatment with PBS or H-Probe for 13 days.

RESULT AND DISCUSSION

Preparation and Characterization of H-Probe

H-Probe was synthesized by solid phase synthesis method. The concrete laboratory procedure was shown in **Supplementary Figure 1**. The structure of H-Probe was verified by ESI-MS (**Supplementary Figure 2**). As illustrated in **Figure 1A**, the fluorescence of FAM was expected to be quenched by Dabcyl through the FRET process. The participation of PEG facilitated the self-assembly of H-Probe into nanomicelles. As suggested in **Figure 1B**, H-Probe exhibited a relatively narrow particle size distribution and good Tyndall effect, which indicated a high dispersion. Moreover, the morphology of H-Probe was also observed by TEM (**Figure 1C**), which further confirmed the effective self-assembly of H-Probe into spherical nanoparticles in aqueous phase. Additionally, the zeta potential of H-Probe was determined to be positive (**Figure 1D**), which was beneficial for its cellular uptake. To evaluate the stability, the changes of particle size (**Figure 1E**) and the PDI (**Figure 1F**) of H-Probe in water, PBS and PBS containing 10% FBS were monitored in 1 week. Particularly, the particle size and PDI of H-Probe in 10% FBS/PBS was found to be larger than that of in water, which might

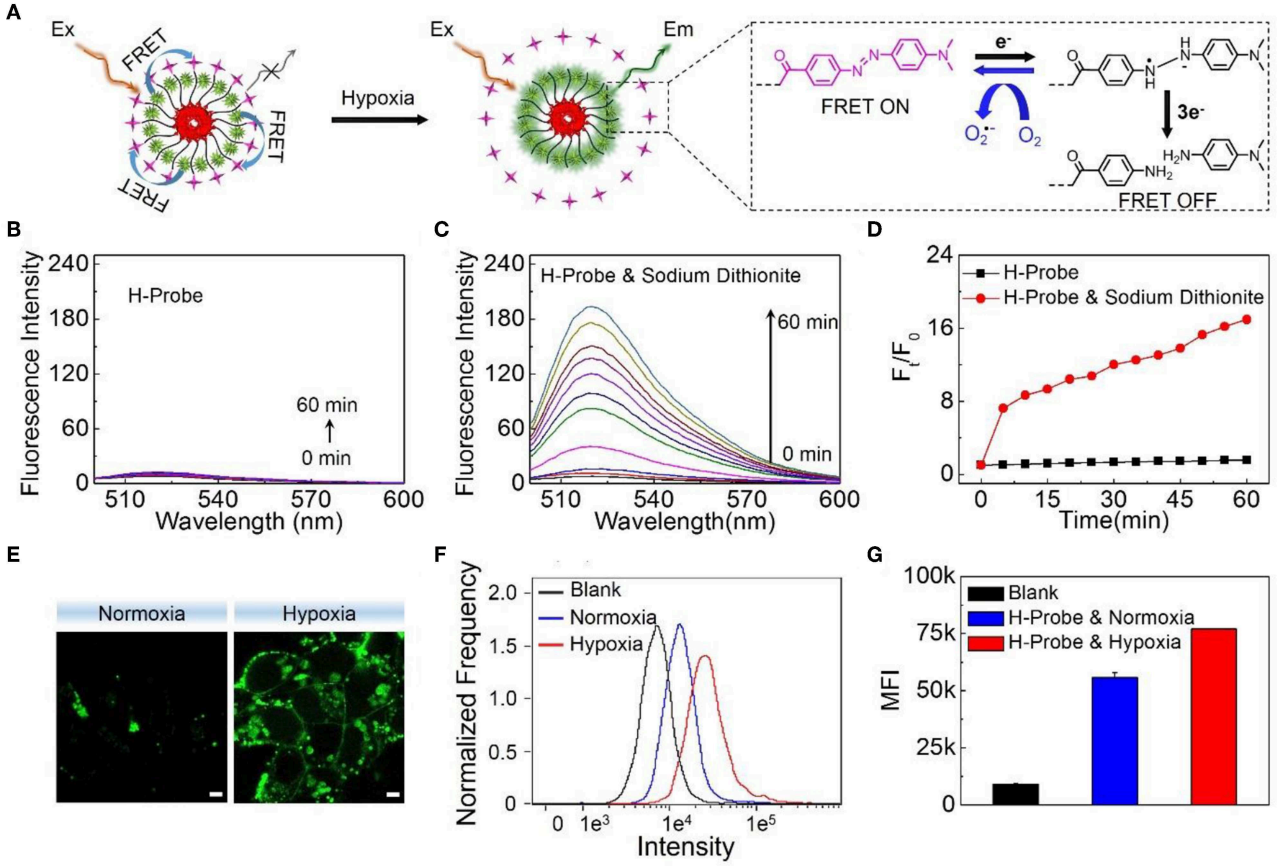

FIGURE 2 | Hypoxia imaging ability of H-Probe. **(A)** Schematic illustration and the proposed mechanism of H-Probe for hypoxia imaging. Real time fluorescence spectra of H-Probe in the **(B)** absence or **(C)** presence of sodium dithionite in 60 min. **(D)** Fluorescence changes of H-Probe in the presence or absence of sodium dithionite. **(E)** CLSM images of 4T1 cells after treatment with H-Probe under normoxia or hypoxia conditions. Scale bar: 5 μm. **(F)** Flow cytometry and **(G)** the quantitative fluorescence analysis of 4T1 cells after treatment with H-Probe under normoxia or hypoxia conditions.

be ascribed to the inevitable adsorption of positive H-Probe to serum. Even so, they still remained relatively stable, which was important for its following hypoxia imaging. Moreover, the UV-vis absorbance of H-Probe and PpIX was also characterized as shown in **Figure 1G**. Compared with PpIX, the sharp Soret band around 400 nm indicated the weakened π-π stacking induced aggregation, demonstrated that the modification of PEG could improve the physicochemical property of PpIX. Due to the improved hydrophobic and aggregation behavior of PpIX, H-Probe would possess an enhanced stability the solubility, which would be favorable to generate ROS for PDT against hypoxic tumor.

Hypoxia Imaging Ability of H-Probe

Under the normoxic condition, the FRET between FAM and Dabcyl could induce the fluorescence quenching. However, the azobenzene bond in H-Probe might be reduced under hypoxic condition, resulting in the interruption of the FRET process with the fluorescence recovery of FAM (**Figure 2A**). Significantly, H-Probe demonstrated a great potential for hypoxia imaging. To confirm it, sodium dithionite as a chemical mimic of azoreductase was used to break the azobenzene bond and terminate the FRET process. Above all, the fluorescence spectra of H-Probe was recorded in the absence of sodium dithionite. As shown in **Figure 2B**, the fluorescence intensity was found to be very low due to the FRET-induced fluorescence quenching. What's more, no obvious fluorescence changes were observed in 60 min, implying the good stability of H-Probe. However, with the addition of sodium dithionite, the fluorescence intensity was enhanced significantly in a time-dependent manner (**Figure 2C**), which was further confirmed by the relative fluorescence changes (**Figure 2D**). These investigations demonstrated that the reduction of the azobenzene bond would really interrupt the FRET and recover the fluorescence of FAM. To determine whether the hypoxia could also trigger the fluorescence recovery, 4T1 cells were treated with H-Probe under normoxia or hypoxia for CLSM observations. As displayed in **Figure 2E**, stronger green fluorescence was found in the cells under hypoxia rather than that of under normoxia, which verified the hypoxia-induced FAM fluorescence recovery. Similar result was also confirmed by the quantitative flow cytometry analysis (**Figures 2F,G**). Based on the above, it could be concluded that H-Probe could be applied for hypoxia imaging by reducing the azobenzene bond and interrupting the FRET to recover the FAM fluorescence.

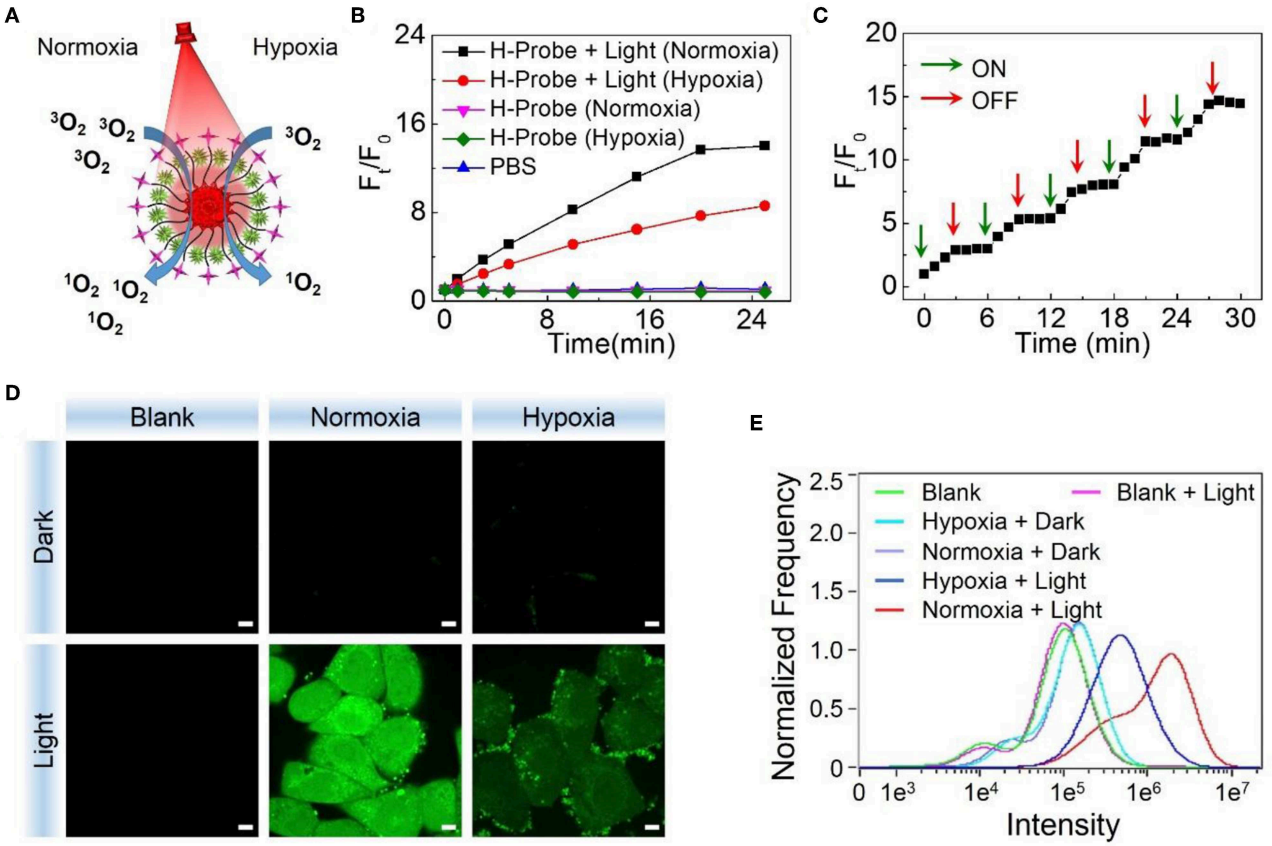

FIGURE 3 | PDT potential of H-Probe. **(A)** Schematic illustration of H-Probe for PDT under normoxia and hypoxia conditions. **(B)** Time related SOSG fluorescence changes of H-Probe under normoxia or hypoxia conditions in the presence or absence of light irradiation. **(C)** Singlet oxygen production of H-Probe under ON-OFF light irradiation. **(D)** CLSM images and **(E)** Flow cytometry analysis of 4T1 cells after treatment with H-Probe under normoxia or hypoxia conditions in the presence or absence of light irradiation. Scale bar: 5 μm.

ROS Generation by H-Probe

After verifying the hypoxia imaging ability, the ROS generation of H-Probe under normoxia or hypoxia was evaluated subsequently. As illustrated in **Figure 3A**, singlet oxygen ($^1O_2$) as a kind of toxic ROS, could be generated in the presence of light irradiation, photosensitizer and oxygen. When without light irradiation, negligible SOSG fluorescence changes were found after treatment with H-Probe in normoxia or hypoxia (**Figure 3B**), suggesting little production of ROS. Once exposed to the light, the fluorescence was obviously increased. H-Probe with light under normoxia exhibited stronger SOSG fluorescence than that of under hypoxia, implying the importance of oxygen for producing ROS. Besides, the SOSG fluorescence changes under ON-OFF irradiation indicated the controllability of H-Probe by light to generate ROS (**Figure 3C**), which highlighted the advantages of PDT for tumor therapy. Further, the cellular ROS generation was also assessed by CLSM and flow analysis. As shown in **Figures 3D,E**, 4T1 cells in the dark with various treatments exhibited ignorable fluorescence, reflecting the indispensability of light. Due to the limitation of oxygen, 4T1 cells treated with H-Probe and light under hypoxia still showed weak green fluorescence. Conversely, intense green fluorescence was observed in 4T1 cells under normoxia after treatment with H-Probe and light, indicating a great potential for PDT. Moreover, the flow analysis also reflected the similar phenomena, suggesting the light- and oxygen-related production of ROS by H-Probe.

In vitro PDT Evaluation of H-Probe

Prior to evaluating the PDT effect of H-Probe *in vitro*, its cellular uptake behavior was investigated by CLSM. As displayed in **Supplementary Figure 3**, after treatment with 4T1 cells for 4 h, obvious red fluorescence of H-Probe was found in cells, indicating an efficient cellular uptake. Besides, there was little overlap between the red H-Probe fluorescence and the blue Hoechst 33342 fluorescence, illustrating that the internalized H-Probe mainly existed in cytoplasm. Furthermore, H-Probe was found to overlay well with LysoTracker Green while separate with MitoTracker Green, implying that H-Probe was internalized into cells by cellular endocytosis pathway.

Subsequently, the internalized H-Probe induced cytotoxicity was evaluated by CCK-8 assay. Nanoprobes for hypoxia imaging

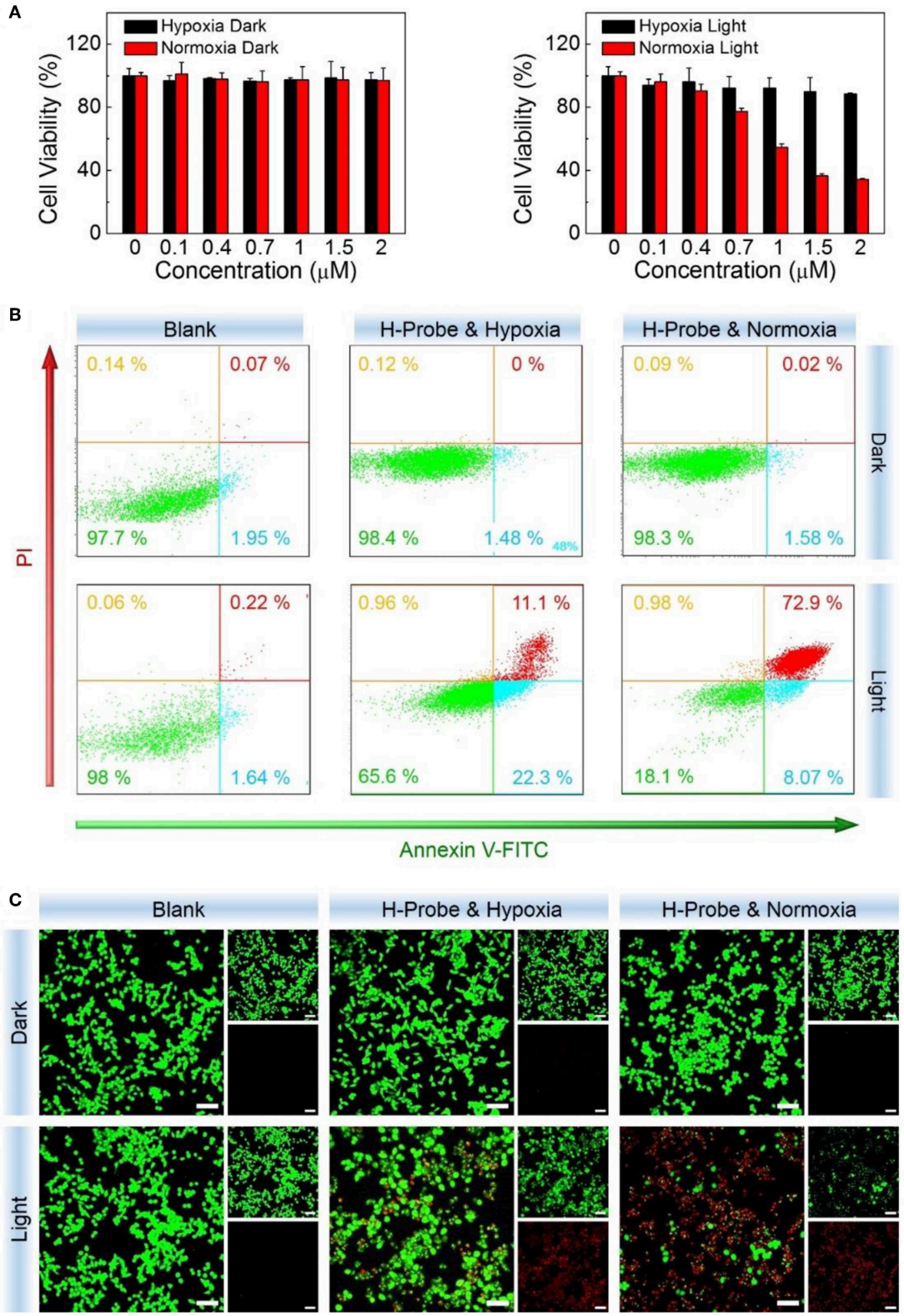

FIGURE 4 | PDT studies of H-Probe *in vitro*. Anti-proliferation ability of H-Probe against 4T1 cells under normoxia or hypoxia conditions in the presence or absence of light irradiation measured by **(A)** CCK-8 kit, **(B)** flow cytometry, and **(C)** live/dead cells staining assay. Scale bar: 5 μm.

should have good biocompatibility with a low cytotoxicity. Based on this, the dark toxicity of H-Probe was firstly detected. As shown in **Figure 4A**, regardless of the oxygen content, H-Probe had very low cytotoxicity, which was favorable for hypoxia imaging. Moreover, owing to the restriction of oxygen, H-Probe in hypoxia also caused a weak PDT effect under light irradiation. However, H-Probe in normoxia exhibited a concentration-dependent photo toxicity, suggesting a robust PDT effect. In addition, the cytotoxicity of H-Probe was also assessed by cell apoptosis assay. As displayed in **Figure 4B**, when without light irradiation, very few cells was in apoptosis state. Even after adding the light, H-Probe under hypoxia only triggered about a third of 4T1 cells apoptosis, reflecting a limited PDT effect. However, after improving the oxygen content, more than 80% of the cells were apoptotic after treatment with H-Probe and light under normoxia. Similar results were also observed by the live/dead cell staining assay (**Figure 4C**). Intense red fluorescence and very weak green fluorescence were found in 4T1 cells treated with H-Probe and light under normoxia, demonstrating the best PDT effect against 4T1 cells.

In vivo Anti-tumor Study of H-Probe

To further investigate the anti-tumor effect *in vivo*, H-Probe was intravenously injected into the 4T1 tumor-bearing mice for PDT. As indicated in **Figure 5A**, just like PBS, H-Probe without light could scarcely inhibited the tumor growth. But H-Probe-induced PDT exhibited an excellent therapeutic effect on 4T1 tumor. Not only that, the relative body weight kept increasing slowly during the treatment (**Figure 5B**). These results highlighted the advantages of H-Probe for the effective PDT with a low system toxicity *in vivo*. After treatment with 13 days, the tumors were harvested for weighting and photographing. As shown in **Figures 5C,D**, compared with PBS and H-Probe without light, H-Probe with light significantly inhibited the tumor growth. Besides, the tumor tissues were also sliced for H&E staining analysis. As displayed in **Figure 5E**, tumor tissues of the mice treated with PBS or H-Probe without light were mainly filled with lots of tumor cells, which exhibited no obvious damage. However, there were many cells without nuclei or with destroyed nuclei in tumors treated with H-Probe and light, suggesting a robust PDT against tumors. Furthermore, the normal tissues of

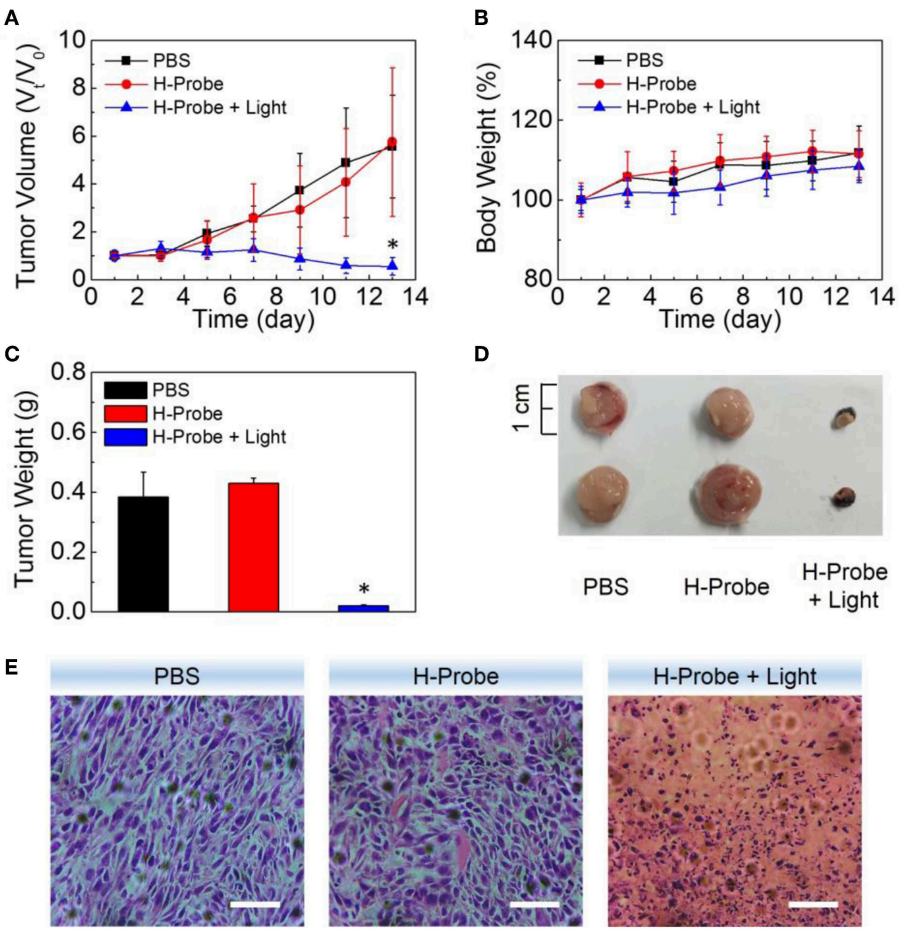

FIGURE 5 | Anti-tumor studies of H-Probe *in vivo*. **(A)** The relative tumor volume and **(B)** the body weight changes of the mice after treatment with PBS, H-Probe, H-Probe and light in 13 days. V_0 and M_0 represented the tumor volume and body weight of the mice at the first day when without any treatments. **(C)** The average tumor weight, **(D)** the represented tumor tissues and **(E)** the H&E staining images of the sacrificed tumor tissues at the 13th day.

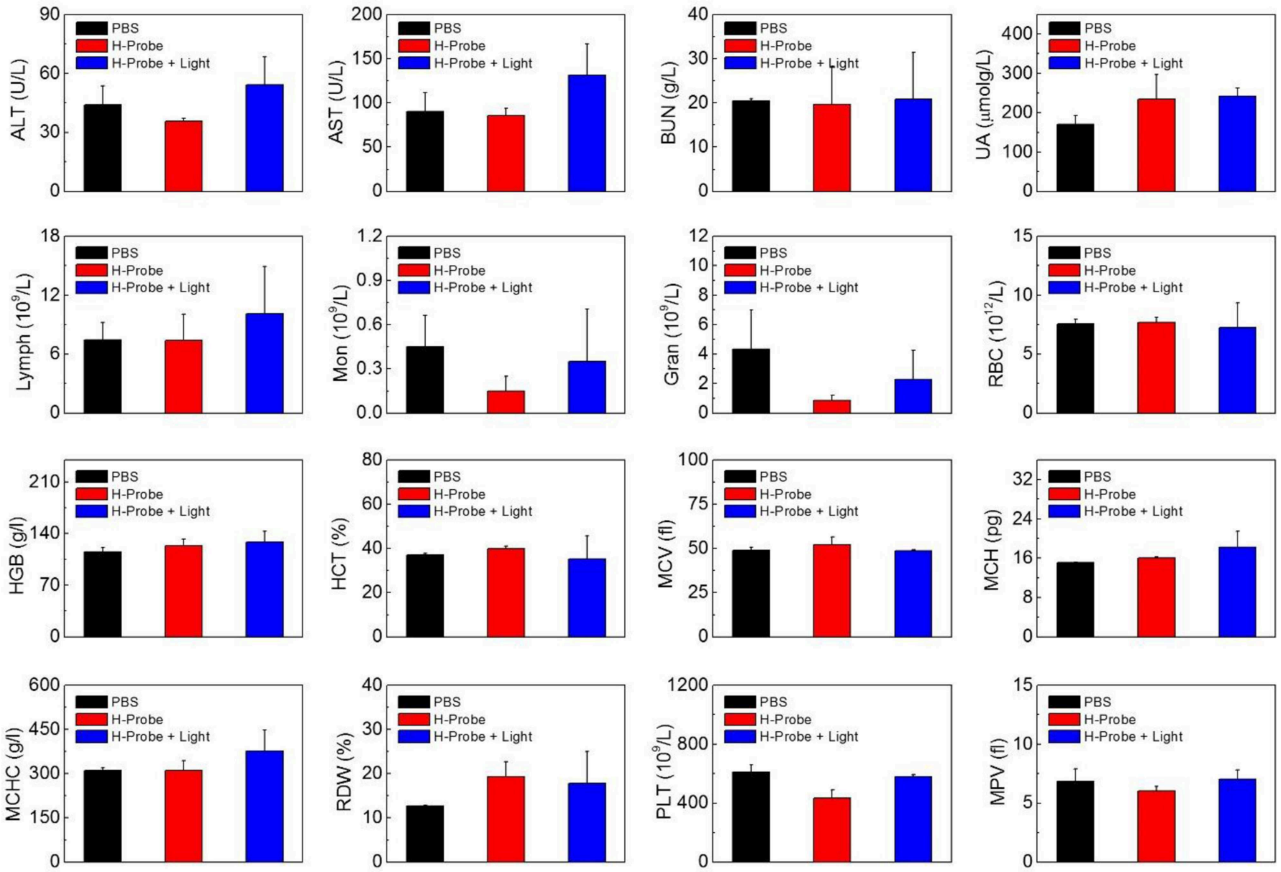

FIGURE 6 | Biocompatibility of H-Probe *in vivo*. ALT, AST, BUN, UA analysis and the hematological parameters of the mice after treatment with PBS, H-Probe, H-Probe, and light at the 13th day.

heart, liver, spleen, lung and kidney were also performed for H&E staining (**Supplementary Figure 4**). After treatment with H-Probe and light, the morphologies of cells in these tissues were basically normal, indicating no apparent toxicity of this PDT to main organs. However, it should be noted that an obvious tumor metastasis was found in liver of the mice treated with PBS or H-Probe without light due to the ineffective treatments. What's more, the blood biochemistry and blood routine of the mice were also carried out to evaluate the biocompatibility of H-Probe. As illustrated in **Figure 6**, although there were some differences in the detection results of the mice between various groups, they were still in the normal range, verifying that H-Probe possessed good biocompatibility and it caused no significant system toxicity. Based on the above, it could be concluded that H-Probe realized a robust PDT *in vivo* under light irradiation to inhibit the tumor growth and metastasis with a minimized side effect.

CONCLUSION

In summary, we designed a smart theranostic nanoprobe for hypoxia imaging and photodynamic tumor therapy. Owing to the FRET process, the fluorescence of FAM could be effectively quenched by Dabcyl in the nanoprobe. However, an effective reduction of azobenzene bond in Dabcyl would terminate the FRET process with a significant fluorescence recovery of FAM, which was able to be used for hypoxia imaging *in vitro*. Furthermore, the photosensitizer of PpIX in nanoprobe could achieve an efficient PDT against hypoxic tumor with a low side effect. In a word, based on FRET, this nanoprobe realized not only the hypoxia imaging but also the photodynamic tumor therapy, which provided a new insight for developing theranostic nanoplatform in tumor precision therapy.

DATA AVAILABILITY STATEMENT

All datasets generated for this study are included in the article/**Supplementary Material**.

ETHICS STATEMENT

The animal study was reviewed and approved by Institutional Animal Care and Use Committee (IACUC) Animal Experiment Center of Guangzhou Medical University (Guangzhou, China).

AUTHOR CONTRIBUTIONS

JF prepared materials and carried out *in vivo* experiments. GF helped to perform *in vitro* experiments. PY helped to characterize materials and incubate cells. FD and XZ helped to characterize materials. LL helped to culture cells. XY supervised the work. HC supervised the work and wrote the manuscript. SL provided an idea and designated the whole research.

FUNDING

This study was financially supported by National Natural Science Foundation of China (81330007, U1601227, 51802049, 51803086), Natural Science Foundation of Guangdong Province (2018030310283), Science and Technology Programs of Guangdong Province (2015B020225006), Science and Technology Programs of Guangzhou (201904010324), Young Elite Scientist Sponsorship Program by CAST (2018QNRC001) and Open Research Fund of the Key Laboratory of Molecular Target & Clinical Pharmacology (Guangzhou Medical University).

SUPPLEMENTARY MATERIAL

The Supplementary Material for this article can be found online at: https://www.frontiersin.org/articles/10.3389/fchem.2019.00868/full#supplementary-material

REFERENCES

Cai, Q., Yu, T., Zhu, W. P., Xu, Y. F., and Qian, X. H. (2015). A turn-on fluorescent probe for tumor hypoxia imaging in living cells. *Chem. Commun.* 51, 14739–14741. doi: 10.1039/C5CC05518K

Castano, A. P., Mroz, P., and Hamblin, M. R. (2006). Photodynamic therapy and anti-tumour immunity. *Nat. Rev. Cancer* 6, 535–545. doi: 10.1038/nrc1894

Celli, J. P., Spring, B. Q., Rizvi, I., Evans, C. L., Samkoe, K. S., Verma, S., et al. (2010). Imaging and photodynamic therapy: mechanisms, monitoring, and optimization. *Chem. Rev.* 110, 2795–2838. doi: 10.1021/cr900300p

Chatterjee, D. K., Fong, L. S., and Zhang, Y. (2008). Nanoparticles in photodynamic therapy: an emerging paradigm. *Adv. Drug Deliv. Rev.* 60, 1627–1637. doi: 10.1016/j.addr.2008.08.003

Cheng, H., Fan, G. L., Fan, J. H., Yuan, P., Deng, F. A., Qiu, X. Z., et al. (2019a). Epigenetics-inspired photosensitizer modification for plasma membrane-targeted photodynamic tumor therapy. *Biomaterials* 224, 119497. doi: 10.1016/j.biomaterials.2019.119497

Cheng, H., Fan, J. H., Zhao, L. P., Fan, G. L., Zheng, R. R., Qiu, X. Z., et al. (2019b). Chimeric peptide engineered exosomes for dual-stage light guided plasma membrane and nucleus targeted photodynamic therapy. *Biomaterials* 211, 14–24. doi: 10.1016/j.biomaterials.2019.05.004

Cheng, H., Zhu, J. Y., Li, S. Y., Zeng, J. Y., Lei, Q., Chen, K. W., et al. (2016). An O_2 self-sufficient biomimetic nanoplatform for highly specific and efficient photodynamic therapy. *Adv. Funct. Mater.* 26, 7847–7860. doi: 10.1002/adfm.201603212

Conley, S. J., Gheordunescu, E., Kakarala, P., Newman, B., Korkaya, H., Heath, A. N., et al. (2011). Antiangiogenic agents increase breast cancer stem cells via the generation of tumor hypoxia. *Proc. Natl. Acad. Sci. U.S.A.* 109, 2784–2789. doi: 10.1073/pnas.1018866109

Cui, L., Zhong, Y., Zhu, W. P., Xu, Y. F., Du, Q. S., Wang, X., et al. (2011). A new prodrug-derived ratiometric fluorescent probe for hypoxia: high selectivity of nitroreductase and imaging in tumor cell. *Org. Lett.* 13, 928–931. doi: 10.1021/ol102975t

Dalton, W. S. (1999). The tumor microenvironment as a determinant of drug response and resistance. *Drug Resist. Update.* 2, 285–288. doi: 10.1054/drup.1999.0097

Dolmans, D. E. J. G. J., Fukumura, D., and Jain, R. K. (2003). Photodynamic therapy for cancer. *Nat. Rev. Cancer* 3, 380–387. doi: 10.1038/nrc1071

Ethirajan, M., Chen, Y. H., Joshi, P., and Pandey, R. K. (2011). The role of porphyrin chemistry in tumor imaging and photodynamic therapy. *Chem. Soc. Rev.* 40, 340–362. doi: 10.1039/B915149B

Gajewski, T., Schreiber, H., and Fu, Y. X. (2013). Innate and adaptive immune cells in the tumor microenvironment. *Nat. Immunol.* 14, 1014–1022. doi: 10.1038/ni.2703

Kessenbrock, K., Plaks, V., and Werb, Z. (2010). Matrix metalloproteinases: regulators of the tumor microenvironment. *Cell* 141, 52–67. doi: 10.1016/j.cell.2010.03.015

Li, S. Y., Cheng, H., Qiu, W. X., Zhang, L., Wan, S. S., Zeng, J. Y., et al. (2017). Cancer cell membrane-coated biomimetic platform for tumor targeted photodynamic therapy and hypoxia-amplified bioreductive therapy. *Biomaterials* 142, 149–161. doi: 10.1016/j.biomaterials.2017.07.026

Li, S. Y., Jiang, X. Y., Zheng, R. R., Zuo, S. J., Zhao, L. P., Fan, G. L., et al. (2018a). An azobenzene-based heteromeric prodrug for hypoxia-activated chemotherapy by regulating subcellular localization. *Chem. Commun.* 54, 7983–7986. doi: 10.1039/C8CC03430C

Li, S. Y., Xie, B. R., Cheng, H., Li, X. C., Zhang, M. K., Qiu, W. X., et al. (2018b). A biomimetic theranostic O_2-meter for cancer targeted photodynamic therapy and phosphorescence imaging. *Biomaterials* 151, 1–12. doi: 10.1016/j.biomaterials.2017.10.021

Li, X., Lee, S., and Yoon, J. (2018). Supramolecular photosensitizers rejuvenate photodynamic therapy. *Chem. Soc. Rev.* 47, 1174–1188. doi: 10.1039/C7CS00594F

Li, X. S., Kolemen, S., Yoon, J., and Akkaya, E. U. (2016). Activatable photosensitizers: agents for selective photodynamic therapy. *Adv. Funct. Mater.* 27:1604053. doi: 10.1002/adfm.201604053

Liang, J., Wu, W. L., Xu, X. D., Zhuo, R. X., and Zhang, X. Z. (2014). pH responsive micelle self-assembled from a new amphiphilic peptide as anti-tumor drug carrier. *Colloid. Surf. B Biointerfaces* 114, 398–403. doi: 10.1016/j.colsurfb.2013.10.037

Liu, J. N., Bu, W. B., and Shi, J. L. (2017). Chemical design and synthesis of functionalized probes for imaging and treating tumor hypoxia. *Chem. Rev.* 117, 6160–6224. doi: 10.1021/acs.chemrev.6b00525

Liu, J. N., Liu, Y., Bu, W. B., Bu, J. W., Sun, Y., Du, J. L., et al. (2014). Ultrasensitive nanosensors based on upconversion nanoparticles for selective hypoxia imaging *in vivo* upon near-infrared excitation. *J. Am. Chem. Soc.* 136, 9701–9709. doi: 10.1021/ja5042989

Lucky, S. S., Soo, K. C., and Zhang, Y. (2015). Nanoparticles in photodynamic therapy. *Chem. Rev.* 115, 1990–2042. doi: 10.1021/cr5004198

Piao, W., Tsuda, S., Tanaka, Y., Maeda, S., Liu, F., Takahashi, S., et al. (2013). Development of azo-based fluorescent probes to detect different levels of hypoxia. *Angew. Chem. Int. Edit.* 52, 13028–13032. doi: 10.1002/anie.201305784

Rankin, E. B., and Giaccia, A. J. (2016). Hypoxic control of metastasis. *Science* 352, 175–180. doi: 10.1126/science.aaf4405

Shen, Y. Z., Shuhendler, A. J., Ye, D. J., Xu, J. J., and Chen, H. Y. (2016). Two-photon excitation nanoparticles for photodynamic therapy. *Chem. Soc. Rev.* 45, 6725–6741. doi: 10.1039/C6CS00442C

Sun, Y. (2016). Tumor microenvironment and cancer therapy resistance. *Cancer Lett.* 1, 205–215. doi: 10.1016/j.canlet.2015.07.044

Sun, Y., Campisi, J., Higano, C., Beer, T. M., Porter, P., Coleman, I., et al. (2012). Treatment-induced damage to the tumor microenvironment promotes

prostate cancer therapy resistance through WNT16B. *Nat. Med.* 18, 1359–1368. doi: 10.1038/nm.2890

Whiteside, T. L. (2008). The tumor microenvironment and its role in promoting tumor growth. *Oncogene* 27, 5904–5912. doi: 10.1038/onc.2008.271

Yu, Q., Huang, T. C., Li, Y. P., Wei, H. J., Liu, S. J., Huang, W., et al. (2017). Rational design of a luminescent nanoprobe for hypoxia imaging *in vivo* via ratiometric and photoluminescence lifetime imaging microscopy. *Chem. Commun.* 53, 4144–4147. doi: 10.1039/C7CC00668C

Zhang, S. J., Hosaka, M., Yoshihara, T., Negishi, K., Lida, Y., Tobita, S., et al. (2010). Phosphorescent light–emitting iridium complexes serve as a hypoxia-sensing probe for tumor imaging in living animals. *Cancer Res.* 70, 4490–4498. doi: 10.1158/0008-5472.CAN-09-3948

Zheng, X. C., Wang, X., Mao, H., Wu, W., Liu, B. R., and Jiang, X. Q. (2015). Hypoxia-specific ultrasensitive detection of tumours and cancer cells *in vivo*. *Nat. Commun.* 6:5834. doi: 10.1038/ncomms683

Zhou, J., Schmid, T., Schnitzer, S., and Brune, B. (2006). Tumor hypoxia and cancer progression. *Cancer Lett.* 237, 10–21. doi: 10.1016/j.canlet.2005.05.028

Conflict of Interest: The authors declare that the research was conducted in the absence of any commercial or financial relationships that could be construed as a potential conflict of interest.

frontiers in Chemistry

ORIGINAL RESEARCH
published: 14 February 2020
doi: 10.3389/fchem.2020.00001

Supramolecular Photothermal Nanomedicine Mediated Distant Tumor Inhibition via PD-1 and TIM-3 Blockage

Tong-Yi Huang[1†], Guang-Liang Huang[1†], Chun-Yang Zhang[1†], Bo-Wen Zhuang[1], Bao-Xian Liu[1], Li-Ya Su[1], Jie-Yi Ye[1], Ming Xu[1], Ming Kuang[1,2] and Xiao-Yan Xie[1*]*

[1] Department of Medical Ultrasonics, Institute of Diagnostic and Interventional Ultrasound, First Affiliated Hospital of Sun Yat-Sen University, Guangzhou, China, [2] Department of Liver Surgery, First Affiliated Hospital of Sun Yat-Sen University, Guangzhou, China

OPEN ACCESS

Edited by:
Tianjiao Ji,
Boston Children's Hospital, Harvard Medical School, United States

Reviewed by:
Xiaoran Deng,
Boston Children's Hospital, Harvard Medical School, United States
Hu Xiong,
Nankai University, China

***Correspondence:**
Ming Xu
xu2004m@sina.com
Xiao-Yan Xie
xxy1992sys@163.com

[†] These authors have contributed equally to this work

Specialty section:
This article was submitted to Supramolecular Chemistry, a section of the journal Frontiers in Chemistry

Received: 30 November 2019
Accepted: 01 January 2020
Published: 14 February 2020

Citation:
Huang T-Y, Huang G-L, Zhang C-Y, Zhuang B-W, Liu B-X, Su L-Y, Ye J-Y, Xu M, Kuang M and Xie X-Y (2020) Supramolecular Photothermal Nanomedicine Mediated Distant Tumor Inhibition via PD-1 and TIM-3 Blockage. Front. Chem. 8:1. doi: 10.3389/fchem.2020.00001

Supramolecular nanoparticles for photothermal therapy (PTT) have shown promising therapeutic efficacy in the primary tumor and great potential for turning the whole-body immune microenvironment from "cold" to "hot," which allows for the simultaneous treatment of the primary tumor and the metastatic site. In this work, we develop a liposome-based PTT nanoparticle through the self-assembly of FDA-approved intravenous injectable lipids and a photothermal agent, indocyanine green (ICG). The obtained ICG-liposome shows long-term storage stability, high ICG encapsulation efficiency (>95%), and enhanced near-infrared (NIR) light-triggered photothermal reaction both *in vitro* and *in vivo*. The ICG-liposome efficiently eradicated the primary tumor upon laser irradiation in two colon cancer animal models (CT26 and MC38) and promoted the infiltration of CD8 T cells to distant tumors. However, PTT from ICG-liposome shows only a minimal effect on the inhibition of distant tumor growth in long-term monitoring, predicting other immunosuppressive mechanisms that exist in the distant tumor. By immune-profiling of the tumor microenvironment, we find that the distant tumor growth after PTT highly correlates to compensatory upregulation of immune checkpoint biomarkers, including program death-1 (PD-1), T-cell immunoglobulin, and mucin domain-containing protein 3 (TIM-3), in tumor-infiltrating CD8 T cells. Based on this mechanism, we combine dual PD-1 and TIM-3 blockade with PTT in an MC38 tumor model. This combo successfully clears the primary tumor, generates a systemic immune response, and inhibits the growth of the distant tumor. The ICG-liposome-combined PD-1/TIM-3 blockade strategy sheds light on the future clinical use of supramolecular PTT for cancer immunotherapy.

Keywords: liposome, ICG, photothermal therapy, distant tumor, PD-1, TIM-3, immune checkpoint blockade

INTRODUCTION

In clinical practice, the clearance of the primary tumor can be realized through surgical removal, thermal-related ablation, and radiation (Chu and Dupuy, 2014; Lee et al., 2014; Chen et al., 2016a; Yang et al., 2017), while the metastatic site often escapes the locoregional destruction due to the limitation of tumor detection or accessibility. Unsolved metastasis is one of the major causes

of tumor recurrence and treatment failure in cancer patients (Mahnken et al., 2013; Sag et al., 2016; Hoffmann, 2017). Compared to traditional surgical removal, ablation and radiation not only help the eradication of the primary tumor but also serve as effective ways to promote tumor-related immune responses, which is also known as the transformation from cold tumor to hot tumor (Finkelstein et al., 2011; Mehta et al., 2016; Tang et al., 2016). As highly focused therapies, ablation and radiation have multiple immunogenic properties, such as inducing immunogenic tumor cell death and initiating tumor antigen presentation, while the host immune system is not compromised (Corso et al., 2011; Rubner et al., 2012; Chu and Dupuy, 2014). Furthermore, they can cause local inflammation mediated by immediate neutrophil infiltration, which can make the cold tumor hot by initiating tumor infiltrating lymphocytes (TILs). The improvement to tumor immune microenvironment shows great promise in controlling the whole-body tumor burden including the metastatic tumor (Slovak et al., 2017).

As one of the thermal ablative approaches, photothermal therapy (PTT) can "burn" tumor with heat generated from the absorbed optical energy by photoabsorbing agents or nanomaterials (Zha et al., 2013; Chen et al., 2016a; Rwei et al., 2017; Yang et al., 2017). The key to complete ablation of the primary tumor is the design of PTT agents that have strong light absorbance, efficient photothermal conversion, excellent biocompatibility, and abundant tumor accumulation (Liu et al., 2015). Various kinds of agents or materials have been reported as effective photothermal agents including carbon nanomaterials (Kim et al., 2015), gold nanoparticles (Ayala-Orozco et al., 2014), organic compounds (Sheng et al., 2014), and indocyanine green (ICG) (Wu et al., 2013; Zheng et al., 2013). Assembly of the supramolecular PTT particles with all FDA-approved materials can promote the clinical translation of photothermal strategy.

Even though ICG is clinically approved for near-infrared (NIR) imagery to identify neoplastic disease during the conduct of surgery, the application of ICG in PTT is limited due to its low photostability and non-tumor-specific distribution *in vivo* (Ma et al., 2013). Free ICG degrades rapidly in aqueous solutions due to the oxidation of double bonds and can be cleared by the liver quickly ($t_{1/2} \approx 2$–4 min) because of high bonding to plasma proteins (Lajunen et al., 2016). Liposomes, as supramolecular self-assembly nanomaterials, have showed promising results in *in vivo* drug delivery (Elsabahy and Wooley, 2015; Feng et al., 2015, 2016; Ji et al., 2017; Liu et al., 2018; Weldon et al., 2019). Liposomal encapsulation could greatly improve the stability and tumor targeting property of free ICG, while not affecting the PTT property (Ding et al., 2015; Ji and Kohane, 2019). Moreover, both ICG and the composition of liposomes are materials approved by FDA for intravenous (IV) injection, which will greatly guarantee the biocompatibility and future clinical translation (Liu et al., 2013; Zheng et al., 2014). Therefore, we propose a self-assembled ICG-encapsulated liposomal platform for PTT treatment.

Numerous evidences support that the ICG loaded liposome nanoparticles can effectively eradicate the primary tumor, but there are still challenges for inhibiting distant tumors. On one hand, PTT is reported to generate tumor antigens available as an *in-situ* cancer vaccine by destroying tumor cells, inducing systemic anti-tumor response to potentially eliminate metastatic tumors in mouse tumor models (Kostarelos et al., 2009; Guo et al., 2014; Tao et al., 2014) and preliminary clinical trial study (Li et al., 2010), which is called abscopal effect. However, this abscopal effect induced by PTT alone has proven to be weak and not durable (Chen et al., 2016b; Slovak et al., 2017). Recently, researchers have tried to explore the immunological changes after PTT, including inducing enhanced infiltration of $CD8^+$ T cells, enhancing the DC maturation, and increasing the secretion of pro-inflammatory cytokines (Chen et al., 2016b; Kleinovink et al., 2017). We deduce that the heat during PTT and overactivation of the immune system after PTT may cause T cell exhaustion-related immune suppression.

T cell exhaustion is a state of T cell dysfunction being well-studied nowadays and is characterized by decreased cytokine production, hypoproliferation, and diminished killing. Cell surface antigen determinants such as program death-1 (PD-1) and T-cell immunoglobulin and mucin domain-containing protein 3 (TIM-3) can be used to identify whether antigen-specific T cells are at an exhaustion stage. Coexpression of different inhibitory receptors has been associated with greater T-cell exhaustion (Fourcade et al., 2010; Wherry and Kurachi, 2015). Reported studies have shown a strong correlation between PD-1 and TIM-3 coexpression, which is a much more severe exhaustion phenotype of CD8 T cells (Sakuishi et al., 2010; Granier et al., 2017). Despite the improvement made on understanding the biologic influence of the expression of PD-1 or TIM-3 on T cell function, the link between PTT treatment and TIM-3 or PD-1 expression in distant tumors has not yet been defined.

This study aimed to implement a highly efficient and stable supramolecular photothermal system, provide new insights into T cell exhaustion-related immune-suppressive mechanisms limiting PTT efficacy, and explore the potential of immune checkpoint blockade in combination with PTT in cancer therapy. Herein, we optimized phospholipids to formulate biocompatible ICG-liposomes, which were composed of liposome as the encapsulating polymer and ICG as the inner core to enable PTT (**Scheme 1A**). We injected the ICG-liposome nanoparticles to mice that bear bilateral tumors and applied NIR-induced PTT to primary tumors. Then, we observed the distant tumor growth and characterized PTT induced immune responses as well as PD-1/TIM-3 mediated immune suppression (**Scheme 1B**). With a comprehensive understanding of the CD8 T cell-related immune microenvironment after PTT, we finally designed a combination therapy with PTT and dual PD-1/TIM-3 blockade for the treatment of distant tumor.

MATERIALS AND METHODS

Materials

Dipalmitoyl phosphatidylcholine (DPPC), phosphoethanolamine-N-[methoxy (polyethylene glycol)-2000] (DSPE-PEG-2000), and cholesterol (CHOL) were obtained from A.V.T. Pharmaceutical Co., Ltd. Company (Shanghai, China). ICG, Non-ionic surfactant Triton X-100 (TX-100), and Cell Counting Kit-8 (CCK-8) were obtained from Sigma-Aldrich.

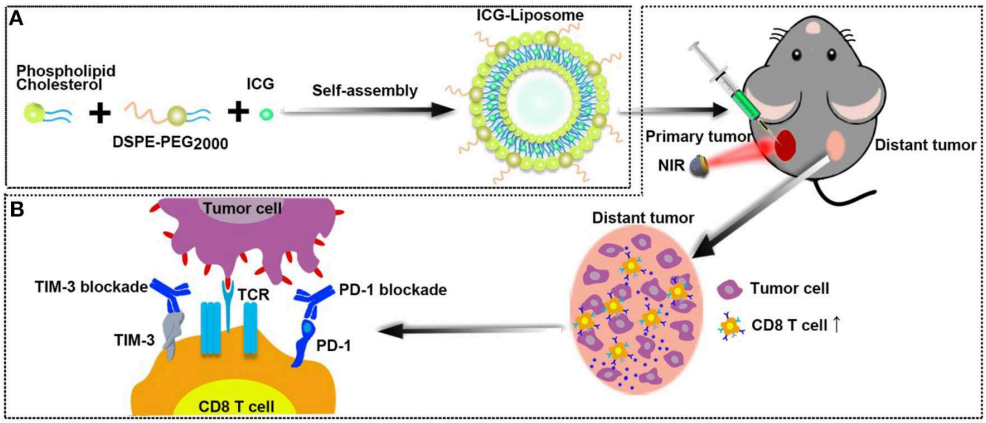

SCHEME 1 | (A) The schematic illustration for ICG-loaded liposome as a theranostic nanoplatform. **(B)** The schematic illustration of PTT in the primary tumor and immunological changes in the distant tumor after PTT with dual blockade of PD-1 and TIM-3.

Anti-PD-1 (clone: RMP1-14) and anti-TIM-3 (clone: RMT3-23) used *in vivo* were obtained from Bioxcell. Antibodies against cell surface markers for flow cytometry assay were purchased from Miltenyi and Biolegend. Fetal bovine serum (FBS), DMEM, and RPMI-1640 medium were both obtained from GIBCO Life Technologies Co. Ltd., (USA).

Preparation of ICG-Liposome Nanoparticles

ICG-loaded liposomes were fabricated using a filming-rehydration method according to the literature (Wang et al., 2014). DPPC, DSPE-PEG-2000, and CHOL were mixed in a round-bottom flask containing 16 ml of chloroform/methanol (5:3) in different ratios (7.2 mg in total). The mixture was dried with a rotary evaporator at 45°C to form a thin film. This film was then hydrated in 5 ml of water with ICG and sonicated for 5 min at 30°C. Furthermore, the obtained solution was sonicated under probe sonication for 30 s. Finally, the prepared ICG-loaded liposome was harvested by removing free ICG through ultrafiltration centrifugation procedure (Millipore, MW 100 kDa).

Nanoparticle Characterization

The morphology and size of the ICG-liposome were measured by transmission electron microscopy (TEM, JEM-2100F). The hydrodynamic size, polydispersity (PDI), and zeta potential of ICG-liposome were further measured in aqueous solutions by dynamic light scattering (DLS) using Malvern Nano ZS90 (Nano ZS, Malvern, USA).

The absorption spectra of free ICG and ICG-liposome were obtained by a UV-vis spectrophotometer (DU730, Beckman Co., USA) at the wavelength range of 400–1,000 nm. In brief, standard ICG solutions were prepared by diluting ICG with ultrapure water to different concentrations. The prepared solution of ICG-liposome was added to a 5-ml ultrafiltration centrifuge tube (MW 100 kDa), centrifuging for 20 min (4,500 rpm), and finally the subnatant was taken out. The absorbance (Abs) at 810 nm was measured and the ICG concentration in the solution was obtained from the standard curve.

The ICG encapsulation efficiency (EE) and the loading efficiency (LE) were then calculated according to the following equations.

$$EE\% = \frac{Weight\ of\ ICG\ in\ liposome}{Weight\ of\ ICG\ fed\ initially} \times 100\%$$

$$LE\% = \frac{Weight\ of\ ICG\ in\ liposome}{Weight\ of\ liposomes} \times 100\%$$

The long-term stability of the ICG-liposome was evaluated in PBS containing 10% fetal bovine serum (FBS) at 37°C by detecting the size distributions with dynamic light scattering (DLS) at various time points.

In vitro Photothermal Efficiency

To measure the photothermal property of ICG-liposome, 4 ml suspensions with different concentrations were placed in a cuvette and irradiated by 808 nm laser (2 W/cm^2, 10 min), with 4 ml of saline as a negative control. The temperature profile of these suspensions was recorded by a digital thermometer per 10 s.

Cytotoxicity and *in vitro* PTT Ability Evaluation

MC-38 cells and HEK-293 cells (Human embryonic kidney 293 cells) were cultured in a DMEM medium, containing 10% FBS and 1% penicillin–streptomycin, at 37°C and 5% CO_2. CT26 cells were cultured in a 1,640 medium containing 10% FBS and 1% penicillin–streptomycin. The culture medium was replaced every other day. The CCK-8 assay was performed on the MC-38 cells, CT26 cells, and HEK-293 cells to investigate the PTT efficiency of ICG-liposome at different concentrations with or without NIR laser irradiation. The cell suspension was dispensed in a 96-well plate, and the plate was preincubated for 24 h in a humidified incubator (at 37°C, 5% CO_2). Then, the medium was removed

and replenished with a fresh medium containing ICG-liposome with different concentrations. After further incubation for 10 h at 37°C, the ICG-liposome suspensions were replaced with a fresh DMEM medium. Besides, the cells in the laser irradiation group were irradiated by 808 nm laser for 5 min at a power density of 2 W/cm^2. After incubation for another 2 h, the cell viability was measured by CCK-8 assay.

In vivo Antitumor Efficacy of PTT

All animal experiments were carried out in accordance with the Institutional Animal Care and Use Committee (IACUCC) of Sun-Yat Sen University. One hundred microliters of MC-38 tumor cells (1×10^6) or CT-26 tumor cells (1×10^6) suspension was subcutaneously injected in the bilateral flanks of the female C57BL/6 mice or BALB/C mice (6–8 weeks). Mice were divided into groups randomly. The tumor size was measured by a Vernier caliper and calculated according to the following formula: Length × Width × Height × 0.5. PTT was applied when the tumor volume reached about 100 mm^3.

In order to evaluate the *in vivo* photothermal ablative property of ICG-liposome, six MC-38 tumor-bearing mice were randomly assigned into the saline group ($n = 3$) and the ICG-liposome group ($n = 3$), respectively, and were intratumorally (i.t.) injected with 100 μl of saline or ICG-liposome (400 μg/ml ICG) on the left tumors. The left tumors of these groups were then irradiated with 808 nm laser at 2 W/cm^2 for 10 min and an IR thermal camera (Ti27, Fluck) was employed to record the region maximum temperature.

To investigate the local PTT effect on distant tumors, 32 MC-38 tumor-bearing mice and 12 CT-26 tumor-bearing mice were randomly divided into the untreated group and the ICG-liposome group, respectively. The left tumors of the ICG-liposome group were treated as described above. After the treatments, the left and right tumor volumes of each mouse were recorded every other day.

Combinational Therapy of PTT With Dual PD-1 and TIM-3 Blockade

Twenty-five MC-38 tumor-bearing mice were randomly divided into five groups: (1) untreated, (2) PTT only, (3) anti-PD-1 + anti-TIM-3, (4) PTT + anti-PD-1, and (5) PTT + anti-PD-1 + anti-TIM-3. PTT was performed the same as described above. PD-1 and TIM-3 blockades were started 1 day before PTT and were accomplished by administering 200 mg of anti-PD-1 (clone: RMP1-14, BioXCell) or anti-TIM-3 (clone: RMT3-23, BioXCell) through i.p. injection to mice every 3 days for a total of three times.

Flow Cytometry Analysis

To study the immune cells in distant tumors, right tumors were harvested from mice in different groups ($n = 5$) and stained with Viobility 405/520 Fixable Dye (Miltenyi), CD45.2 APC-CY7 (Biolegend, Clone: 104), CD3e FITC (Biolegend, Clone: 17A2), CD8a PE-vio615 (Miltenyi, Clone: REA601), PD-1 PE (Biolegend, Clone: 29F.1A12), TIM3 APC (Miltenyi, Clone: REA602), CD4 VioBlue (Miltenyi, Clone: REA604), and Foxp3 Alexa Fluor 700(Biolegend, Clone: MF-14.1A12) antibodies, according to the manufacturer's protocols.

Briefly, tumor tissues were cut into small pieces and digested with collagenase and DNase. Then, cell suspension was filtered through a 75-μm cell mesh and resuspended in PBS (pH 7.4) with 0.5% FBS for further analysis. Flow cytometric analysis was performed using a FACS LSRFortessa flow cytometer (BD).

Tumor-infiltrating cytotoxic T lymphocytes (CTL) and helper T cells were $CD45^+CD3^+CD4^-CD8^+$ and $CD45^+CD3^+CD4^+CD8^-$, respectively. Then, the expressions of PD-1 and TIM-3 in cytotoxic T lymphocytes were analyzed. Further, $CD4^+$ helper T cells were classified into regulatory T cells (Tregs) ($CD3^+CD4^+Foxp3^+$) and effective T cells ($CD3^+CD4^+Foxp3^-$).

Immunofluorescence

Tumor tissue samples obtained were frozen in OCT immediately and stored at −80°C. Frozen samples were sectioned at 5 mm with a cryostat, placed on slides, and air-dried. Then, the slides were fixed for 5 min with 100% acetone, pretreated with avidin/biotin blocker (DAKO) for 10 min, and blocked with 5% donkey serum (DAKO) in PBST for 30 min. Staining for CD8 (Biolegend, Clone: 53-6.7) was performed using non-labeled primary antibodies followed by Cy3 fluorophore-labeled secondary antibodies. Nuclei were then highlighted with a DAPI mounting medium.

Statistical Analysis

Statistical analyses were performed using Prism 8 software (GraphPad Software Inc.). Data from animal experiments were expressed as mean ± SEM or mean ± SD for biologic replicates. Statistical significance was calculated by Student's *t*-test. Statistical significance for survival analysis was calculated by the log-rank test (***$P < 0.001$, **$P < 0.01$, *$P < 0.05$).

RESULTS AND DISCUSSION

Supramolecular ICG-Liposomes Formulation and Characterization

We first synthesized and optimized the formulation of ICG-loaded liposomes. DPPC, DSPE-PEG-2000, and cholesterol were used to encapsulate the NIR dye ICG by a filming-rehydration method, wherein the mixed lipids were employed to form the liposome loaded with ICG. Different weight ratios of lipid compositions (DPPC/CHOL/DSPE-PEG2000) with different ICG/lipid weight ratios were prepared and their sizes as well as ICG loading efficiency were analyzed (**Table S1**). The final ICG-loaded liposomes had a mean diameter from 82.8 to 165.9 nm, and low polydispersity indexes (PdI) from 0.194 to 0.349, indicating a relatively uniform size distribution, which is consistent with the TEM result (**Figure S1**). The high ICG/lipid ratio (1:5) reduced the encapsulation efficiency of ICG in the liposomes, compared to the relative lower ICG/lipid ratio (1:10). Formulation F with a lipid compositions ratio of 6:3:1 and an ICG/lipid ratio of 1:10 had the highest ICG loading efficiency (**Table S1**). Thus, the formulation F was used in further experiments.

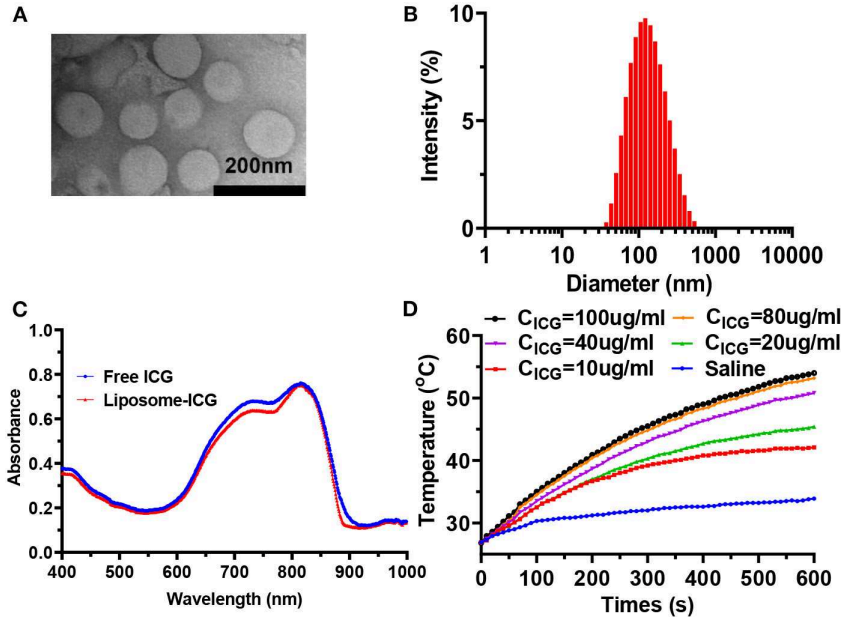

FIGURE 1 | (A) TEM image of ICG-liposome. **(B)** Hydrodynamic diameters of ICG-liposome measured by DLS. **(C)** UV-vis-NIR spectra of ICG-liposome and free ICG, indicating the successful loading of ICG into hybrid liposome. **(D)** Temperature curves of saline and ICG-liposome at various concentrations under the 808 nm light irradiation (2 W/cm^2, 10 min).

In the transmission electron microscope (TEM) image, the obtained supramolecular nanoparticles (Formulation F) showed homogenous sizes and a well-defined spherical shape (**Figure 1A**). The average hydrodynamic size of nanoparticles (**Figure 1B**) was 121.4 ± 1.2 nm, with a PDI of 0.254 ± 0.008, measured by the DLS, which is consistent with the TEM result. Moreover, the zeta potential of liposome was measured to be −6.4 ± 0.5 mV in water. The characteristic absorption peak of ICG was found in the ultraviolet-visible-NIR absorption spectrum of nanoparticles, showing the successful encapsulation of ICG in the core (**Figure 1C**). The ICG-liposome exhibited remarkable absorption at 810 nm in the UV-vis spectrum, which is suitable for biological application. The encapsulation efficiency of ICG was 98.6% and the ICG loading efficiency in the liposome was 9.1%, as measured by the UV-vis spectroscopy and calculated through the ICG standard curve (**Figure S2**).

The photothermal properties of ICG-liposome were then investigated under 808 nm laser irradiation (**Figure 1D**, **Figure S3**). Significant temperature elevation was observed when the ICG-liposome suspension was irradiated by an 808 nm laser (2 W/cm^2 for 10 min), while saline solution showed no obvious temperature increase under the same condition, indicating that the NIR laser is safe for normal tissue. TEM imaging of ICG-liposome showed that a substantial number of liposome microbubbles were observed after 808 nm laser irradiation, which was consistent with the DLS result (**Figures S4A,B**). Moreover, the ICG-liposome showed an ICG concentration-dependent temperature increment. The temperature of ICG-liposome solution (40 μg/ml) notably increased about 23.9°C at 2 W/cm^2 after irradiation for 10 min, with no obvious temperature elevation in saline. All these results show that the ICG-liposome has an efficient photothermal conversion ability.

ICG-Liposome Showed Favorable Photothermal Abilities Both *in vitro* and *in vivo*

ICG-liposome showed remarkable stability in 10% FBS-containing PBS over 96 h, with nearly unchanged size (**Figure S5**). The cytotoxicity and enhanced photothermal therapeutic effect of ICG-liposome at the cellular level were evaluated by CCK-8 assay of MC-38 cells, CT26 cells, and HEK-293 cells (**Figure 2A**). No obvious cytotoxicity of ICG-liposome was found at the concentration of 320 μg/ml without laser irradiation in MC-38 cells, with a cell viability of 85.5%, suggesting good biocompatibility. As a contrast, the viabilities of MC-38 cells receiving ICG-liposome + laser treatment decreased dramatically to 29.18%, much lower than that of MC-38 cells (85.5%) treated with ICG-liposome only. Similar results were also found in CT26 cells and HEK-293 cells (**Figure S6**).

The PTT effect of ICG-liposome was studied in MC-38 tumor-bearing C57BL/6 mice, compared with saline (**Figure 2B**). When the tumors reached approximately 100 mm^3, 100 μl of ICG-liposome or saline was intratumorally (i.t.) injected. After being irradiated by 808 nm laser for 10 min, the temperature of the tumor in the saline group increases slightly to 43.7°C. However, the temperature of the tumor in the ICG-liposome group was 57.0°C, which was much

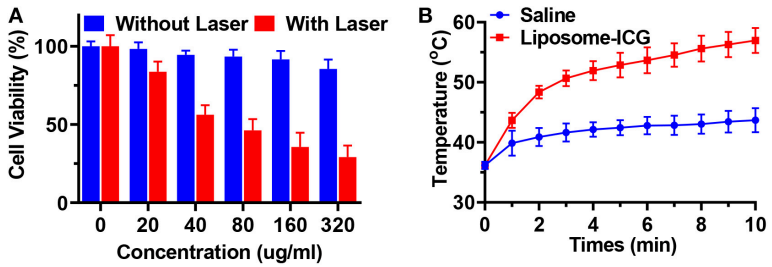

FIGURE 2 | (A) The cell-killing effect of MC-38 cells incubated with ICG-liposome of different concentration with or without NIR laser irradiation (808 nm, 2 W/cm^2, 10 min, $n = 4$). **(B)** Temperature elevations of MC-38 tumor-bearing mice ($n = 3$). Data are presented as means ± SD.

higher than that in the saline group. The mice treated with the ICG-liposome + NIR group presented obvious tumor growth inhibition, and tumors were fully cleared about 3 days later with black scars left. These results indicated that the encapsulated ICG could efficiently ablate tumors *in vivo* by converting the NIR light into heat. Taken together, ICG-liposome may be applied as an efficient PTT-enhancing agent for tumor ablation.

Local PTT Induced Effective but Short-Lived Growth Inhibition of Distant Tumors

In further *in vivo* experiment, BALB/c mice and C57BL/6 mice were inoculated with CT26 and MC-38 on bilateral flanks, respectively. PTT was then performed on the tumor at the left flank once tumors reached approximately 100 mm^3. BALB/c mice bearing CT26 tumors and C57BL/6 mice bearing MC-38 tumors in the PTT treatment group were intratumorally (i.t.) injected with ICG-liposome on the left tumor. Then, the left tumors of treatment groups were irradiated with 808 nm laser at 2 W/cm^2 for 10 min (**Figure 3A**). The left tumor temperature of mice injected with ICG-liposome under laser irradiation quickly rose to nearly 60°C, as monitored by an infrared thermal camera (**Figure 2B**). After the treatments, the right tumor volume of each mouse was recorded every other day. PTT-treated left tumors in two tumor-bearing mice regressed and were soon cleared (**Figures 3B,C**). On day 3, the left treated tumors almost disappeared with only black scars left.

Furthermore, in both the CT26 and MC-38 tumor model, we found that untreated distant tumors grew significantly slower at the early stage, if the contralateral tumors received PTT treatment (**Figures 3D,E**). In the MC-38 tumor model, the average distant tumor volume in the PTT group was 199.0 mm^3, much smaller than that of the untreated group (342.6 mm^3) on day 6 after PTT. Similarly, the average distant tumor volume in the PTT group of CT-26 tumors was 41% smaller than that of the untreated group on day 5. These systemic antitumor effects by local ablative therapy are also known as the abscopal effect and have been shown in many localized ablation therapies (Formenti and Demaria, 2009; Bastianpillai et al., 2015). However, on around days 6–8, the distant tumor restored its progressive growth and there were no significant difference ($P > 0.05$) of tumor volume between the PTT group and the untreated group at the final stage in both MC-38 and CT-26 tumor models.

Enhanced Tumor-Infiltrating T Cells Played an Important Role in Distant Tumor Growth Inhibition

To further understand the dynamic changes and mechanisms of antitumor immune responses induced by PTT, we conducted an immune analysis of the distant MC-38 tumor at an earlier and later time point after PTT treatment. In flow cytometry analyses, we digested the distant tumors into single-cell suspension and used CD45 as well as CD3 as the markers to gate tumor-infiltrating T cells (**Figure 4A**). Then, CD8 and CD4 markers were used to further gate out the CD8 T cells and CD4 T cells (**Figure S7**). Furthermore, we analyzed the PD-1 and TIM-3 expression on CD8 T cells, which indicated the exhaustion of CD8 T cells. Besides, CD4 T cells could be further classified into immune active effective T cells ($CD4^+Foxp3^-$) and regulatory T cells (Tregs) ($CD4^+Foxp3^+$), which could inhibit antitumor immune responses.

As a result, a roughly two-fold increase in the percentage of $CD45^+CD3^+$ T cells was observed in the right tumor of PTT-treated mice (**Figure 4B**) on day 3 after PTT treatment, compared with the untreated group. This increase in T cells can still be found on day 12, which indicates that primary tumor PTT therapy induced a durable immune response in the distant tumors even when the tumor regained rapid growth at a later stage.

Furthermore, increased frequencies of $CD8^+$ T cells contributed the most to the T cell infiltration (**Figures 3F**, **4C**), as $CD4^+$ T cells only slightly increased on day 3 and had no significant difference with the untreated group on day 12 (**Figure S8**). Interestingly, the percentage of CD8 T cells further increased to 24.48% on day 12, revealed by immunofluorescence staining and flow cytometry (**Figures 3E**, **4C**), suggesting that $CD8^+$ T cells may directly mediate the abscopal effect of local PTT. Besides, increase in the CD8/Tregs ratio (3.26-fold increase; **Figure 4D**) indicates an enhanced antitumor immunity on day 3. However, on day 12, this increase in the CD8/Tregs ratio became less significant (2.81-fold increase), as Tregs of the PTT-treated mice increased to a similar level of the untreated ones.

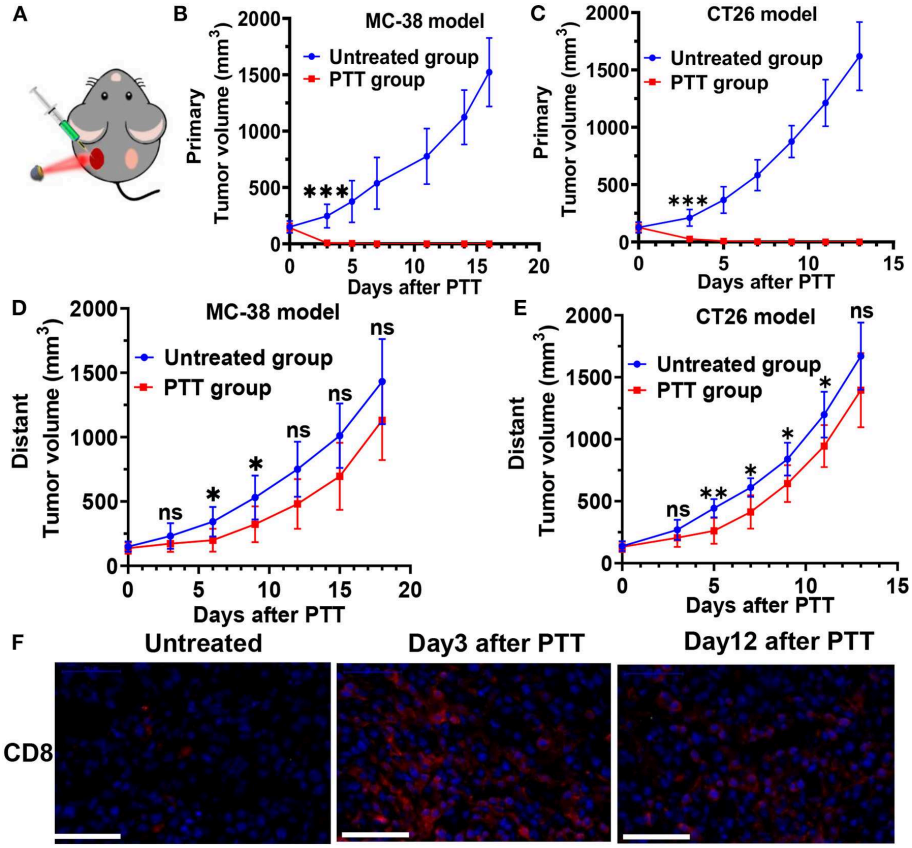

FIGURE 3 | (A) Schematic illustration of ICG-liposome-based PTT on mice. Primary tumor growth profile of MC-38-bearing **(B)** and CT26-bearing **(C)** mice from each group. Distant tumor outgrowth curves of double MC-38 tumor-bearing mice **(D)** and double CT-26 tumor-bearing mice **(E)** in which the primary tumor was left untreated or PTT-treated. **(F)** CD8 T cells infiltration of each group in the MC-38 tumor microenvironment on day 3 and 12 after treatment was examined by immunofluorescence. $n = 6$ in each group. Data are presented as means ± SD. Statistical significance was calculated by Student's *t*-test: $^{***}P < 0.001$, $^{**}P < 0.01$, $^{*}P < 0.05$.

This effect is likely caused by enhanced cross-presentation of tumor antigens by dendritic cells, as well as the immunostimulatory effects of PTT-induced cell death (Mroz et al., 2011). This observation is consistent with the reported results (Kleinovink et al., 2017; Chen et al., 2019). Intracellular tumor-specific antigens are released during the thermal ablation reduced tumor destruction and captured by antigen-presenting cells (APCs). Moreover, the hyperthermic temperature can also fire up adaptive immunity and increase the ability of APCs to sense ongoing tumor antigens, to present these antigens to T cells (Knippertz et al., 2011). Published data show that exposure of dendritic cells to hyperthermic temperatures (39.5–41.5°C) *in vitro* could upregulate their expression of MHC class II, TLR4, and the co-stimulatory molecules CD80 and CD86 (Ostberg et al., 2003; Yan et al., 2007). Once mature antigen-loaded dendritic cells reached lymph nodes, T cells are activated and expanded. Exposure of tumor-bearing mice to hyperthermic temperatures was also found to increase the trafficking of activated CD8 T cells to tumor sites (Evans et al., 2015).

Thus, all these results provide evidence that local PTT treatment triggers a systemic CD8 T cell-dependent anti-tumor effect on untreated distant tumors.

Restored Progressive Distant Tumor Growth Later After PTT Was Correlated to Compensatory Upregulation of PD-1 and TIM-3 in Tumor-Infiltrating CD8 T Cells

Local PTT treatment inhibited the growth of distant tumors via increased $CD8^+$ T cell infiltration but failed to fully clear them, resulting in the rapid tumor progression at a later stage. To understand which pathways may drive immune suppression and limit T cell activity, we analyzed the typical exhaustion markers to explore whether the increased CD8 T cells became exhausted after PTT treatment. Here, we tried to examine the PD-1 and TIM-3 expression of CD8 T cells in the TME of distant MC-38 tumors after PTT therapy (**Figure 5A**). Our flow cytometry data showed that nearly 79.9% of CD8 T cells expressed PD-1 and about 16.1% of CD8 T cells expressed TIM-3 in MC-38 tumors from untreated mice (**Figures 5B,C**). On day 3, we observed a rapid downregulation of both PD-1 and TIM-3 expression on tumor-infiltrating CD8 T cells of the PTT group. The percentage of PD-1^+ CD8 T cells decreased to about 67.2% ($p < 0.001$), while TIM-3 expression decreased to nearly 7.4% ($p < 0.01$) (**Figures 5B,C**). Interestingly, the percentage of cells

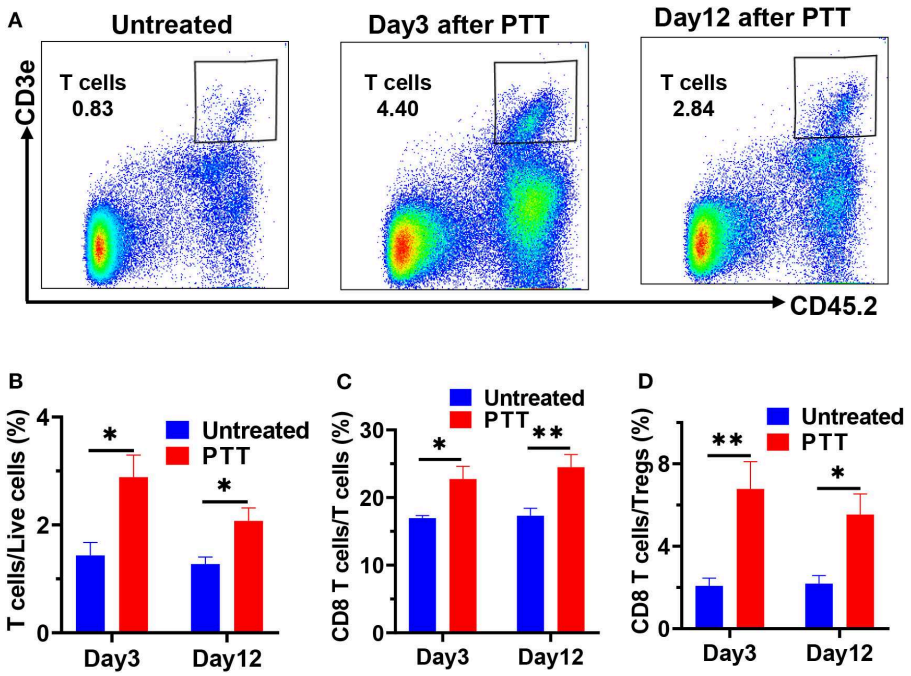

FIGURE 4 | (A) Representative flow cytometric plots showing $CD45^+CD3^+$ T cells in single live cell suspension of MC-38 tumors on days 3 and 8 after PTT. Flow cytometry results showing the percentage of $CD45^+CD3^+$ T cells **(B)**, $CD8^+$ tumor-infiltrating T cells **(C)**, and the ratio of CD8 T cells to Tregs **(D)** on days 3 and 12 after PTT in distant MC-38 tumors. $n = 5$ in each group. Data are presented as means ± SEM. Statistical significance was calculated by Student's *t*-test: $^{**}P < 0.01$, $^{*}P < 0.05$.

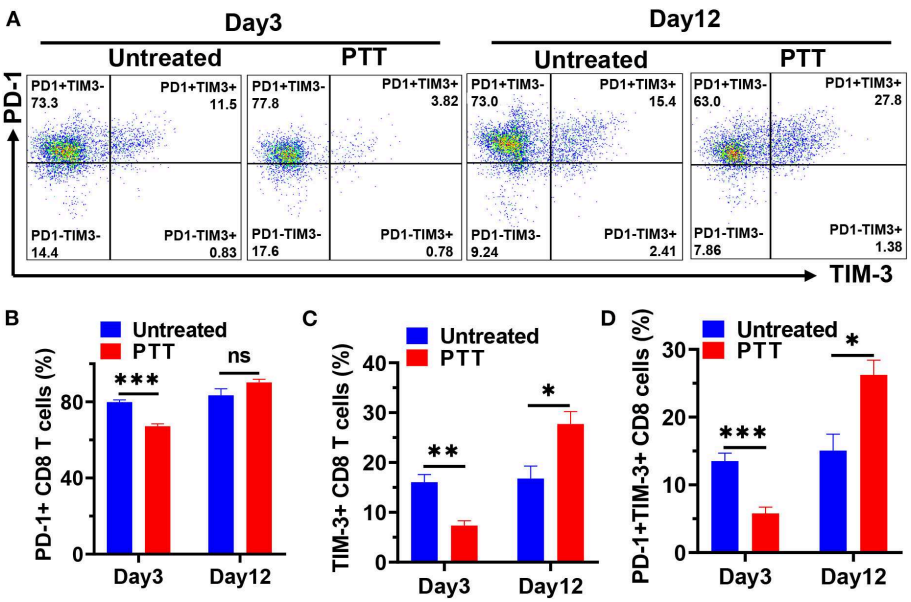

FIGURE 5 | (A) Representative flow cytometric plots showing PD-1 and TIM-3 expression in tumor-infiltrating CD8 T cells on days 3 and 12 after PTT. Flow cytometry results showing the percentage of PD-1^+ **(B)**, TIM-3^+ **(C)**, and PD-1^+TIM-3^+ **(D)** CD8 T cells on days 3 and 12. $n = 5$ in each group. Data are presented as means ± SEM. Statistical significance was calculated by Student's *t*-test: $^{***}P < 0.001$, $^{**}P < 0.01$, $^{*}P < 0.05$.

coexpressing PD-1 and TIM-3 was also significantly decreased from about 13.5% to 5.8% ($p < 0.001$; **Figure 5D**). These results indicated that CD8 T cells expressed less exhausted markers and had better function in the early time after PTT, consistent with the efficient inhibition of tumor growth. However, the frequency of PD-1^+ CD8 T cells of PTT-treated mice increased to a similar

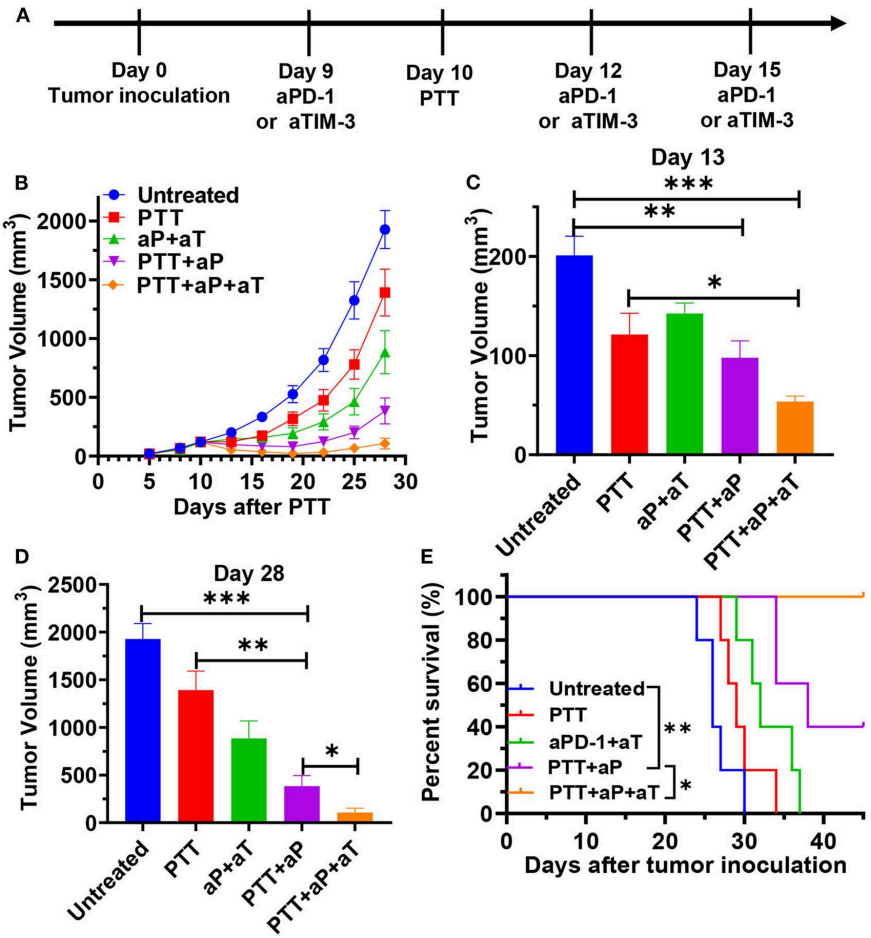

FIGURE 6 | (A) Schematic illustration of ICG-liposome-based PTT and dual blocking PD-1 and Tim-3 combination therapy to inhibit distal tumor growth. MC-38-bearing mice were then treated with PTT, anti-PD-1 + anti-TIM-3, PTT + anti-PD-1, and PTT + anti-PD-1 + anti-TIM-3. Tumor growth **(B)** and Kaplan–Meier survival curves **(E)** of tumor-bearing mice are shown. Pooled data of day 13 **(C)** and day 28 **(D)** from the experiments shown in **(B)**. aP and aT represent anti-PD-1 and anti-TIM-3 therapy, respectively. $n = 5$ in each group. Data are presented as means ± SEM. Statistical significance in **(B–D)** was calculated by Student's *t*-test. Statistical significance for survival analysis in (E) was calculated by the log-rank test. $^{***}P < 0.001$, $^{**}P < 0.01$, $^{*}P < 0.05$.

level of untreated ones on day 12. Meanwhile, TIM-3 on CD8 T cells was elevated to 27.7% on day 12 and was significantly higher than that in the untreated mice ($p < 0.05$). Besides, on day 12, PD-1^{+}TIM^{+} CD8 T cells, which represented the most exhausted type, were observed to increase five-fold than that on day 3 and two-fold than untreated ones (**Figure 5D**).

In this study, we show for the first time in PTT-treated tumor-bearing mice that PD-1 and TIM-3 coexpression in tumor-infiltrating CD8 T cells predominantly increased at the later stage of the distant tumor progression. These PD-1 and TIM-3 double-positive CD8 T cells were highly exhausted and had markedly reduced cytokine production as reported in patients with metastatic melanoma (Fourcade et al., 2010). The deceased PD-1 and TIM-3 expression in the early stage may be caused by the fact that a new subset of CD8 T cells expressing low levels of PD-1 and TIM-3 were activated in the peripheral immune organ and trafficked to distant tumors. In the later stage, these newly trafficked CD8 T cells were exposed to high levels of tumor antigens and reformed in the tumor microenvironment to become exhausted.

Collectively, these results showed that the expression of both PD-1 and TIM-3 underwent dynamic changes after PTT treatment, with significant decrease at the early time point and dramatic increase at a later stage. The data indicating that tumor-infiltrating CD8 T cells underwent functional exhaustion by compensatory upregulation of checkpoint receptors may explain the rapid regression later after PTT.

Dual Blocking PD-1 and TIM-3 in the PTT-Treated Mice Induces Robust Systemic Antitumor Immunity to Inhibit the Growth of Distant Tumors

The results described above provide a basis for testing rational combination treatments of immune checkpoint blockade with PTT treatment. Therefore, we analyzed whether enhancing the PPT-induced CD8 T cell response by PD-1 or TIM-3 blockade would enable enhanced tumor eradication. We treated double MC38 tumor-bearing mice with PTT of left tumors and

conducted systemic PD-1 blockade or dual blocking PD-1 and TIM-3 during the treatment phase. MC-38 bearing mice were treated with PTT alone, PTT plus anti-PD-1 antibodies (PTT + aPD-1), PTT plus anti-PD-1, and anti-TIM-3 antibodies (PTT + aPD-1 + aTIM-3), anti-PD-1 plus anti-TIM-3 antibodies (aPD-1 + aTIM-3), or left without treatment (**Figure 6A**). As a result, we found that PTT alone modestly inhibited distant tumor growth at an early stage, consistent with our previous data (**Figures 6B,C**). Dual blocking PD-1 and TIM-3 themselves also modestly delayed tumor growth, as compared with the untreated group, similar to the reported result (Sakuishi et al., 2010). However, both PTT treatment alone and immune checkpoint blockade alone were not efficient enough to fully control the distant tumors. In contrast, combination treatment with PPT and PD-1 blockade combined the strong respective effects of each treatment and exhibited superior tumor regression (with an average tumor volume 72.4% smaller than the PTT group on day 28), longer tumor inhibition duration, and prolonged survival ($p < 0.0001$) compared to the PTT treatment alone (**Figures 6D,E**).

Additional blockade of the TIM-3 pathway further enhanced the synergistic effect of PTT and blocking PD-1 on antitumor immunity in the MC-38 tumor-bearing mice and had an additive effect in delaying distant tumor growth (277.6 mm^3 smaller on day 28) and prolonging survival time ($p < 0.05$) as compared with the PTT + aPD-1 group (**Figures 6D,E**). Above all, PTT combined with dual antibody blockade against PD-1/TIM-3 resulted in tumor-free survival in 40% of treated mice, compared to that combination with single PD-1 blockade that led to tumor outgrowth in all animals. This advanced synergistic effect may be due to the further upregulation of TIM-3 resulting from single blockade of PD-1, which has been reported (Huang et al., 2017). Single blockade of PD-1 can lead to a compensatory induction of TIM-3, LAG-3, and CTLA-4 and other checkpoint inhibitors, which builds a feedback loop that acts to mediate local immune suppression (Huang et al., 2017). Based on the reported data, we hypothesized that compensatory and/or overlapping functionality for PD-1 and TIM-3 may limit the efficacy of a single checkpoint blockade. PTT combined with a dual block of PD-1 and TIM-3 would lead to the best distant tumor control.

Taken together, these results suggest that the combinatorial blockade of PD-1 and TIM-3 has significant benefit in controlling distant tumor growth when the primary tumor is completely ablated by PTT. These data provide a basis for PTT with combinatorial checkpoint blockade in clinical intervention for tumor therapy.

CONCLUSIONS

In summary, an ICG-loaded supramolecular theranostic nanomedicine ICG-liposome was synthesized to achieve NIR triggered photothermal ablation. Compared to the free compound, packing ICG with optimized phospholipids in a self-assembly way exhibited enhanced water solubility and superior stability and obtained high encapsulation yields (>95%), as well as excellent NIR light-triggered PTT ability. After irradiation, the encapsulated ICG can efficiently transfer NIR light into tumor-ablating heat. We find that PTT of mouse colon tumors mediated strong primary tumor ablation and eradication, which also delayed distant tumor growth at the early time by increasing tumor infiltrating T cells. Our data further reveal that restored progressive distant tumor growth later after PTT may be caused by compensatory upregulation of PD-1 and TIM-3 in tumor-infiltrating CD8 T cells, limiting T cell antitumor efficacy. This compensatory upregulation of immune checkpoints also provides an opportunity for choosing appropriate blockade agent(s) for combinatorial treatment. Furthermore, using a mouse colon cancer model, we observed that a combination of localized PTT and anti-PD-1 antibodies significantly enhanced distant tumor growth inhibition and prolonged survival. Interestingly, additional blockade of the TIM-3 pathway further enhanced the synergistic effect. The efficacy of photodynamic therapy and all these synergistic effects of supramolecular ICG-loaded liposome prove it to be a good antitumor agent.

DATA AVAILABILITY STATEMENT

All datasets generated for this study are included in the article/**Supplementary Material**.

ETHICS STATEMENT

The animal study was reviewed and approved by ICE for Clinical Research and Animal Trials of the First Affiliated Hospital of Sun Yat-sen University.

AUTHOR CONTRIBUTIONS

T-YH, MX, MK, and X-YX conceived and designed the experiments and also analyzed the data. C-YZ synthesized the liposomes. G-LH, B-WZ, B-XL, J-YY, and L-YS performed animal experiments. The manuscript was prepared by T-YH and edited by MX. All authors have approved the final version of the manuscript.

FUNDING

This work was supported by the National Natural Science Foundation of China (Nos. 81501489, 81530055, and 81701696).

SUPPLEMENTARY MATERIAL

The Supplementary Material for this article can be found online at: https://www.frontiersin.org/articles/10.3389/fchem.2020.00001/full#supplementary-material

REFERENCES

Ayala-Orozco, C., Urban, C., Knight, M. W., Urban, A. S., Neumann, O., Bishnoi, S. W., et al. (2014). Au nanomatryoshkas as efficient near-infrared photothermal transducers for cancer treatment: benchmarking against nanoshells. *ACS Nano* 8, 6372–6381. doi: 10.1021/nn501871d

Bastianpillai, C., Petrides, N., Shah, T., Guillaumier, S., Ahmed, H. U., and Arya, M. (2015). Harnessing the immunomodulatory effect of thermal and non-thermal ablative therapies for cancer treatment. *Tumour Biol.* 36, 9137–9146. doi: 10.1007/s13277-015-4126-3

Chen, Q., Hu, Q., Dukhovlinova, E., Chen, G., Ahn, S., Wang, C., et al. (2019). Photothermal therapy promotes tumor infiltration and antitumor activity of CAR T cells. *Adv. Mater.* 31:e1900192. doi: 10.1002/adma.201900192

Chen, Q., Wen, J., Li, H., Xu, Y., Liu, F., and Sun, S. (2016a). Recent advances in different modal imaging-guided photothermal therapy. *Biomaterials* 106, 144–166. doi: 10.1016/j.biomaterials.2016.08.022

Chen, Q., Xu, L., Liang, C., Wang, C., Peng, R., and Liu, Z. (2016b). Photothermal therapy with immune-adjuvant nanoparticles together with checkpoint blockade for effective cancer immunotherapy. *Nat. Commun.* 7:13193. doi: 10.1038/ncomms13193

Chu, K. F., and Dupuy, D. E. (2014). Thermal ablation of tumours: biological mechanisms and advances in therapy. *Nat. Rev. Cancer* 14, 199–208. doi: 10.1038/nrc3672

Corso, C. D., Ali, A. N., and Diaz, R. (2011). Radiation-induced tumor neoantigens: imaging and therapeutic implications. *Am. J. Cancer Res.* 1, 390–412. Available online at: www.ajcr.us/ISSN:2156-6976/ajcr0000029

Ding, Y., Ji, T., Zhao, Y., Zhang, Y., Zhao, X., Zhao, R., et al. (2015). Improvement of stability and efficacy of C16Y therapeutic peptide via molecular Self-assembly into tumor-responsive nanoformulation. *Mol. Cancer Ther.* 14, 2390–2400. doi: 10.1158/1535-7163.MCT-15-0484

Elsabahy, M., and Wooley, K. L. (2015). Data mining as a guide for the construction of cross-linked nanoparticles with low immunotoxicity via control of polymer chemistry and supramolecular assembly. *Acc. Chem. Res.* 48, 1620–1630. doi: 10.1021/acs.accounts.5b00066

Evans, S. S., Repasky, E. A., and Fisher, D. T. (2015). Fever and the thermal regulation of immunity: the immune system feels the heat. *Nat. Rev. Immunol.* 15, 335–349. doi: 10.1038/nri3843

Feng, Q., Sun, J., and Jiang, X. (2016). Microfluidics-mediated assembly of functional nanoparticles for cancer-related pharmaceutical applications. *Nanoscale* 8, 12430–12443. doi: 10.1039/c5nr07964k.

Feng, Q., Zhang, L., Liu, C., Li, X., Hu, G., Sun, J., et al. (2015). Microfluidic based high throughput synthesis of lipid-polymer hybrid nanoparticles with tunable diameters. *Biomicrofluidics* 9:052604. doi: 10.1063/1.4922957

Finkelstein, S. E., Timmerman, R., McBride, W. H., Schaue, D., Hoffe, S. E., Mantz, C. A., et al. (2011). The confluence of stereotactic ablative radiotherapy and tumor immunology. *Clin. Dev. Immunol.* 2011:439752. doi: 10.1155/2011/439752

Formenti, S. C., and Demaria, S. (2009). Systemic effects of local radiotherapy. *Lancet. Oncol.* 10, 718–726. doi: 10.1016/S1470-2045(09)70082-8

Fourcade, J., Sun, Z., Benallaoua, M., Guillaume, P., Luescher, I. F., Sander, C., et al. (2010). Upregulation of Tim-3 and PD-1 expression is associated with tumor antigen-specific CD8+ T cell dysfunction in melanoma patients. *J. Exp. Med.* 207, 2175–2186. doi: 10.1084/jem.20100637

Granier, C., Dariane, C., Combe, P., Verkarre, V., Urien, S., Badoual, C., et al. (2017). Tim-3 expression on tumor-infiltrating PD-1(+)CD8(+) T cells correlates with poor clinical outcome in renal cell carcinoma. *Cancer Res.* 77, 1075–1082. doi: 10.1158/0008-5472.CAN-16-0274

Guo, L., Yan, D. D., Yang, D., Li, Y., Wang, X., Zalewski, O., et al. (2014). Combinatorial photothermal and immuno cancer therapy using chitosan-coated hollow copper sulfide nanoparticles. *ACS Nano* 8, 5670–5681. doi: 10.1021/nn5002112

Hoffmann, R. T. (2017). Liver metastases of colorectal cancer. *Radiologe* 57, 90–96. doi: 10.1007/s00117-017-0208-0

Huang, R. Y., Francois, A., McGray, A. R., Miliotto, A., and Odunsi, K. (2017). Compensatory upregulation of PD-1, LAG-3, and CTLA-4 limits the efficacy of single-agent checkpoint blockade in metastatic ovarian cancer. *Oncoimmunology* 6:e1249561. doi: 10.1080/2162402x.2016.1249561

Ji, T., and Kohane, D. S. (2019). Nanoscale systems for local drug delivery. *Nano Today* 28:100765. doi: 10.1016/j.nantod.2019.100765

Ji, T., Lang, J., Wang, J., Cai, R., Zhang, Y., Qi, F., et al. (2017). Designing liposomes to suppress extracellular matrix expression to enhance drug penetration and pancreatic tumor therapy. *ACS Nano* 11, 8668–8678. doi: 10.1021/acsnano.7b01026

Kim, Y. K., Na, H. K., Kim, S., Jang, H., Chang, S. J., and Min, D. H. (2015). One-pot synthesis of multifunctional Au@graphene oxide nanocolloid core@shell nanoparticles for Raman bioimaging, photothermal, and photodynamic therapy. *Small* 11, 2527–2535. doi: 10.1002/smll.201402269

Kleinovink, J. W., Fransen, M. F., Lowik, C. W., and Ossendorp, F. (2017). Photodynamic-immune checkpoint therapy eradicates local and distant tumors by CD8(+) T cells. *Cancer Immunol. Res.* 5, 832–838. doi: 10.1158/2326-6066.Cir-17-0055

Knippertz, I., Stein, M. F., Dorrie, J., Schaft, N., Muller, I., Deinzer, A., et al. (2011). Mild hyperthermia enhances human monocyte-derived dendritic cell functions and offers potential for applications in vaccination strategies. *Int. J. Hyperthermia* 27, 591–603. doi: 10.3109/02656736.2011.589234

Kostarelos, K., Bianco, A., and Prato, M. (2009). Promises, facts and challenges for carbon nanotubes in imaging and therapeutics. *Nat. Nanotechnol.* 4, 627–633. doi: 10.1038/nnano.2009.241

Lajunen, T., Kontturi, L. S., Viitala, L., Manna, M., Cramariuc, O., Rog, T., et al. (2016). Indocyanine green-loaded liposomes for light-triggered drug release. *Mol. Pharm.* 13, 2095–2107. doi: 10.1021/acs.molpharmaceut.6b00207

Lee, D. H., Lee, J. M., Lee, J. Y., Kim, S. H., Yoon, J. H., Kim, Y. J., et al. (2014). Radiofrequency ablation of hepatocellular carcinoma as first-line treatment: long-term results and prognostic factors in 162 patients with cirrhosis. *Radiology* 270, 900–909. doi: 10.1148/radiol.13130940

Li, X., Naylor, M. F., Le, H., Nordquist, R. E., Teague, T. K., Howard, C. A., et al. (2010). Clinical effects of *in situ* photoimmunotherapy on late-stage melanoma patients: a preliminary study. *Cancer Biol. Ther.* 10, 1081–1087. doi: 10.4161/cbt.10.11.13434

Liu, J., Yu, M., Zhou, C., Yang, S., Ning, X., and Zheng, J. (2013). Passive tumor targeting of renal-clearable luminescent gold nanoparticles: long tumor retention and fast normal tissue clearance. *J. Am. Chem. Soc.* 135, 4978–4981. doi: 10.1021/ja401612x

Liu, J., Zheng, X., Yan, L., Zhou, L., Tian, G., Yin, W., et al. (2015). Bismuth sulfide nanorods as a precision nanomedicine for in vivo multimodal imaging-guided photothermal therapy of tumor. *ACS Nano* 9, 696–707. doi: 10.1021/nn506137n

Liu, Y., Jia, Z., Akhter, M. P., Gao, X., Wang, X., Wang, X., et al. (2018). Bone-targeting liposome formulation of Salvianic acid A accelerates the healing of delayed fracture Union in Mice. *Nanomedicine* 14, 2271–2282. doi: 10.1016/j.nano.2018.07.011

Ma, Y., Tong, S., Bao, G., Gao, C., and Dai, Z. (2013). Indocyanine green loaded SPIO nanoparticles with phospholipid-PEG coating for dual-modal imaging and photothermal therapy. *Biomaterials* 34, 7706–7714. doi: 10.1016/j.biomaterials.2013.07.007

Mahnken, A. H., Pereira, P. L., and de Baere, T. (2013). Interventional oncologic approaches to liver metastases. *Radiology* 266, 407–430. doi: 10.1148/radiol.12112544

Mehta, A., Oklu, R., and Sheth, R. A. (2016). Thermal ablative therapies and immune checkpoint modulation: can locoregional approaches effect a systemic response? *Gastroenterol Res. Pract.* 2016:9251375. doi: 10.1155/2016/9251375

Mroz, P., Hashmi, J. T., Huang, Y. Y., Lange, N., and Hamblin, M. R. (2011). Stimulation of anti-tumor immunity by photodynamic therapy. *Expert Rev. Clin. Immunol.* 7, 75–91. doi: 10.1586/eci.10.81

Ostberg, J. R., Kabingu, E., and Repasky, E. A. (2003). Thermal regulation of dendritic cell activation and migration from skin explants. *Int. J. Hyperthermia* 19, 520–533. doi: 10.1080/0265673031000160798 6

Rubner, Y., Wunderlich, R., Ruhle, P. F., Kulzer, L., Werthmoller, N., Frey, B., et al. (2012). How does ionizing irradiation contribute to the induction of anti-tumor immunity? *Front. Oncol.* 2:75. doi: 10.3389/fonc.2012.00075

Rwei, A. Y., Wang, B. Y., Ji, T., Zhan, C., and Kohane, D. S. (2017). Enhanced triggering of local anesthetic particles by photosensitization and photothermal effect using a common wavelength. *Nano Lett.* 17, 7138–7145. doi: 10.1021/acs.nanolett.7b04176

Sag, A. A., Selcukbiricik, F., and Mandel, N. M. (2016). Evidence-based medical oncology and interventional radiology paradigms for liver-dominant

colorectal cancer metastases. *World J. Gastroenterol.* 22, 3127–3149. doi: 10.3748/wjg.v22.i11.3127

Sakuishi, K., Apetoh, L., Sullivan, J. M., Blazar, B. R., Kuchroo, V. K., and Anderson, A. C. (2010). Targeting Tim-3 and PD-1 pathways to reverse T cell exhaustion and restore anti-tumor immunity. *J. Exp. Med.* 207, 2187–2194. doi: 10.1084/jem.20100643

Sheng, Z., Hu, D., Zheng, M., Zhao, P., Liu, H., Gao, D., et al. (2014). Smart human serum albumin-indocyanine green nanoparticles generated by programmed assembly for dual-modal imaging-guided cancer synergistic phototherapy. *ACS Nano* 8, 12310–12322. doi: 10.1021/nn5062386

Slovak, R., Ludwig, J. M., Gettinger, S. N., Herbst, R. S., and Kim, H. S. (2017). Immuno-thermal ablations - boosting the anticancer immune response. *J. Immunother Cancer* 5:78. doi: 10.1186/s40425-017-0284-8

Tang, H., Wang, Y., Chlewicki, L. K., Zhang, Y., Guo, J., Liang, W., et al. (2016). Facilitating T cell infiltration in tumor microenvironment overcomes resistance to PD-L1 blockade. *Cancer Cell* 29, 285–296. doi: 10.1016/j.ccell.2016.02.004

Tao, Y., Ju, E., Ren, J., and Qu, X. (2014). Immunostimulatory oligonucleotides-loaded cationic graphene oxide with photothermally enhanced immunogenicity for photothermal/immune cancer therapy. *Biomaterials* 35, 9963–9971. doi: 10.1016/j.biomaterials.2014.08.036

Wang, F., Chen, L., Zhang, R., Chen, Z., and Zhu, L. (2014). RGD peptide conjugated liposomal drug delivery system for enhance therapeutic efficacy in treating bone metastasis from prostate cancer. *J. Control Release* 196, 222–233. doi: 10.1016/j.jconrel.2014.10.012

Weldon, C., Ji, T., Nguyen, M. T., Rwei, A., Wang, W., Hao, Y., et al. (2019). Nanoscale bupivacaine formulations to enhance the duration and safety of intravenous regional anesthesia. *ACS Nano* 13, 18–25. doi: 10.1021/acsnano.8b05408

Wherry, E. J., and Kurachi, M. (2015). Molecular and cellular insights into T cell exhaustion. *Nat. Rev. Immunol.* 15, 486–499. doi: 10.1038/nri3862

Wu, L., Fang, S., Shi, S., Deng, J., Liu, B., and Cai, L. (2013). Hybrid polypeptide micelles loading indocyanine green for tumor imaging and photothermal effect study. *Biomacromolecules* 14, 3027–3033. doi: 10.1021/bm400839b

Yan, X., Xiu, F., An, H., Wang, X., Wang, J., and Cao, X. (2007). Fever range temperature promotes TLR4 expression and signaling in dendritic cells. *Life Sci.* 80, 307–313. doi: 10.1016/j.lfs.2006.09.022

Yang, T., Liu, L., Deng, Y., Guo, Z., Zhang, G., Ge, Z., et al. (2017). Ultrastable near-infrared conjugated-polymer nanoparticles for dually photoactive tumor inhibition. *Adv. Mater.* 29. doi: 10.1002/adma.201700487

Zha, Z., Yue, X., Ren, Q., and Dai, Z. (2013). Uniform polypyrrole nanoparticles with high photothermal conversion efficiency for photothermal ablation of cancer cells. *Adv. Mater.* 25, 777–782. doi: 10.1002/adma.201202211

Zheng, M., Yue, C., Ma, Y., Gong, P., Zhao, P., Zheng, C., et al. (2013). Single-step assembly of DOX/ICG loaded lipid–polymer nanoparticles for highly effective chemo-photothermal combination therapy. *ACS Nano* 7, 2056–2067. doi: 10.1021/nn400334y

Zheng, M., Zhao, P., Luo, Z., Gong, P., Zheng, C., Zhang, P., et al. (2014). Robust ICG theranostic nanoparticles for folate targeted cancer imaging and highly effective photothermal therapy. *ACS Appl. Mater. Interfaces* 6, 6709–6716. doi: 10.1021/am5004393

Conflict of Interest: The authors declare that the research was conducted in the absence of any commercial or financial relationships that could be construed as a potential conflict of interest.

frontiers in Chemistry

ORIGINAL RESEARCH
published: 20 February 2020
doi: 10.3389/fchem.2020.00009

Effects of Terminal Motif on the Self-Assembly of Dexamethasone Derivatives

Hui Liu, Ailing Yu, Mali Dai, Dan Lin, Deqing Lin, Xu Xu, Xingyi Li and Yuqin Wang**

School of Ophthalmology & Optometry and Eye Hospital, Institute of Biomedical Engineering, Wenzhou Medical University, Wenzhou, China

Tailoring the terminal motif of molecules including drugs might significantly affect their self-assembly tendency in aqueous solution, thus providing a rational strategy to modulate its macroscopic characteristics of supramolecular assembly. A model drug of dexamethasone (Dex) was esterified by different fatty acids [succinic acid (SA), glutaric acid (GA), and adipic acid (AA)] and aromatic acid [phthalic acid (PA)] to generate a series of Dex derivatives. Aqueous solution of Dex-SA, Dex-GA, and Dex-AA turned into hydrogel spontaneously after a period time of incubation (24, 48, and 72 h, respectively) via the auto-hydrolytic strategy, while aqueous solution of Dex-PA did not result in hydrogelation during 3 days of incubation. Aqueous solutions of Dex-SA, Dex-GA, and Dex-AA underwent apparent hydrolysis (10.73 ± 0.64%, 15.17 ± 2.24%, and 17.29 ± 1.39%, respectively), while Dex-PA exhibited a minimal hydrolysis (<1%) in a period of 28 days study, as indicated by *in vitro* hydrolytic test. Morphological observation showed that the hydrogel formed by Dex-SA was composed of uniform nanofibers, while hydrogels formed by Dex-GA, and Dex-AA were derived from irregular particles. The mechanical strength of hydrogel formed by Dex-SA was much bigger than that of hydrogels formed by Dex-GA and Dex-AA, as indicated by rheological test. Moreover, the acylation of Dex did not compromise its potent anti-inflammatory activity in a lipopolysaccharide (LPS)-activated RAW 264.7 macrophage.

Keywords: dexamethasone, self-assembly, terminal motif, drug delivery, hydrogel

OPEN ACCESS

Edited by:
Tianjiao Ji,
Boston Children's Hospital, Harvard Medical School, United States

Reviewed by:
Jiayan Lang,
Cornell University, United States
Wenshu Zheng,
Tulane University, United States

****Correspondence:***
Xingyi Li
lixingyi_1984@163.com
Yuqin Wang
yqwang57@163.com

Specialty section:
This article was submitted to Supramolecular Chemistry, a section of the journal Frontiers in Chemistry

Received: *28 November 2019*
Accepted: *07 January 2020*
Published: *20 February 2020*

Citation:
Liu H, Yu A, Dai M, Lin D, Lin D, Xu X, Li X and Wang Y (2020) Effects of Terminal Motif on the Self-Assembly of Dexamethasone Derivatives. Front. Chem. 8:9. doi: 10.3389/fchem.2020.00009

INTRODUCTION

Self-assembly of nanomaterials from molecular building block is a promising approach to construct new functional materials for various biomedical applications (e.g., drug delivery, tissue engineering; Blanco et al., 2015; Kalepu and Nekkanti, 2015; Adawiyah et al., 2016; Vader et al., 2016; Zylberberg and Matosevic, 2016; Wu et al., 2017b). Self-assembly is primarily dominated by various non-covalent interactions such as electrostatic, hydrophobic, hydrogen bond, and van der Walls interactions (Zhou and Li, 2017; Yang et al., 2018). The biggest challenge in molecular self-assembly is to precisely control the self-assembly process (nucleation and growth of nanostructure; Zhao et al., 2009; Vemula et al., 2013). In the past several decades, a number of strategies including enzyme, pH condition, light, and so on have been proposed to achieve a spatial and temporal controlled self-assembly of nanomaterials (e.g., peptide, lipid; Vemula et al., 2009, 2013; Mao et al., 2012; Li et al., 2013; Lin and Cui, 2015; Ma et al., 2016; Wang et al., 2017b; Wu et al., 2018). Among these strategies, approaches involving hydrolytic or enzymatic reactions have

gained considerable attention, because they offered great opportunities to elaborately tailor the characteristics of assemblies.

One emerging class of self-assembly system is steroidal agents (e.g., bile salts, sodium deoxycholate) that form numerous supramolecular assemblies (e.g., fiber, tube, particle) and have been reported for a long time (Terech et al., 2002, 2009; Svobodová et al., 2012; Zhang et al., 2017). Similarly, steroidal drugs (e.g., dexamethasone, triamcinolone acetonide) have been widely used to construct supramolecular hydrogel owing to their excellent self-assembly capacity (Wu et al., 2017a; Xiong et al., 2018; Zhou et al., 2018). For instance, Samuel I. Stupp and co-workers reported a dexamethasone-peptide amphiphile that was able to self-assemble into nanofibers via ionic cross-linking strategy, acting as a novel drug delivery system to provide prolonged and localized drug delivery at the site of injection (Webber et al., 2012). More recently, we occasionally found that the succinated dexamethasone (Dex-SA) underwent auto-hydrolysis in phosphate buffered saline (PBS, pH 7.4) to generate a transparent hydrogel (Zhang et al., 2018). Notably, gelation time and mechanical strength of Dex-SA supramolecular hydrogel can be readily modulated by the pH condition of medium and incubation temperature, as well as the hydrogelator concentration. However, since these parameters dramatically influence the macroscopic properties of hydrogels, the effect of terminal motif on the self-assembly behaviors of dexamethasone has not yet been reported. In this study, we investigated the effects of terminal motif on the self-assembly of dexamethasone derivatives, thus providing the basis to precisely modulate macroscopic characteristics in the supramolecular assemblies.

MATERIALS AND METHODS

Materials

Dex and succinic anhydride were purchased from J&K Scientific Ltd (Beijing, China). Glutaric anhydride was purchased from Beijing Bailingwei Technology Co., Ltd. (Beijing, China). Adpic anhydride was purchased from Nanjing Kangmanlin Biology Technology Co., Ltd. (Nanjing, China). Phthalic anhydride was purchased from Adamas-beta Co., Ltd. (Shanghai, China). Mouse TNF-α DuoSet ELISA (DY410-05) and mouse IL-6 DuoSet ELISA (DY406-05) were obtained from R&D SYSTEMS® (Minneapolis, MN, USA). All other used agents were of analytical grade.

Synthesis and Characterization of Dex Derivatives

As reported previously (Zhang et al., 2018), Dex-SA, Dex-GA, Dex-AA, and Dex-PA derivatives were synthesized via an esterification reaction at room temperature. Briefly, Dex,

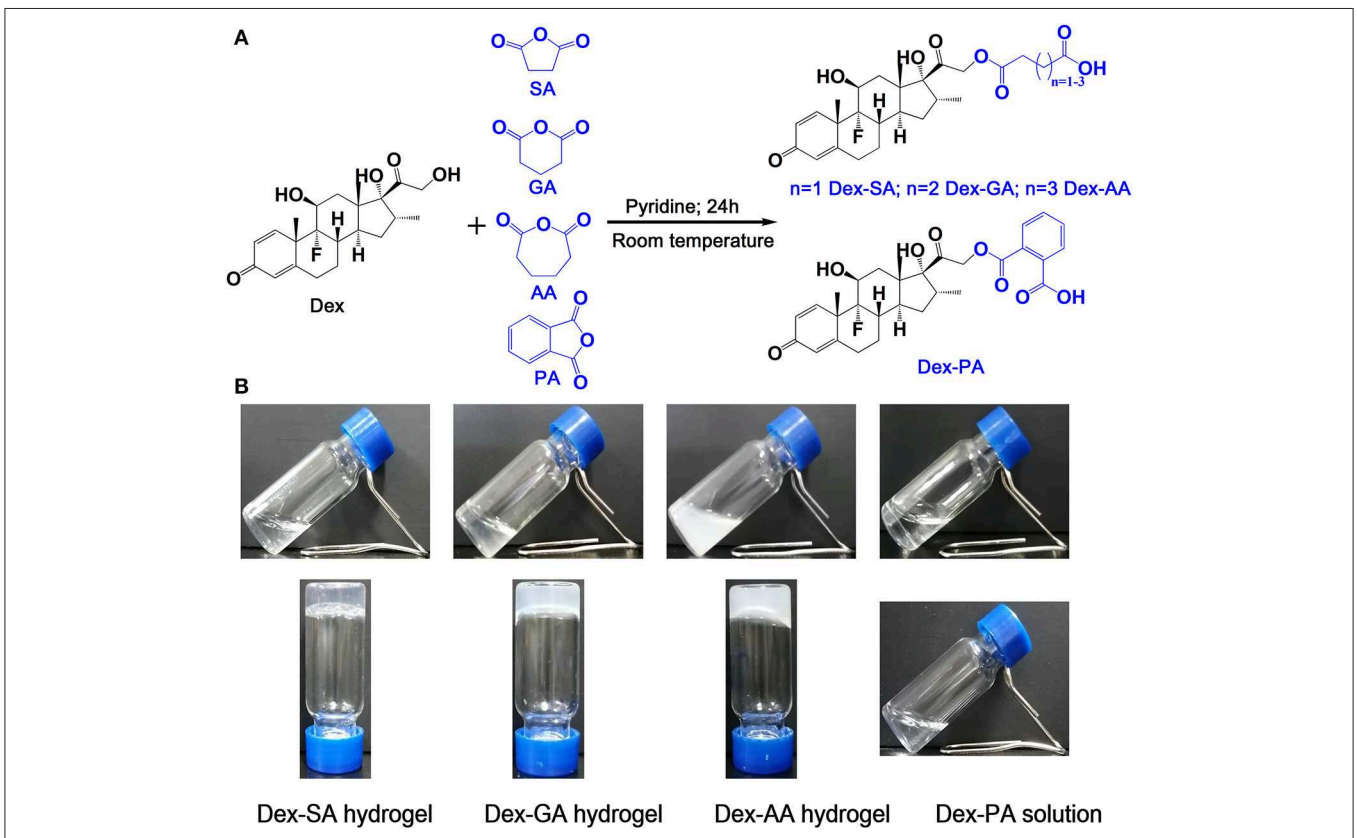

FIGURE 1 | (A) Synthetic scheme of Dex-SA, Dex-GA, Dex-AA, and Dex-PA. **(B)** Appearance of Dex-SA, Dex-GA, and Dex-AA hydrogels and Dex-PA aqueous solution; Dex-SA, Dex-GA, and Dex-AA hydrogels formed at 24, 48, and 72 h with a final concentration at 2 wt%.

and anhydrides with molar ratio at 1:3 were co-dissolved into pyridine for reaction at room temperature overnight. After that, the pyridine was evaporated using a rotary evaporator, and the resulting residues were recrystallized in petroleum ether to afford a series of Dex derivatives. Finally, the obtained products were further confirmed by LC-MS and ^{1}H-NMR (**Figures S1–S8**).

Self-Assembly of Dex Derivatives

An indicated amount of Dex derivatives (Dex-SA, Dex-GA, Dex-AA, and Dex-PA) were suspended in PBS (pH 7.4), followed by the addition of a Na_2CO_3 solution (1 equiv to Dex derivatives) to afford a transparent solution at a final concentration of 2 wt%. Sol–gel transition was monitored by an inverted test tube method as reported previously (Joo et al., 2007).

In vitro Hydrolytic Study

The hydrolytic ratio of Dex-SA, Dex-GA, and Dex-AA supramolecular hydrogels and Dex-PA aqueous solution as a function with time was measured by the quantification of the hydrolytic product Dex using HPLC assay. Briefly, 1 ml of Dex-SA, Dex-GA, Dex-AA, and Dex-PA aqueous solution was stored at room temperature for a period of 28 days of study. At predetermined time points, 0.01 ml aliquot of samples were collected and the hydrolytic product Dex was quantified by high-performance liquid chromatography (HPLC, Agilent 1290) with a reversed-phase C18 column (ZORBAX Eclipse XDB-C18, 150 × 4.6 mm i.d., 5 μm, Agilent). The mobile phase for the detection of Dex-SA, Dex-GA, and Dex-AA was composed of methanol and 0.1% acetic acid (60/40; v/v), while the mobile phase for the measurement of Dex-PA was composed of methanol and 0.1% acetic acid (70/30; v/v) at a flow rate of 1 ml/min. Aliquots of 20 μl of tested samples were injected for HPLC analysis. Detection was performed by a diode array detector (DAD) at 220 nm. The hydrolytic ratio of substrate was calculated using the following equation: Hydrolytic ratio (%) = The amount of Dex at the indicated time point/Total amount of substrate × 100.

Morphology Observation

The morphology of Dex-SA, Dex-GA, and Dex-AA supramolecular hydrogel and Dex-PA aqueous solution was observed by transition electron microscopy (TEM). Samples were pipetted onto a copper grid and stained with a 0.5 wt% phosphotungstic acid solution for TEM observation.

Rheology Test

The rheological properties of Dex-SA, Dex-GA, and Dex-AA supramolecular hydrogels were measured using a TA-AR 2000 rheometer (New Castle, DE, USA). A 40-mm cone plate was used for the experiment. A 0.4 ml hydrogel sample was loaded and a frequency sweep from 0.1 to 100 rad/s was performed.

In vitro Anti-inflammatory Efficacy

To assess the *in vitro* anti-inflammatory efficacy of Dex derivatives (Dex-SA, Dex-GA, Dex-AA, and Dex-PA), we measured the pro-inflammatory cytokine levels in the culture medium using LPS-activated RAW264.7 macrophages. Briefly, RAW264.7 macrophages were seeded at a density of 0.7 × 10^4 cells per well in a 24-well plate and pre-treated by 10 μM Dex, Dex-SA, Dex-GA, Dex-AA, and Dex-PA aqueous solution for 2 h, followed by the challenge with 1000 ng/ml lipopolysaccharide (LPS) for 24 h. Thereafter, the supernatant from each well was collected, and the pro-inflammatory factors including tumor necrosis factor-α (TNF-α) and interleukin-6 (IL-6) levels were measured using an ELISA kit (Neobioscience, Shenzhen, China). The level of nitrite (NO) was detected by the Griess assay

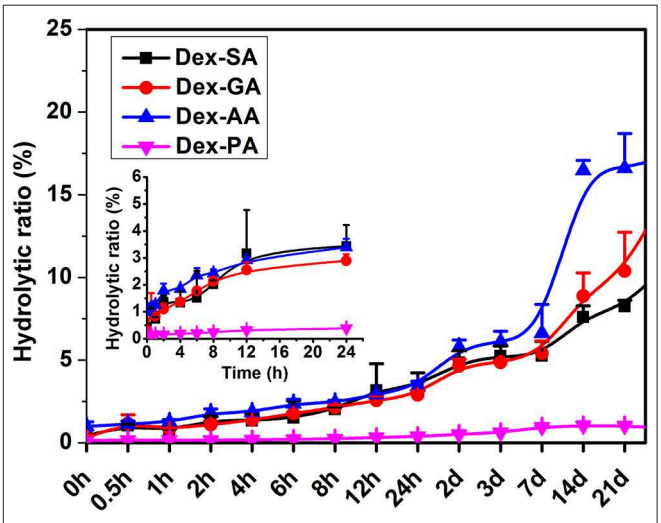

FIGURE 2 | Hydrolytic ratio of Dex-SA, Dex-GA, Dex-AA, and Dex-PA after incubation in phosphate buffered saline (PBS; pH 7.4) at room temperature.

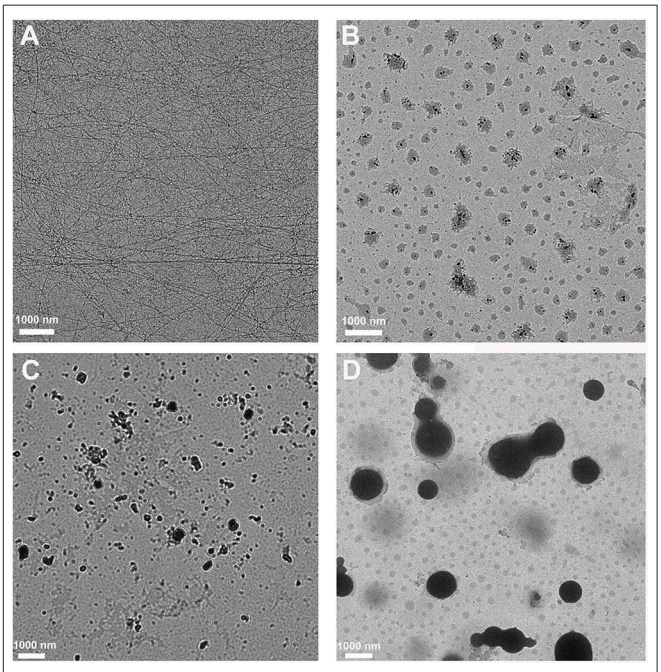

FIGURE 3 | TEM images of **(A)** Dex-SA hydrogel, **(B)** Dex-GA hydrogel, **(C)** Dex-AA hydrogel, and **(D)** Dex-PA aqueous solution.

as reported previously (Zhou et al., 2018). Cells without any manipulation were used as the negative control.

Statistical Analysis

The values of all experiments were expressed as the mean ± SD and statistically analyzed by Origin 8.5. *In vitro* anti-inflammatory efficacy data were analyzed by one-way analysis of variance (ANOVA) with Tukey's multiple comparisons test using GraphPad Prism 7.00. Statistical significance was considered at a probability level of $P < 0.05$.

RESULTS AND DISCUSSION

Self-Assembly of Dex Derivatives

Pilot studies have illustrated that the terminal motif of molecules (e.g., drugs, peptide) exhibited a strong influence over the self-assembling capacity of the same self-assembling core (Zhang et al., 2010; Ryan et al., 2011; Wang et al., 2017a). We therefore rationally designed and synthesized four precursors of Dex (**Figure 1A**; Dex-SA, Dex-GA, Dex-AA, and Dex-PA, respectively). We speculated that the acyl and alkyl chain lengths of the four precursors might dramatically influence the self-assembly tendency of Dex, thus resulting in precisely control macroscopic properties of supramolecular assemblies. We thereafter dissolved the compounds into PBS (pH 7.4) at a final concentration of 2 wt% (20 mg/ml). It is clearly observed that the Dex-SA, Dex-GA, and Dex-PA resulted into a transparent solution in PBS, while the Dex-AA exhibited a translucent solution (**Figure 1B**). Aqueous solutions of Dex-SA, Dex-GA, and Dex-AA turned into hydrogels upon incubation at ambient temperature for 24, 48, and 72 h, respectively. The resulting three hydrogels exhibited different appearances. Hydrogel formed by Dex-SA is transparent, and hydrogels formed by Dex-GA and Dex-AA are turbid (**Figure 1B**). Notably, the hydrogels formed by Dex-GA and Dex-AA occurred the precipitation after 7 days of incubation, while the hydrogel formed by Dex-SA was very stable even up to 7 days storage (Data not shown). Interestingly, there were no obvious changes in aqueous solution of Dex-PA during 3 days of incubation at ambient temperature. All these results suggested that the acyl and alkyl chain lengths had a significant effect on the self-assembly behavior of Dex conjugates.

Hydrolytic Study

The hydrolytic ratio of various Dex conjugates (Dex-SA, Dex-GA, Dex-AA, and Dex-PA) was monitored by measuring the hydrolytic product Dex by HPLC assay. As shown in **Figure 2**, it is clearly observed that Dex-SA, Dex-GA, and Dex-AA underwent similar hydrolytic behavior with about 3% hydrolysis of total substrate after 24 h incubation in PBS (pH 7.4). It seems to suggest that the hydrolytic rate of Dex-SA, Dex-GA, and Dex-AA was very slow in PBS solution and alkyl chain lengths in the range of 4–6 had no effect on the hydrolytic rate of ester bond. By extending incubation to 28 days, the

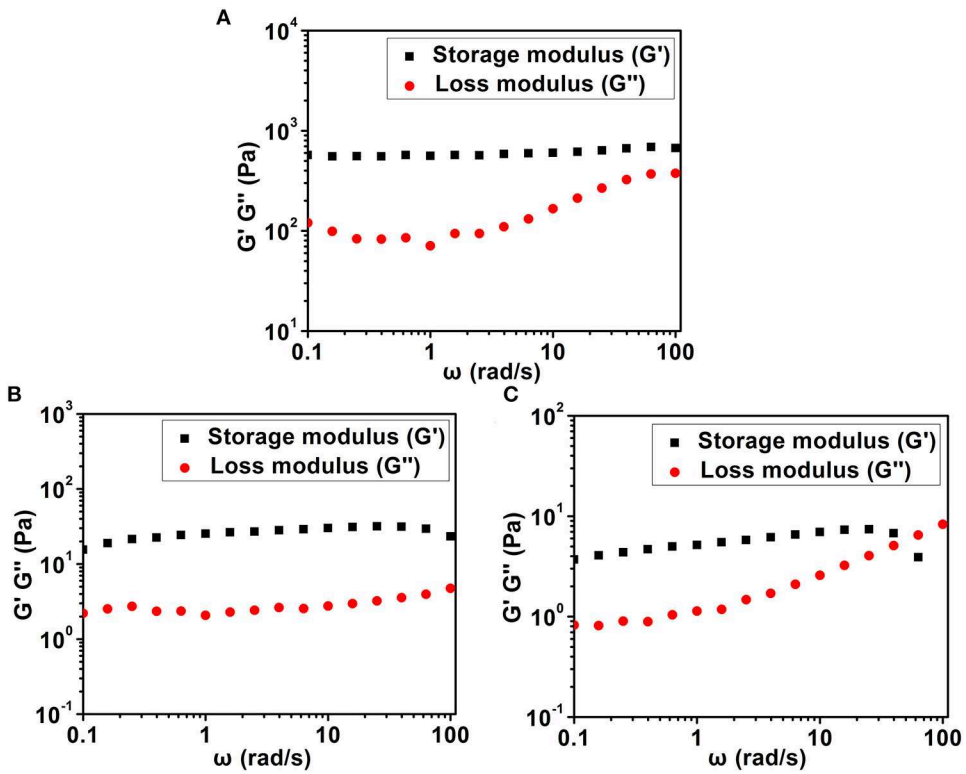

FIGURE 4 | Dynamic frequency sweep of **(A)** Dex-SA hydrogel, **(B)** Dex-GA hydrogel, and **(C)** Dex-AA hydrogel at a strain of 1%.

hydrolytic rate of Dex-SA, Dex-GA, and Dex-AA accelerated significantly and the hydrolytic ratio of Dex-SA, Dex-GA, and Dex-AA achieved 10.73 ± 0.64%, 15.17 ± 2.24%, and 17.29 ± 1.39%, respectively. Interestingly, Dex-PA resulted in a distinct reduction of the hydrolytic rate in PBS, and the hydrolytic ratio of Dex-PA was <0.5% after 24 h incubation. Even after 28 days of incubation, the hydrolytic ratio of Dex-PA was still <1%, indicating the relatively stable Dex-PA in PBS solution. This result was in accordance with the previous report of aromatic esters that are relatively stable over the fatty acid esters in most cases owing to the steric hindrance of the aromatic group to increase the activation energy of the hydrolysis (Khuwijitjaru et al., 2004).

Morphological Observation

We then adopted transmission electron microscopy (TEM) to visualize the morphology of nanostructures in the resulting hydrogels or solution. As shown in **Figure 3A**, Dex-SA hydrogel displayed the dense and three-dimensional networks of nanofibers. Unlike the Dex-SA hydrogel, Dex-GA, and Dex-AA hydrogels were composed of some irregular particles (**Figures 3B,C**), which tends to aggregate, resulting in the precipitation after 7 days of incubation. It is not surprising that Dex-PA solution was composed of spherical particles ranging 600–1,200 nm in size (**Figure 3D**). These results indicated that the acyl and alkyl chain lengths exert a profound influence on self-assembly propensity and morphology.

Rheology Test

We then used a rheometer to characterize the mechanical properties of various hydrogels. As shown in **Figure 4**, all hydrogels exhibited weak frequency dependence in the range of 0.1–100 rad/s, suggesting the relative elasticity of the hydrogels. More importantly, the storage modulus (*G'*) value of hydrogel formed by Dex-SA was much larger than that of hydrogel formed by Dex-GA and Dex-AA. For instance, the *G'* value was about 560, 25, and 5 Pa at a frequency of 1 rad/s for hydrogels formed by Dex-SA, Dex-GA, and Dex-AA, respectively. The relatively higher mechanical strength of hydrogel formed by Dex-SA might be ascribed to the formation of nanofibers to support its three-dimensional structure (**Figure 3A**). These results strongly indicated that the mechanical strength of hydrogels were also greatly influenced by the terminal motif of Dex.

In vitro Anti-inflammatory Test

Since macrophage played a very important role in the inflammatory response via the secretion of a variety of factors (Perry et al., 1993; Mantovani et al., 2005; Cohen and Mosser, 2013), such as nitric oxide (NO) and pro-inflammatory cytokines (e.g., IL-1β, TNF-α, IL-6) after the challenge with an activating stimulus (e.g., lipopolysaccharide), we have investigated the anti-inflammatory activity of various Dex conjugates in an LPS-activated RAW 264.7 macrophage. As presented in **Figure 5**, it was clearly observed that the untreated RAW 264.7 macrophage produced low levels of nitrite (NO), IL-6, and TNF-α in cell culture medium, while the

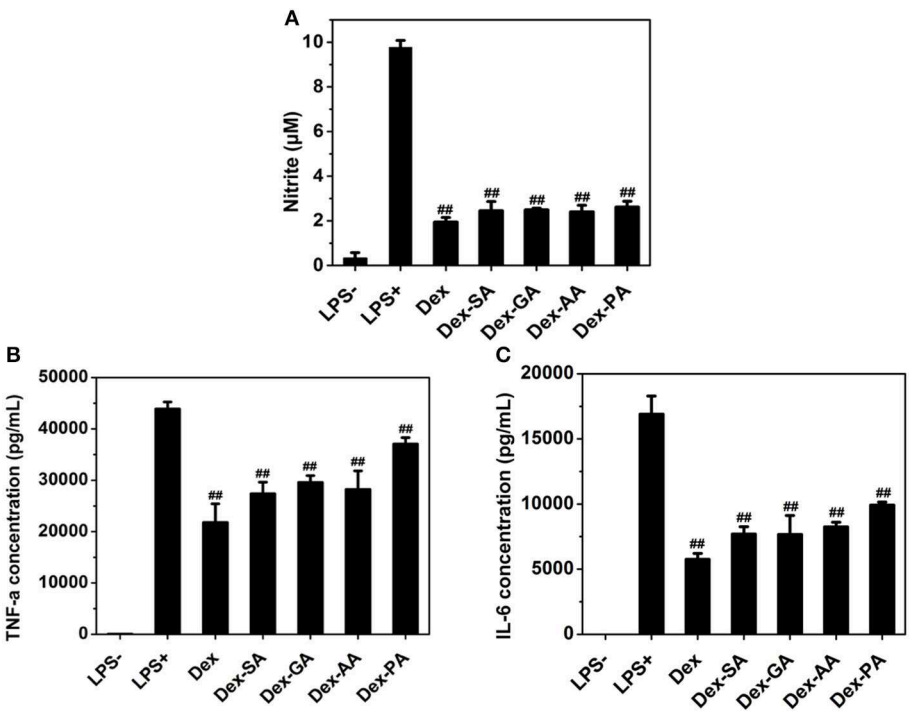

FIGURE 5 | (A) NO **(B)** TNF-α, and **(C)** IL-6 expression in cell culture medium after treatment by 10 μM Dex, Dex-SA, Dex-GA, Dex-AA, and Dex-PA in LPS-actived RAW 264.7 macrophage; $^{\#\#}p < 0.05$ vs. LPS-activated group.

activated RAW 264.7 macrophage by 1000 ng/ml LPS resulted in the high release of NO, IL-6, and TNF-α to the culture medium. Pretreatment with various Dex conjugates (Dex, Dex-SA, Dex-GA, Dex-AA, and Dex-PA) gave rise to the significant reduction of the NO, IL-6, and TNF-α production to cell culture medium ($^{\#\#}p < 0.05$ vs. LPS-activated group), suggesting that the acylation of Dex did not compromise its potent anti-inflammatory activity.

CONCLUSION

The terminal motif of Dex significantly affects the self-assembly behavior of Dex in aqueous solution. Aqueous solution of Dex-SA, Dex-GA, and Dex-AA turned into hydrogel within 72 h of incubation, and Dex-PA solution kept the clear solution within 7 days of incubation. Dex-SA, Dex-GA, and Dex-AA exhibited a progressive hydrolysis in PBS solution for a period of 28 days study, and Dex-PA did not result in the apparent hydrolysis within 28 days of incubation. Hydrogel formed by Dex-SA was composed of dense and uniform nanofibers, while hydrogels formed by Dex-GA and Dex-AA were made of irregular particles. More importantly, the acylation of Dex did not compromise its potent anti-inflammatory activity in an LPS-activated RAW 264.7 macrophage. Based on these results, we provided the basis to rationally tailor the terminal motif of drugs and thus precisely modulate the self-assembly behavior of Dex conjugates and control the macroscopic characteristics of its supramolecular assemblies without compromising its pharmacological activities.

DATA AVAILABILITY STATEMENT

All datasets generated for this study are included in the article/**Supplementary Material**.

AUTHOR CONTRIBUTIONS

XL and YW contributed to the conception and design of the study. HL performed the study and organized the database. XX performed the statistical analysis. HL and AY wrote the first draft of the manuscript. MD, DaL, and DeL wrote sections of the manuscript. All authors contributed to manuscript revision, and read and approved the submitted version.

FUNDING

This research was supported by the Zhejiang Provincial Natural Science Foundation of China (Grant No. LR18H300002), the National Natural Science Foundation of China (Grant No. 31671022, 81971732), the Zhejiang Medicines Health Science and Technology Program (Grant No. WKJ-ZJ-1529), and the Scientific Research Fund of National Health Commission (Grant No. WKJ-ZJ-1707).

SUPPLEMENTARY MATERIAL

The Supplementary Material for this article can be found online at: https://www.frontiersin.org/articles/10.3389/fchem.2020.00009/full#supplementary-material

REFERENCES

Adawiyah, N., Moniruzzaman, M., Hawatulaila, S., and Goto, M. (2016). Ionic liquids as a potential tool for drug delivery systems. *Medchemcomm* 7, 1881–1897. doi: 10.1039/C6MD00358C

Blanco, E., Shen, H., and Ferrari, M. (2015). Principles of nanoparticle design for overcoming biological barriers to drug delivery. *Nat. Biotechnol.* 33, 941–951. doi: 10.1038/nbt.3330

Cohen, H. B., and Mosser, D. M. (2013). Extrinsic and intrinsic control of macrophage inflammatory responses. *J. Leukocyte. Biol.* 94, 913–919. doi: 10.1189/jlb.0413236

Joo, M. K., Sohn, Y. S., and Jeong, B. (2007). Stereoisomeric effect on reverse thermal gelation of poly (ethylene glycol)/poly (lactide) multiblock copolymer. *Macromolecules* 40, 5111–5115. doi: 10.1021/ma070008u

Kalepu, S., and Nekkanti, V. (2015). Insoluble drug delivery strategies: review of recent advances and business prospects. *Acta Pharm. Sin. B* 5, 442–453. doi: 10.1016/j.apsb.2015.07.003

Khuwijitjaru, P., Fujii, T., Adachi, S., Kimura, Y., and Matsuno, R. (2004). Kinetics on the hydrolysis of fatty acid esters in subcritical water. *Chem. Eeg. J.* 99, 1–4. doi: 10.1016/j.cej.2003.08.002

Li, J., Li, X., Kuang, Y., Gao, Y., Du, X., Shi, J., et al. (2013). Self-delivery multifunctional anti-hiv hydrogels for sustained release. *Adv. Healthc. Mater.* 2, 1586–1590. doi: 10.1002/adhm.201300041

Lin, R., and Cui, H. (2015). Supramolecular nanostructures as drug carriers. *Curr. Opin. Chem. Eng.* 7, 75–83. doi: 10.1016/j.coche.2014.11.005

Ma, W., Cheetham, A. G., and Cui, H. (2016). Building nanostructures with drugs. *Nano Today* 11, 13–30. doi: 10.1016/j.nantod.2015.11.003

Mantovani, A., Sica, A., and Locati, M. (2005). Macrophage polarization comes of age. *Immunity* 23, 344–346. doi: 10.1016/j.immuni.2005.10.001

Mao, L., Wang, H., Tan, M., Ou, L., Kong, D., and Yang, Z. (2012). Conjugation of two complementary anti-cancer drugs confers molecular hydrogels as a co-delivery system. *Chem. Commun.* 48, 395–397. doi: 10.1039/C1CC16250K

Perry, V. H., Andersson, P. B., and Gordon, S. (1993). Macrophages and inflammation in the central nervous system. *Trends Neurosci.* 16, 268–273. doi: 10.1016/0166-2236(93)90180-T

Ryan, D. M., Doran, T. M., Anderson, S. B., and Nilsson, B. L. (2011). Effect of C-terminal modification on the self-assembly and hydrogelation of fluorinated Fmoc-Phe derivatives. *Langmuir* 27, 4029–4039. doi: 10.1021/la1048375

Svobodová, H., Noponen, V., Kolehmainen, E., and Sievänen, E. (2012). Recent advances in steroidal supramolecular gels. *RSC Adv.* 2, 4985–5007. doi: 10.1039/c2ra01343f

Terech, P., de Geyer, A., Struth, B., and Talmon, Y. (2002). Self-assembled monodisperse steroid nanotubes in water. *Adv. Mater.* 14, 495–498. doi: 10.1002/1521-4095(20020404)14:7<495::AID-ADMA495>3.0.CO;2-9

Terech, P., Dourdain, S., Bhat, S., and Maitra, U. (2009). Self-assembly of bile steroid analogues: molecules, fibers, and networks. *J. Phys. Chem. B* 113, 8252–8267. doi: 10.1021/jp811217b

Vader, P., Mol, E. A., Pasterkamp, G., and Schiffelers, R. M. (2016). Extracellular vesicles for drug delivery. *Adv. Drug. Deliver. Rev.* 106, 148–156. doi: 10.1016/j.addr.2016.02.006

Vemula, P. K., Cruikshank, G. A., Karp, J. M., and John, G. (2009). Self-assembled prodrugs: an enzymatically triggered drug-delivery platform. *Biomaterials* 30, 383–393. doi: 10.1016/j.biomaterials.2008.09.045

Vemula, P. K., Wiradharma, N., Ankrum, J. A., Miranda, O. R., John, G., and Karp, J. M. (2013). Prodrugs as self-assembled hydrogels: a new paradigm for biomaterials. *Curr. Opin. Biotech.* 24, 1174–1182. doi: 10.1016/j.copbio.2013.02.006

Wang, H., Lu, Z., Wang, L., Guo, T., Wu, J., Wan, J., et al. (2017a). New generation nanomedicines constructed from self-assembling small-molecule prodrugs alleviate cancer drug toxicity. *Cancer Res.* 77, 6963–6974. doi: 10.1158/0008-5472.CAN-17-0984

Wang, Y., Cheetham, A. G., Angacian, G., Su, H., Xie, L., and Cui, H. (2017b). Peptide-drug conjugates as effective prodrug strategies for targeted delivery. *Adv. Drug Deliv. Rev.* 110–111, 112–126. doi: 10.1016/j.addr.2016.06.015

Webber, M. J., Matson, J. B., Tamboli, V. K., and Stupp, S. I. (2012). Controlled release of dexamethasone from peptide nanofiber gels to modulate inflammatory response. *Biomaterials* 33, 6823–6832. doi: 10.1016/j.biomaterials.2012.06.003

Wu, D., Xie, X., Kadi, A. A., and Zhang, Y. (2018). Photosensitive peptide hydrogels as smart materials for applications. *Chinese Chem. Lett.* 29, 1098–1104. doi: 10.1016/j.cclet.2018.04.030

Wu, W., Zhang, Z., Xiong, T., Zhao, W., Jiang, R., Chen, H., et al. (2017a). Calcium ion coordinated dexamethasone supramolecular hydrogel as therapeutic alternative for control of non-infectious uveitis. *Acta Biomater.* 61, 157–158. doi: 10.1016/j.actbio.2017.05.024

Wu, X. R., Wu, C. W., Ding, F., Tian, C., Jiang, W., Mao, C. D., et al. (2017b). Binary self-assembly of highly symmetric DNA nanocages via sticky-end engineering. *Chinese Chem. Lett.* 28, 851–856. doi: 10.1016/j.cclet.2017.01.012

Xiong, T., Li, X., Zhou, Y., Song, Q., Zhang, R., Lei, L., et al. (2018). Glycosylation-enhanced biocompatibility of the supramolecular hydrogel of an anti-inflammatory drug for topical suppression of inflammation. *Acta Biomater.* 73, 275–284. doi: 10.1016/j.actbio.2018.04.019

Yang, P., Yang, C., Zhang, K., Wang, L., and Wang, H. (2018). KLVFF peptide functionalized nanoparticles capture $A\beta_{42}$ by co-assembly for decreasing cytotoxicity. *Chinese Chem. Lett.* 29, 1811–1814. doi: 10.1016/j.cclet.2018.10.003

Zhang, M., Fives, C., Waldron, K. C., and Zhu, X. X. (2017). Self-assembly of a bile acid dimer in aqueous solutions: from nanofibers to nematic hydrogels. *Langmuir* 33, 1084–1089. doi: 10.1021/acs.langmuir.6b04033

Zhang, Y., Kuang, Y., Gao, Y., and Xu, B. (2010). Versatile small-molecule motifs for self-assembly in water and the formation of biofunctional supramolecular hydrogels. *Langmuir* 27, 529–537. doi: 10.1021/la10 20324

Zhang, Z., Yu, J., Zhou, Y., Zhang, R., Song, Q., Lei, L., et al. (2018). Supramolecular nanofibers of dexamethasone derivatives to form hydrogel for topical ocular drug delivery. *Colloids Surf. B Biointerfaces* 164, 436–443. doi: 10.1016/j.colsurfb.2018.01.051

Zhao, F., Ma, M. L., and Xu, B. (2009). Molecular hydrogels of therapeutic agents. *Chem. Soc. Rev.* 38, 883–891. doi: 10.1039/b806410p

Zhou, Y., Lei, L., Zhang, Z., Zhang, R., Song, Q., and Li, X. (2018). Cation instructed steroidal prodrug supramolecular hydrogel. *J. Colloid Interface Sci.* 528, 10–17. doi: 10.1016/j.jcis.2018.05.059

Zhou, Y., and Li, X. (2017). Self-assembled small molecular weight hydrogels of prodrugs. *Chinese Chem. Lett.* 28, 1835–1840. doi: 10.1016/j.cclet.2017. 04.033

Zylberberg, C., and Matosevic, S. (2016). Pharmaceutical liposomal drug delivery: a review of new delivery systems and a look at the regulatory landscape. *Drug Deliv.* 23, 3319–3329. doi: 10.1080/10717544.2016.11 77136

Conflict of Interest: The authors declare that the research was conducted in the absence of any commercial or financial relationships that could be construed as a potential conflict of interest.

frontiers in Chemistry

MINI REVIEW
published: 25 May 2020
doi: 10.3389/fchem.2020.00380

Supramolecular Self-Assembled Nanostructures for Cancer Immunotherapy

Zichao Huang[1,2], *Wantong Song*[1,3]* *and Xuesi Chen*[1,2,3]*

[1] *Key Laboratory of Polymer Ecomaterials, Changchun Institute of Applied Chemistry, Chinese Academy of Sciences, Changchun, China,* [2] *School of Applied Chemistry and Engineering, University of Science and Technology of China, Hefei, China,* [3] *Jilin Biomedical Polymers Engineering Laboratory, Changchun, China*

Functional materials and nanostructures have been widely used for enhancing the therapeutic potency and safety of current cancer immunotherapy. While profound nanostructures have been developed to participate in the development of cancer immunotherapy, the construction of intricate nanostructures with easy fabrication and functionalization properties to satisfy the diversified requirements in cancer immunotherapy are highly required. Hierarchical self-assembly using supramolecular interactions to manufacture organized architectures at multiple length scales represents an interesting and promising avenue for sophisticated nanostructure construction. In this mini-review, we will outline the recent progress made in the development of supramolecular self-assembled nanostructures for cancer immunotherapy, with special focus on the supramolecular interactions including supramolecular peptide assembly, supramolecular DNA assembly, lipid hydrophobic assembly, host-guest assembly, and biomolecular recognition assembly.

Keywords: supramolecular, cancer immunotherapy, nanostructure, self-assembly, modularization

OPEN ACCESS

Edited by:
Huaimin Wang,
Westlake University, China

Reviewed by:
Zhaoqianqi Feng,
Harvard University, United States
Chengbiao Yang,
Wayne State University, United States

***Correspondence:**
Wantong Song
wtsong@ciac.ac.cn
Xuesi Chen
xschen@ciac.ac.cn

Specialty section:
This article was submitted to Supramolecular Chemistry, a section of the journal Frontiers in Chemistry

Received: *13 March 2020*
Accepted: *14 April 2020*
Published: *25 May 2020*

Citation:
Huang Z, Song W and Chen X (2020) Supramolecular Self-Assembled Nanostructures for Cancer Immunotherapy. Front. Chem. 8:380. doi: 10.3389/fchem.2020.00380

INTRODUCTION

Cancer immunotherapy is re-defining the field of cancer therapy by activating the immune system to fight cancer. Since the approval of ipilimumab in 2011, cancer immunotherapy is playing an increasingly important role in cancer therapy (Mellman et al., 2011). Nowadays, cancer immunotherapy can be divided into three major classes by the intervention into the cancer-immunity circle: cancer vaccines, adoptive-cell transfer (ACT) therapy, and tumor immune microenvironment (TIME) modulation (Chen and Mellman, 2013; Rosenberg and Restifo, 2015; Van Der Burg et al., 2016; Zou et al., 2016). Leading products like immune checkpoint inhibitors [antibodies against programmed death 1 or its ligand (PD-1/PD-L1)] or chimeric antigen receptor T cell (CAR-T) therapy have entered the market and achieved great success in many cancer types (Hoos, 2016; June and Sadelain, 2018). However, there are still problems for current immunotherapy. One key problem is the low response rate—the overall response rate of immune checkpoint therapy in the majority of cancer types is lower than 20% (Yarchoan et al., 2017; Sanmamed and Chen, 2018), while CAR-T therapy is only effective in blood cancer (Martinez and Moon, 2019). Moreover, immune-related adverse effects

(irAEs) have always been observed in clinic in association with immunotherapy, which is becoming a more and more serious problem (Hamamoto et al., 2018; Postow et al., 2018).

Nanotechnology has been widely used to enhance the therapeutic potency and safety of current cancer immunotherapy (Goldberg, 2015; Dacoba et al., 2017; Jiang et al., 2017; Song et al., 2020). Due to their unique size and surface effect, nanostructures can not only serve as carriers of small molecular drugs or proteins for targeted delivery and controlled release, but also be built with multifunctional modules to regulate the immune microenvironment in multiple dimensions (Song et al., 2017; Wang et al., 2017b; Yuan et al., 2017). In cancer vaccines, nanomaterials encapsulating tumor antigens and adjuvants can delay them from perfusion and degradation, and promote antigen presentation efficiency by an intrinsic uptake by antigen-presenting cells (APCs) and enhancing subsequent cross-presentation (Bachmann and Jennings, 2010; Fan and Moon, 2015; Irvine et al., 2015). In cell-based therapy, backpacked nanogels could promote the response of CAR-T cells in a solid tumor while *ex vivo*-generated artificial nanostructured APCs could stimulate the proliferation of tumor antigen-specific T cells *in vivo* (Wang et al., 2017a; Tang et al., 2018). In TIME modulation, the size and shape design of the nanostructures can alter the metabolic behaviors of the loaded cargos *in vivo*, which can enhance the treatment efficiency and reduce non-specific side effects (Milling et al., 2017; Ma et al., 2020a,b). As multimodular constructions, nanomaterials with multiple functional modules like antibody fragments for targeting, environmental responsive linkers for intelligent release, and secondary treatment molecules for combined therapy can deliver more powerful therapeutic successes in cancer immunotherapy (Sau et al., 2018).

In general, functional nanostructures are constructed through a bottom-up approach, in which different molecules clump together into nanosized particles. The forces inducing molecules aggregation are usually covalent bonds from chemical reactions or non-covalent bonds from various weak interactions (Zheng et al., 2018). Non-covalent interactions are weaker than covalent bonds but they widely exist in natural assemblies, like protein structures, DNA double helixes, phospholipid bilayers, and the recognition of ligands with receptors. Supramolecular interactions are a class of interactions categorized by their non-covalent character. Due to its flexibility and reversibility, supramolecular assembly is an appropriate way to construct complicated multi-module hierarchical structures in cancer immunotherapy, similar to building frameworks in LEGO pieces (Huang and Anslyn, 2015; Yang et al., 2015). Moreover, supramolecular-assembled nanostructures make it easier to control multiple modules with the relatively weak and dynamic noncovalent interactions (Ma and Zhao, 2015).

In this mini review, we will summarize some typical supramolecular self-assembled nanostructures in cancer immunotherapy, and describe the modularization idea embodied in the supramolecular assembly. Limited by length, we will mainly introduce some representative nano-assemblies from five typical supramolecular interactions, including supramolecular peptide assembly (SPA), supramolecular DNA assembly (SDA), lipid hydrophobic assembly (LHA), host-guest assembly (HGA), and biomolecular recognition assembly (BRA).

SUPERMOLECULAR ASSEMBLY FOR CANCER IMMUNOTHERAPY

Supramolecular Peptide Assembly (SPA)

As a subunit of proteins, some peptides can undergo a similar supramolecular assembly by non-covalent intermolecular interactions, including hydrogen bonding, electrostatic interactions, and π-π stacking (Yuan et al., 2019). Moreover, some of the assembled peptides can form similar secondary structure as proteins, like α-helix and β-sheet (Zhang et al., 2020). These natural self-assembly advantages make peptides good assembly modules for the construction of supramolecular nanostructures for cancer immunotherapy (Li et al., 2019; Cai et al., 2020).

With tumor antigens covalently linking to the peptide domains before the assembly or non-covalently incorporated into the peptide together with the assembly, supramolecular peptide assembly has been applied for cancer vaccine construction (Wen and Collier, 2015; Wu et al., 2017). The peptide assembly can not only play a role as a carrier, but may also work as the adjuvant. For example, Collier and co-workers have reported that supramolecular peptide nanofibers assembled from some specific peptide sequences [e.g., QQKFQFQFEQQ (Q11), FKFEFKFE(KFE8)] have self-adjuvanting properties (Rudra et al., 2012; Hudalla et al., 2013). The assembly of peptide domains is essential for the self-adjuvating property, as loss of fibrillization of a peptide module leads to the loss of adjuvant activity. Bacterial lipopeptide Pam_3-Cys-Ser-Lys_4 (Pam_3CSK_4) is another synthetic peptide adjuvant which is a potent activator of Toll-like receptor 2 and 6. Pam_3Cys can self-assemble into well-defined nanostructures in aqueous solutions and its coupling with antigen peptide could elicit immune responses without the use of any external adjuvant (Ingale et al., 2007; Cai et al., 2014).

Peptide-assembled nanostructures can also be applied for the loading or conjugating of small molecular immunomodulators for TIME modulation. For example, Cheng et al. designed a sequentially responsive therapeutic peptide for dual-targeted cancer immunotherapy. The peptide contained a short D-peptide antagonist (^{D}PPA-1) of PD-L1, and could self-assemble into nanostructures for the loading inhibitor of indoleamine 2,3-dioxygenase (IDO). The nanostructure swelled in a weakly acidic tumor niche due to the protonation of the functional 3-diethylaminopropyl isothiocyanate (DEAP), and released the loaded NLG919 due to the cleavage of the peptide substrate by matrix metalloproteinase-2 (MMP-2) (Cheng et al., 2018). In another study, Han et al. reported a peptide-drug conjugate containing a targeting motif (arginyl-glycyl-aspartic acid, RGD), two protonatable histidines, and an ester bond-linked IDO inhibitor. The conjugate self-assembled into nanostructures in an aqueous solution and exhibited pH-responsive disassembly and esterase-catalyzed drug release after arriving at the tumor tissue, which greatly enhanced the therapeutic potency of PD-L1 blockade in murine Pan02 tumor model (Han et al., 2020).

Peptide materials are biodegradable and normally have good biocompatibility. Their well-defined structure and viability in sequence design also means they have a wide range of functionalities. The assembly behavior not only occurs between peptides, but also appears between peptides and the organism. In an interesting study, Ji et al. utilized a pH low insertion peptide (pHLIP) for anchoring Fc fragments on tumor cell surfaces. The pHLIP can selectively assemble onto the membrane of tumor cells via the conformational transformation in response to the acidic tumor microenvironment, and the inserted Fc fragments or antibodies can subsequently induce antibody-dependent cell-mediated cytotoxicity (ADCC) effects to kill tumor cells (Ji et al., 2019). The recognition between immune cells and the tumor cells is a key step in cancer immunotherapy. This study inspires applying peptide assembly for modifying cell surface and enhancing this recognition effect.

Supramolecular DNA Assembly (SDA)

Deoxyribonucleic acid (DNA), a type of nucleic acid, is an important biological molecule carrying genetic information, mostly existing as a double helix with another DNA chain. The double helix structure is built through exquisite Watson-Crick base pairing, a non-covalent interaction driven by multiple strong hydrogen bonds. The stable and specific conjugation from two complementary DNA chains is suitable to serve as a linker between two modules, therefore, using supramolecular DNA assembly interactions is another way to construct nanostructures (Chhabra et al., 2010; Chou et al., 2014).

Various DNA nanoassemblies with good stability and high cargo loading capacity have been reported in cancer immunotherapy, and a certain amount of them focus on delivery of CpG—the most commonly used vaccine adjuvant (Chi et al., 2020). These nanostructures include DNA cages, DNA nanotubes, spherical nucleic acids (SNAs), DNA polypods, and so on. For example, DNA tetrahedron architectures assembled from DNA strands can mimic the complex structure of virus-like particles, and provide a multifunctional platform for building DNA vaccines (Liu et al., 2012). SNAs with a solid or hollow core could induce higher inflammatory responses than its linear counterpart due to its special geometry, which generates the ability to target lymph nodes in a high-affinity multivalent fashion (Radovic-Moreno et al., 2015). DNA nanococoons (DNCs) were developed through an enzymatic rolling circle amplification method with long-chain single-stranded DNA repeatedly containing interval CpG sequences and cutting sites of restriction enzyme HhaI. In a tumor inflammatory microenvironment, the DNCs are degraded and release the CpG fragments as well as the loaded cargos (anti-PD-1 antibody) to promote synergistic treatment for melanoma (Wang et al., 2016).

The supramolecular interactions between DNA base pairs have also been employed for antibody conjugation on nanostructures to enable modular and tunable control of cell-based cancer immunotherapies. Huang et al. developed an artificial immune cell engager (AICE) nanoplatform for the modular and tunable control of cell-based cancer immunotherapies (Huang et al., 2019). Multiple proteins and antibodies were decorated on the surface of biodegradable nanoparticles via complementary DNA-scaffolding through the direct hybridization. The bases pairing recognition based on multiple hydrogen bonds is very precise and stable, and the hierarchical construction strategy enabled precise and ratiometic loading of multiple cargos on the nanoparticle surface. AICE constructed by this way have been proven to be effective for *ex vivo* expansion of T cells and providing priming signals for systemically administered AND-gate CAR-T cells (Huang et al., 2019).

Lipid Hydrophobic Assembly (LHA)

Phospholipid and its derivatives are typical amphiphilic molecules that can self-assemble into nanostructures such as liposomes and bilayer sheets through hydrophilic-hydrophobic interactions. Just like the function of vesicles in organisms, liposomes have been widely exploited as nanocarriers to deliver functional molecules (Sercombe et al., 2015). In cancer immunotherapy, liposomes have been widely used for tumor antigens or TIME modulators loading for lymph node or tumor-specific delivery (Kwong et al., 2013; Koshy et al., 2017; Miao et al., 2017; Chen et al., 2019). In addition, the hydrophobic driving forces between lipids can enable "plug in" construction of these cargos. Functional molecules modified with a lipidation motif can be incorporated into the lipid bilayer through lipid hydrophobic interaction in a simple manner. This incorporation strategy presents a new way to construct well-organized multimodular nanostructures.

In a typical example, Moon et al. reported a synthetic high-density lipoprotein nanodiscs composed of phospholipids and apolipoprotein A1-mimetic peptides as a cancer vaccine platform (Kuai et al., 2017). These designed vaccine nanodiscs can easily load antigens and adjuvants by simple incubation with antigen peptides modified with Dioleoyl-sn-glycero-3-phosphoethanolamine-N-[3-(2-pyridyldithio)propionate] (DOPE-PDP) and CpG modified with cholesterol (Cho-CpG), and was shown to elicit up to 47-fold greater frequencies of antigen-specific cytotoxic T-lymphocytes than soluble vaccines (Kuai et al., 2017). Meanwhile, the incorporating types of antigens can be controlled conveniently, making this lipidation incorporation strategy a suitable route for personalized vaccination with patient-specific neoantigens. In another study, they employed the nanodisc to deliver doxorubicin (DOX) for triggering immunogenic cell death (ICD) in the tumor. ICD is a kind of cell death characterized by calreticulin exposure, adenosine triphosphate (ATP), and high mobility group protein B1 (HMGB1) release, which could elicit cell-specific immune responses (Kroemer et al., 2013; Galluzzi et al., 2017). DOX was conjugated to a lipid tail with a pH-sensitive linker, and self-assembled into nanodiscs at mild conditions by simple mixing and incubation. In *in vivo* studies, the delivery of DOX via this way elicited robust antitumor $CD8^+$ T cell responses, while the free DOX did not show this effect. The combination of this DOX in nanodiscs plus anti-PD-1 antibody therapy

induced complete regression of established murine tumors (Kuai et al., 2018).

Besides small molecule therapeutics, the lipid hydrophobic assembly may also be applied for incorporating auxiliary modules into the liposomes, and enable hierarchical construction of functional structures for cancer immunotherapy. For example, Kulkarni et al. prepared a modular bifunctional therapeutic (anti-SIRPα-AK750) consisting of both signal regulatory protein alpha (SIPRα)-blocking antibodies and colony stimulating factor 1 receptor (CSF-1R) inhibitors by lipid hydrophobic supramolecular assembly to simultaneously block the CD47-SIPRα and MCSF-CSF-1R signaling axis (Kulkarni et al., 2018). Song et al. applied a lipid-protamine-DNA (LPD) nanoparticle for tumor tissue-specific expression of checkpoint inhibition proteins (PD-L1 trap) to reduce the irAEs of anti-PD-L1 antibodies (Song et al., 2018a). The LPD nanoparticle was constructed in a hierarchical self-assembled manner with the inner core firstly formed by the electronic interactions between protamine and DNA, then coated with preformed cationic liposomes, and finally PEG and targeting ligands were modified on the surface by lipid hydrophobic assembly. Surface PEG density can be easily changed to optimize the *in vitro* and *in vivo* behavior of the nanoparticles (Li et al., 1998; Wang et al., 2013). This construction method can be expanded for other systems by changing the DNA plasmid or targeting ligands on the nanoparticle surface (Song et al., 2018b; Wang et al., 2018).

Host-Guest Assembly (HGA)

The host-guest system first began to gain attention in 1987, along with the first proposal of the concept of supramolecular chemistry (Lehn, 1988). Macrocyclic molecules as the host molecules can bind guest molecules into their cavities via non-covalent forces such as hydrophobic interaction, electrostatic interaction, and hydrogen-bonding interaction, while the external property of the host molecules favors the interaction with surrounding solvents to make the system soluble (Ma and Zhao, 2015). The most commonly used host molecule for supramolecular assembly construction is β-cyclodextrin (β-CD) (Hu et al., 2014; Antoniuk and Amiel, 2016), which has been approved by the US Food and Drug Administration for medical use.

The host molecules can encapsulate hydrophobic drugs as guest molecules into their hydrophobic cavities (Ma and Zhao, 2015). The hydrophobicity of many small molecular immunomodulators limits their direct administration, and sometimes common nanomaterials like liposomes and micelles have only a modest capacity for their incorporation. By modifying macromolecules with β-CD, many hydrophobic small

TABLE 1 | Representative supramolecular assemblies applied in cancer immunotherapy discussed in this paper.

Supramolecular assembly types	Assembly domain	Immune agents	Immunotherapy types	References
Supramolecular Peptide Assembly (SPA)	Fibrillized Peptide (Q11, KFE8)	Model antigen OVA	Cancer vaccine	Rudra et al., 2012; Hudalla et al., 2013
	Bacterial lipopeptide (Pam_3CSK_4)	Peptide antigen	Cancer vaccine	Ingale et al., 2007; Cai et al., 2014
	Amphiphilic peptide (DEAP-^{D}PPA-1, NLG-RGD NI)	IDO inhibitor (NLG919), PD-L1 inhibitor	TIME modulation	Cheng et al., 2018; Han et al., 2020
	pH low insertion peptide (pHLIP)	Fc fragment	Cell-based immunotherapy	Ji et al., 2019
Supramolecular DNA Assembly (SDA)	DNA cage	DNA antigen	Cancer vaccination	Liu et al., 2012
	SNAs	Model antigen OVA	Cancer vaccination	Radovic-Moreno et al., 2015
	DNA nano-cocoon (DNCs)	Anti-PD-1 antibody, CpG	TIME modulation	Wang et al., 2016
	DNA base pairs	Anti-CD3, anti-CD28, IL-2, etc.	Cell-based immunotherapy	Huang et al., 2019
Lipid hydrophobic assembly (LHA)	Lipid nanodiscs	Peptide antigens, CpG	Cancer vaccination	Kuai et al., 2017
	Lipid nanodiscs	DOX (inducing ICD)	TIME modulation	Kuai et al., 2018
	Lipid bilayer	anti-SIRPα, CSF-1R inhibitor (BLZ945)	TIME modulation	Kulkarni et al., 2018
	Liposomes	Plasmid DNA	TIME modulation	Song et al., 2018a
Host-guest assembly (HGA)	β-CD	TGF-β receptor-I inhibitor, R848, IDO-1 inhibitor, etc.	TIME modulation	Park et al., 2012; Rodell et al., 2018; Hu et al., 2020
Biomolecular recognition assembly (BRA)	Avidin-biotin	Anti-4-1BB, anti-PD-L1, anti-CD28, MHC-Ig dimer	Cell-based immunotherapy	Perica et al., 2014; Kosmides et al., 2017
	Antigen-antibody, Fc fragment	anti-TCR, anti-CD19	Cell-based immunotherapy	Schütz et al., 2014
	Membrane-anchored lipoprotein (ASSET)	Antibodies against leukocytes, siRNA	Cell-based immunotherapy	Kedmi et al., 2018

molecular immunomodulators or protein therapeutics can be directly loaded into the cavity of β-CD or entrapped into the nanoassemblies formed by the host-guest interaction between CD and guest molecules like amantadine or azobenzene (Park et al., 2012; Xu et al., 2019; Si et al., 2020). For example, Rodell reported a β-CD nanoparticle (CDNPs) through a reaction between succinyl-β-CD and L-lysine for R848 loading. As a monotherapy, the administered CDNP-R848 could promote the polarization of tumor-associated macrophages into an M1 phenotype (Rodell et al., 2018). Hu et al. prepared a host-guest prodrug nanovectors for combating tumor immune tolerance. Reduction-labile heterodimer of Pheophorbide A (PPa) and NLG919 were integrated with hyaluronic acid via host-guest interactions between β-CD and NLG919. When near infrared laser irradiation was applied, this nanovector could completely eradicate CT26 colorectal tumors through combination immunotherapy (Hu et al., 2020).

Biomolecular Recognition Assembly (BRA)

The unique interactions between biomolecules for recognition and binding may be used as another supramolecular driving force for nanostructure constructions. This kind of interaction includes antigen-antibody recognition, receptor-ligand recognition, avidin-biotin recognition, and so on (Fritz et al., 2000; Kahn and Plaxco, 2010; Gong et al., 2019). The biomolecular recognition interaction is typically highly specific, with a high affinity and reversibility. For example, the avidin-biotin interaction, which is thought to be the strongest known non-covalent interaction between a protein and a ligand ($K_d = 10^{-15}$ M), has been applied for the conjugation of biotinylated antibodies to commercial antibiotin-coated microbeads. This design enables microbeads as bispecific engagers with anti-4-1BB and anti-PD-L1 antibodies for blocking the inhibitory checkpoint while simultaneously activating the stimulatory signal (Kosmides et al., 2017), or with MHC-Ig dimer and CD28 antibodies as aAPC to activate and expand tumor-specific T cells (Perica et al., 2014).

The interaction between antigen-antibody recognition has also been developed to modify antibodies on nanostructures. A major interaction applied is through the primary antibody binding to the Fc fragment of the secondary antibody, which will not interfere with the ability of the secondary antibody to bind with antigens. Commercial microbeads coated with anti-mouse IgG1 have been used to conjugate peptide-MHC complexes or clonotypic anti-TCR (1B2) and α-human CD19 as bispecific engagers to redirect T cells to target and destroy tumor cells (Schütz et al., 2014). One of the advantages of this strategy is that the binding site is limited at the Fc domain without interference from the antigen-binding domain and the orientation of the antibody is kept for ligand binding. Inspired by the protein displaying strategies on the inner membranes of bacteria, Kedmi et al. developed a flexible modular platform for non-covalently coating various antibodies on lipid-based nanoparticles. They

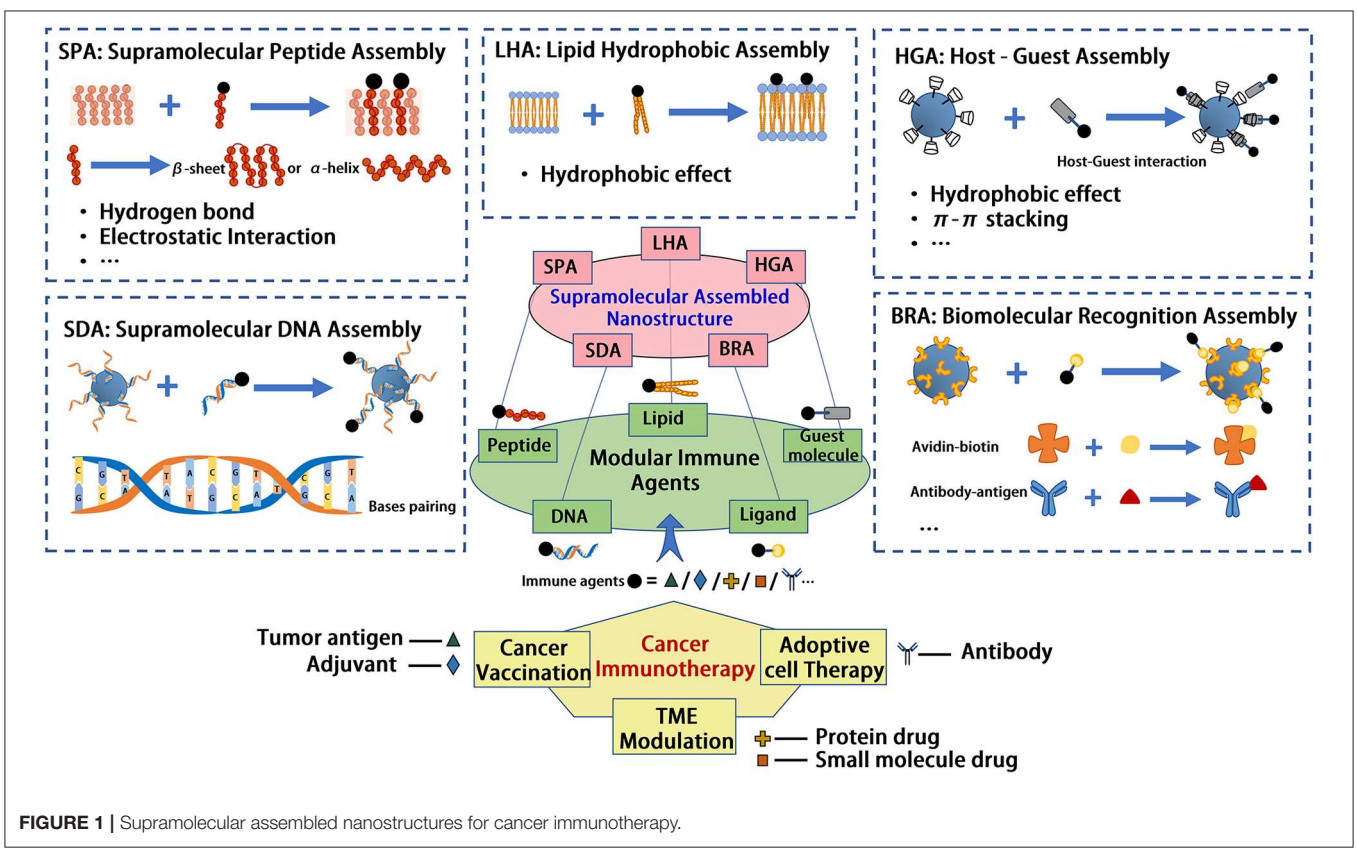

FIGURE 1 | Supramolecular assembled nanostructures for cancer immunotherapy.

used a recombinant membrane-anchored lipoprotein (anchored secondary scFv enabling targeting, ASSET) which contains an N-terminal signal sequence for membrane insertion and an scFv for Fc binding. The nanoplatform enables the simple switch of several monoclonal antibodies for diverse leukocytes targeted siRNA delivery (Kedmi et al., 2018).

CONCLUSIONS

Our world is constructed from molecules. While molecular chemistry is concerned with the role of covalent bond in small- and macro- molecules governing the structures, properties, and transformation, supramolecular chemistry is defined as "chemistry beyond the molecule" (Lehn, 1988). Through hierarchical self-assembly, supramolecular chemistry exploits various non-covalent interactions between small- or macro- molecules and manufactures sophisticated organized systems at multiple length scales. Importantly, supramolecular materials and structures are generally tunable, modular, and reversible, as a result of the weak, specific, and multiplicate interactions they use (Webber et al., 2016). These unique properties make supramolecular interactions more attractive in constructing various structures, such as nanostructures, for drug delivery and controlled release. Considering the complexity of nanostructures as well as the therapeutic agents used in immunotherapy, supramolecular assembly provides a biomimetic and cost-efficient way for constructing multimodal nanotherapeutics in immunotherapy, which have been further proved meaningful in expanding the success of cancer immunotherapy. In this mini review, we summarized some of the representative supramolecular nanoassemblies leveraged for cancer immunotherapy, as concluded briefly in **Table 1**. Five common supramolecular assembled models introduced here are supramolecular peptide assembly (SPA), supramolecular DNA assembly (SDA), lipid hydrophobic assembly (LHA), host-guest assembly (HGA), and biomolecular recognition assembly (BRA), involving supramolecular forces of hydrogen bond, electrostatic interaction, hydrophobic effect, and π-π stacking, etc. The main idea of this construction strategy for nanoimmunotherapeutics is to modularize immune agents with functionalized domains, as shown in **Figure 1**, to give them the ability to incorporate into the supramolecular nanostructures. Some immune agents serve as the supramolecular assembly modules themselves. For example, some hydrophobic immune modulators can be encapsulated into β-CD as cargo through host-guest assembly, and adjuvant CpG oligodeoxynucleotide can assemble into a DNA backbone directly through bases pairing, while most other immune agents need pre-modifications with supramolecular assembled modules. The summary of these supramolecular assembly strategies may provide some guidance to researchers in using supramolecular interactions in the design of nanostructures for cancer immunotherapy.

With the rapid integration of nanotechnology and cancer immunotherapy, abundant novel nanoimmunotherapeutics have emerged. Due to the weak interaction and assembly from simple structures, supramolecular-based structures offer more potential for clinical translation. For example, an RNA vaccine based on lipid nanoparticles named Lipo-MERIT, an immune agonist CpG with the format of a spherical nucleic acid named AST-008, and nanogels named TRQ15-01 acting as a "backpack" to modify and activate ACT cells have entered phase I clinical trials recently. These three drugs use lipid hydrophobic assembly, supramolecular DNA assembly, and biomolecular recognition assembly, respectively, to construct nanostructures or to combine nanostructures with cells to form larger functionalized structures, suggesting the potential of utilizing supramolecular interactions for cancer immunotherapy. However, compared with traditional nanomaterials, certain differences should be considered in utilizing supramolecular interactions for nanostructure construction as well as clinical translation: (1) as opposed to nanostructures based on amphiphilic copolymers typically prepared by nanoprecipitation or emulsion evaporation method, supramolecular self-assembly is mainly performed in water without the use of organic solvent or surfactants; (2) functional modules for supramolecular assembly are mostly made from simple materials with clear structures, which possess more potential for clinical translation; (3) since supramolecular structures utilize complexity in assembly instead of complexity in molecular structure, the feasibility and controllability of a scaling up of the hierarchical self-assembly system should be a major point for consideration.

AUTHOR CONTRIBUTIONS

ZH and WS wrote the manuscript. WS and XC finalized the manuscript.

FUNDING

This work was supported by the National Natural Science Foundation of China (51673185, 51973215, 51833010, and 51520105004), as well as the support from the Youth Innovation Promotion Association of Chinese Academy of Sciences.

REFERENCES

Antoniuk, I., and Amiel, C. (2016). Cyclodextrin- mediated hierarchical self-assembly and its potential in drug delivery applications. *J. Pharmaceut. Sci.* 105, 2570–2588. doi: 10.1016/j.xphs.2016.05.010

Bachmann, M. F., and Jennings, G. T. (2010). Vaccine delivery: a matter of size, geometry, kinetics and molecular patterns. *Nat. Rev. Immunol.* 10, 787–796. doi: 10.1038/nri2868

Cai, H., Sun, Z.-Y., Chen, M.-S., Zhao, Y.-F., Kunz, H., and Li, Y.-M. (2014). Synthetic multivalent glycopeptide-lipopeptide antitumor vaccines: impact of the cluster effect on the killing of tumor cells. *Angew. Chem. Int. Edn.* 53, 1699–1703. doi: 10.1002/anie.201308875

Cai, Y., Ran, W., Zhai, Y., Wang, J., Zheng, C., Li, Y., et al. (2020). Recent progress in supramolecular peptide assemblies as virus mimics for cancer immunotherapy. *Biomater. Sci.* 8, 1045–1057. doi: 10.1039/C9BM01380F

Chen, D. S., and Mellman, I. (2013). Oncology meets immunology: the cancer-immunity cycle. *Immunity* 39, 1–10. doi: 10.1016/j.immuni.2013.07.012

Chen, Y., Song, W., Shen, L., Qiu, N., Hu, M., Liu, Y., et al. (2019). Vasodilator hydralazine promotes nanoparticle penetration in advanced desmoplastic tumors. *ACS Nano* 13, 1751–1763. doi: 10.1021/acsnano.8b07830

Cheng, K. M., Ding, Y. P., Zhao, Y., Ye, S. F., Zhao, X., Zhang, Y. L., et al. (2018). Sequentially responsive therapeutic peptide assembling nanoparticles for dual-targeted cancer immunotherapy. *Nano Lett.* 18, 3250–3258. doi: 10.1021/acs.nanolett.8b01071

Chhabra, R., Sharma, J., Liu, Y., Rinker, S., and Yan, H. (2010). DNA self-assembly for nanomedicine. *Adv. Drug Deliv. Rev.* 62, 617–625. doi: 10.1016/j.addr.2010.03.005

Chi, Q. J., Yang, Z. C., Xu, K., Wang, C. L., and Liang, H. P. (2020). DNA nanostructure as an efficient drug delivery platform for immunotherapy. *Front. Pharmacol.* 10:1585. doi: 10.3389/fphar.2019.01585

Chou, L. Y. T., Zagorovsky, K., and Chan, W. C. W. (2014). DNA assembly of nanoparticle superstructures for controlled biological delivery and elimination. *Nat. Nanotechnol.* 9, 148–155. doi: 10.1038/nnano.2013.309

Dacoba, T. G., Olivera, A., Torres, D., Crecente-Campo, J., and Alonso, M. J. (2017). Modulating the immune system through nanotechnology. *Semin. Immunol.* 34, 78–102. doi: 10.1016/j.smim.2017.09.007

Fan, Y., and Moon, J. J. (2015). Nanoparticle drug delivery systems designed to improve cancer vaccines and immunotherapy. *Vaccines* 3, 662–685. doi: 10.3390/vaccines3030662

Fritz, J., Baller, M. K., Lang, H. P., Rothuizen, H., Vettiger, P., Meyer, E., et al. (2000). Translating biomolecular recognition into nanomechanics. *Science* 288, 316–318. doi: 10.1126/science.288.5464.316

Galluzzi, L., Buqué, A., Kepp, O., Zitvogel, L., and Kroemer, G. (2017). Immunogenic cell death in cancer and infectious disease. *Nat. Rev. Immunol.* 17, 97–111. doi: 10.1038/nri.2016.107

Goldberg, M. S. (2015). Immunoengineering: how nanotechnology can enhance cancer immunotherapy. *Cell* 161, 201–204. doi: 10.1016/j.cell.2015.03.037

Gong, C. C., Sun, S. W., Zhang, Y. J., Sun, L., Su, Z. Q., Wu, A. G., et al. (2019). Hierarchical nanomaterials via biomolecular self-assembly and bioinspiration for energy and environmental applications. *Nanoscale* 11, 4147–4182. doi: 10.1039/C9NR00218A

Hamamoto, Y., Shin, N., Hoshino, T., and Kanai, T. (2018). Management of challenging immune-related gastrointestinal adverse events associated with immune checkpoint inhibitors. *Fut. Oncol.* 14, 3187–3198. doi: 10.2217/fon-2018-0509

Han, X. X., Cheng, K. M., Xu, Y., Wang, Y. Z., Mm, H., Zhang, Y. L., et al. (2020). Modularly designed peptide nanoprodrug augments antitumor immunity of PD-L1 checkpoint blockade by targeting indoleamine 2,3-dioxygenase. *J. Am. Chem. Soc.* 142, 2490–2496. doi: 10.1021/jacs.9b12232

Hoos, A. (2016). Development of immuno-oncology drugs - from CTLA4 to PD1 to the next generations. *Nat. Rev. Drug Discov.* 15, 235–247. doi: 10.1038/nrd.2015.35

Hu, Q. D., Tang, G. P., and Chu, P. K. (2014). Cyclodextrin-based host-guest supramolecular nanoparticles for delivery: from design to applications. *Acc. Chem. Res.* 47, 2017–2025. doi: 10.1021/ar500055s

Hu, X., Hou, B., Xu, Z., Saeed, M., Sun, F., Gao, Z., et al. (2020). Supramolecular prodrug nanovectors for active tumor targeting and combination immunotherapy of colorectal cancer. *Adv. Sci.* 7, 1903332. doi: 10.1002/advs.201903332

Huang, F., and Anslyn, E. V. (2015). Introduction: supramolecular chemistry. *Chem. Rev.* 115, 6999–7000. doi: 10.1021/acs.chemrev.5b00352

Huang, X., Williams, J. Z., Chang, R., Li, Z., Gai, E., Patterson, D. M., et al. (2019). DNA-scaffolded biomaterials enable modular and tunable control of cell-based cancer immunotherapies. *BioRxiv [Preprint].* 587105. doi: 10.1101/587105

Hudalla, G. A., Modica, J. A., Tian, Y. F., Rudra, J. S., Chong, A. S., Sun, T., et al. (2013). A self-adjuvanting supramolecular vaccine carrying a folded protein antigen. *Adv. Healthc. Mater.* 2, 1114–1119. doi: 10.1002/adhm.201200435

Ingale, S., Wolfert, M. A., Gaekwad, J., Buskas, T., and Boons, G.-J. (2007). Robust immune responses elicited by a fully synthetic three-component vaccine. *Nat. Chem. Biol.* 3, 663–667. doi: 10.1038/nchembio.2007.25

Irvine, D. J., Hanson, M. C., Rakhra, K., and Tokatlian, T. (2015). Synthetic nanoparticles for vaccines and immunotherapy. *Chem. Rev.* 115, 11109–11146. doi: 10.1021/acs.chemrev.5b00109

Ji, T. J., Lang, J. Y., Ning, B., Qi, F. F., Wang, H., Zhang, Y. L., et al. (2019). Enhanced natural killer cell immunotherapy by rationally assembling Fc fragments of antibodies onto tumor membranes. *Adv. Mater.* 31:1804395. doi: 10.1002/adma.201804395

Jiang, W., Von Roemeling, C. A., Chen, Y. X., Qie, Y. Q., Liu, X. J., Chen, J. Z., et al. (2017). Designing nanomedicine for immuno-oncology. *Nat. Biomed. Eng.* 1:0029. doi: 10.1038/s41551-017-0029

June, C. H., and Sadelain, M. (2018). Chimeric antigen receptor therapy. *N. Engl. J. Med.* 379, 64–73. doi: 10.1056/NEJMra1706169

Kahn, K., and Plaxco, K. W. (2010). "Principles of Biomolecular Recognition," in *Recognition Receptors in Biosensors*, ed. M. Zourob (New York, NY: Springer New York), 3–45. doi: 10.1007/978-1-4419-0919-0_1

Kedmi, R., Veiga, N., Ramishetti, S., Goldsmith, M., Rosenblum, D., Dammes, N., et al. (2018). A modular platform for targeted RNAi therapeutics. *Nat. Nanotechnol.* 13, 214–219. doi: 10.1038/s41565-017-0043-5

Koshy, S. T., Cheung, A. S., Gu, L., Graveline, A. R., and Mooney, D. J. (2017). Liposomal delivery enhances immune activation by STING agonists for cancer immunotherapy. *Adv. Biosyst.* 1:1600013. doi: 10.1002/adbi.201600013

Kosmides, A. K., Sidhom, J. W., Fraser, A., Bessell, C. A., and Schneck, J. P. (2017). Dual targeting nanoparticle stimulates the immune system to inhibit tumor growth. *ACS Nano* 11, 5417–5429. doi: 10.1021/acsnano.6b08152

Kroemer, G., Galluzzi, L., Kepp, O., and Zitvogel, L. (2013). Immunogenic cell death in cancer therapy. *Annu. Rev. Immunol.* 31, 51–72. doi: 10.1146/annurev-immunol-032712-100008

Kuai, R., Ochyl, L. J., Bahjat, K. S., Schwendeman, A., and Moon, J. J. (2017). Designer vaccine nanodiscs for personalized cancer immunotherapy. *Nat. Mater.* 16, 489–496. doi: 10.1038/nmat4822

Kuai, R., Yuan, W. M., Son, S., Nam, J., Xu, Y., Fan, Y. C., et al. (2018). Elimination of established tumors with nanodisc-based combination chemoimmunotherapy. *Sci. Adv.* 4:aao1736. doi: 10.1126/sciadv.aao1736

Kulkarni, A., Chandrasekar, V., Natarajan, S. K., Ramesh, A., Pandey, P., Nirgud, J., et al. (2018). A designer self-assembled supramolecule amplifies macrophage immune responses against aggressive cancer. *Nat. Biomed. Eng.* 2, 589–599. doi: 10.1038/s41551-018-0254-6

Kwong, B., Gai, S. A., Elkhader, J., Wittrup, K. D., and Irvine, D. J. (2013). Localized immunotherapy via liposome-anchored Anti-CD137 + IL-2 prevents lethal toxicity and elicits local and systemic antitumor immunity. *Cancer Res.* 73, 1547–1558. doi: 10.1158/0008-5472.CAN-12-3343

Lehn, J.-M. (1988). Supramolecular chemistry—scope and perspectives molecules, supermolecules, and molecular devices (Nobel Lecture). *Angew. Chem. Int. Edn. English* 27, 89–112. doi: 10.1002/anie.198800891

Li, L. L., Qiao, Z. Y., Wang, L., and Wang, H. (2019). Programmable construction of peptide-based materials in living subjects: from modular design and morphological control to theranostics. *Adv. Mater.* 31:e1901049. doi: 10.1002/adma.201970321

Li, S., Rizzo, M. A., Bhattacharya, S., and Huang, L. (1998). Characterization of cationic lipid-protamine-DNA (LPD) complexes for intravenous gene delivery. *Gene Therapy* 5, 930–937. doi: 10.1038/sj.gt.3300683

Liu, X., Xu, Y., Yu, T., Clifford, C., Liu, Y., Yan, H., et al. (2012). A DNA nanostructure platform for directed assembly of synthetic vaccines. *Nano Lett.* 12, 4254–4259. doi: 10.1021/nl301877k

Ma, S., Song, W., Xu, Y., Si, X., Lv, S., Zhang, Y., et al. (2020a). Rationally designed polymer conjugate for tumor-specific amplification of oxidative stress and boosting antitumor immunity. *Nano Lett.* 20:2514–2521. doi: 10.1021/acs.nanolett.9b05265

Ma, S., Song, W., Xu, Y., Si, X., Zhang, D., Lv, S., et al. (2020b). Neutralizing tumor-promoting inflammation with polypeptide-dexamethasone conjugate for microenvironment modulation and colorectal cancer therapy. *Biomaterials* 232:119676. doi: 10.1016/j.biomaterials.2019.119676

Ma, X., and Zhao, Y. (2015). Biomedical applications of supramolecular systems based on host-guest interactions. *Chem. Rev.* 115, 7794–7839. doi: 10.1021/cr500392w

Martinez, M., and Moon, E. K. (2019). CAR T cells for solid tumors: new strategies for finding, infiltrating, and surviving in the tumor microenvironment. *Front. Immunol.* 10:128. doi: 10.3389/fimmu.2019.00128

Mellman, I., Coukos, G., and Dranoff, G. (2011). Cancer immunotherapy comes of age. *Nature* 480, 480–489. doi: 10.1038/nature10673

Miao, L., Li, J., Liu, Q., Feng, R., Das, M., Lin, C. M., et al. (2017). Transient and local expression of chemokine and immune checkpoint traps to treat pancreatic cancer. *ACS Nano* 11, 8690–8706. doi: 10.1021/acsnano.7b01786

Milling, L., Zhang, Y., and Irvine, D. J. (2017). Delivering safer immunotherapies for cancer. *Adv. Drug Deliv. Rev.* 114, 79–101. doi: 10.1016/j.addr.2017.05.011

Park, J., Wrzesinski, S. H., Stern, E., Look, M., Criscione, J., Ragheb, R., et al. (2012). Combination delivery of TGF-beta inhibitor and IL-2 by nanoscale liposomal polymeric gels enhances tumour immunotherapy. *Nat. Mater.* 11, 895–905. doi: 10.1038/nmat3355

Perica, K., Tu, A., Richter, A., Bieler, J. G., Edidin, M., and Schneck, J. P. (2014). Magnetic field-induced T cell receptor clustering by nanoparticles enhances T cell activation and stimulates antitumor activity. *ACS Nano* 8, 2252–2260. doi: 10.1021/nn405520d

Postow, M. A., Sidlow, R., and Hellmann, M. D. (2018). Immune-related adverse events associated with immune checkpoint blockade. *N. Engl. J. Med.* 378, 158–168. doi: 10.1056/NEJMra1703481

Radovic-Moreno, A. F., Chernyak, N., Mader, C. C., Nallagatla, S., Kang, R. S., Hao, L., et al. (2015). Immunomodulatory spherical nucleic acids. *Proc. Natl. Acad. Sci. U.S.A.* 112, 3892–3897. doi: 10.1073/pnas.1502850112

Rodell, C. B., Arlauckas, S. P., Cuccarese, M. F., Garris, C. S., Li, R., Ahmed, M. S., et al. (2018). TLR7/8-agonist-loaded nanoparticles promote the polarization of tumour-associated macrophages to enhance cancer immunotherapy. *Nat. Biomed. Eng.* 2, 578–588. doi: 10.1038/s41551-018-0236-8

Rosenberg, S. A., and Restifo, N. P. (2015). Adoptive cell transfer as personalized immunotherapy for human cancer. *Science* 348, 62–68. doi: 10.1126/science.aaa4967

Rudra, J. S., Sun, T., Bird, K. C., Daniels, M. D., Gasiorowski, J. Z., Chong, A. S., et al. (2012). Modulating adaptive immune responses to peptide self-assemblies. *ACS Nano* 6, 1557–1564. doi: 10.1021/nn204530r

Sanmamed, M. F., and Chen, L. P. (2018). A paradigm shift in cancer immunotherapy: from enhancement to normalization. *Cell* 175, 313–326. doi: 10.1016/j.cell.2018.09.035

Sau, S., Alsaab, H. O., Bhise, K., Alzhrani, R., Nabil, G., and Iyer, A. K. (2018). Multifunctional nanoparticles for cancer immunotherapy: a groundbreaking approach for reprogramming malfunctioned tumor environment. *J. Control. Release* 274, 24–34. doi: 10.1016/j.jconrel.2018.01.028

Schütz, C., Perica, K., Varela, J., Haupt, C., Oelke, M., and Schneck, J. (2014). Antigen-specific T cell redirectors (ATR) for antigen-specific redirection of T cells to tumors. *J. Immunother. Cancer* 2:P36. doi: 10.1186/2051-1426-2-S3-P36

Sercombe, L., Veerati, T., Moheimani, F., Wu, S. Y., Sood, A. K., and Hua, S. (2015). Advances and challenges of liposome assisted drug delivery. *Front. Pharmacol.* 6:286. doi: 10.3389/fphar.2015.00286

Si, X., Ma, S., Xu, Y., Zhang, D., Shen, N., Yu, H., et al. (2020). Hypoxia-sensitive supramolecular nanogels for the cytosolic delivery of ribonuclease A as a breast cancer therapeutic. *J. Control. Release* 320, 83–95. doi: 10.1016/j.jconrel.2020.01.021

Song, W., Das, M., and Chen, X. (2020). Nanotherapeutics for immuno-oncology: a crossroad for new paradigms. *Trends Cancer* 6, 288–298. doi: 10.1016/j.trecan.2020.01.011

Song, W., Musetti, S. N., and Huang, L. (2017). Nanomaterials for cancer immunotherapy. *Biomaterials* 148, 16–30. doi: 10.1016/j.biomaterials.2017.09.017

Song, W., Shen, L., Wang, Y., Liu, Q., Goodwin, T. J., Li, J., et al. (2018a). Synergistic and low adverse effect cancer immunotherapy by immunogenic chemotherapy and locally expressed PD-L1 trap. *Nat. Commun.* 9:2237. doi: 10.1038/s41467-018-04605-x

Song, W. T., Tiruthani, K., Wang, Y., Shen, L. M., Hu, M. Y., Dorosheva, O., et al. (2018b). Trapping of lipopolysaccharide to promote immunotherapy against colorectal cancer and attenuate liver metastasis. *Adv. Mater.* 30:201805007. doi: 10.1002/adma.201805007

Tang, L., Zheng, Y. R., Melo, M. B., Mabardi, L., Castano, A. P., Xie, Y. Q., et al. (2018). Enhancing T cell therapy through TCR-signaling-responsive nanoparticle drug delivery. *Nat. Biotechnol.* 36, 707–716. doi: 10.1038/nbt.4181

Van Der Burg, S. H., Arens, R., Ossendorp, F., Van Hall, T., and Melief, A. J. M. (2016). Vaccines for established cancer: overcoming the challenges posed by immune evasion. *Nat. Rev. Cancer* 16, 219–233. doi: 10.1038/nrc.2016.16

Wang, C., Sun, W., Ye, Y., Bomba, H. N., and Gu, Z. (2017a). Bioengineering of artificial antigen presenting cells and lymphoid organs. *Theranostics* 7, 3504–3516. doi: 10.7150/thno.19017

Wang, C., Sun, W. J., Wright, G., Wang, A. Z., and Gu, Z. (2016). Inflammation-triggered cancer immunotherapy by programmed delivery of CpG and anti-PD1 antibody. *Adv. Mater.* 28, 8912–8920. doi: 10.1002/adma.201506312

Wang, C., Ye, Y. Q., Hu, Q. Y., Bellotti, A., and Gu, Z. (2017b). Tailoring biomaterials for cancer immunotherapy: emerging trends and future outlook. *Adv. Mater.* 29:1606036. doi: 10.1002/adma.201606036

Wang, Y., Song, W. T., Hu, M. Y., An, S., Xu, L. G., Li, J. J., et al. (2018). Nanoparticle-mediated HMGA1 silencing promotes lymphocyte infiltration and boosts checkpoint blockade immunotherapy for cancer. *Adv. Funct. Mater* 28:201802847. doi: 10.1002/adfm.201802847

Wang, Y. H., Xu, Z. H., Guo, S. T., Zhang, L., Sharma, A., Robertson, G. P., et al. (2013). Intravenous delivery of siRNA targeting CD47 effectively inhibits melanoma tumor growth and lung metastasis. *Mol Therapy* 21, 1919–1929. doi: 10.1038/mt.2013.135

Webber, M. J., Appel, E. A., Meijer, E. W., and Langer, R. (2016). Supramolecular biomaterials. *Nat. Mater* 15, 13–26. doi: 10.1038/nmat4474

Wen, Y., and Collier, J. H. (2015). Supramolecular peptide vaccines: tuning adaptive immunity. *Curr. Opin. Immunol.* 35, 73–79. doi: 10.1016/j.coi.2015.06.007

Wu, Y., Norberg, P. K., Reap, E. A., Congdon, K. L., Fries, C. N., Kelly, S. H., et al. (2017). A supramolecular vaccine platform based on α-helical peptide nanofibers. *ACS Biomater. Sci. Eng.* 3, 3128–3132. doi: 10.1021/acsbiomaterials.7b00561

Xu, J., Ren, X., Guo, T., Sun, X., Chen, X., Patterson, L. H., et al. (2019). NLG919/cyclodextrin complexation and anti-cancer therapeutic benefit as a potential immunotherapy in combination with paclitaxel. *Eur. J. Pharm. Sci.* 138:105034. doi: 10.1016/j.ejps.2019.105034

Yang, L., Tan, X., Wang, Z., and Zhang, X. (2015). Supramolecular polymers: historical development, preparation, characterization, and functions. *Chem. Rev.* 115, 7196–7239. doi: 10.1021/cr500633b

Yarchoan, M., Hopkins, A., and Jaffee, E. M. (2017). Tumor mutational burden and response rate to PD-1 inhibition. *N. Engl. J. Med.* 377, 2500–2501. doi: 10.1056/NEJMc1713444

Yuan, C., Ji, W., Xing, R., Li, J., Gazit, E., and Yan, X. (2019). Hierarchically oriented organization in supramolecular peptide crystals. *Nat. Rev. Chem.* 3, 567–588. doi: 10.1038/s41570-019-0129-8

Yuan, H. F., Jiang, W., Von Roemeling, C. A., Qie, Y. Q., Liu, X. J., Chen, Y. X., et al. (2017). Multivalent bi-specific nanobioconjugate engager for targeted cancer immunotherapy. *Nat. Nanotechnol.* 12, 763–769. doi: 10.1038/nnano.2017.69

Zhang, L., Jing, D., Jiang, N., Rojalin, T., Baehr, C. M., Zhang, D. L., et al. (2020). Transformable peptide nanoparticles arrest HER2 signalling and cause cancer cell death *in vivo*. *Nat. Nanotechnol.* 15, 145–153. doi: 10.1038/s41565-019-0626-4

Zheng, C.-X., Zhao, Y., and Liu, Y. (2018). Recent advances in self-assembled nano-therapeutics. *Chinese J. Polymer Sci.* 36, 322–346. doi: 10.1007/s10118-018-2078-y

Zou, W. P., Wolchok, J. D., and Chen, L. P. (2016). PD-L1 (B7-H1) and PD-1 pathway blockade for cancer therapy: mechanisms, response biomarkers, and combinations. *Sci. Transl. Med.* 8:328rv324. doi: 10.1126/scitranslmed.aad7118

Conflict of Interest: The authors declare that the research was conducted in the absence of any commercial or financial relationships that could be construed as a potential conflict of interest.

frontiers in Chemistry

ORIGINAL RESEARCH
published: 28 May 2020
doi: 10.3389/fchem.2020.00407

Rapamycin-Loaded mPEG-PLGA Nanoparticles Ameliorate Hepatic Steatosis and Liver Injury in Non-alcoholic Fatty Liver Disease

Ruifang Zhao[1,2†], *Meilin Zhu*[3,4†], *Shuang Zhou*[3], *Weiyue Feng*[3] *and Hanqing Chen*[1,3*]

[1] *Department of Gastroenterology, Guangzhou Digestive Disease Center, Guangzhou First People's Hospital, School of Medicine, South China University of Technology, Guangzhou, China,* [2] *National Center for Nanoscience and Technology, Beijing, China,* [3] *CAS Key Laboratory for Biomedical Effects of Nanomaterials and Nanosafety, Institute of High Energy Physics, Chinese Academy of Sciences (CAS), Beijing, China,* [4] *Institute of Physical Science and Information Technology, Anhui University, Hefei, China*

Non-alcoholic fatty liver disease (NAFLD) is characterized by excessive lipid accumulation and liver injury, and is the leading cause of chronic liver disease worldwide. There is an urgent need to develop novel pathophysiology-oriented therapy in human. Rapamycin (RAPA) has been recognized as a promising drug for alleviating hepatic steatosis on NAFLD, but the poorly water-soluble properties and side effects of RAPA limit their clinical use. In this study, we aimed to investigate the *in vitro* and *in vivo* therapeutic efficacy of biodegradable mPEG-PLGA polymers loaded with RAPA (NP-RAPA) on NAFLD. NP-RAPA were prepared by a green process using an emulsion/solvent evaporation method, the therapeutic efficacy on NAFLD were investigated on HepG2 cells incubated with oleic acid (OA) and in the livers of mice with NAFLD induced by high-fat diet (HFD). Compared with free RAPA, NP-RAPA significantly reduced lipid accumulation in HepG2 cells, and obviously ameliorated hepatic steatosis and liver injury in mice though enhancing the therapeutic efficacy of RAPA through reducing SREBP-1c-dependent *de novo* lipogenesis (DNL) and promoting PPARα-mediated fatty acid oxidation. This study suggests that mPEG-PLGA can be used as the potential therapeutic strategy and novel drug delivery for improving the efficacy of rapamycin for treatment of NAFLD.

Keywords: non-alcoholic fatty liver disease, mPEG-PLGA, rapamycin, hepatic steatosis, SREBP-1c, *de novo* lipogenesis, fatty acid oxidation

OPEN ACCESS

Edited by:
Huaimin Wang,
Westlake University, China

Reviewed by:
Xingyi Li,
Affiliated Eye Hospital of Wenzhou Medical College, China
Guocan Yu,
National Institutes of Health (NIH), United States

***Correspondence:**
Hanqing Chen
chenhq@ihep.ac.cn

[†] *These authors have contributed equally to this work*

Specialty section:
This article was submitted to Supramolecular Chemistry, a section of the journal Frontiers in Chemistry

Received: *09 March 2020*
Accepted: *17 April 2020*
Published: *28 May 2020*

Citation:
Zhao R, Zhu M, Zhou S, Feng W and Chen H (2020) Rapamycin-Loaded mPEG-PLGA Nanoparticles Ameliorate Hepatic Steatosis and Liver Injury in Non-alcoholic Fatty Liver Disease. Front. Chem. 8:407. doi: 10.3389/fchem.2020.00407

INTRODUCTION

Non-alcoholic fatty liver disease (NAFLD) is a prevalent hepatic manifestation of the metabolic syndrome, and encompasses a wide spectrum of chronic liver diseases, ranging from non-alcoholic fatty liver (NAFL) to non-alcoholic steatosis (NASH), liver fibrosis, cirrhosis, and ultimately hepatocellular carcinoma (HCC) (Rotman and Sanyal, 2017; Liu et al., 2020). In retrospective study, NAFLD afflicts ∼30% of the adult population worldwide (Younossi et al., 2019), and its prevalence has increased about 2-fold over the past two decades (Fan, 2013). In clinical practice, NAFLD is characterized by excessive triglyceride accumulation and hepatocyte injury in the liver, which is not caused by alcohol uptake and other factors (Liu et al., 2018; Chen, 2020). However, there are no effective strategies available for NAFLD treatment. There is an urgent need to develop novel pathophysiology-oriented therapy in human NAFLD.

Recent works have revealed that sterol regulatory element-binding protein (SREBP)-1c, a critical transcription factor in regulation of *de novo* lipogenesis (DNL) and hepatic lipid accumulation, has been implicated in alcoholic and non-alcoholic steatosis (Yeh and Brunt, 2014; Chen et al., 2018). DNL, accounting for 26% of hepatic triglyceride in human subjects (Smith et al., 2020), is increased in NAFLD patients compared with healthy (Shimano and Sato, 2017), suggesting the potential therapeutic strategy through inhibition of DNL for the treatment of NAFLD. Mechanistic target of rapamycin complex 1 (mTORC1), as a central hub of nutrient sensor contributes to cellular metabolism and growth in response to physiological fluctuations of nutrients (Kim and Guan, 2019; Chen, 2020). Several studies reveal the mTORC1 signaling as an important checkpoint for SREBP-1c-mediated DNL and NAFLD pathogenesis (Lee et al., 2017; Kim and Guan, 2019). The use of specifically pharmacological inhibitor of mTOR, such as rapamycin (RAPA) as approved by the United States Food and Drug Administration (FDA) (Flaxman et al., 2019), has become the standard of care for improving fatty liver condition in alcoholic and non-alcoholic fatty liver diseases via reducing lipid synthesis or promoting lipid oxidation (Lin et al., 2013). RAPA is firstly isolated in 1975 from *Streptomyces hygroscopicus* (Othman et al., 2016), and its clinical applications for amelioration of hepatic steatosis is due to formation of the ternary complex between 12-kDa FK506-binding protein (FKBP12) and the FKBP12-rapamycin binding (FRB) (FKBP12-rapamycin-FRB) (Flaxman et al., 2019), which allosterically inhibits the kinase activity of mTORC1. RAPA administration exhibited significantly improved insulin resistance and hepatic steatosis in type 2 diabetes (T2DM) through inhibition of mTOR and alleviation of disorders of lipid metabolism (Zhou and Ye, 2018). However, the therapeutic efficacy for NAFLD is impeded by its poor solubility and low bioavailability in physiological conditions (Othman et al., 2016), and serious adverse effects have occurred due to the side effect of RAPA, which limits the clinical use (Bee et al., 2018). Therefore, more effective and safer therapy and drug delivery for RAPA in treatment of NAFLD is needed through using lower doses of RAPA to obtain the equal benefit with fewer side effects.

Rapid progress in nanotechnology in biomedicine has led to the development of the novel drug carriers for poorly water-soluble drugs to overcome their poor bioavailability and reduce their side effects (Teng et al., 2019; van der Meel et al., 2019). Polymeric nanoparticles (NPs) have been extensively reported for their prominent superiorities in potential drug delivery vehicles due to their controlled/sustained release properties, biocompatibility, and applicability to many water-insoluble drugs. Poly (D, L-lactide-co-glycolide) (PLGA) is a biodegradable polymer and is approved by FDA for biomedical applications in humans (Qureshi et al., 2016). Monomethoxy-poly(ethylene glycol) (mPEG) is the most widely used "stealth" polymer in modifying drug delivery and is classified as Generally Regarded as Safe (GRAS) by FDA (Suk et al., 2016). Now, there are more than nine FDA-approved PEGylated therapeutics in disease treatment due to their extended-circulation properties and "accelerated blood clearance (ABC)" phenomenon (Ishida et al., 2008; Weissig et al., 2014). Recently, several mPEG-PLGA copolymers, with mPEG as the hydrophilic shell and PLGA as the fabrication of bone substitute constructs, have been designed to deliver hydrophobic drugs for disease treatment (Liu et al., 2019), indicating the promising for mPEG-PLGA encapsulated with RAPA in treatment with NAFLD.

Herein, we designed and developed an efficient encapsulation of RAPA into mPEG-PLGA polymer nanoparticles (NP-RAPA) with narrow size distribution and well-dispersion stability. The NP-RAPA exerts significantly decreased triglyceride accumulation on NAFLD in HepG2 cells and in mice, compared with free RAPA. Moreover, NP-RAPA significantly improved lipid homeostasis through reducing SREBP-1c-mediated *de novo* lipogenesis and promoting PPARα-dependent fatty acid oxidation. These findings altogether demonstrated that mPEG-PLGA could be used as the new drug delivery platforms for potential therapeutic strategy in improving the efficacy of rapamycin for NAFLD treatment.

MATERIALS AND METHODS

Chemicals and Reagents

Monomethoxy-poly(ethylene glycol) (mPEG, 5,000 Da) and poly(lactic-co-glycolic acid) (PLGA, molar ratio of D, L-lactic to glycolic acid, 75:25) were purchased from Jinan Daigang Biotechnology Co. Ltd. (Jinan, China). Rapamycin (RAPA, purity ≥99%), N,N-Diethylnicotinamide (DENA), polyvinyl alcohol (PVA), and Rhodamine B (RHO) were obtained from Sigma-Aldrich (St. Louis, MO, USA). Dulbecco's modified Eagle medium (DMEM), fetal bovine serum (FBS), penicillin, and streptomycin were obtained from by Gibco (Grand Island, NY, USA). The bicinchoninic acid (BCA) protein assay kit was obtained from Beyotime Institute of Biotechnology (Beijing, China). Liver triglyceride and cholesterol contents were determined by analytical kit from Jiancheng Bioengineering (Nanjing, China). The other chemicals and reagents with used in this study were obtained from the Sinopharm Chemical Reagent Co., Ltd. (Beijing, China) and were of analytical grade.

Preparation and Characterization of Rapamycin-Loaded mPEG-PLGA Nanoparticles

mPEG-PLGA polymers (mPEG-PLGA) and rapamycin-loaded mPEG-PLGA nanoparticles (NP-RAPA) were prepared using an emulsion/solvent evaporation method described previously (Wang et al., 2011). In brief, 20 mg of mPEG-PLGA and 1 mg of rapamycin (RAPA) were dissolved in 1 mL of methylene chloride, and then the solution was stirred for 10 min at room temperature. After being mixed with 10 mL of 1% PVA (1% w/v), the mixture was emulsified by sonication and the solvent was evaporated by vacuum. After evaporation, the NP-RAPA was collected by centrifugation at 10,000 rpm/min for 10 min at room temperature and re-suspended in Milli-Q water for experiment.

Characterization of Rapamycin-Loaded mPEG-PLGA Nanoparticles

The morphology and size of mPEG-PLGA polymers (mPEG-PLGA) and rapamycin-loaded mPEG-PLGA nanoparticles (NP-RAPA) were characterized by TEM (JEM-200CX, Jeol Ltd., Tokyo, Japan). The hydrodynamic diameter, zeta potential, and polydisperse index (PDI) were measured via dynamic light scattering (DLS) using a Zetasizer Nano ZS (Malvern Instrument Ltd., Worcestershire, UK).

In vitro Drug Release

In vitro release performance of RAPA from NP-RAPA was determined using a dialysis method (Othman et al., 2016). Free rapamycin is almost insoluble in water (Chen et al., 2013). Lyophilized NP-RAPA (20–30 mg) were suspended in dissolution medium (v/v) containing 10% pure ethanol, 10% Tween-20, 25.9% N,N-Diethylnicotinamide (DENA, 3M), 10% phosphate-buffered saline (pH 7.4 and 5.5), and 44.1% Milli-Q water and transferred into the centrifuge tube (5 mL/tube) (Othman et al., 2016). To mimic the human bloodstream conditions, the tube was kept in a shaking bath at 37°C with 50 rpm. At the predetermined time intervals, the tubes were centrifuged at 15,000 rpm/min for 30 min at −4°C. The released rapamycin was quantified by high-performance liquid chromatographic (HPLC, Waters, Elstree, U.K.) method. The accumulative ratio of the released RAPA was calculated as a function of time.

Drug Loading and Encapsulation Efficiency

Rapamycin (RAPA) was dissolved in ethanol in concentrations ranging from 0.2 to 1 mg/mL, and RAPA solution (0.2 mL) was mixed with 2 mL of mPEG-PLGA solution (2 mg/mL). Under stirring at room temperature for 2 days, the resulting NP-RAPA were collected by centrifugation at 1,000 g for 30 min. The ethanol was removed by rotary evaporation and the free RAPA was quantified by HPLC method. The drug loading capacity and encapsulation efficiency of RAPA were calculated by following formulas: Loading Content = (weight of loaded RAPA)/(total weight of NP-RAPA) × 100%, and Encapsulation Efficiency = (weight of loaded RAPA)/(weight of initially added RAPA) × 100%.

In vitro Cell Model of NAFLD and Treatment

Human hepatocellular carcinoma HepG2 cells were purchased from Cell Culture Center, Institute of Basic Medical Sciences of Chinese Academy of Medical Sciences (Beijing, China) and grown in Dulbecco's modified Eagle medium (DMEM) supplemented with 10% fetal bovine serum (FBS), 100 U/mL penicillin, 100 μg/mL streptomycin, and 1% penicillin/streptomycin in a humidified atmosphere of 95% air/5% CO_2 at 37°C. To establish the *in vitro* cell model of NAFLD, HepG2 cells were incubated with 0.4 mM oleic acid (OA, dissolved in DMEM containing 0.67% bovine serum albumin, w/v) for 24 h induce steatosis. After 24 h, the OA was withdrawn, and the cells at a density of 10^6 cells/well were treated with mPEG-PLGA, free RAPA (0.5 μM, dissolved in 0.1% DMSO) and NP-RAPA (containing 0.5 μM RAPA) for 8 h, the cells were stained with Oil Red O to image and determine the lipid content.

NAFLD Mouse Model and Treatment

Seven- to eight-week-old C57BL/6J male mice (22–24 g) were obtained from Beijing Vital River Experimental Animal Technology Co. Ltd (Beijing, China) and acclimatized for 1 week before the experiment. The mice were maintained in a standard environment and were fed with sterilized chow and deionized water *ad libitum* (Chen et al., 2017, 2018). All the studies were performed according to the animal protocols in compliance with laboratory animal regulations of the Ministry of Science and Technology of China and Ethics Committee of National Center for Nanoscience and Technology of China (Sep. 06, 2019, PONY-2019-FL-24).

To establish the mouse model of NAFLD, mice were fed with normal chow diet (ND, TP23302, Tophic, Nongtong, China) or high-fat diet (HFD) containing 60% calories fat (TP23302, Tophic, Nongtong, China) for 13 weeks. Free rapamycin was dosed in 4% ethanol/5% PEG 400/5% Tween-80 in water for injection solution (Chen et al., 2013). After fed with ND or HFD for 4 weeks, the mice were intravenously injected with injection solution, mPEG-PLGA, free RAPA (5 mg/kg) and NP-RAPA (mPEG-PLGA polymers containing 5 mg/kg RAPA) once a week for 8 weeks. The body weight were weighted and recorded every week.

Histological Analysis

For histological analysis, the liver samples were collected and fixed with 10% formalin for 48 h at room temperature, and then embedded with paraffin for hematoxylin and eosin staining.

For Oil Red O study, the liver samples were embedded in OTC and cut into 7 mm thick cryosections. The cryosections were stained with Oil Red O (ORO) for steatosis levels and were counter-stained with hematoxylin for nuclei.

Biochemistry Analysis in Plasma and Liver

For serum biochemical assess, the plasma was collected by centrifugation at 3,000 rpm/min for 10 min at 37°C. The serum biochemical parameters, including alanine aminotransferase (ALT), aspartate aminotransferase (AST), and triglyceride (TG), were determined by automatic chemistry analyzer (Celltac, MEK-6358; Nihon Kohden Co., Tokyo, Japan). For evaluation of liver function, the liver lipid was extracted following our previous protocols (Chen et al., 2018), and the content of TG was measured by commercial kits from Jiancheng Bioengineering (Nanjing, China).

Quantitative Real-Time Polymerase Chain Reaction (qPCR) Assay

Total RNA from the frozen liver tissues (20–30 mg) was extracted by TRNzol reagent (Tiangen Biotech, Beijing, China). cDNA was reverse transcribed from the RNA (1 μg) according to the cDNA reverse transcription kit (Takara Biotechnology, Otsu, Japan) and the qPCR were performed using SYBR Green qPCR Mix kit (Life Technologies, MA, USA) on a Bio-Rad CFX Connect Real-Time PCR Detection system (Chen et al., 2018). The

relative mRNA expression was normalized to internal control GAPDH. The qPCR primers used for gene expression are listed in **Table 1**.

TABLE 1 | List of the sequences of qPCR primers used in this study.

Genes	Forward primers sequences (5′-3′)	Reverse primers sequences (5′-3′)
Srebp-1c	5′-GGAGCCATGGATTGCA CATT-3′	5′-GGCCCGGGAAGTC ACTGT-3′
Acc1	5′-TGACAGACTGATCGCAGAG AAAG-3′	5′-TGGAGAGCCCCACA CACA-3′
Fasn	5′-GCTGCGGAAACTTCAGG AAAT-3′	5′-AGAGACGTGTCACTCCTG GACTT-3′
Scd1	5′-TTCTTCTCTCACGTGG GTTG-3′	5′-CGGGCTTGTAGTACCT CCTC-3′
Dgat2	5′-TACTCCAAGCCCATC ACCAC-3′	5′-CAGTTCACCTCCAGCA CCTC-3′
Pparα	5′-GGGCAGAGCAAGTCAT CTTC-3′	5′-CCTCTGGAAGCACTGA GGAC-3′
Cpt-1α	5′-CCAGGCTACAGTGGGA CATT-3′	5′-GAACTTGCCCATGTCC TTGT-3′
Pgc-1α	5′-AAGAGCGCCGTGTGAT TTAC-3′	5′-ACGGTGCATTCCTCAA TTTC-3′
Gapdh	5′-TGCGACTTCAACAGCA ACTC-3′	5′-CTTGCTCAGTGTCCTT GCTG-3′

Statistical Analysis

All the tests were repeated at least three times and all the data were presented as means ± standard deviations (SD). Statistical analysis was performed using GraphPad prism 6 and statistical differences were assessed using Student's *t*-test or one-way of analysis (ANOVA). $p < 0.05$ was considered as statistical significance.

RESULTS AND DISCUSSIONS

Physicochemical Characterization of Rapamycin-Loaded mPEG-PLGA Nanoparticles

The designed structure and preparation of mPEG-PLGA polymers and rapamycin-loaded mPEG-PLGA nanoparticles (NP-RAPA) is presented in **Figure 1A**, which was prepared by a green process via a water/oil/water solvent evaporation technique (Wang et al., 2011). The baseline physicochemical characteristics of the NPs are showed and listed in **Figure 1** and **Table 2**. TEM images showed that the mPEG-PLGA and NP-RAPA yielded the monodisperse nanospheres with a smooth surface. The size distribution of the mPEG-PLGA and NP-RAPA well-dispersed in Milli-Q water had a narrow size uniformity through coulter counter analysis from TEM images, and the average size of NP-RAPA is increased from 130.4 ± 17.3 to 132.6

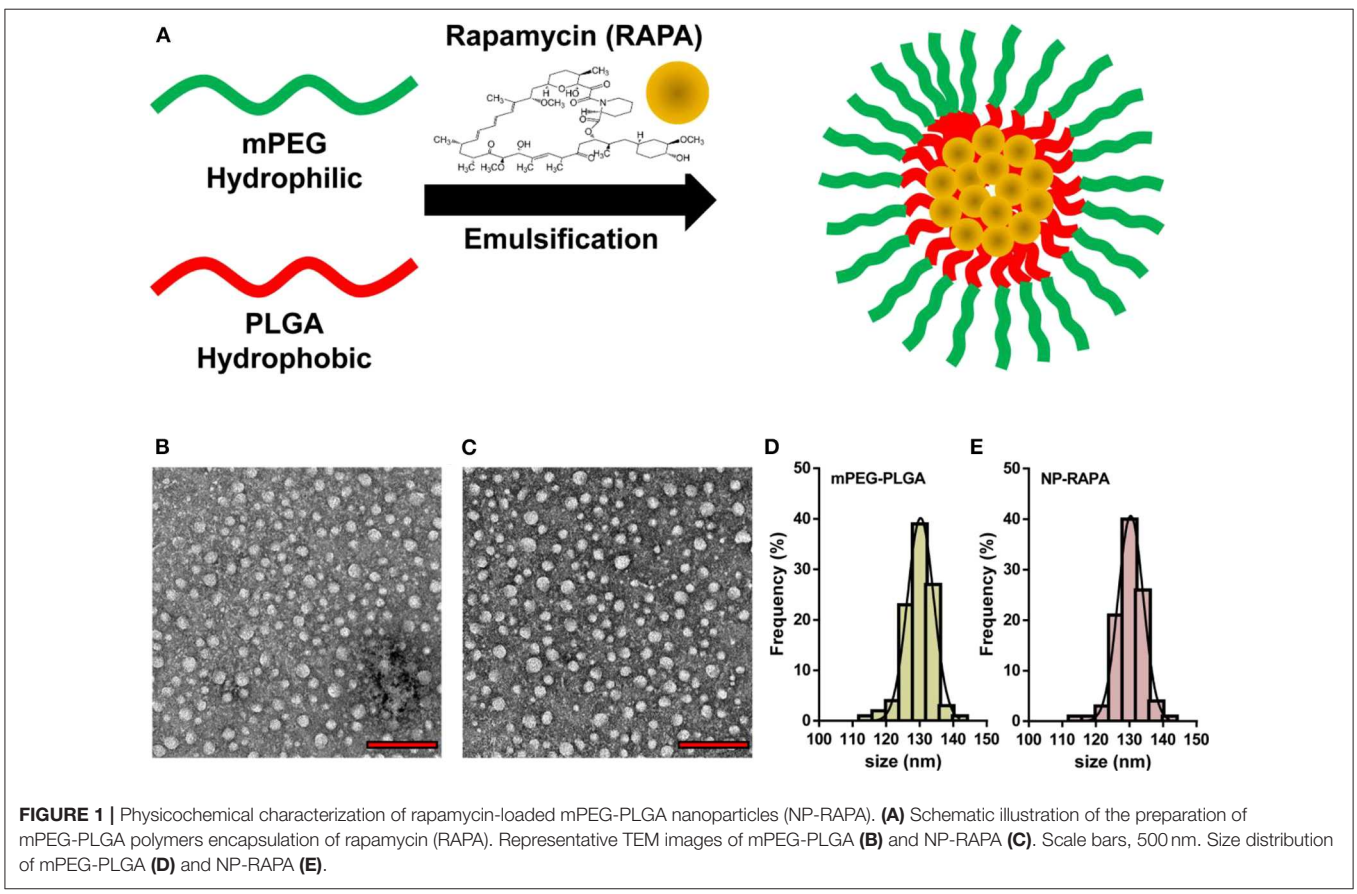

FIGURE 1 | Physicochemical characterization of rapamycin-loaded mPEG-PLGA nanoparticles (NP-RAPA). **(A)** Schematic illustration of the preparation of mPEG-PLGA polymers encapsulation of rapamycin (RAPA). Representative TEM images of mPEG-PLGA **(B)** and NP-RAPA **(C)**. Scale bars, 500 nm. Size distribution of mPEG-PLGA **(D)** and NP-RAPA **(E)**.

TABLE 2 | Statistical analysis of average size, hydrodynamic diameter, zeta potential, and polydispersity index (PDI) of mPEG-PLGA polymers and rapamycin-loaded mPEG-PLGA nanoparticles (NP-RAPA).

Properties / NPs	Size (TEM)	Hydrodynamic dimeter	Zeta potential	PDI
mPEG-PLGA	130.4 ± 17.3 nm	154.3 ± 14.9 nm	−33.9 ± 0.9 mV	0.166 ± 0.35
NP-RAPA	132.6 ± 13.5 nm	157.5 ± 19.5 nm	−33.7 ± 0.5 mV	0.173 ± 0.23

± 13.5 nm, indicating the successful loading and encapsulation of RAPA on mPEG-PLGA polymer (Othman et al., 2016). The hydrodynamic diameter, zeta potential, and polydisperse index (PDI) were further measured to analyze the stability of mPEG-PLGA and NP-RAPA solution. The hydrodynamic diameter of mPEG-PLGA and NP-RAPA was 154.3 ± 14.9 to 157.5 ± 19.5 nm, and the zeta potential was −33.9 ± 0.9 to −33.7 ± 0.5 mV, respectively. The PDI was comparable between mPEG-PLGA and NP-RAPA, indicating that rapamycin-loading do not affect the stability and dispersion of mPEG-PLGA polymers.

Drug Loading and Release Profile of Rapamycin From NP-RAPA

In vitro release profile can be used to determine whether dissolution of the targeted drug into carrier is enhanced by the novel drug delivery platform (Cao et al., 2018). The release curve of RAPA from NP-RAPA *in vitro* at pH 5.5 and 7.4 was shown in **Figure 2A** with zero time corresponding to the start of the incubation period. The NP-RAPA at pH 7.4 presented a burst release of more than 40% of RAPA in the initial 4 h. The faster release of RAPA was observed from NP-RAPA at pH 5.5 due to the simulated acidic environment of lysosome (Wang et al., 2011). After that, the release rate of RAPA from NP-RAPA was slower from 4 to 24 h (32.9–48.2% at pH 7.4, and 47.3–62.3% at pH 5.5). The release profile was approaching its plateau, and the final cumulative release of RAPA from the NP-RAPA was 56.4 and 66.3% at pH 7.4 and 5.5, respectively. For NP-RAPA, RAPA was efficiently loaded in mPEG-PLGA polymer with the highest drug loading content (LC) of 23.8% at the mPEG-PLGA/RAPA weight ratio of 20:1 (**Figure 2B**). The encapsulation efficiency (EE) of NP-RAPA was reduced when increasing the weight ratio of mPEG-PLGA/RAPA, and the highest EE of RAPA in mPEG-PLGA was 77.9% at the ratio of 100:1 (**Figure 2C**).

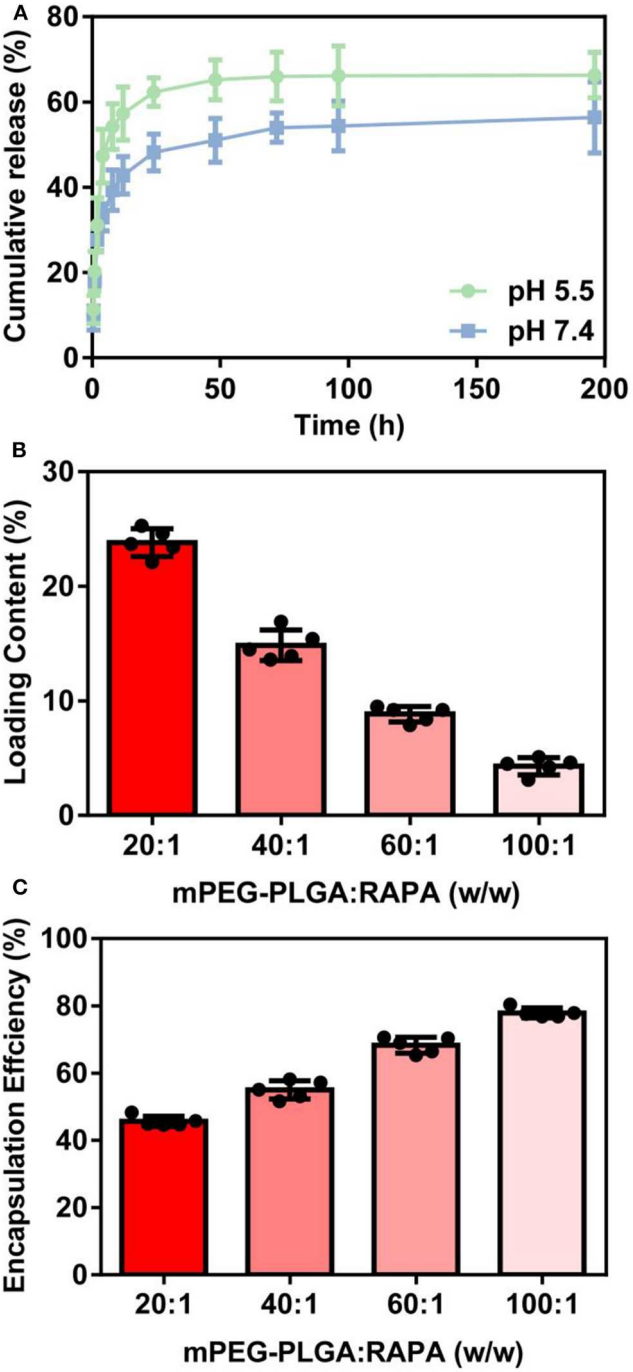

FIGURE 2 | (A) *In vitro* drug release profiles of rapamycin (RAPA) from rapamycin-loaded mPEG-PLGA nanoparticles (NP-RAPA) at pH 5.5 and 7.4. **(B)** The loading content of RAPA in NP-RAPA. **(C)** The encapsulation efficiency of RAPA in NP-RAPA.

Effects of NP-RAPA on *in vitro* Cell Model of NAFLD

NAFLD is characterized by excessive lipid accumulation in the hepatocytes (Yu et al., 2019). In the physiological condition, intracellular lipid homeostasis is tightly controlled by nutrient sensor or signaling (Hart, 2019). Dysregulation of lipid metabolism in the liver caused by lipid accumulation leads to metabolic syndrome and contributes to the pathogenesis of NAFLD (Liangpunsakul and Chalasani, 2019). To explore the therapeutic potential of NP-RAPA on NAFLD, we first tested the effect of NP-RAPA in cellular lipid accumulation on *in vitro* cell model of NAFLD (**Figure 3**). HepG2 cells treated with 0.4 mM oleic acid (OA) for 24 h exhibited obvious dense ORO staining, indicating the potential of lipid accumulation and steatosis in the hepatocytes. The ORO stained lipid droplets induced by OA were significantly reduced in RAPA- and NP-RAPA-treated

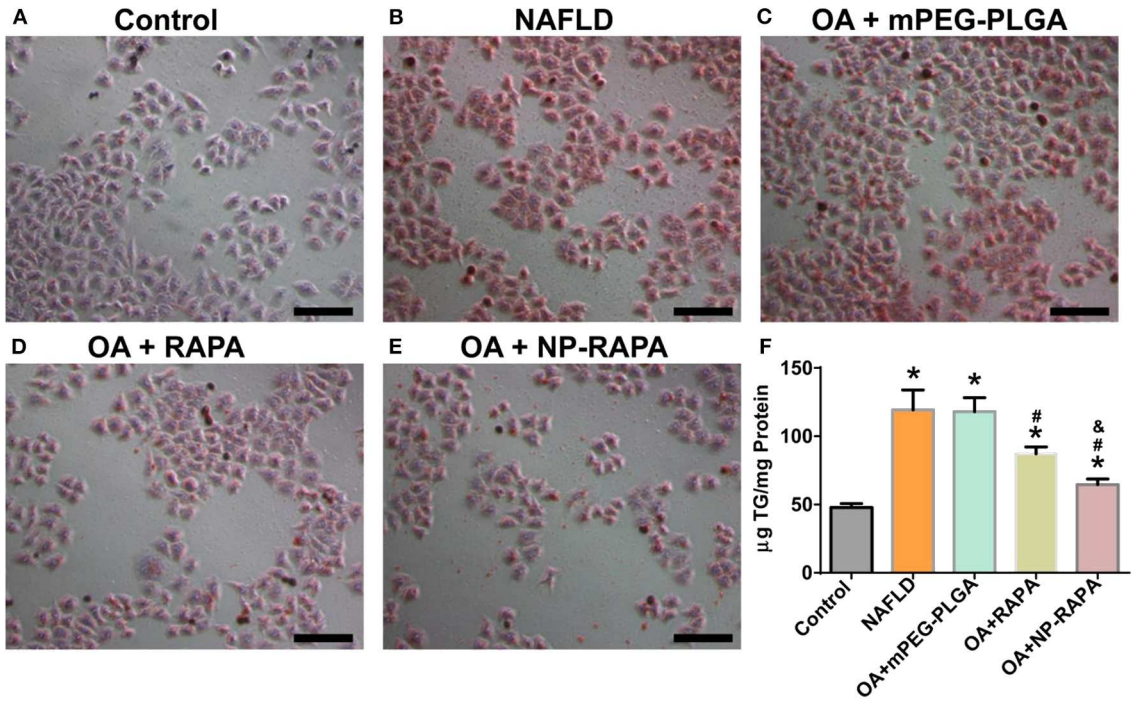

FIGURE 3 | The therapeutic efficacy of biodegradable mPEG-PLGA nanoparticles loaded with rapamycin (NP-RAPA) on non-alcoholic fatty liver disease (NAFLD) in HepG2 cells. HepG2 cells were incubated with 0.4 mM OA for 24 h to induce *in vitro* cell model of NAFLD. Oil Red O staining of the cells treated with blank DMEM **(A)**, OA **(B)**, mPEG-PLGA **(C)**, free RAPA **(D)**, and NP-RAPA **(E)**. Scale bars, 50 μm. **(F)** The triglyceride content of HepG2 cells in the *in vitro* NAFLD experiment. $^{*}p < 0.05$ vs. control group; $^{\#}p < 0.05$ vs. OA-treated group; $^{\&}p < 0.05$ vs. RAPA-treated group.

HepG2 cells compared with untreated and mPEG-PLGA-treated cells. More interestingly, the content of lipid accumulation was reduced to a greater extent when HepG2 cells treated with NP-RAPA than with free RAPA only. Taken together, our data indicate that NP-RAPA treatment can enhance the efficacy of RAPA on abrogation of OA-mediated lipid droplet accumulation on *in vitro* cell model of NAFLD.

Effects of NP-RAPA on NAFLD in Mice

In order to explore the effect of NP-RAPA on NAFLD, and compare the therapeutic efficacy, mPEG-PLGA, RAPA, and NP-RAPA were intravenously injected into C57BL/6J mice during the period of HFD feeding (**Figure 4**). Hematoxylin and eosin (H&E) staining showed that HFD treatment resulted in lipid droplets in the hepatocytes compared with ND-treated mice, indicating the successful establishment of a mouse model of NAFLD, which has been described previously (Cao et al., 2018; Zhao et al., 2018). However, administration of mPEG-PLGA polymers did not induce the reduction in the hepatic lipid accumulation at all. RAPA only showed significantly reduced the hepatic lipid content compared with HFD group, and the NP-RAPA administration was able to more obviously ameliorate the content of hepatic lipid droplet on NAFLD, compared with free RAPA only. Results of ORO staining were also in agreement to H&E staining confirming the potential of NP-RAPA treatment to ameliorate HFD-induced NAFLD via reducing hepatic accumulation in mice.

Quantitative analysis of the plasma and hepatic lipid content and liver function was shown in **Figure 5**. Mice treated with RAPA and NP-RAPA displayed much less hepatic triglyceride (TG) accumulation, and significantly reduced the level of serum alanine aminotransferase (ALT), aspartate aminotransferase (AST), and TG compared with HFD-induced NAFLD mice and mPEG-PLGA-treated NAFLD mice. Hepatic and plasma cholesterol levels were comparable among all the treated groups. These results altogether suggested that NP-RAPA could efficiently protect the mice from HFD-induced hepatic steatosis and liver injury in mice with NAFLD, the effects of which were better than free RAPA, confirming the potential and novel drug delivery for mPEG-PLGA in NAFLD treatment.

NP-RAPA Reduced SREBP-1c-Mediated *de novo* Lipogenesis in NAFLD Treatment

In order to elucidate the underlying mechanisms of therapeutic efficacy of NP-RAPA in NAFLD, we determined the lipogenesis-related gene expression in the liver (**Figure 6**). SREBP-1c-mediated *de novo* lipogenesis (DNL) is associated with hepatic triglyceride accumulation, which contributes to hepatic steatosis and is the mainly pathological character of NAFLD (Brunt, 2010; Kawano and Cohen, 2013; Shimano and Sato, 2017; Chen et al., 2018; Chen, 2020). Consistent with an important role of RAPA as an upstream inhibitor of mTORC1 signaling in regulation of SREBP-1c-mediated *de novo* lipogenesis (DNL) (Chen et al., 2018; Chen, 2020), gene expression of lipogenesis

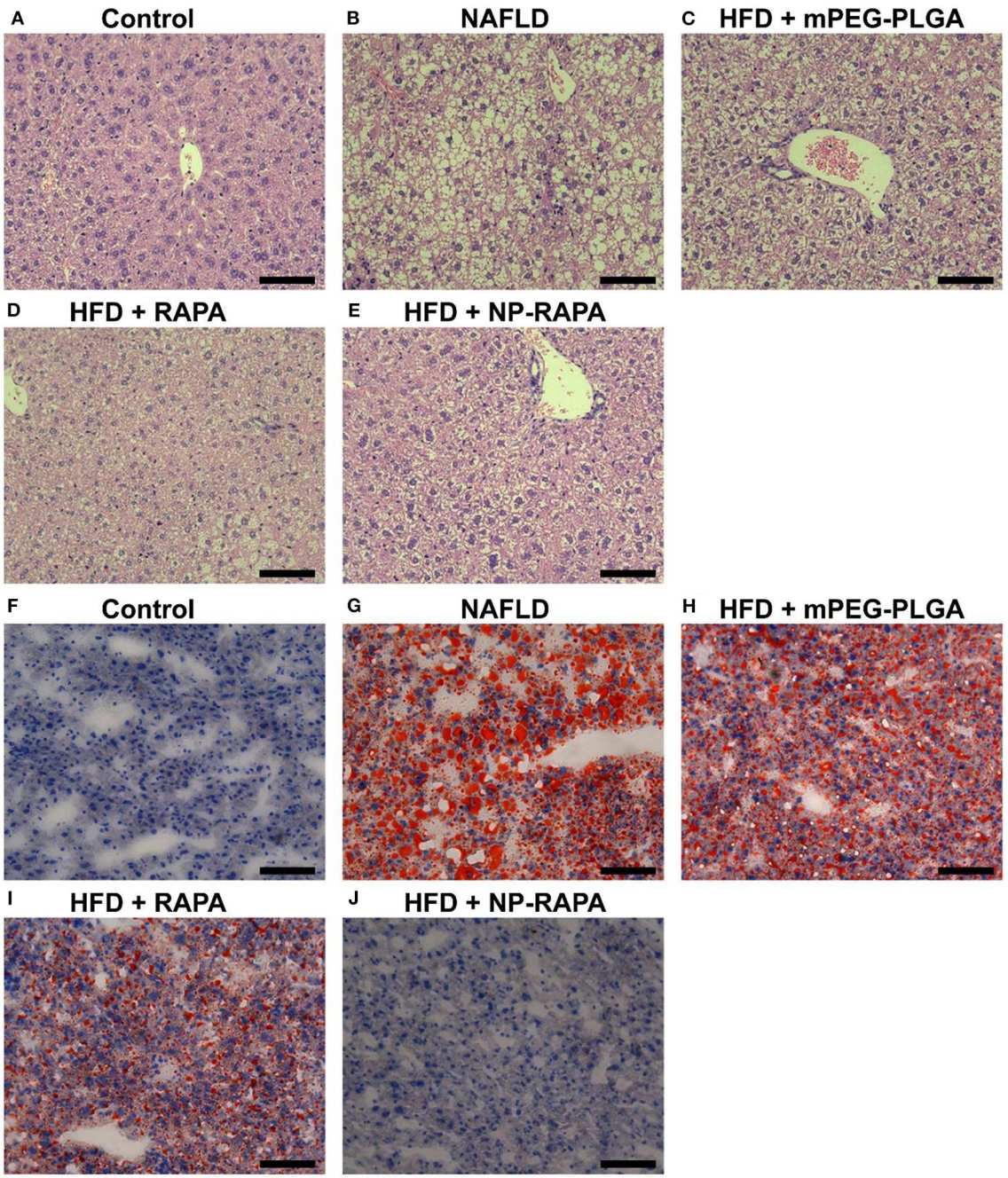

FIGURE 4 | Rapamycin-loaded mPEG-PLGA nanoparticles (NP-RAPA) ameliorated HFD-induced hepatic steatosis and liver injury on NAFLD in mice. **(A–E)** Representative hematoxylin and eosin (H&E) staining of hepatic steatosis in a mouse of HFD-induced NAFLD. **(F–J)** Representative Oil Red O (ORO) staining of liver cryosections of the mice with NAFLD. Mice fed with HFD for 13 weeks together with intravenous injection of mPEG-PLGA, free RAPA and NP-RAPA. **(A,F)** NS; **(B,G)** HFD-induced NAFLD; **(C,H)** mPEG-PLGA; **(D,I)** RAPA; **(E,J)** NP-RAPA.

in the liver took place. Analysis of gene expression in the liver indicated that mRNA levels of key genes involved in SREBP-1c-dependent DNL, such as *Srebp-1c* and its target genes, including *Acc1*, *Fasn*, *Scd1,* and *Dgat2* (Kawano and Cohen, 2013), were significantly increased in HFD-induced NAFLD mice. mPEG-PLGA failed to ameliorate hepatic steatosis and TG accumulation because there was no significant difference of gene expression of hepatic lipogenesis between HFD group and mPEG-PLGA group. Free RAPA significantly reduced HFD-mediated up-regulation of *Srebp-1c* and its target genes in the liver. However, NP-RAPA decreased the hepatic steatosis and triglyceride accumulation even more significantly determined by gene expression of hepatic lipogenesis. Meanwhile, HFD-induced the inhibition of peroxisome proliferator-activator receptor

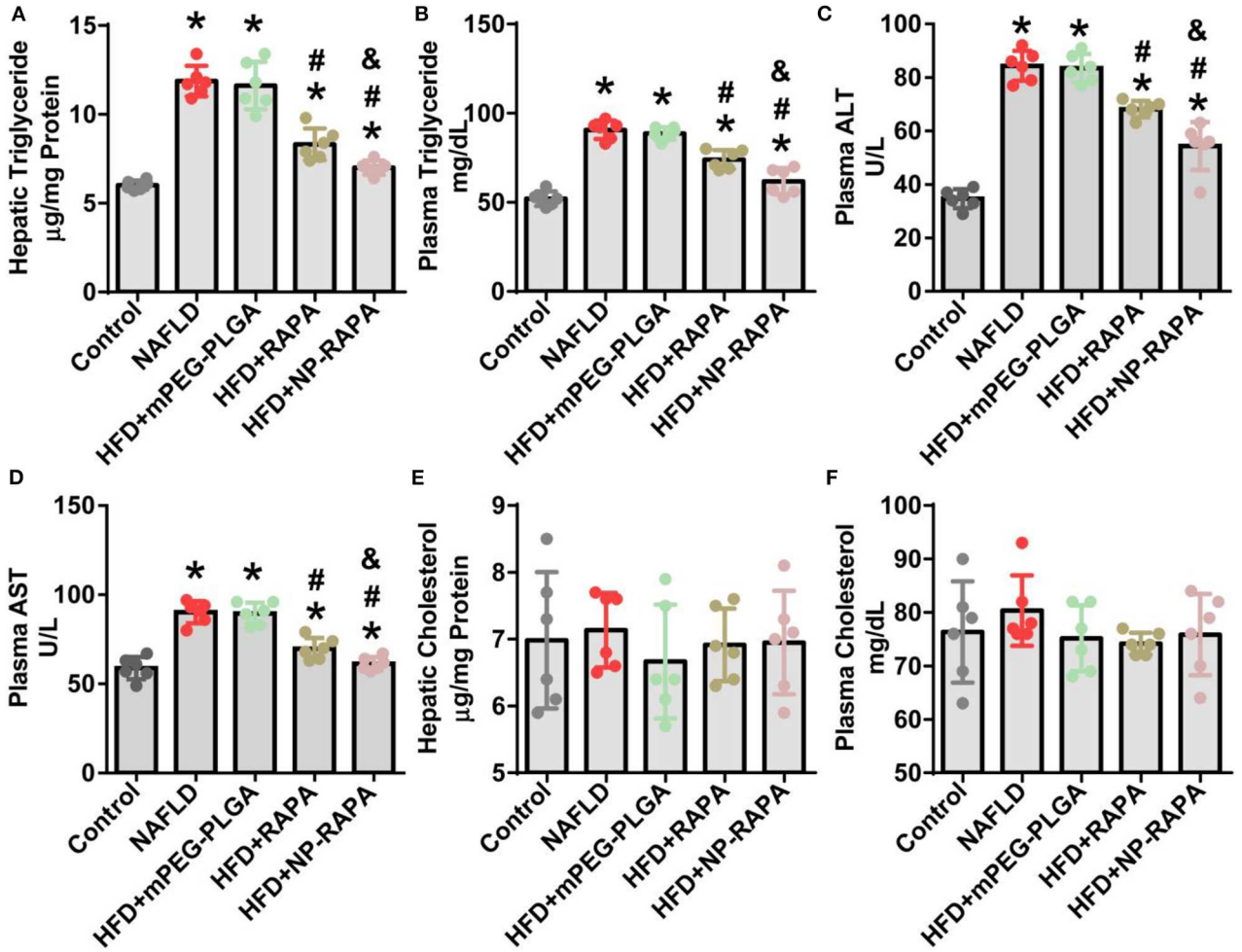

FIGURE 5 | The effect of rapamycin-loaded mPEG-PLGA nanoparticles (NP-RAPA) on liver function and serum biochemical index. Compared with free RAPA, NP-RAPA administration significantly improved hepatic steatosis and ameliorated liver injury in HFD-induced NAFLD in mice. **(A)** Hepatic triglyceride; **(B)** Plasma triglyceride; **(C)** Plasma alanine aminotransferase (ALT); **(D)** Plasma aspartate aminotransferase (AST); **(E)** Hepatic cholesterol; **(F)** Plasma cholesterol. Scale bars, 100 μm. $^{*}p < 0.05$ vs. control group; $^{\#}p < 0.05$ vs. HFD-treated group; $^{\&}p < 0.05$ vs. RAPA-treated group.

alpha (PPARα)-mediated fatty acid oxidation was recovered in RAPA treatment, especially in NP-RAPA group, as evidenced by increased expression of genes *Pparα*, *Cpt-1α*, and *Pgc-1α* (Brocker et al., 2018; Chen et al., 2018). Thus, NP-RAPA protects against HFD-induced hepatic steatosis and liver injury at least in part through enhancing the role of the therapeutic efficacy of RAPA in down-regulation of SREBP-1c-mediated *de novo* lipogenesis and up-regulation of PPARα-dependent fatty acid oxidation in NAFLD.

CONCLUSIONS

NAFLD is the leading cause of chronic liver disease worldwide, and there are no effective strategies available for NAFLD treatment currently (Eshraghian, 2017; Issa et al., 2018; Younossi et al., 2019). In this study, we successfully designed and developed a novel drug delivery using biodegradable mPEG-PLGA polymers for enhancing the therapeutic efficacy of rapamycin in treatment of NAFLD *in vitro* and *in vivo*. RAPA-loaded mPEG-PLGA nanoparticles (NP-RAPA) were prepared using an emulsion/solvent evaporation method and its therapeutic efficacy on NAFLD was investigated in HepG2 cells and in mice. Compared to free RAPA, NP-RAPA significantly decreased lipid content in HepG2 cells treated with OA and ameliorated hepatic steatosis and liver injury in mice with NAFLD induced by high-fat diet (HFD). The molecular mechanism of the inhibitory effects of NP-RAPA on NALFD is due to reduce REBP-1c-dependent *de novo* lipogenesis (DNL) and promote PPARα-mediated fatty acid oxidation in the liver of mice. This study suggests that mPEG-PLGA can be used as the potential therapeutic strategy and novel drug delivery for improving the efficacy of rapamycin for treatment of NAFLD.

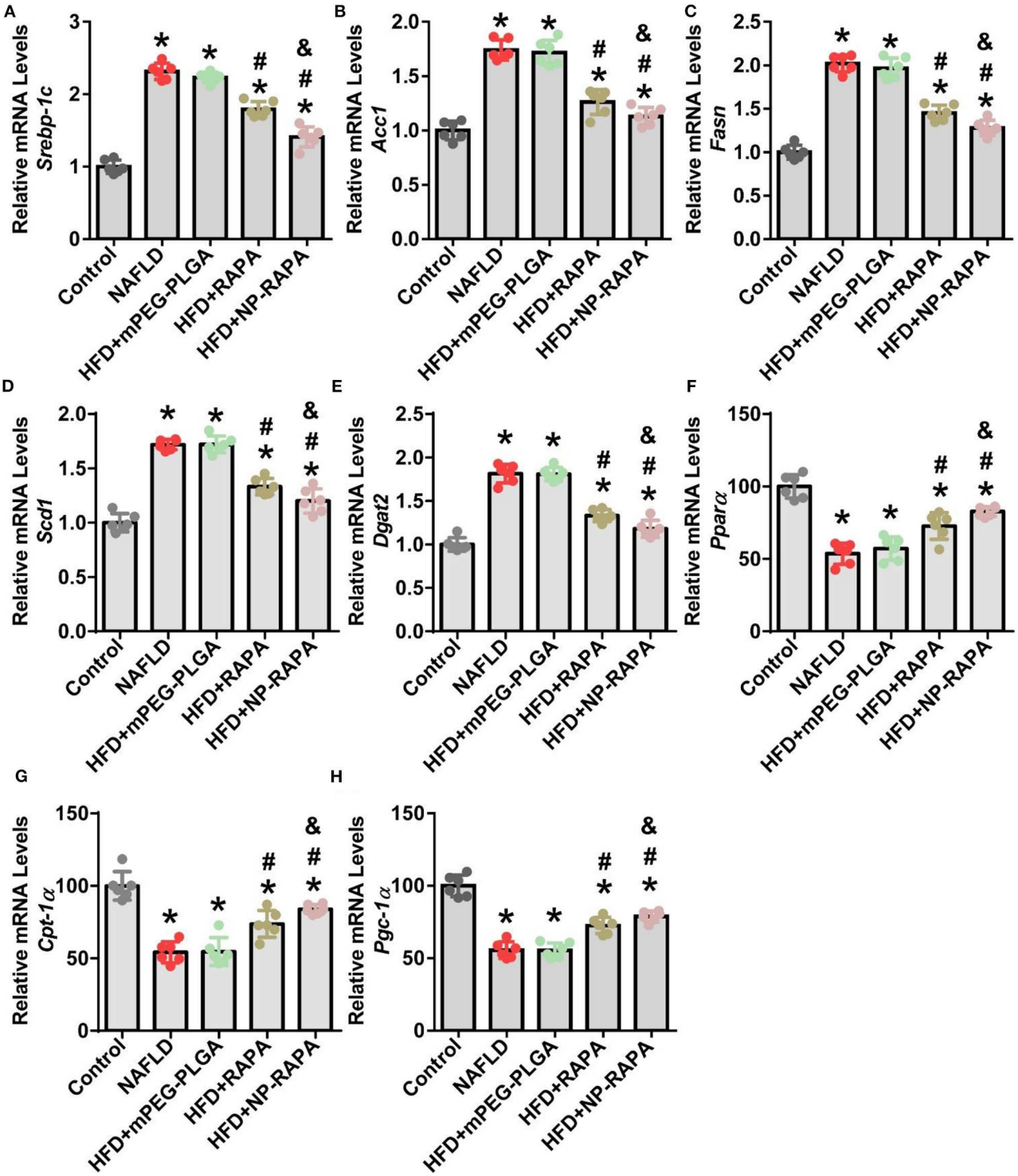

FIGURE 6 | Evaluation of lipid homeostasis in the liver of HFD-induced NAFLD in mice together with NP-RAPA. Hepatic mRNA expression of SREBP-1c-mediated *de novo* lipogenesis (DNL), including *Srebp-1c* **(A)**, *Acc1* **(B)**, *Fasn* **(C)**, *Scd1* **(D)**, and *Dgat2* **(E)** in mice treated with mPEG-PLGA, free RAPA and NP-RAPA. Transcription levels of mRNAs encoding PPARα-mediated hepatic fatty acid oxidation, including *Ppara* **(F)**, *Cpt-1a* **(G)**, and *Pgc-1α* **(H)** in mice. $^{*}p < 0.05$ vs. control group; $^{\#}p < 0.05$ vs. HFD-treated group; $^{\&}p < 0.05$ vs. RAPA-treated group.

DATA AVAILABILITY STATEMENT

The raw data supporting the conclusions of this article will be made available by the authors, without undue reservation, to any qualified researcher.

ETHICS STATEMENT

The animal study was reviewed and approved by the Ethics Committee of the National Center for Nanoscience and Technology of China.

AUTHOR CONTRIBUTIONS

The project was conceptually designed by HC. The majority of the experiments were performed by RZ and MZ, assisted SZ and WF. Data analysis and interpretation were carried out by RZ and HC. The manuscript was prepared by HC. All authors discussed the results and implications and commented on the manuscript.

FUNDING

This work was supported by the National Basic Research Program of China (Grant no. 2018YFE0205300 and 2016YFA0201600) and the National Natural Science Foundation of China (Grant no. 31800799, 81970507, and 11505193).

ACKNOWLEDGMENTS

We sincerely thank Dr. Zhoujian Zhou (Guangzhou First People's Hospital) for insightful and helpful discussions about the therapeutic efficacy of Rapamycin-Loaded mPEG-PLGA Nanoparticles on NAFLD.

REFERENCES

Bee, J., Fuller, S., Miller, S., and Johnson, S. R. (2018). Lung function response and side effects to rapamycin for lymphangioleiomyomatosis: a prospective national cohort study. *Thorax* 73, 369–375. doi: 10.1136/thoraxjnl-2017-210872

Brocker, C. N., Patel, D. P., Velenosi, T. J., Kim, D., Yan, T., Yue, J., et al. (2018). Extrahepatic pparα modulates fatty acid oxidation and attenuates fasting-induced hepatosteatosis in mice. *J. Lipid. Res.* 59, 2140–2152. doi: 10.1194/jlr.M088419

Brunt, E. M. (2010). Pathology of nonalcoholic fatty liver disease. *Nat. Rev. Gastro. Hepat.* 7, 195–203. doi: 10.1038/nrgastro.2010.21

Cao, Y. N., Baiyisaiti, A., Wong, C. W., Hsu, S. H., and Qi, R. (2018). Polyurethane nanoparticle-loaded fenofibrate exerts inhibitory effects on nonalcoholic fatty liver disease in mice. *Mol. Pharm.* 15, 4550–4557. doi: 10.1021/acs.molpharmaceut.8b00548

Chen, H. (2020). Nutrient mTORC1 signaling contributes to hepatic lipid metabolism in the pathogenesis of non-alcoholic fatty liver disease. *Liver Res.* 4, 15–22. doi: 10.1016/j.livres.2020.02.004

Chen, H., Shen, F., Sherban, A., Nocon, A., Li, Y., Wang, H., et al. (2018). Dep domain–containing mtor–interacting protein suppresses lipogenesis and ameliorates hepatic steatosis and acute-on-chronic liver injury in alcoholic liver disease. *Hepatology* 68, 496–514. doi: 10.1002/hep.29849

Chen, H., Zhao, R., Wang, B., Cai, C., Zheng, L., Wang, H., et al. (2017). The effects of orally administered ag, tio 2 and sio 2 nanoparticles on gut microbiota composition and colitis induction in mice. *NanoImpact* 8, 80–88. doi: 10.1016/j.impact.2017.07.005

Chen, Y. C., Lo, C. L., Lin, Y. F., and Hsiue, G. H. (2013). Rapamycin encapsulated in dual-responsive micelles for cancer therapy. *Biomaterials* 34, 1115–1127. doi: 10.1016/j.biomaterials.2012.10.034

Eshraghian, A. (2017). Current and emerging pharmacological therapy for non-alcoholic fatty liver disease. *World J. Gastroenterol.* 23:7495. doi: 10.3748/wjg.v23.i42.7495

Fan, J.-G. (2013). Epidemiology of alcoholic and nonalcoholic fatty liver disease in china. *J. Gastroenterol. Hepatol.* 28, 11–17. doi: 10.1111/jgh.12036

Flaxman, H. A., Chang, C.-F., Wu, H.-Y., Nakamoto, C. H., and Woo, C. M. (2019). A binding site hotspot map of the fkbp12–rapamycin–frb ternary complex by photoaffinity labeling and mass spectrometry-based proteomics. *J. Am. Chem. Soc.* 141, 11759–11764. doi: 10.1021/jacs.9b03764

Hart, G. W. (2019). Nutrient regulation of signaling and transcription. *J. Biol. Chem.* 294, 2211–2231. doi: 10.1074/jbc.AW119.003226

Ishida, T., Kashima, S., and Kiwada, H. (2008). The contribution of phagocytic activity of liver macrophages to the accelerated blood clearance (abc) phenomenon of pegylated liposomes in rats. *J. Control. Release* 126, 162–165. doi: 10.1016/j.jconrel.2007.11.009

Issa, D., Patel, V., and Sanyal, A. J. (2018). Future therapy for non-alcoholic fatty liver disease. *Liver Int.* 38, 56–63. doi: 10.1111/liv.13676

Kawano, Y., and Cohen, D. E. (2013). Mechanisms of hepatic triglyceride accumulation in non-alcoholic fatty liver disease. *J. Gastroenterol.* 48, 434–441. doi: 10.1007/s00535-013-0758-5

Kim, J., and Guan, K.-L. (2019). Mtor as a central hub of nutrient signalling and cell growth. *Nat. Cell Biol.* 21, 63–71. doi: 10.1038/s41556-018-0205-1

Lee, G., Zheng, Y., Cho, S., Jang, C., England, C., Dempsey, J. M., et al. (2017). Post-transcriptional regulation of *de novo* lipogenesis by mtorc1-s6k1-srpk2 signaling. *Cell 171*, 1545–1558. e1518. doi: 10.1016/j.cell.2017.10.037

Liangpunsakul, S., and Chalasani, N. (2019). Lipid mediators of liver injury in nonalcoholic fatty liver disease. *Am. J. Physiol. Gastrointest. Liver Physiol.* 316, G75–G81. doi: 10.1152/ajpgi.00170.2018

Lin, C. W., Zhang, H., Li, M., Xiong, X., Chen, X., Chen, X., et al. (2013). Pharmacological promotion of autophagy alleviates steatosis and injury in alcoholic and non-alcoholic fatty liver conditions in mice. *J. Hepatol.* 58, 993–999. doi: 10.1016/j.jhep.2013.01.011

Liu, D., Wong, C. C., Fu, L., Chen, H., Zhao, L., Li, C., et al. (2018). Squalene epoxidase drives nafld-induced hepatocellular carcinoma and is a pharmaceutical target. *Sci. Transl. Med.* 10:eaap9840. doi: 10.1126/scitranslmed.aap9840

Liu, J., Zhang, R., and Xu, Z. P. (2019). Nanoparticle-based nanomedicines to promote cancer immunotherapy: recent advances and future directions. *Small* 15:1900262. doi: 10.1002/smll.201900262

Liu, X. L., Pan, Q., Cao, H. X., Xin, F. Z., Zhao, Z. H., Yang, R. X., et al. (2020). Lipotoxic hepatocyte-derived exosomal mir-192-5p activates macrophages via rictor/akt/foxo1 signaling in nafld. *Hepatology.* doi: 10.1002/hep.31050

Othman, R., Vladisavljevic, G. T., Nagy, Z. K., and Holdich, R. G. (2016). Encapsulation and controlled release of rapamycin from polycaprolactone nanoparticles prepared by membrane micromixing combined with antisolvent precipitation. *Langmuir* 32, 10685–10693. doi: 10.1021/acs.langmuir.6b03178

Qureshi, W. A., Zhao, R., Wang, H., Ji, T., Ding, Y., Ihsan, A., et al. (2016). Co-delivery of doxorubicin and quercetin via mpeg–plga copolymer assembly for synergistic anti-tumor efficacy and reducing cardio-toxicity. *Sci. Bull.* 61, 1689–1698. doi: 10.1007/s11434-016-1182-z

Rotman, Y., and Sanyal, A. J. (2017). Current and upcoming pharmacotherapy for non-alcoholic fatty liver disease. *Gut* 66, 180–190. doi: 10.1136/gutjnl-2016-312431

Shimano, H., and Sato, R. (2017). Srebp-regulated lipid metabolism: Convergent physiology — divergent pathophysiology. *Nat. Rev. Endocrinol.* 13, 710–730. doi: 10.1038/nrendo.2017.91

Smith, G. I., Shankaran, M., Yoshino, M., Schweitzer, G. G., Chondronikola, M., Beals, J. W., et al. (2020). Insulin resistance drives hepatic *de novo* lipogenesis in nonalcoholic fatty liver disease. *J. Clin. Invest.* 130, 1453–1460. doi: 10.1172/JCI134165

Suk, J. S., Xu, Q., Kim, N., Hanes, J., and Ensign, L. M. (2016). Pegylation as a strategy for improving nanoparticle-based drug and gene delivery. *Adv. Drug Deliv. Rev.* 99, 28–51. doi: 10.1016/j.addr.2015.09.012

Teng, W., Zhao, L., Yang, S., Zhang, C., Liu, M., Luo, J., et al. (2019). The hepatic-targeted, resveratrol loaded nanoparticles for relief of high fat diet-induced nonalcoholic fatty liver disease. *J. Control. Release* 307, 139–149. doi: 10.1016/j.jconrel.2019.06.023

van der Meel, R., Sulheim, E., Shi, Y., Kiessling, F., Mulder, W. J. M., and Lammers, T. (2019). Smart cancer nanomedicine. *Nat. Nanotechnol.* 14, 1007–1017. doi: 10.1038/s41565-019-0567-y

Wang, H., Zhao, Y., Wu, Y., Hu, Y. L., Nan, K., Nie, G., et al. (2011). Enhanced anti-tumor efficacy by co-delivery of doxorubicin and paclitaxel with amphiphilic methoxy peg-plga copolymer nanoparticles. *Biomaterials* 32, 8281–8290. doi: 10.1016/j.biomaterials.2011.07.032

Weissig, V., Pettinger, T. K., and Murdock, N. (2014). Nanopharmaceuticals (part 1): Products on the market. *Int. J. Nanomed.* 9:4357. doi: 10.2147/IJN.S46900

Yeh, M. M., and Brunt, E. M. (2014). Pathological features of fatty liver disease. *Gastroenterology* 147, 754–764. doi: 10.1053/j.gastro.2014.07.056

Younossi, Z., Tacke, F., Arrese, M., Chander Sharma, B., Mostafa, I., Bugianesi, E., et al. (2019). Global perspectives on nonalcoholic fatty liver disease and nonalcoholic steatohepatitis. *Hepatology* 69, 2672–2682. doi: 10.1002/hep.30251

Yu, Y., Cai, J., She, Z., and Li, H. (2019). Insights into the epidemiology, pathogenesis, and therapeutics of nonalcoholic fatty liver diseases. *Adv. Sci.* 6:1801585. doi: 10.1002/advs.201801585

Zhao, X. Y., Xiong, X., Liu, T., Mi, L., Peng, X., Rui, C., et al. (2018). Long noncoding rna licensing of obesity-linked hepatic lipogenesis and nafld pathogenesis. *Nat. Commun.* 9:2986. doi: 10.1038/s41467-018-05383-2

Zhou, W., and Ye, S. (2018). Rapamycin improves insulin resistance and hepatic steatosis in type 2 diabetes rats through activation of autophagy. *Cell Biol. Int.* 42, 1282–1291. doi: 10.1002/cbin.11015

Conflict of Interest: The authors declare that the research was conducted in the absence of any commercial or financial relationships that could be construed as a potential conflict of interest.

frontiers in Chemistry

ORIGINAL RESEARCH
published: 21 July 2020
doi: 10.3389/fchem.2020.00500

Co-assembled Supramolecular Nanofibers With Tunable Surface Properties for Efficient Vaccine Delivery

Zhongyan Wang[1†], Chunhua Ren[1†], Yuna Shang[2], Cuihong Yang[1], Qingxiang Guo[1], Liping Chu[1] and Jianfeng Liu[1*]*

[1] Tianjin Key Laboratory of Radiation Medicine and Molecular Nuclear Medicine, Institute of Radiation Medicine, Chinese Academy of Medical Sciences & Peking Union Medical College, Tianjin, China, [2] College of Life Sciences, Nankai University, Tianjin, China

The utilization of nanotechnology to deliver vaccines and modulate immunity has shown great potential in cancer therapy. Peptide-based supramolecular hydrogels as novel vaccine adjuvants have been found to effectively improve the immune response and tumor curative effect. In this study, we designed a set of reduction-responsive self-assembled peptide precursors (Fbp-G^{D}F^{D}F^{D}Y^{D}(E, S, or K)-ss-ERGD), which can be reduced by glutathione (GSH) into Fbp-G^{D}F^{D}F^{D}Y^{D}(E, S or K)-SH for forming of hydrogel with different surface properties (E-gel, S-gel, and K-gel, respectively). Using the same method, co-assembled hydrogel vaccines (E-vac, S-vac, and K-vac, respectively) can also be prepared by mixing different precursors with antigens before GSH reduction. Through TEM observation of the nanostructure, we found that all the co-assembled hydrogels, especially K-vac, possessed much denser and more unified nanofiber networks as compared with antigen-free hydrogels, which were very suitable for antigen storage and vaccine delivery. Although the three peptides adopted similar β-sheet secondary structures, the mechanical properties of their resulted co-assembled hydrogel vaccines were obviously different. Compared to E-vac, S-vac had a much weaker mechanical property, while K-vac had a much higher. *In vivo* experiments, co-assembled hydrogel vaccines, especially K-vac, also promoted antibody production and anti-tumor immune responses more significantly than the other two vaccines. Our results demonstrated that co-assembled hydrogels formed by peptides and antigens co-assembly could act as effective vaccine delivery systems for boosting antibody production, and different immune effects can be acquired by tuning the surface properties of the involved self-assembling peptides.

Keywords: co-assembly, peptide, antigen, surface properties, vaccine, tumor therapy

OPEN ACCESS

Edited by:
Huaimin Wang,
Westlake University, China

Reviewed by:
Chengbiao Yang,
Wayne State University, United States
Xingyi Li,
Affiliated Eye Hospital of Wenzhou Medical College, China

***Correspondence:**
Liping Chu
chulp89@163.com
Jianfeng Liu
liujianfeng@irm-cams.ac.cn

†These authors have contributed equally to this work

Specialty section:
This article was submitted to Supramolecular Chemistry, a section of the journal Frontiers in Chemistry

Received: *01 April 2020*
Accepted: *14 May 2020*
Published: *21 July 2020*

Citation:
Wang Z, Ren C, Shang Y, Yang C, Guo Q, Chu L and Liu J (2020) Co-assembled Supramolecular Nanofibers With Tunable Surface Properties for Efficient Vaccine Delivery. Front. Chem. 8:500. doi: 10.3389/fchem.2020.00500

INTRODUCTION

In recent years, tumor vaccines have been widely and deeply studied, and it has become one of the most attractive tumor immunotherapies (Melief et al., 2015; Romero et al., 2016). In addition to exploring tumor antigens that represent tumor characteristics, developing adjuvants that can effectively stimulate the maturation and activation of immune cells are also essential in tumor

immunotherapy (Melief, 2018; Keskin et al., 2019). Through reasonably selecting tumor antigens and immune adjuvant, the resultant tumor vaccine can potentially prevent and eliminate many kinds of malignant tumors (Min et al., 2017; Ott et al., 2017; Sahin et al., 2017). However, due to the insufficient distribution of tumor vaccine in immune organs, the limited antigen uptake and presentation by antigen presenting cells, and the rapid degradation of antigen and adjuvant in the extracellular environment, the therapeutic effect of tumor vaccines is very limited in clinical practice (van der Burg et al., 2016). At present, nanotechnology has been confirmed to be very useful to regulate the body's immune system, and many studies have begun to move toward clinical applications (Irvine et al., 2015; Rodell et al., 2018; Feng et al., 2019). The development of nano-medicine provides a good platform for the delivery of tumor vaccines (Cai et al., 2019). Through skillfully optimizing particle size or adjusting surface properties, nano-delivery systems can effectively deliver different types of antigens and adjuvants, such as peptides, proteins, and nucleic acids, etc. (Bachmann and Jennings, 2010). These strategies not only improve the tumor vaccine's targeted ability toward immune cells, but also enhance its stability *in vivo*, which significantly enhanced immune therapeutic effect of tumor vaccines as a consequence.

Supramolecular hydrogels based on peptide self-assembly as potential nanocarriers have shown important applications in drug delivery, tissue engineering, cancer treatment and analysis (Wang et al., 2016a, 2018, 2020a; Yang et al., 2017, 2020; Shigemitsu et al., 2018; Ren et al., 2019; Shang et al., 2019b). Peptide monomolecules can self-assemble into specific nanostructures by non-covalent bonds including hydrophobic interaction, aromatic-aromatic stacking, hydrogen bond, etc., endowing them with ease of design, good biocompatibility and adjustable functions (Du et al., 2015; Chen et al., 2018; Shang et al., 2019a; Yuan et al., 2019; Bera et al., 2020). In recent years, self-assembled peptides have been reported to exhibit immune-stimulating effects such as self-adjuvants. Self-assembling peptide conjugated with antigen epitope can promote the production of large numbers of antibodies (Rudra et al., 2010). However, they suffer from activating the cellular immunity. Physical packages of antigen can efficiently activate both the humoral and cellular immunity, and can also protect antigen activity, but this method, requiring a specific sequence, is not versatile (Luo et al., 2017). Co-assembly, as a characteristic form of multiple molecular organization, can be utilized to deliver functional molecules like small molecule drugs, proteins, and nucleic acids for increasing their activity, which is also very useful for the development of subunit vaccines (Hudalla et al., 2014; Wang et al., 2016b, 2020b). Antigens embedded in nanostructures have good tolerance to the extracellular environment, which can ensure sustained stimulation against the immune system. A recent research showed that three kind of co-assembled nanofibers with different surface properties induced by glutathione reduction could be used for intracellular protein delivery (Wang et al., 2015). The surface properties of nanomaterials are also important and often are used to tune the immunogenicity of antigen (Wen et al., 2016; Yang et al., 2018). In this study, we introduced three supramolecular hydrogels formed by disulfide bond reduction for the development of cancer vaccines.

MATERIALS AND METHODS

Materials

2-Cl-trityl chloride resin was obtained from Nankai resin Co., Ltd. Fmoc-amino acids and O-Benzotriazole-N,N,N′,N′-tetramethyl-uronium-hexafluorophosphate (HBTU) were obtained from GL Biochem (Shanghai). Flurbiprofen was obtained from Aladdin. Chemical reagents and solvents were used as received from commercial sources. Fetal bovine serum (FBS), RPMI-1640 medium and penicillin/streptomycin were purchased from Gibco Corporation. EndoFit ovalbumin (OVA) (endotoxins <1 EU mg^{-1}) was purchased from InvivoGen (CA, USA). Horseradish peroxidase-conjugated goat anti-mouse IgG, IgG1, IgG2a, and IgG2b were obtained from Southern Biotechnologies (AL, USA). Mouse IL-4/IFN-γ ELISA kits were purchased from Biolegend. Six-week-old female C57BL/6 mice were purchased from the Beijing Vital River Laboratory Animal Technology Co., Ltd.

General Methods

^{1}H NMR (Bruker ARX 400) was used to characterize the synthesized compounds. HPLC was conducted with the LUMTECH HPLC (Germany) system using a C_{18} RP column with MeOH (0.05% of TFA) and water (0.05% of TFA) as the eluents. TEM images were done on a HT7700 Exalens system (Hitachi, Japan). Circular dichroism spectrum was done using a circular dichrometer (MOS-450, BioLogic). Rheology was performed on an AR 1500ex (TA instrument) system using a parallel plate (25 mm) at the gap of 500 μm. Optical density values were obtained by a microreader (Synergy 4, BioTek).

Synthesis of Fmoc-Cystamine Succinic Acid (Fmoc-CS)

As shown in **Figure S1**, cystamine dihydrochloride (10 mmol) and NaHCO3 (30 mmol) were firstly dissolved in 10 mL H2O, then 100 mL of dioxane was added with stirring. After being cooled to 0°C in the ice bath for 10 min, succinic anhydride (10 mmol) was added to the above mixture. The resulting reaction mixture was stirred overnight. After reaction overnight, 3.3 mL of DIPEA and 10 mL of DMF solution containing 10 mmol of Fmoc-OSu were successively added to the reaction mixture in the ice bath. A filtration was applied to remove the solid from the reaction mixture. The filtrate was then concentrated by the rotary evaporator. Two hundred milliliters of water was added to the resulting viscous liquid. Then the precipitate was collected by filtration and dried in vacuum.

Peptide Synthesis

All peptides were synthesized by using 2-chlorotrityl chloride resin with a loading efficiency of about 1.2 mmol/g and the corresponding N-Fmoc protected amino acids with side chains properly protected by the standard solid phase peptide synthesis (SPPS) method (Ren et al., 2011; Yang et al., 2014). The C-terminal of the first amino acid was firstly conjugated

on the resin. Twenty percentage of piperidine in anhydrous N,N-dimethylformamide (DMF) was used to remove the Fmoc protecting group. Then the next Fmoc-protected amino acid was coupled to the free amino group using HBTU as the coupling reagent. The growth of the peptide chain was according to the established SPPS protocol. Fmoc-CS was added using same method. After the last coupling step, excessive reagents were removed by five times DMF wash, followed by washing five times using DCM. The peptide was cleaved from resin using 95% trifluoroacetic acid. The ice ethyl ether was then added to the obtained concentrated solution for precipitating the crude product.

Preparation of Hydrogel

Five milligrams of peptide precursor was evenly scattered into 1 mL of phosphate buffer solution (PBS). 1 eq Na2CO3 were used to adjust the final pH value to 7.4. Then the peptide solution was evenly mixed with 2 eq glutathione (GSH) and placed in an incubator (37°C). Gel formed in about 30 min.

Transmission Electron Microscopy

Negative staining technique was used to observe the nanostructures of hydrogels. A 10 μL hydrogel sample was firstly loaded on the carbon-coated copper grids for 2 min and rinsed with water twice. Subsequently the sample was stained with 1% uranyl acetate for 1 min. Finally, the grid was placed in a desiccator overnight before observation.

Circular Dichroism Spectrum

Circular dichroism (CD) spectrum was obtained by a BioLogic (MOS-450) system. Hydrogel samples were placed in 0.1 cm quartz spectrophotometer cell (20-C/Q/0.1). The wavelength range varied from 190 to 280 nm. The acquisition period was 0.5 s and the step was 0.5 nm. The resultant CD spectrum was acquired after subtracting the solvent background.

Rheology

The Rheology test was performed on an AR 1500ex (TA instrument) system, and a 25 mm parallel plate was used during the experiment with a gap of 500 μm. For the dynamic frequency sweep, the samples were directly transferred to the rheometer and it was tested from 1 to 100 rad/s at the strain of 1%. All samples were tested at the temperature of 37°C.

Hydrogel Vaccine Formulation

All hydrogel vaccines were prepared by using endotoxin-free PBS buffer (pH = 7.4) at final concentration of 0.5 wt%. Endotoxin-free OVA solution was added and evenly mixed with peptide solution. After GSH was added, the solution was placed in an incubator (37°C) for hydrogel formation.

Vaccination and Measurement of Specific Antibody

The hydrogel vaccines were firstly shaken into a viscous liquid before immunization. Female C57BL/6 mice were randomly distributed into four groups and each group contained 5 mice. Mice were executed by subcutaneous injection with 100 μL different vaccines (0.5 wt% hydrogels composed of 50 μg OVA vaccine, 100 μL PBS with 50 μg OVA and 50 μg OVA with 25 times Alum, respectively) in the groin at day 0. The second immunization was given at day 14. On day 21, serum was collected for the antibody detection. OVA-specific antibody responses in mice were examined by enzyme-linked immunosorbent assay (ELISA). The 96-well ELISA plates were coated with 10 μg/mL OVA and stored at 4°C overnight. After washing with PBST four times (PBS buffer containing 0.05% tween 20), the plates were blocked by blocking buffer (1% BSA in PBST) for 1 h at room temperature. Individual antisera were serially diluted in the blocking buffer and incubated in the plates for 2 h at room temperature. After 5 times wash with PBST, the plates were incubated with goat anti-mouse IgG horseradish peroxidase for 1 h. Antibody binding was assessed by adding 100 μL 3,3′,5,5′-tetramethylbenzidine peroxidase substrate (TMB). The substrate reaction was terminated by adding 100 μL of 2 M H_2SO_4. The plates were immediately read at 450 nm by an ELISA reader. Antibody titers were calculated as the reciprocal serum dilution giving O. D. values >0.1 standard deviations above background levels as calculated using PBS at the same dilution.

Measurement of Splenocytes Cytokines

After the serum was extracted, the spleen of each group was taken out and grinded. After erythrocytes lysis operation, splenocytes (5×10^6 cells/mL) were collected and seeded in 24-well plates with 1640 medium containing 10% FBS and 1% PS, and subsequently were re-simulated with soluble OVA (50 μg/mL) in a carbon dioxide incubator for 96 h. The quantity of IL-4 and IFN-γ in splenocyte culture supernatants was detected by using an ELISA kit (Biolegend, San Diego, CA, USA).

Evaluation of Anti-tumor Immunity *in vivo*

E.G.7-OVA cells were first cultured in 1640 medium containing 0.4 mg/mL G418 (Geneticin). Six to eight week-old female C57BL/6 mice were subcutaneously injected with 50 μL cell suspension (PBS containing 5×10^5 cells) on the right buttock. When the tumor volume reached about 100 mm^3 on day 7, the mice were randomly divided into four groups and received100 μL different vaccine treatments (PBS, E-vac, S-vac, or K-vac, respectively) by subinguinal injection. The other two vaccinations were administered on day 13 and 19. Tumor volume was measured every 3 days.

Statistical Analysis

Statistical analysis was processed in GraphPad Prism 7. All data were shown as the mean ± standard deviation (SD). The difference among groups in antibody and cytokine analysis were determined with one-way analysis of variance analysis (ANOVA), and the difference among groups in tumor analysis were determined with unpaired student's *t*-test. $^{*}p < 0.05$, $^{**}p < 0.01$ and $^{***}p < 0.001$ were used to show statistical significance.

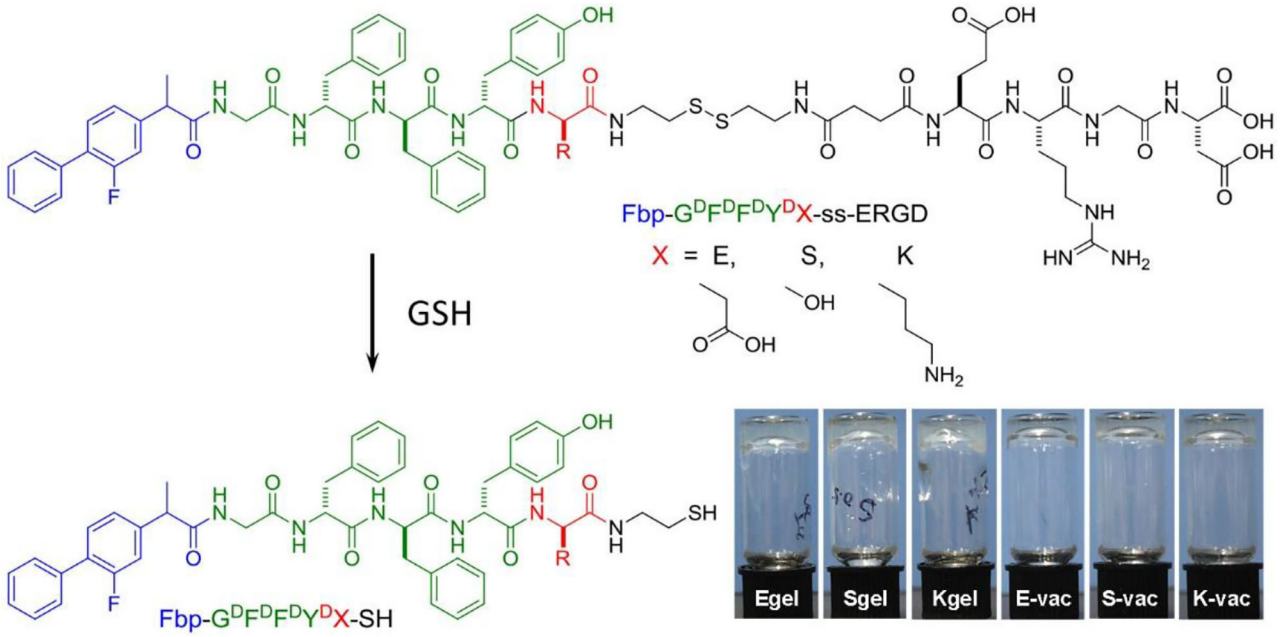

FIGURE 1 | Chemical structure of precursors Fbp-$G^DF^DF^DY^D$(X)-ss-ERGD and hydrogelators Fbp-$G^DF^DF^DY^D$(X)-SH, and the optical images of E-gel, S-gel, K-gel, E-vac, S-vac, and K-vac.

RESULTS AND DISCUSSION

Peptide Synthesis and Hydrogel Preparation

The flurbiprofen (Fbp, a non-steroidal anti-inflammatory drug) was selected as the capping group of peptide due to its distinct immunomodulatory effect (Wang et al., 2017). We first synthesized three precursors of Fbp-$G^DF^DF^DY^D$(E, S or K)-ss-ERGD by standard solid phase peptide synthesis (SPPS) (**Figure 1**, Pre-E, Pre-S, or Pre-K, respectively). All compounds were depurated by using reverse phase high performance liquid chromatography (RP-HPLC). To acquire the hydrogels, all the precursors were evenly dispersed in phosphate buffer saline (PBS) solution first. After adjusting the pH to about 7.4 by adding Na_2CO_3, the precursors formed transparent solution at the concentration of 1 wt%. Then 2 eq glutathione (GSH) was evenly mixed in the dilute solution with the concentration of 0.5 wt%. Hydrogelators of Fbp-$G^DF^DF^DY^D$(E, S or K)-SH continually self-assembled into nanofibers accompanied with the reduction of disulfide bond by GSH. As shown in the **Figure 1**, the transparent hydrogels formed after incubation (37°C) for half an hour and can remain stable in inverted glass bottles (E-gel, S-gel, and K-gel, respectively). Similarly, the three precursor solutions containing ovalbumin (OVA) also can form transparent co-assembled hydrogel vaccines after adding GSH for half an hour at 37°C (**Figure 1**, E-vac, S-vac, and K-vac, respectively).

Nanostructure Characterization of Hydrogels

Subsequently, we observed the nanostructures of the three hydrogels by transmission electron microscopy (TEM). Both the E-gel and S-gel showed unified nanofibers with diameters of about 15 nm (**Figures 2A,B**). In addition to containing nanofibers similar to those of E-gel and S-gel, K-gel also exhibited a kind of bundled structure with a diameter of about 40∼50 nm (**Figure 2C**). We also obtained the TEM images of the three co-assembled hydrogel vaccines. As shown in the **Figures 2D–F**, the nanofiber networks in these hydrogels containing OVA became much denser. Particularly, K-vac had unified nanofibers with narrower diameter. The results indicated that the incorporation of protein OVA improved the properties of the resultant hydrogels and facilitated the formation of uniform co-assembled nanostructure, which was very beneficial for antigen storage and vaccine delivery.

Secondary Structure of Peptide

The secondary structures of all hydrogels were measured by circular dichrometer. As shown in the **Figure 3A**, all the three co-assembled hydrogel vaccines exhibited a similar CD spectrum to corresponding hydrogel without OVA at the concentration of 0.5 wt% in the range of 190∼280 nm. E-gel and E-vac showed a β-sheet structure with a negative peak at 195 nm and a positive peak at 216 nm. S-gel and S-vac also exhibited a β-sheet structure with a weak negative peak at 198 nm and a positive peak at 219 nm. Similarly, K-gel and K-vac had a weak negative absorption at 191 nm and a positive peak at 212 nm. Such molecular arrangement made the peptides in co-assembled hydrogels self-assemble into uniform nanofibers, while proteins also were integrated into the formation of nanofibers.

Mechanical Properties of Hydrogels

We measured the mechanical properties of all hydrogels at 37°C by a rheometer. As shown in **Figure 3B**, the hydrogels exhibited weak frequency dependences at the range of 0.1–100

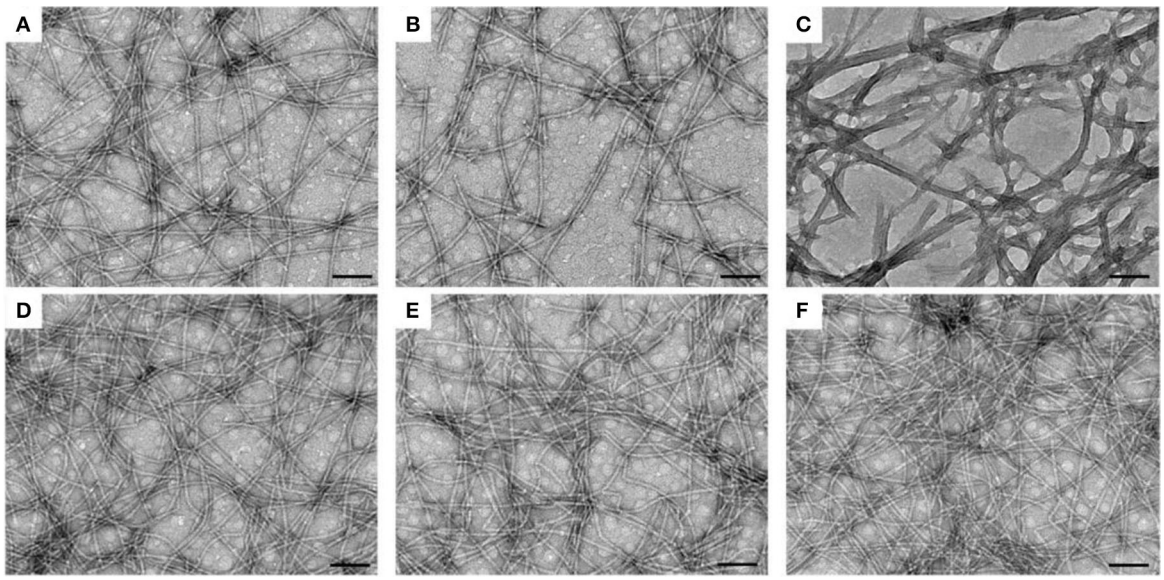

FIGURE 2 | TEM images of nanofibers in **(A)** E-gel, **(B)** S-gel, **(C)** K-gel, **(D)** E-vac **(E)** S-vac, and **(F)** K-vac. Scale bar = 100 nm.

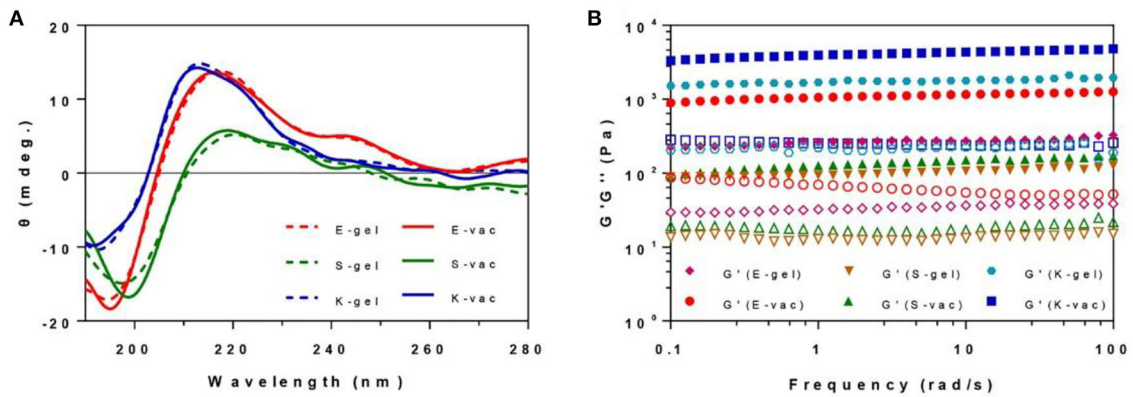

FIGURE 3 | (A) The CD spectrum of E-gel, S-gel, K-gel, E-vac, S-vac, and K-vac. **(B)** The dynamical frequency sweep of E-gel, S-gel, K-gel, E-vac, S-vac, and K-vac (solid icon representing G′, corresponding hollow icon representing G″).

rad/s, the co-assembled hydrogels had slightly higher rheological properties than their hydrogel without OVA. The G′ (storage modulus) values of the E-vac, S-vac and K-vac were all about 8∼20 times bigger than their corresponding G″ (loss modulus) values. The G′ values of S-vac and E-vac were more than 1×10^2 Pa and 1×10^3, respectively. While the G′ value of K-vac was $\sim 1 \times 10^4$ Pa. Denser nanofiber networks endowed the co-assembled hydrogel vaccines, particularly K-vac, with high mechanical properties and resistance to external forces, which showed great potential for antigen storage and vaccine delivery.

Immunization and Antibodies Measurement

The immune efficiency of the co-assembled hydrogel vaccines was subsequently evaluated by a twice vaccination program. Six-weeks-old female C57BL/6 mice were randomly divided into five groups and immunized with different vaccines at day 0 in the groin. PBS containing OVA and aluminum hydroxide (Alum) containing OVA were assigned as the control groups. After 14 days, the mice received the same dose of secondary vaccination. The serum was separated from immunized mice on the 21st day. The OVA-specific antibody titers were measured by enzyme-linked immunosorbent assay (ELISA). The three co-assembled hydrogel vaccines with different surface properties exhibited excellent vaccine potency. As shown in **Figure 4A**, compared to the pure antigen group, the expression of IgG antibodies in the groups treated with E-vac, S-vac, and K-vac increased 760-fold, 560-fold, and 1800-fold, respectively. Even comparing with the clinically used aluminum adjuvant, E-vac, S-vac, and K-vac enhanced IgG expression by 6.3-, 4.6-, and 15-fold, respectively. In promoting the production of IgG subtypes, the three co-assembled hydrogel vaccines still held the edge over

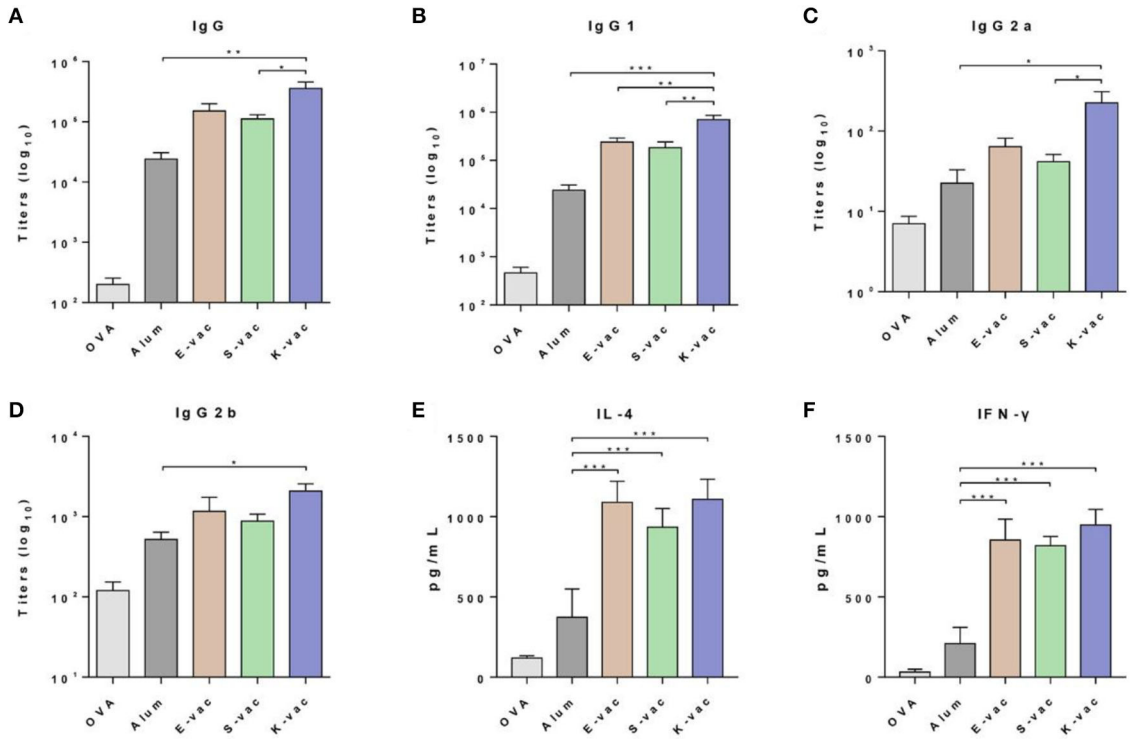

FIGURE 4 | Specific anti-OVA antibody titers of **(A)** IgG, **(B)** IgG1, **(C)** IgG2a, and **(D)** IgG2b. Cytokines of **(E)** IL-4 and **(F)** IFN-γ secreted from splenocyte of vaccinated mice. The asterisks represent the difference between the two groups. $^{*}p < 0.05$, $^{**}p < 0.01$, $^{***}p < 0.001$.

Alum. Most notably, the effect of K-vac was more prominent than the other co-assembled hydrogel vaccines, which may be attributed to the higher mechanical property of K-vac and the higher affinity to antigens.

Splenocyte Cytokines Analysis

We then analyzed the production of two kinds of splenocyte cytokines including IL-4 and IFN-γ. The splenocytes were isolated from immunized mice and then restimulated by the antigens. The cytokines in splenocyte supernatants were measured following the ELISA kit instructions. As shown in **Figure 4E**, the three co-assembled hydrogel vaccines greatly increased the production of both IL-4 and IFN-γ. Comparing to Alum, E-vac, S-vac, and K-vac promoted the expression of IL-4 by 2.9-, 2.5- and 2.9-fold, respectively. K-vac showed equivalent efficiency to E-vac in increasing Th2 cytokine production, suggesting that surface properties of the hydrogels had little impact on regulating humoral immune responses. However, the co-assembled hydrogel vaccines with different surface properties showed distinction in promoting Th1 immune responses. Compared to Alum, E-vac, S-vac, and K-vac enhanced the expression of IFN-γ by 4.0-, 3.9-, and 4.5-fold, respectively (**Figure 4F**). The results indicated that K-vac was much more prominent in regulating cellular immune responses, implying the great potential of K-vac in tumor immnuotherapy.

In vivo Evaluation of Therapeutical Effect

Subsequently we tested the therapeutic effect of co-assembled hydrogel vaccines against E.G.7-OVA tumor *in vivo*. On day 0, E.G.7-OVA cells were first inoculated on the buttock of C57BL/6 mice. The mice were vaccinated when the tumors' volumes grew to about 100 mm^3, and then the tumor size was measured every 3 days. The results revealed that the three hydrogel vaccines exhibited different abilities to suppress tumor growth. As shown in **Figure 5A** and **Figure S2**, on day 25, the group treated with S-vac showed effective tumor growth inhibition, and the inhibition ratio was about 32% when compared to the PBS group. E-vac treated group also showed enhanced therapeutic effect and the inhibition ratio was about 42%. In particular, the group treated with K-vac exhibited much better effects than the other groups and the inhibition ratio reached up to about 64% (**Figure S2**). Besides, the tumor weight of mice treated by K-vac was also significantly lower than any other groups (**Figure S3**). These results demonstrated that co-assembled hydrogels were helpful for the tumor vaccine delivery and treatment effect enhancement. In addition, different surface properties endowed the co-assembled hydrogel vaccines with distinct immunotherapeutic effect. Simultaneously, we obtained the weight curves of mice during the treatment. As shown in **Figure 5B**, from the difference between the mice's weights in PBS group fluctuated obviously, the weight of mice treated with the co-assembled hydrogel vaccines almost did not change,

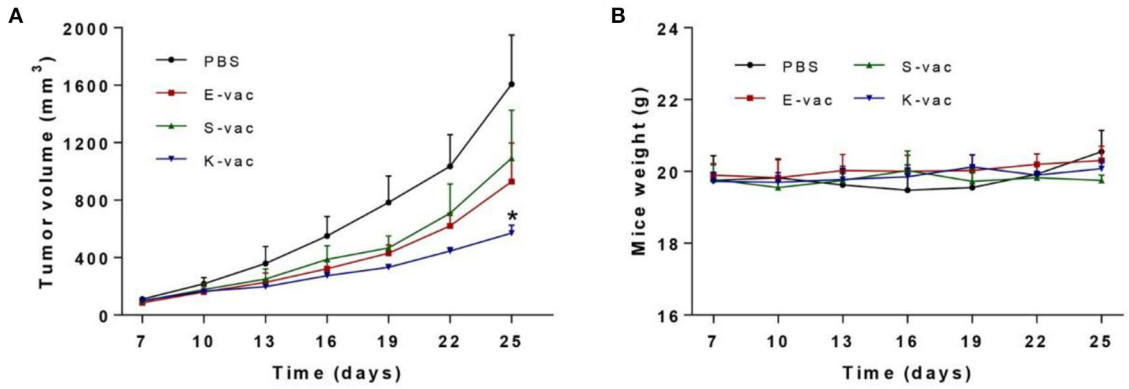

FIGURE 5 | (A) Immunotherapeutic effect of co-assembled hydrogel vaccines against E.G.7-OVA tumor. **(B)** The weight curve of mice during treatment. The asterisks represent the difference between the PBS group and the other group. $^*p < 0.05$.

suggesting stable therapeutic effect and good biocompatibility of co-assembled hydrogel vaccines.

CONCLUSION

In summary, we have developed a set of co-assembled hydrogel vaccines with different surface properties, which could induce high antibody production and potent anti-tumor immunoreaction. The incorporation of protein antigen promoted the formation of unified and denser nanofibers in the co-assembled hydrogels. The peptides in the three co-assembled hydrogels also adopted a similar β-sheet secondary structure. However, the co-assembled hydrogels were obviously different in mechanical properties. As compared with E-vac and S-vac, K-vac had a better mechanical property. The distinction also further affected the storage and release of antigen. Compared to aluminum adjuvant vaccine, all of them promoted the antibody production and cytokine expression to different degrees. Furthermore, these vaccines effectively inhibited E.G.7-OVA tumor growth *in vivo*. Especially the tumor inhibition rate of the mice treated with K-vac reached up to about 64%. Our results demonstrated that the co-assembled hydrogels could be viewed as effective vaccine delivery systems for antibody production and therapeutic tumor vaccine development, and different immune effects can be acquired by tuning the surface properties of self-assembling peptides.

DATA AVAILABILITY STATEMENT

The original contributions generated in the study are included in the article/**Supplementary Materials**, further inquiries can be directed to the corresponding authors.

ETHICS STATEMENT

The animal study was reviewed and approved by Animal Experiments and Ethics Review Committee of Institute of Radiation Medicine, Chinese Academy of Medical Sciences.

AUTHOR CONTRIBUTIONS

ZW conceived and designed the project. JL supervised this project. ZW and YS conducted the experiments, analyzed experimental data, and performed *in vivo* mice test. CR performed the statistical analysis. ZW and CR wrote the manuscript, and all authors discussed the results and proofread this paper. All authors contributed to the article and approved the submitted version.

FUNDING

This work was supported by NSFC (81722026, 31900998, and 81971731), the CAMS Innovation Fund for Medical Sciences (CIFMS, 2016-I2M-3-022), the Non-profit Central Research Institute Fund of Chinese Academy of Medical Sciences (2018PT35031), the Science Foundation for Distinguished Young Scholars of Tianjin (18JCJQJC47300), and the Drug Innovation Major Project (2018ZX09711-001).

SUPPLEMENTARY MATERIAL

The Supplementary Material for this article can be found online at: https://www.frontiersin.org/articles/10.3389/fchem.2020.00500/full#supplementary-material

REFERENCES

Bachmann, M. F., and Jennings, G. T. (2010). Vaccine delivery: a matter of size, geometry, kinetics and molecular patterns. *Nat. Rev. Immunol.* 10, 787–796. doi: 10.1038/nri2868

Bera, S., Xue, B., Rehak, P., Jacoby, G., Ji, W., Shimon, L. J., et al. (2020). Self-assembly of aromatic amino acid enantiomers into supramolecular materials of high rigidity. *ACS Nano* 14, 1694–1706. doi: 10.1021/acsnano.9b07307

Cai, J., Wang, H., Wang, D., and Li, Y. (2019). Improving cancer vaccine efficiency by nanomedicine. *Adv. Biosyst.* 3:1800287. doi: 10.1002/adbi.201800287

Chen, C. H., Palmer, L. C., and Stupp, S. I. (2018). Self-repair of structure and bioactivity in a supramolecular nanostructure. *Nano Lett.* 18, 6832–6841. doi: 10.1021/acs.nanolett.8b02709

Du, X., Zhou, J., Shi, J., and Xu, B. (2015). Supramolecular hydrogelators and hydrogels: from soft matter to molecular biomaterials. *Chem. Rev.* 115, 13165–13307. doi: 10.1021/acs.chemrev.5b00299

Feng, X., Xu, W., Li, Z., Song, W., Ding, J., and Chen, X. (2019). Immunomodulatory nanosystems. *Adv. Sci.* 6:1900101. doi: 10.1002/advs.201900101

Hudalla, G. A., Sun, T., Gasiorowski, J. Z., Han, H., Tian, Y. F., Chong, A. S., et al. (2014). Gradated assembly of multiple proteins into supramolecular nanomaterials. *Nat. Mater.* 13, 829–836. doi: 10.1038/nmat3998

Irvine, D. J., Hanson, M. C., Rakhra, K., and Tokatlian, T. (2015). Synthetic nanoparticles for vaccines and immunotherapy. *Chem. Rev.* 115, 11109–11146. doi: 10.1021/acs.chemrev.5b00109

Keskin, D. B., Anandappa, A. J., Sun, J., Tirosh, I., Mathewson, N. D., Li, S., et al. (2019). Neoantigen vaccine generates intratumoral T cell responses in phase Ib glioblastoma trial. *Nature* 565, 234–239. doi: 10.1038/s41586-018-0792-9

Luo, Z., Wu, Q., Yang, C., Wang, H., He, T., Wang, Y., et al. (2017). A powerful CD8+ T-cell stimulating D-tetra-peptide hydrogel as a very promising vaccine adjuvant. *Adv. Mater.* 29:1601776. doi: 10.1002/adma.201601776

Melief, C. J. (2018). Smart delivery of vaccines. *Nat. Mater.* 17, 482–483. doi: 10.1038/s41563-018-0085-6

Melief, C. J., van Hall, T., Arens, R., Ossendorp, F., and van der Burg, S. H. (2015). Therapeutic cancer vaccines. *J. Clin. Invest.* 125, 3401–3412. doi: 10.1172/JCI80009

Min, Y., Roche, K. C., Tian, S., Eblan, M. J., McKinnon, K. P., Caster, J. M., et al. (2017). Antigen-capturing nanoparticles improve the abscopal effect and cancer immunotherapy. *Nat. Nanotechnol.* 12, 877–882. doi: 10.1038/nnano.2017.113

Ott, P. A., Hu, Z., Keskin, D. B., Shukla, S. A., Sun, J., Bozym, D. J., et al. (2017). An immunogenic personal neoantigen vaccine for patients with melanoma. *Nature* 547, 217–221. doi: 10.1038/nature22991

Ren, C., Song, Z., Zheng, W., Chen, X., Wang, L., Kong, D., et al. (2011). Disulfide bond as a cleavable linker for molecular self-assembly and hydrogelation. *Chem. Commun.* 47, 1619–1621. doi: 10.1039/C0CC04135A

Ren, C., Wang, Z., Wang, Q., Yang, C., and Liu, J. (2019). Self-assembled peptide-based nanoprobes for disease theranostics and disease-related molecular imaging. *Small Methods* 4:900403. doi: 10.1002/smtd.201900403

Rodell, C. B., Arlauckas, S. P., Cuccarese, M. F., Garris, C. S., Li, R., Ahmed, M. S., et al. (2018). TLR7/8-agonist-loaded nanoparticles promote the polarization of tumour-associated macrophages to enhance cancer immunotherapy. *Nat. Biomed. Eng.* 2, 578–588. doi: 10.1038/s41551-018-0236-8

Romero, P., Banchereau, J., Bhardwaj, N., Cockett, M., Disis, M. L., Dranoff, G., et al. (2016). The Human Vaccines Project: a roadmap for cancer vaccine development. *Sci. Transl. Med.* 8, 334–339. doi: 10.1126/scitranslmed.aaf0685

Rudra, J. S., Tian, Y. F., Jung, J. P., and Collier, J. H. (2010). A self-assembling peptide acting as an immune adjuvant. *Proc. Natl. Acad. Sci. U.S.A.* 107, 622–627. doi: 10.1073/pnas.0912124107

Sahin, U., Derhovanessian, E., Miller, M., Kloke, B. P., Simon, P., Löwer, M., et al. (2017). Personalized RNA mutanome vaccines mobilize poly-specific therapeutic immunity against cancer. *Nature* 547, 222–226. doi: 10.1038/nature23003

Shang, Y., Wang, Z., Zhang, R., Li, X., Zhang, S., Gao, J., et al. (2019a). A novel thermogel system of self-assembling peptides manipulated by enzymatic dephosphorylation. *Chem. Commun.* 55, 5123–5126. doi: 10.1039/C9CC00401G

Shang, Y., Zhi, D., Feng, G., Wang, Z., Mao, D., Guo, S., et al. (2019b). Supramolecular nanofibers with superior bioactivity to insulin-like growth factor-I. *Nano Lett.* 19, 1560–1569. doi: 10.1021/acs.nanolett.8b04406

Shigemitsu, H., Fujisaku, T., Tanaka, W., Kubota, R., Minami, S., Urayama, K., et al. (2018). An adaptive supramolecular hydrogel comprising self-sorting double nanofibre networks. *Nat. Nanotechnol.* 13, 165–172. doi: 10.1038/s41565-017-0026-6

van der Burg, S. H., Arens, R., Ossendorp, F., van Hall, T., and Melief, C. J. (2016). Vaccines for established cancer: overcoming the challenges posed by immune evasion. *Nat. Rev. Cancer* 16, 219–233. doi: 10.1038/nrc.2016.16

Wang, H., Feng, Z., Qin, Y., Wang, J., and Xu, B. (2018). Nucleopeptide assemblies selectively sequester ATP in cancer cells to increase the efficacy of doxorubicin. *Angew. Chem. Int. Ed.* 57, 4931–4935. doi: 10.1002/anie.201712834

Wang, H., Feng, Z., Wang, Y., Zhou, R., Yang, Z., and Xu, B. (2016a). Integrating enzymatic self-assembly and mitochondria targeting for selectively killing cancer cells without acquired drug resistance. *J. Am. Chem. Soc.* 138, 16046–16055. doi: 10.1021/jacs.6b09783

Wang, H., Luo, Z., Wang, Y., He, T., Yang, C., Ren, C., et al. (2016b). Enzyme-catalyzed formation of supramolecular hydrogels as promising vaccine adjuvants. *Adv. Funct. Mater.* 26, 1822–1829. doi: 10.1002/adfm.201505188

Wang, H., Wang, Y., Zhang, X., Hu, Y., Yi, X., Ma, L., et al. (2015). Supramolecular nanofibers of self-assembling peptides and proteins for protein delivery. *Chem. Commun.* 51, 14239–14242. doi: 10.1039/C5CC03835A

Wang, Z., Liang, C., Shi, F., He, T., Gong, C., Wang, L., et al. (2017). Cancer vaccines using supramolecular hydrogels of NSAID-modified peptides as adjuvants abolish tumorigenesis. *Nanoscale* 9, 14058–14064. doi: 10.1039/C7NR04990K

Wang, Z., Ma, C., Shang, Y., Yang, L., Zhang, J., Yang, C., et al. (2020a). Simultaneous co-assembly of fenofibrate and ketoprofen peptide for the dual-targeted treatment of nonalcoholic fatty liver disease (NAFLD). *Chem. Commun.* 56, 4922–4925. doi: 10.1039/D0CC00513D

Wang, Z., Shang, Y., Tan, Z., Li, X., Li, G., Ren, C., et al. (2020b). A supramolecular protein chaperone for vaccine delivery. *Theranostics* 10, 657–670. doi: 10.7150/thno.39132

Wen, Y., Waltman, A., Han, H. F., and Collier, J. H. (2016). Switching the immunogenicity of peptide assemblies using surface properties. *ACS Nano* 10, 9274–9286. doi: 10.1021/acsnano.6b03409

Yang, C., Hu, F., Zhang, X., Ren, C., Huang, F., Liu, J., et al. (2020). Combating bacterial infection by *in situ* self-assembly of AIEgen-peptide conjugate. *Biomaterials* 244:119972. doi: 10.1016/j.biomaterials.2020.119972

Yang, C., Ren, C., Zhou, J., Liu, J., Zhang, Y., Huang, F., et al. (2017). Dual fluorescent- and isotopic-labelled self-assembling vancomycin for *in vivo* imaging of bacterial infections. *Angew. Chem. Int. Ed.* 56, 2356–2360. doi: 10.1002/anie.201610926

Yang, C., Shi, F., Li, C., Wang, Y., Wang, L., and Yang, Z. (2018). Single dose of protein vaccine with peptide nanofibers as adjuvants elicits long-lasting antibody titer. *ACS. Biomater. Sci. Eng.* 4, 2000–2006. doi: 10.1021/acsbiomaterials.7b00488

Yang, C., Wang, Z., Ou, C., Chen, M., Wang, L., and Yang, Z. (2014). A supramolecular hydrogelator of curcumin. *Chem. Commun.* 50, 9413–9415. doi: 10.1039/C4CC03139C

Yuan, C., Ji, W., Xing, R., Li, J., Gazit, E., and Yan, X. (2019). Hierarchically oriented organization in supramolecular peptide crystals. *Nat. Rev. Chem.* 3, 567–588. doi: 10.1038/s41570-019-0129-8

Conflict of Interest: The authors declare that the research was conducted in the absence of any commercial or financial relationships that could be construed as a potential conflict of interest.

frontiers in Chemistry

MINI REVIEW
published: 22 July 2020
doi: 10.3389/fchem.2020.00549

Tumor Microenvironment–Responsive Peptide-Based Supramolecular Drug Delivery System

Wenbo Zhang[1], *Lanlan Yu*[1], *Tianjiao Ji*[2]* *and Chenxuan Wang*[1]*

[1] State Key Laboratory of Medical Molecular Biology, Department of Biophysics and Structural Biology, Peking Union Medical College, Institute of Basic Medical Sciences, Chinese Academy of Medical Sciences, Beijing, China, [2] Laboratory for Biomaterials and Drug Delivery, Department of Anesthesiology, Boston Children's Hospital, Harvard Medical School, Boston, MA, United States

Physical and biochemical differences between tumor tissues and normal tissues provide promising triggering factors that can be utilized to engineer stimuli-responsive drug delivery platforms for cancer treatment. Rationally designed peptide-based supramolecular architectures can perform structural conversion by responding to the tumor microenvironment and achieve the controlled release of antitumor drugs. This mini review summarizes recent approaches for designing internal trigger-responsive drug delivery platforms using peptide-based materials. Peptide assemblies that exhibit a stimuli-responsive structural conversion upon acidic pH, high temperature, high oxidative potential, and the overexpressed proteins in tumor tissues are emphatically introduced. We also discuss the challenges of current peptide-based supramolecular delivery platforms against cancer.

Keywords: peptide, supramolecular assembly, stimuli–response, drug delivery, tumor microenvironment

OPEN ACCESS

Edited by:
Suying Xu,
Beijing University of Chemical Technology, China

Reviewed by:
Lei Feng,
Dalian Medical University, China
Tangxin Xiao,
Changzhou University, China

***Correspondence:**
Tianjiao Ji
tianjiao.ji@childrens.harvard.edu
Chenxuan Wang
wangcx@ibms.pumc.edu.cn

Specialty section:
This article was submitted to Supramolecular Chemistry, a section of the journal Frontiers in Chemistry

Received: *20 April 2020*
Accepted: *28 May 2020*
Published: *22 July 2020*

Citation:
Zhang W, Yu L, Ji T and Wang C (2020) Tumor Microenvironment–Responsive Peptide-Based Supramolecular Drug Delivery System. Front. Chem. 8:549. doi: 10.3389/fchem.2020.00549

INTRODUCTION

The clinical efficacy and outcome of conventional molecular chemotherapeutics against tumors are limited by several undesirable properties, including the poor solubility, the short half-life *in vivo*, the weak penetration capability, and the low specificity (Tang et al., 2014; Liu et al., 2016; Wang et al., 2017, 2018; Luo et al., 2019). To overcome these drawbacks of conventional cancer chemotherapeutics, various nanoparticle-based drug delivery systems (DDSs) have been developed (Versluis et al., 2016; Gerbelli et al., 2019; Xiao et al., 2019b). Ingeniously designed DDSs can improve the bioavailability of drugs and/or minimize the adverse effects of drugs on normal tissues (Liu et al., 2016; Wang et al., 2017). Currently, there are a diverse range of nanoscale carriers to meet different practical requirements, including inorganic nanoparticles (e.g., silica nanoparticles, quantum dots, gold nanoparticles, carbon-based, and magnetic iron oxide–based nanostructures), synthetic organic nanoparticles (e.g., polymer-based nanostructures and dendrimers), and bio-original nanomaterials (e.g., lipid-based nanoparticles, peptide assemblies, protein cages, exosomes, and DNA origami) (Li et al., 2017). Among these, peptide-based supramolecular nanostructures are an important type of carriers for drug delivery because of the following reasons: (i) the unique biochemical functionality encoded by peptide sequences enables an active targeting (i.e., peptides are targeted to receptors that are overexpressed on cancer cells) or cell membrane–penetrating processes (Wei et al., 2013; Kebebe et al., 2018); (ii) the structure of peptide assembly can be programmatically modulated by intrinsic or/and external stimuli to achieve a controllable release of

the payload into the target region (Wei et al., 2013; Raza et al., 2019); (iii) peptides are biocompatible compared to the synthetic organic compounds; (iv) solid-phase synthesis benefits peptide synthesis with the simplicity of operation; (v) the reactive terminus or/and side chains of peptides can be used as a reactive site to conjugate chemotherapeutics (Wyatt et al., 2017; An et al., 2019).

The distinct physical and biochemical characteristics of tumors differing from normal tissues provide promising targets for engineering stimuli–response peptide-assembled DDSs (Ji et al., 2013; Raza et al., 2019; Xiao et al., 2019a; Lian and Ji, 2020). Several hallmarks can be utilized as the triggers to construct stimuli–response DDSs: (i) Acidosis. The overproduction of lactic acid generated by the enhanced glycolysis in tumor cells leads to a slightly acidic tumor microenvironment, i.e., pH 6.5 to 6.8, which is lower than the pH of normal tissues around 7.4 (Romero-Garcia et al., 2011; Ji et al., 2013). (ii) High local temperature. The intrinsic pyrogenic substances secreted by tumor cells induce distinct hyperthermia in the temperature range of 37 to 42°C (Danhier et al., 2010). Typical pyrogenic substances include, inflammatory cytokines, serotonin, catecholamine, and so on. (iii) Redox imbalance. The activation of oncogenes in tumor cells alters the expression and assembly of mitochondrial electron transport chain enzymes and causes a hyperactive reactive oxygen species (ROS) production (Purohit et al., 2019). (iv) Overexpression of certain enzymes such as, the fibroblast-activation protein-α (FAP-α) expressed by cancer-associated fibroblasts (CAFs) (Kalluri and Zeisberg, 2006; Tlsty and Coussens, 2006; Erez et al., 2010; Ji et al., 2013) and matrix metalloproteinases (MMPs) secreted by tumor-associated inflammatory cells in the extracellular matrix (Lu et al., 2012; Ji et al., 2013).

We review recent approaches to the development of stimuli–response self-assembled peptide-based materials that exhibit promising therapeutic effects to deliver drugs to tumor vasculature or tumor cells. The pH, temperature, redox potential, and overexpressed proteins accumulated in tumor cells or tumor microenvironment serve as stimuli to trigger the switch of peptide assemblies. Such sensitive structural conversion of the peptide-assembled delivery systems executes controlling drug release and the intracellular uptake/penetration.

pH-RESPONSIVE PLATFORMS

Peptides that spontaneously undergo morphological transitions in response to the slightly acidic microenvironments of tumor tissues have the potential to amplify the accumulation of agents used in drug delivery and medical imaging. One method of designing this pH-responsive peptide is using the acidic pH of the solution to toggle the ionic side chains between their charged and neutral states and lead to a structural change driven by the change in charge attractions or repulsions. For example, the pH (low) insertion peptides (pHLIP) derived from the C-helix of a membrane protein bacteriorhodopsin are applied for targeting acidic tissues. The deprotonated side chains of aspartic acid and glutamic acid interspersed throughout the hydrophobic middle region and the C-terminal are negatively charged at physiological pH (pH 7.4), which contributes to an equilibrium between the solvated state and the membrane-attached state of the pHLIP (Reshetnyak et al., 2007). In the acidic environment (pH <6.8), the side chains of aspartic acid and glutamic acid are protonated; the hydrophobicity of pHLIP is increased because the hydration free energy of carboxylic acid (propionic acid, −27 kJ/mol) is less than that of carboxylate (propionate, −331 kJ/mol). The protonated pHLIP inserts into the cell membrane and forms a transmembrane helix. In the membrane-inserted state, pHLIP is oriented with the C-terminus located in the cytosol and the N-terminus exposed to the extracellular space (Wyatt et al., 2018). Cargo molecules can be covalently conjugated with the N-terminus (e.g., fluorescent or radioactive labels) or/and the C-terminus (e.g., translocating cargos) (a cleavable linker is usually needed when conjugating the cargo to the C-terminus). Thus, pHLIP and its derivatives exhibit a wide range of promising applications including intracellular delivery of therapeutic agents (An et al., 2010; Yao et al., 2013; Burns et al., 2015) and fluorescence-guided surgery and imaging (Reshetnyak et al., 2011; Adochite et al., 2014; Tapmeier et al., 2015; Golijanin et al., 2016), as well as diagnostic nuclear imaging (Macholl et al., 2012; Demoin et al., 2016) (**Figure 1A**). One of the most attractive applications of pHLIP is its ability to facilitate the translocation of cyclic toxins, such as, amanitin, phalloidin, and phallacidin from *Amanita phalloides*, across the lipid bilayer to reach the cytoplasmic targets (An et al., 2010; Wijesinghe et al., 2011). The extracellular delivery of polar cargos expands the drug pipeline and benefits the clinical trial of drug candidates that exhibit promising activity but are too polar by normal drug criteria. Besides pHLIP, the design strategy that the weak acidity of solution switches the charge state of peptides has been implemented to create a series of pH-responsive DDSs, such as, pH-sensitive polyhistidine (PolyHis) (Zhao et al., 2012, 2016) and collagens (Xu et al., 2016; Yang et al., 2017; Yao et al., 2019).

Another strategy to construct pH-responsive peptide DDSs is to introduce an acid-active protecting group into the charged side chains of a peptide. When the peptide is encountering acidic media, the protecting group is removed by acid and converts peptide structure. For example, the positively charged lysine side chains within a cell-penetrating peptide, transactivator of transcription (TAT), can be amidized to be neutral succinyl amides (^{a}TAT) (Jin et al., 2013). At physiological pH, the amidized modification of lysine side chains efficiently reduces the non-specific interactions between ^{a}TAT and cell membranes. The ^{a}TAT-functionalized PEG-PCL micelles (where PEG presents polyethylene glycol, and PCL presents poly ε-caprolactone) loaded with doxorubicin showed a long circulation time in the blood compartment. Once the micelles extravasated from the bloodstream into an acidic environment (tumor tissues or endosomes/lysosomes), the succinyl amides in the ^{a}TAT were quickly hydrolyzed (Helmlinger et al., 1997), leading to a fast intracellular uptake/penetration of the nanoparticles.

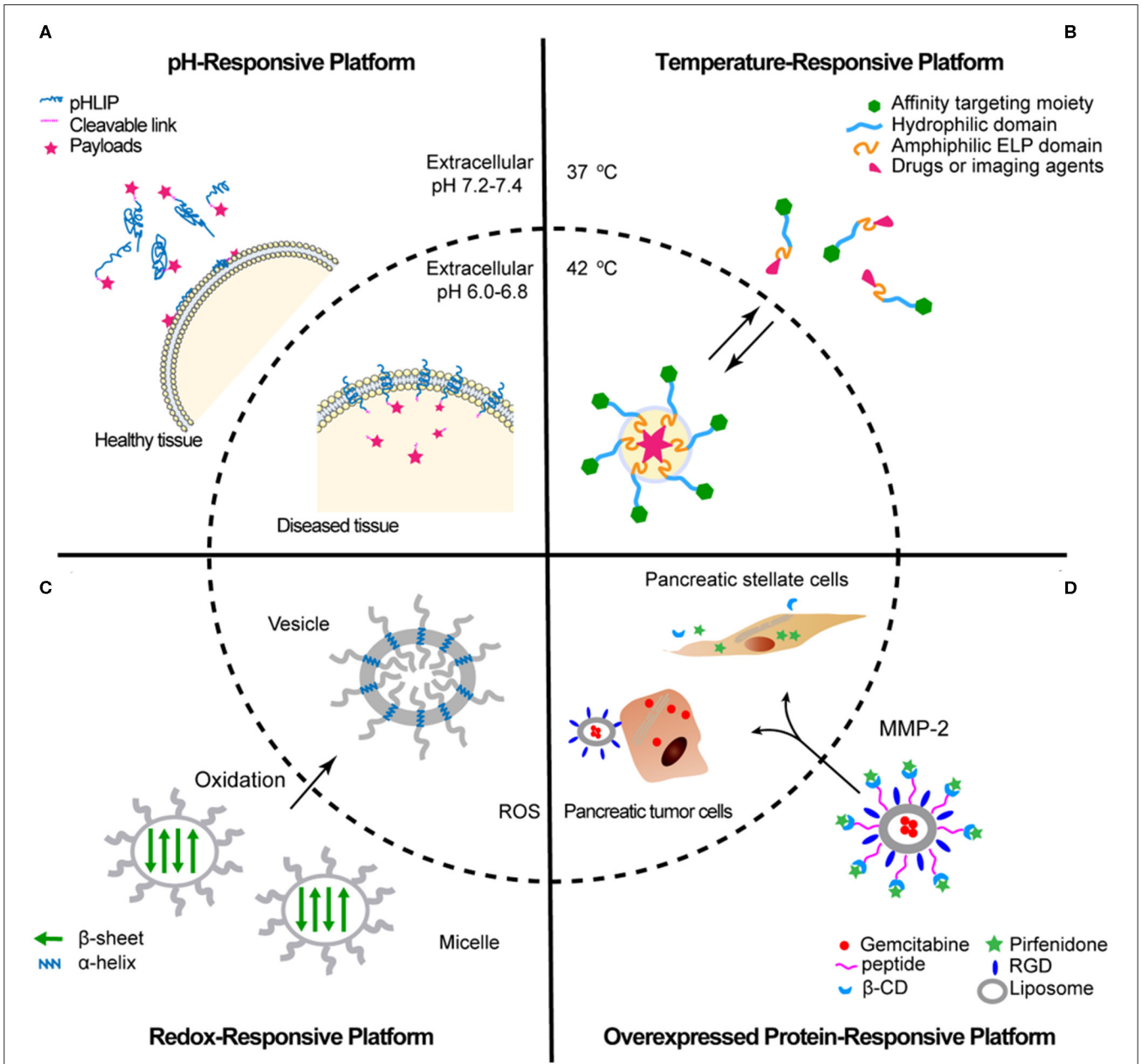

FIGURE 1 | Schematic representations of peptide in response to the acidic pH **(A)**, high temperature **(B)**, the high oxidative potential **(C)**, and the overexpressed protein MMP-2 **(D)**.

TEMPERATURE-RESPONSIVE PLATFORMS

Hydrophobic interactions, which are encoded by amino acid composition and the non-polar domain size, determine the tertiary and quaternary structure stability and guide the temperature-dependence of peptide assembly (Li and Walker, 2012; Davis et al., 2013). Specifically, the temperature dependence of hydrophobic hydration energy is positive when the size of the non-polar solute is smaller than 1 nm. In contrast, the temperature dependence is negative when the size of the non-polar solute is larger than 1 nm (Li and Walker, 2012; Davis et al., 2013). This analysis provides a theoretical basis for understanding the temperature-triggered assembly structural transition. For example, elastin-like polypeptide (ELP) is a set of commonly used thermally active biopolymers consisting of repeats of VPGXG (where X can be any amino acid except proline) (Urry, 1992). The hydrodynamic diameter of each non-polar patch within an ELP is smaller than 1 nm. Thus, ELPs display a facilitated hydrophobic aggregation upon

heating; i.e., a phase transition occurs from clear solution to insoluble aggregate as the temperature increases from below their transition temperature (T_t) to above their T_t (Urry, 1992; Urry and Pattanaik, 1997; Li et al., 2001). Herein, the T_t of the polypeptide is a function of residue composition, residue arrangement, biopolymer persistence length, molecular concentration, and coexisted molecules (Meyer and Chilkoti, 2002, 2004). Usually, the T_t of the polypeptide is designed to be in the temperature range of hyperthermia (ca. 38–42°C).

By using ELP as a skeleton, thermally triggered peptide delivery systems were usually designed as a diblock copolymer consisting of an amphiphilic ELP domain and a hydrophilic domain to covalently tether chemotherapeutic compound (Dreher et al., 2008; McDaniel et al., 2013). In normal tissues, where the physiological temperature is 37°C, chimeric peptides stay in a freely monomeric state. In tumor regions, where the local temperature is >37°C exceeding T_t, the amphiphilic ELP domains assemble to a micelle, and the hydrophilic domains act as linkers to expose the affinity targeting moieties on the outside surface of the micelle (**Figure 1B**). This feature leads to chimeric peptide–drug complex aggregation and accumulation in tumor tissues by hyperthermia.

REDOX-RESPONSIVE PLATFORMS

Excess production of ROS by tumor cells results in pathological stress to cells and tissues, including essential protein damage, lipid peroxidation, DNA strand breakage, and so on (Darley-Usmar and Halliwell, 1996). In terms of protein structure, the thiol groups of cysteine (Cys, C) side chains are attractive oxidative targets for chemical modification by ROS, such as, hydrogen peroxide (H_2O_2). The fluctuation in the non-covalent interactions associated with the oxidization of cysteine can lead to the emergence of changed protein tertiary and quaternary structures. This observation motivates researchers to design redox-stimulated peptide assemblies by using cysteine or cysteine derivative as a ROS sensor. In their systems, a change in the intermolecular interactions encoded by cysteine, which results from the presence of ROS, is amplified into a range of structural outputs. For instance, cholesterol-decorated peptide PEG-PCys-Chol adopted an antiparallel β-sheet conformation and assembled into micelles in solution (where PEG presents polyethylene glycol, PCys presents polyC, and Chol presents cholesterol) (Liu et al., 2018). After treatment with 10% H_2O_2 in the presence of 5% acetic, the side chains of polyC were oxidized. The oxidation of PEG-PCYs-Chol (PEG-PCys-Chol-O_2) adopted a helical conformation and displayed a micelle-to-vesicle structural transformation (**Figure 1C**). The oxidized PEG-PCys-Chol-O_2 vesicle exhibited a strong potency to deliver a model chemotherapeutic agent doxorubicin (DOX) into HeLa tumor cells. In contrast, HeLa cells were inert to the reductive PEG-PCys-Chol/DOX micelle. The high internalization efficiency of PEG-PCys-Chol-O_2/DOX is due to the cholesterol-bearing α-helical structure that facilitates cell membrane penetration (Kulkarni et al., 2012; Yin et al., 2013; Sevimli et al., 2015). Collectively, this effort demonstrates a strategy of triggering a controllable release of cargos by hyperactive ROS in tumor tissues.

OVEREXPRESSED PROTEIN-RESPONSIVE PLATFORMS

Overexpressed proteins within tumor tissues provide specific binding targets for recruiting drug/delivery systems to improve the bioavailability of drugs (Kalluri and Zeisberg, 2006; Tlsty and Coussens, 2006; Erez et al., 2010; Sagnella et al., 2014). Biocatalysis-dependent delivery systems that target these characteristic proteins were delicately designed. The system usually contains two functional moieties: a sensor moiety that acts as an enzyme substrate and a cohesion moiety that drives peptide to assembly. Thus, the process of biocatalysis-dependent recognition involves an enzyme-mediated change with peptide assembly structures.

For example, FAP-α is selectively overexpressed by CAFs, the predominant cell type in the tumor stroma. Several stimuli-responsive nanostructures for drug delivery and release have been constructed inspired by the catalytic function of FAP-α. Ji et al. (2016b) designed a biocatalytic amphiphilic peptide Ac-ATK(C_{18})DATGPAK(C_{18})TA-NH_2 (where C_{18} represents an octadecanoic acid chain) that exhibited morphological changes mediated by FAP-α. The moiety of -GPAX- is a specific cleavage substrate of FAP-α, and the moieties of -ATK(C_{18})- and -(C_{18})TA- provide hydrophobic attractions for peptide assembly (Ji et al., 2016b). In water environment, hydrophobic drug Dox coassembled with Ac-ATK(C_{18})DATGPAK(C_{18})TA-NH_2 to form spherical nanoparticles. When interacting with CAFs, nanoparticles disassembled rapidly under FAP-α's cleavage and efficiently released DOX specifically at the tumor sites. Thus, the peptide assemblies could enhance the drug perfusion in solid tumor treatment.

Similarly, the diverse chemokines, cytokines, and matrix-degrading enzymes secreted by tumor-associated inflammatory cells, such as, MMPs, are also promising targets for the design of an enzyme-active peptide-based delivery system. Ji et al. (2016a) developed an MMP-2–sensitive peptide linker CSSSGPLG-IAGQSSS to tether (i) a gemcitabine/RGD (tumor cell–binding peptide) loaded liposome and (ii) a pirfenidone-loaded β-cyclodextrin (β-CD) (**Figure 1D**). This peptide–β-CD–liposome supramolecular architecture was cleaved into two active units when they reached the tumor tissues to exert a synergy effect against pancreatic tumor: (i) The gemcitabine/RGD-loaded liposome unit targeted and directly killed pancreatic tumor cells. (ii) The β-CD–pirfenidone unit was maintained in the tumor stroma to down-regulate the fibrosis and decrease the stromal barrier.

CONCLUSION AND CHALLENGES

In summary, we present a brief overview of the strategies available to the rational design of peptide-assembled agent delivery nanoplatforms. The architectures of peptide-based DDSs are precisely engineered to achieve active drug transportations

and release upon tumor microenvironment stimuli, including pH, temperature, redox potential, and tumor-associated overexpressed proteins. Despite the promising activity, there still exist challenges that limit the application of stimuli-responsive peptide-based nanomaterials in tumor treatment.

(i) High interstitial fluid pressure in most solid tumors impedes the penetration of compounds and delivery systems (Heldin et al., 2004). The reasons for increased interstitial fluid pressure probably involve blood-vessel leakiness, lymph-vessel abnormalities, interstitial fibrosis, and a contraction of the interstitial space mediated by stromal fibroblasts. High-molecular-weight compounds, such as, peptide assemblies, are transported in the interstitium mainly via convection rather than via diffusion (Heldin et al., 2004; An et al., 2019). Thus, a high interstitial fluid pressure induces a reduction of transcapillary transport and weakens the streaming of therapeutic drugs and delivery platforms from the circulation system through the interstitial space. Some of the cytokine antagonists, such as, vascular endothelial cell growth factor antagonist and platelet-derived growth factor (PDGF) antagonist, can be applied to lower tumor interstitial fluid pressure and facilitate the cellular uptake of drugs. However, it is still a challenge to reduce the interstitial fluid pressure of tumors without affecting normal tissues (Heldin et al., 2004). In addition, drugs or drug-loaded supramolecules that self-assemble *in situ* and exhibit high retention efficiency in the specific tumor tissues also provide a promising solution for overcoming the high interstitial fluid pressure obstacle to adequate drug delivery (Gao et al., 2013; An et al., 2019), but these studies are still in the preliminary stage of exploration.

(ii) Advanced methodologies and technologies are required to track the fate of stimuli-responsive peptide-based DDSs *in vivo* (Kreyling et al., 2015; Chen et al., 2017). Recent *in vivo* studies with a few numbers of nanosystems indicate that the surface chemistry, the corona of adsorbed proteins, and integrity of assembly nanostructures can be dramatically degraded by enzymes and immune cells and consequently change the pharmacokinetics, biodistribution, and immunological effects of drug carriers (Kreyling et al., 2015; Chen et al., 2017). It is important to investigate whether the stimuli response of peptide-based DDSs *in vitro* can be manifested *in vivo*. However, such measurement is challenging because of the lack of a feasible analytical instrument or methodology to reveal the structural transitions of peptide-based DDSs *in vivo*. Inspired by other nanomedicine research (Shan et al., 2018, 2019), some potential strategies are expected to solve this thorny problem, including high performance liquid chromatography measurement of plasma level of the loaded drugs, detection of specific overexpressing proteins/micromoles in the blood, and development of harmless tracer/probe. This research direction needs more efforts in the future.

(iii) The clinical evaluation of the stimuli-responsive peptide DDSs is absent because of the expensive and lengthy regulatory process (Jang et al., 2016). The behaviors of DDSs in human bodies might deviate from that in animal models as they possess different inherited characteristics (Jang et al., 2016). Innovative preclinical testing platforms, such as, patient-derived organoids, are needed to accurately evaluate the efficacy and safety of stimuli-responsive peptide-based DDSs before clinical trials (Tiriac et al., 2018; Saito et al., 2019).

Efforts to address the aforementioned challenges will substantially promote the medical application of stimuli–response peptide-assembled nanomaterials as a chemotherapeutics delivery platform and finally benefit cancer treatment in the clinic.

AUTHOR CONTRIBUTIONS

All authors listed have made a substantial, direct and intellectual contribution to the work, and approved it for publication.

FUNDING

This work was funded by CAMS Innovation Fund for Medical Sciences (2018-I2M-3-006), the National Natural Science Foundation of China (31901007), the Fundamental Research Funds for the Central Universities (2018PT31028), the Open Project Fund provided by Key Laboratory for Biomedical Effects of Nanomaterials and Nanosafety, CAS (NSKF201812), and State Key Laboratory Special Fund 2060204.

REFERENCES

Adochite, R. C., Moshnikova, A., Carlin, S. D., Guerrieri, R. A., Andreev, O. A., Lewis, J. S., et al. (2014). Targeting breast tumors with pH (low) insertion peptides. *Mol. Pharm.* 11, 2896–2905. doi: 10.1021/mp5002526

An, H. W., Li, L. L., Wang, Y., Wang, Z., Hou, D., Lin, Y. X., et al. (2019). A tumour-selective cascade activatable self-detained system for drug delivery and cancer imaging. *Nat. Commun.* 10, 4861. doi: 10.1038/s41467-019-12848-5

An, M., Wijesinghe, D., Andreev, O. A., Reshetnyak, Y. K., and Engelman, D. M. (2010). pH-(low)-insertion-peptide (pHLIP) translocation of membrane impermeable phalloidin toxin inhibits cancer cell proliferation. *Proc. Natl. Acad. Sci. U.S.A.* 107, 20246–20250. doi: 10.1073/pnas.1014403107

Burns, K. E., Robinson, M. K., and Thevenin, D. (2015). Inhibition of cancer cell proliferation and breast tumor targeting of pHLIP-monomethyl auristatin E conjugates. *Mol. Pharm.* 12, 1250–1258. doi: 10.1021/mp500779k

Chen, F., Wang, G., Griffin, J. I., Brenneman, B., Banda, N. K., Holers, V. M., et al. (2017). Complement proteins bind to nanoparticle protein corona and undergo dynamic exchange *in vivo*. *Nat. Nanotechnol.* 12, 387–393. doi: 10.1038/nnano.2016.269

Danhier, F., Feron, O., and Preat, V. (2010). To exploit the tumor microenvironment: passive and active tumor targeting of nanocarriers for anti-cancer drug delivery. *J. Control. Release* 148, 135–146. doi: 10.1016/j.jconrel.2010.08.027

Darley-Usmar, V., and Halliwell, B. (1996). Blood radicals: Reactive nitrogen species, reactive oxygen species, transition metal ions, and the vascular system. *Pharm. Res.* 13, 649–662. doi: 10.1023/A:1016079012214

Davis, J. G., Rankin, B. M., Gierszal, K. P., and Ben-Amotz, D. (2013). On the cooperative formation of non-hydrogen-bonded water at molecular hydrophobic interfaces. *Nat. Chem.* 5, 796–802. doi: 10.1038/nchem.1716

Demoin, D. W., Wyatt, L. C., Edwards, K. J., Abdel-Atti, D., Sarparanta, M., Pourat, J., et al. (2016). PET imaging of extracellular pH in tumors with ^{64}Cu- and ^{18}F-labeled pHLIP peptides: a structure-activity optimization study. *Bioconjug. Chem.* 27, 2014–2023. doi: 10.1021/acs.bioconjchem.6b00306

Dreher, M. R., Simnick, A. J., Fischer, K., Smith, R. J., Patel, A., Schmidt, M., et al. (2008). Temperature triggered self-assembly of polypeptides into multivalent spherical micelles. *J. Am. Chem. Soc.* 130, 687–694. doi: 10.1021/ja0764862

Erez, N., Truitt, M., Olson, P., Arron, S. T., and Hanahan, D. (2010). Cancer-associated fibroblasts are activated in incipient neoplasia to orchestrate tumor-promoting inflammation in an NF-kappaB-dependent manner. *Cancer Cell* 17, 135–147. doi: 10.1016/j.ccr.2009.12.041

Gao, Y., Berciu, C., Kuang, Y., Shi, J., Nicastro, D., and Xu, B. (2013). Probing nanoscale self-assembly of nonfluorescent small molecules inside live mammalian cells. *ACS Nano* 7, 9055–9063. doi: 10.1021/nn403664n

Gerbelli, B. B., Vassiliades, S. V., Rojas, J. E. U., Pelin, J. N. B. D., Mancini, R. S. N., Pereira, W. S. G., et al. (2019). Hierarchical self-assembly of peptides and its applications in bionanotechnology. *Macromol. Chem. Phys.* 220:1900085. doi: 10.1002/macp.201900085

Golijanin, J., Amin, A., Moshnikova, A., Brito, J. M., Tran, T. Y., Adochite, R. C., et al. (2016). Targeted imaging of urothelium carcinoma in human bladders by an ICG pHLIP peptide *ex vivo*. *Proc. Natl. Acad. Sci. U.S.A.* 113, 11829–11834. doi: 10.1073/pnas.1610472113

Heldin, C. H., Rubin, K., Pietras, K., and Ostman, A. (2004). High interstitial fluid pressure - an obstacle in cancer therapy. *Nat. Rev. Cancer* 4, 806–813. doi: 10.1038/nrc1456

Helmlinger, G., Yuan, F., Dellian, M., and Jain, R. K. (1997). Interstitial pH and pO_2 gradients in solid tumors *in vivo*: high-resolution measurements reveal a lack of correlation. *Nat. Med.* 3, 177–182. doi: 10.1038/nm0297-177

Jang, H. L., Zhang, Y. S., and Khademhosseini, A. (2016). Boosting clinical translation of nanomedicine. *Nanomedicine (Lond)* 11, 1495–1497. doi: 10.2217/nnm-2016-0133

Ji, T., Li, S., Zhang, Y., Lang, J., Ding, Y., Zhao, X., et al. (2016a). An MMP-2 responsive liposome integrating antifibrosis and chemotherapeutic drugs for enhanced drug perfusion and efficacy in pancreatic cancer. *ACS Appl. Mater. Interfaces* 8, 3438–3445. doi: 10.1021/acsami.5b11619

Ji, T., Zhao, Y., Ding, Y., and Nie, G. (2013). Using functional nanomaterials to target and regulate the tumor microenvironment: diagnostic and therapeutic applications. *Adv. Mater.* 25, 3508–3525. doi: 10.1002/adma.201300299

Ji, T., Zhao, Y., Ding, Y., Wang, J., Zhao, R., Lang, J., et al. (2016b). Transformable peptide nanocarriers for expeditious drug release and effective cancer therapy via cancer-associated fibroblast activation. *Angew. Chem. Int. Ed. Engl.* 55, 1050–1055. doi: 10.1002/anie.201506262

Jin, E., Zhang, B., Sun, X., Zhou, Z., Ma, X., Sun, Q., et al. (2013). Acid-active cell-penetrating peptides for *in vivo* tumor-targeted drug delivery. *J. Am. Chem. Soc.* 135, 933–940. doi: 10.1021/ja311180x

Kalluri, R., and Zeisberg, M. (2006). Fibroblasts in cancer. *Nat. Rev. Cancer* 6, 392–401. doi: 10.1038/nrc1877

Kebebe, D., Liu, Y., Wu, Y., Vilakhamxay, M., Liu, Z., and Li, J. (2018). Tumor-targeting delivery of herb-based drugs with cell-penetrating/tumor-targeting peptide-modified nanocarriers. *Int J Nanomedicine* 13, 1425–1442. doi: 10.2147/IJN.S156616

Kreyling, W. G., Abdelmonem, A. M., Ali, Z., Alves, F., Geiser, M., Haberl, N., et al. (2015). *In vivo* integrity of polymer-coated gold nanoparticles. *Nat. Nanotechnol.* 10, 619–623. doi: 10.1038/nnano.2015.111

Kulkarni, A., DeFrees, K., Hyun, S. H., and Thompson, D. H. (2012). Pendant polymer:Amino-beta-cyclodextrin:siRNA guest:Host nanoparticles as efficient vectors for gene silencing. *J. Am. Chem. Soc.* 134, 7596–7599. doi: 10.1021/ja300690j

Li, B., Alonso, D. O., Bennion, B. J., and Daggett, V. (2001). Hydrophobic hydration is an important source of elasticity in elastin-based biopolymers. *J. Am. Chem. Soc.* 123, 11991–11998. doi: 10.1021/ja010363e

Li, I. T., and Walker, G. C. (2012). Single polymer studies of hydrophobic hydration. *Acc. Chem. Res.* 45, 2011–2021. doi: 10.1021/ar200285h

Li, Z., Tan, S., Li, S., Shen, Q., and Wang, K. (2017). Cancer drug delivery in the nano era: an overview and perspectives (review). *Oncol. Rep.* 38, 611–624. doi: 10.3892/or.2017.5718

Lian, Z., and Ji, T. (2020). Functional peptide-based drug delivery systems. *J. Mater. Chem. B*. doi: 10.1039/D0TB00713G

Liu, D., Yang, F., Xiong, F., and Gu, N. (2016). The smart drug delivery system and its clinical potential. *Theranostics* 6, 1306–1323. doi: 10.7150/thno.14858

Liu, H., Wang, R., Wei, J., Cheng, C., Zheng, Y., Pan, Y., et al. (2018). Conformation-directed micelle-to-vesicle transition of cholesterol-decorated polypeptide triggered by oxidation. *J. Am. Chem. Soc.* 140, 6604–6610. doi: 10.1021/jacs.8b01873

Lu, P., Weaver, V. M., and Werb, Z. (2012). The extracellular matrix: A dynamic niche in cancer progression. *J. Cell Biol.* 196, 395–406. doi: 10.1083/jcb.201102147

Luo, Z., Dai, Y., and Gao, H. (2019). Development and application of hyaluronic acid in tumor targeting drug delivery. *Acta Pharm. Sin. B* 9, 1099–1112. doi: 10.1016/j.apsb.2019.06.004

Macholl, S., Morrison, M. S., Iveson, P., Arbo, B. E., Andreev, O. A., Reshetnyak, Y. K., et al. (2012). *In vivo* pH imaging with ^{99m}Tc-pHLIP. *Mol. Imaging Biol.* 14, 725–734. doi: 10.1007/s11307-012-0549-z

McDaniel, J. R., Bhattacharyya, J., Vargo, K. B., Hassouneh, W., Hammer, D. A., and Chilkoti, A. (2013). Self-assembly of thermally responsive nanoparticles of a genetically encoded peptide polymer by drug conjugation. *Angew. Chem. Int. Ed. Engl.* 52, 1683–1687. doi: 10.1002/anie.201200899

Meyer, D. E., and Chilkoti, A. (2002). Genetically encoded synthesis of protein-based polymers with precisely specified molecular weight and sequence by recursive directional ligation: Examples from the elastin-like polypeptide system. *Biomacromolecules* 3, 357–367. doi: 10.1021/bm015630n

Meyer, D. E., and Chilkoti, A. (2004). Quantification of the effects of chain length and concentration on the thermal behavior of elastin-like polypeptides. *Biomacromolecules* 5, 846–851. doi: 10.1021/bm034215n

Purohit, V., Simeone, D. M., and Lyssiotis, C. A. (2019). Metabolic regulation of redox balance in cancer. *Cancers (Basel)* 11:955. doi: 10.3390/cancers11070955

Raza, A., Rasheed, T., Nabeel, F., Hayat, U., Bilal, M., and Iqbal, H. M. N. (2019). Endogenous and exogenous stimuli-responsive drug delivery systems for programmed site-specific release. *Molecules* 24:1117. doi: 10.3390/molecules24061117

Reshetnyak, Y. K., Segala, M., Andreev, O. A., and Engelman, D. M. (2007). A monomeric membrane peptide that lives in three worlds: In solution, attached to, and inserted across lipid bilayers. *Biophys. J.* 93, 2363–2372. doi: 10.1529/biophysj.107.109967

Reshetnyak, Y. K., Yao, L., Zheng, S., Kuznetsov, S., Engelman, D. M., and Andreev, O. A. (2011). Measuring tumor aggressiveness and targeting metastatic lesions with fluorescent pHLIP. *Mol. Imaging Biol.* 13, 1146–1156. doi: 10.1007/s11307-010-0457-z

Romero-Garcia, S., Lopez-Gonzalez, J. S., Baez-Viveros, J. L., Aguilar-Cazares, D., and Prado-Garcia, H. (2011). Tumor cell metabolism: an integral view. *Cancer Biol. Ther.* 12, 939–948. doi: 10.4161/cbt.12.11.18140

Sagnella, S. M., McCarroll, J. A., and Kavallaris, M. (2014). Drug delivery: Beyond active tumour targeting. *Nanomedicine* 10, 1131–1137. doi: 10.1016/j.nano.2014.04.012

Saito, Y., Muramatsu, T., Kanai, Y., Ojima, H., Sukeda, A., Hiraoka, N., et al. (2019). Establishment of patient-derived organoids and drug screening for biliary tract carcinoma. *Cell Rep.* 27, 1265–1276 e1264. doi: 10.1016/j.celrep.2019.03.088

Sevimli, S., Sagnella, S., Macmillan, A., Whan, R., Kavallaris, M., Bulmus, V., et al. (2015). The endocytic pathway and therapeutic efficiency of doxorubicin conjugated cholesterol-derived polymers. *Biomater. Sci.* 3, 323–335. doi: 10.1039/C4BM00224E

Shan, L., Gao, G., Wang, W., Tang, W., Wang, Z., Yang, Z., et al. (2019). Self-assembled green tea polyphenol-based coordination nanomaterials to improve chemotherapy efficacy by inhibition of carbonyl reductase 1. *Biomaterials* 210, 62–69. doi: 10.1016/j.biomaterials.2019.04.032

Shan, L., Zhuo, X., Zhang, F., Dai, Y., Zhu, G., Yung, B. C., et al. (2018). A paclitaxel prodrug with bifunctional folate and albumin binding moieties for both passive and active targeted cancer therapy. *Theranostics* 8, 2018–2030. doi: 10.7150/thno.24382

Tang, L., Yang, X., Yin, Q., Cai, K., Wang, H., Chaudhury, I., et al. (2014). Investigating the optimal size of anticancer nanomedicine. *Proc. Natl. Acad. Sci. U. S. A.* 111, 15344–15349. doi: 10.1073/pnas.1411499111

Tapmeier, T. T., Moshnikova, A., Beech, J., Allen, D., Kinchesh, P., Smart, S., et al. (2015). The pH low insertion peptide pHLIP variant 3 as a novel marker of acidic malignant lesions. *Proc. Natl. Acad. Sci. U.S.A.* 112, 9710–9715. doi: 10.1073/pnas.1509488112

Tiriac, H., Belleau, P., Engle, D. D., Plenker, D., Deschenes, A., Somerville, T. D. D., et al. (2018). Organoid profiling identifies common responders

to chemotherapy in pancreatic cancer. *Cancer Discov.* 8, 1112–1129. doi: 10.1158/2159-8290.CD-18-0349

Tlsty, T. D., and Coussens, L. M. (2006). Tumor stroma and regulation of cancer development. *Annu. Rev. Pathol.* 1, 119–150. doi: 10.1146/annurev.pathol.1.110304.100224

Urry, D. W. (1992). Free energy transduction in polypeptides and proteins based on inverse temperature transitions. *Prog. Biophys. Mol. Biol.* 57, 23–57. doi: 10.1016/0079-6107(92)90003-O

Urry, D. W., and Pattanaik, A. (1997). Elastic protein-based materials in tissue reconstruction. *Ann. N. Y. Acad. Sci.* 831, 32–46. doi: 10.1111/j.1749-6632.1997.tb52182.x

Versluis, F., van Esch, J. H., and Eelkema, R. (2016). Synthetic self-assembled materials in biological environments. *Adv. Mater.* 28, 4576–4592. doi: 10.1002/adma.201505025

Wang, S., Yu, G., Wang, Z., Jacobson, O., Tian, R., Lin, L. S., et al. (2018). Hierarchical tumor microenvironment-responsive nanomedicine for programmed delivery of chemotherapeutics. *Adv. Mater.* 31:e1803926. doi: 10.1002/adma.201803926

Wang, Y. F., Liu, L., Xue, X., and Liang, X. J. (2017). Nanoparticle-based drug delivery systems: what can they really do *in vivo*? *F1000Res* 6,681. doi: 10.12688/f1000research.9690.1

Wei, T., Liu, J., Ma, H., Cheng, Q., Huang, Y., Zhao, J., et al. (2013). Functionalized nanoscale micelles improve drug delivery for cancer therapy *in vitro* and *in vivo*. *Nano Lett.* 13, 2528–2534. doi: 10.1021/nl400586t

Wijesinghe, D., Engelman, D. M., Andreev, O. A., and Reshetnyak, Y. K. (2011). Tuning a polar molecule for selective cytoplasmic delivery by a pH (low) insertion peptide. *Biochemistry* 50, 10215–10222. doi: 10.1021/bi2009773

Wyatt, L. C., Lewis, J. S., Andreev, O. A., Reshetnyak, Y. K., and Engelman, D. M. (2017). Applications of pHLIP technology for cancer imaging and therapy. *Trends Biotechnol.* 35, 653–664. doi: 10.1016/j.tibtech.2017.03.014

Wyatt, L. C., Moshnikova, A., Crawford, T., Engelman, D. M., Andreev, O. A., and Reshetnyak, Y. K. (2018). Peptides of pHLIP family for targeted intracellular and extracellular delivery of cargo molecules to tumors. *Proc. Natl. Acad. Sci. U.S.A.* 115, E2811–E2818. doi: 10.1073/pnas.1715350115

Xiao, T., Qi, L., Zhong, W., Lin, C., Wang, R., and Wang, L. (2019a). Stimuli-responsive nanocarriers constructed from pillar[n]arene-based supra-amphiphiles. *Mater. Chem. Front.* 3, 1973–1993. doi: 10.1039/C9QM00428A

Xiao, T., Zhong, W., Xu, L., Sun, X. Q., Hu, X. Y., and Wang, L. (2019b). Supramolecular vesicles based on pillar[n]arenes: Design, construction, and applications. *Org. Biomol. Chem.* 17, 1336–1350. doi: 10.1039/C8OB03095B

Xu, H., Cao, C. S., Kang, X. M., and Zhao, B. (2016). Lanthanide-based metal-organic frameworks as luminescent probes. *Dalton Trans.* 45, 18003–18017. doi: 10.1039/C6DT02213H

Yang, X., Lin, X., Zhao, Y., Zhao, Y. S., and Yan, D. (2017). Lanthanide metal-organic framework microrods: Colored optical waveguides and chiral polarized emission. *Angew. Chem. Int. Ed. Engl.* 56, 7853–7857. doi: 10.1002/anie.201703917

Yao, L., Daniels, J., Wijesinghe, D., Andreev, O. A., and Reshetnyak, Y. K. (2013). pHLIP(R)-mediated delivery of pegylated liposomes to cancer cells. *J. Control. Release* 167, 228–237. doi: 10.1016/j.jconrel.2013.01.037

Yao, L., Hu, Y., Liu, Z., Ding, X., Tian, J., and Xiao, J. (2019). Luminescent lanthanide-collagen peptide framework for pH-controlled drug delivery. *Mol. Pharm.* 16, 846–855. doi: 10.1021/acs.molpharmaceut.8b01160

Yin, L., Tang, H., Kim, K. H., Zheng, N., Song, Z., Gabrielson, N. P., et al. (2013). Light-responsive helical polypeptides capable of reducing toxicity and unpacking DNA: toward nonviral gene delivery. *Angew. Chem. Int. Ed. Engl.* 52, 9182–9186. doi: 10.1002/anie.201302820

Zhao, B. X., Zhao, Y., Huang, Y., Luo, L. M., Song, P., Wang, X., et al. (2012). The efficiency of tumor-specific pH-responsive peptide-modified polymeric micelles containing paclitaxel. *Biomaterials* 33, 2508–2520. doi: 10.1016/j.biomaterials.2011.11.078

Zhao, Y., Ren, W., Zhong, T., Zhang, S., Huang, D., Guo, Y., et al. (2016). Tumor-specific pH-responsive peptide-modified pH-sensitive liposomes containing doxorubicin for enhancing glioma targeting and anti-tumor activity. *J. Control. Release* 222, 56–66. doi: 10.1016/j.jconrel.2015.12.006

Conflict of Interest: The authors declare that the research was conducted in the absence of any commercial or financial relationships that could be construed as a potential conflict of interest.

frontiers in Chemistry

ORIGINAL RESEARCH
published: 11 September 2020
doi: 10.3389/fchem.2020.00787

Deliver Anti-inflammatory Drug Baicalein to Macrophages by Using a Crystallization Strategy

Jianming Zhang[1,2†], *Chao Teng*[2†], *Caolong Li*[3] *and Wei He*[4,2*]

[1] Shanghai Mental Health Center, Shanghai Jiao Tong University School of Medicine, Shanghai, China, [2] School of Pharmacy, China Pharmaceutical University, Nanjing, China, [3] School of Science, China Pharmaceutical University, Nanjing, China, [4] Shanghai Skin Disease Hospital, Tongji University School of Medicine, Shanghai, China

Macrophages are potent to modulate inflammation *via* phenotypic switch and production of inflammatory factors. Baicalein (BCL) is frequently used to alleviate inflammation; however, its application is always hindered due to low solubility. Herein, BCL nanocrystals (BNRs) were prepared to improve its delivery to macrophages. The prepared BNRs have a diameter of 150 nm with a rod-like structure. The nanocrystals could be well-taken up by macrophages *via* the caveolar pathway and, therefore, promote the polarization switch from proinflammatory phenotype to anti-inflammatory macrophages and alleviate the inflammation *via* reducing production cytokine IL-12. In conclusion, the crystallization strategy is promising for the improvement of the solubility of BCL and promotion of its anti-inflammatory activities.

Keywords: anti-inflammation, baicalein, macrophages, nanocrystals, low solubility

OPEN ACCESS

Edited by:
Tianjiao Ji,
Boston Children's Hospital and Harvard Medical School, United States

Reviewed by:
Xingwang Zhang,
Jinan University, China
Hao Qin,
National Center for Nanoscience and Technology (CAS), China

***Correspondence:**
Wei He
weihe@cpu.edu.cn

[†] *These authors have contributed equally to this work*

Specialty section:
This article was submitted to Supramolecular Chemistry, a section of the journal Frontiers in Chemistry

Received: *09 July 2020*
Accepted: *28 July 2020*
Published: *11 September 2020*

Citation:
Zhang J, Teng C, Li C and He W (2020) Deliver Anti-inflammatory Drug Baicalein to Macrophages by Using a Crystallization Strategy. Front. Chem. 8:787. doi: 10.3389/fchem.2020.00787

INTRODUCTION

Inflammation is an important life activity, protecting the body from infection with foreign organisms; however, chronic inflammation always results in exacerbation of numerous diseases such as cardiovascular diseases, arthritis, and inflammatory bowel disease (He W. et al., 2019). Macrophages play a central role in the regulation of inflammation *via* phenotypic switch and production of inflammatory factors (Leitinger and Schulman, 2013).

Baicalein (BCL), a major flavonoid of *Scutellaria baicalensis*, is a potent anti-inflammatory agent predominantly acting through associating with a variety of chemokines including IL-8, macrophage inflammatory protein (MIP)-1β, and monocyte chemotactic protein (MCP)-2 and limiting their biological function (Li et al., 2000). Moreover, baicalein can polarize proinflammatory phenotype M1 to anti-inflammatory M2 and alleviate inflammatory response (Zhu et al., 2016). As a result, BCL has a promising potential to combat inflammation. However, its use is always limited due to low solubility in water (Zhang et al., 2009). Nanotechnology, such as liposomes, nanoemulsions, polymeric micelles, and nanocrystals, is potent to enhance the solubilization of poorly water-soluble active compounds, along with over 65 products approved for clinical use (Anselmo and Mitragotri, 2016; He H. et al., 2019; He et al., 2020; Yu et al., 2020). Of them, nanocrystal technology prepared by formulating drug particles into nanosized particles by top-down or bottom-up approaches is one of the most promising means to solve the solubility (Lu et al., 2019), owing to its advantages including its high drug loading, enhanced dissolution rate and saturation solubility, reproducibility of oral absorption, improved dose-bioavailability proportionality, and increased patient compliance (He et al., 2013, 2016; Lv et al., 2018; Zhou et al., 2018; Zhao et al., 2019). So far, over 15

nanocrystal formulations such as Rapamune®, Emend®, Tricor®, Megace ES®, Avinza®, Focalin XR®, Ritalin®, and Zanaflex Capsules™ have been approved. In particular, the formulation of nanocrystals has an extremely high drug-loading capacity that is markedly greater than that from conventional nanocarriers with the capacity of <10% (He et al., 2013; Anselmo and Mitragotri, 2019). Accordingly, nanocrystal technology has a potential to address the solubility of BCL and improve its delivery.

In this study, BCL nanocrystals (BNRs) were prepared and characterized. Moreover, the uptake and internalization pathway in macrophages, phenotypic switch, and anti-inflammation *in vitro* were investigated, and finally, biocompatibility of BNRs was evaluated.

MATERIALS AND METHODS

Materials

Beta-lactoglobulin (β-LG), fluorescein isothiocyanate isomer I (FITC), rhodamine B isothiocyanate (RITC), 3-(4,5-dimethylthiazol-2yl)-2,5-diphenyltetrazoliumbromide (MTT), and polyethylenimine (PEI, 408727, 25,000 Da) were provided by Sigma-Aldrich Co., Ltd. (St. Louis, MO, USA). Fetal bovine serum (FBS), Dulbecco's Modified Eagle Medium (DMEM), and trypsin were from Thermo Fisher Scientific, Inc. (Waltham, MA, USA). 4,6-Diamino-2-phenyl indole (DAPI) were brought from the Beyotime Institute of Biotechnology (Haimen, China). Nystain and methyl-β-cyclodextrin (M-CD) were supplied by Aladdin Co., Ltd. (Aladdin Co., Ltd., Shanghai, China). BCL was obtained from Chengdu Pufei De Biotech Co., Ltd. (Chengdu, China). Antibodies of CD206 and INOS were obtained from Proteintech Co., Ltd. (Rosemont, USA). Cy5 was obtained from Solarbio Science & Technology Co., Ltd. (Shanghai, China). Alexa Fluor® 488-Cave-1/F-actin/CTB was from Abcam Trading Co., Ltd. (Shanghai, China). ELISA kits of mouse interferon-α (INF-α) and interleukin-12 (IL-12) were purchased from Enzyme-linked Biotechnology Co. Ltd. (Shanghai, China).

Cell Cultures and Animals

RAW 264.7 cells were cultured in DMEM containing 10% FBS and 1% penicillin/streptomycin at 37°C, 5% CO_2, and 100% humidity and were split when confluent. Before use, the cells were polarized into M1 phenotype by incubation with lipopolysaccharides (100 ng/mL) and interferon-γ (20 ng/mL) for 24 h.

The animals used in all experiments received care in compliance with the Principles of Laboratory Animal Care and the Guide for the Care and Use of Laboratory Animals. Animal experiments followed a protocol approved by the China Pharmaceutical University Institutional Animal Care and Use Committee.

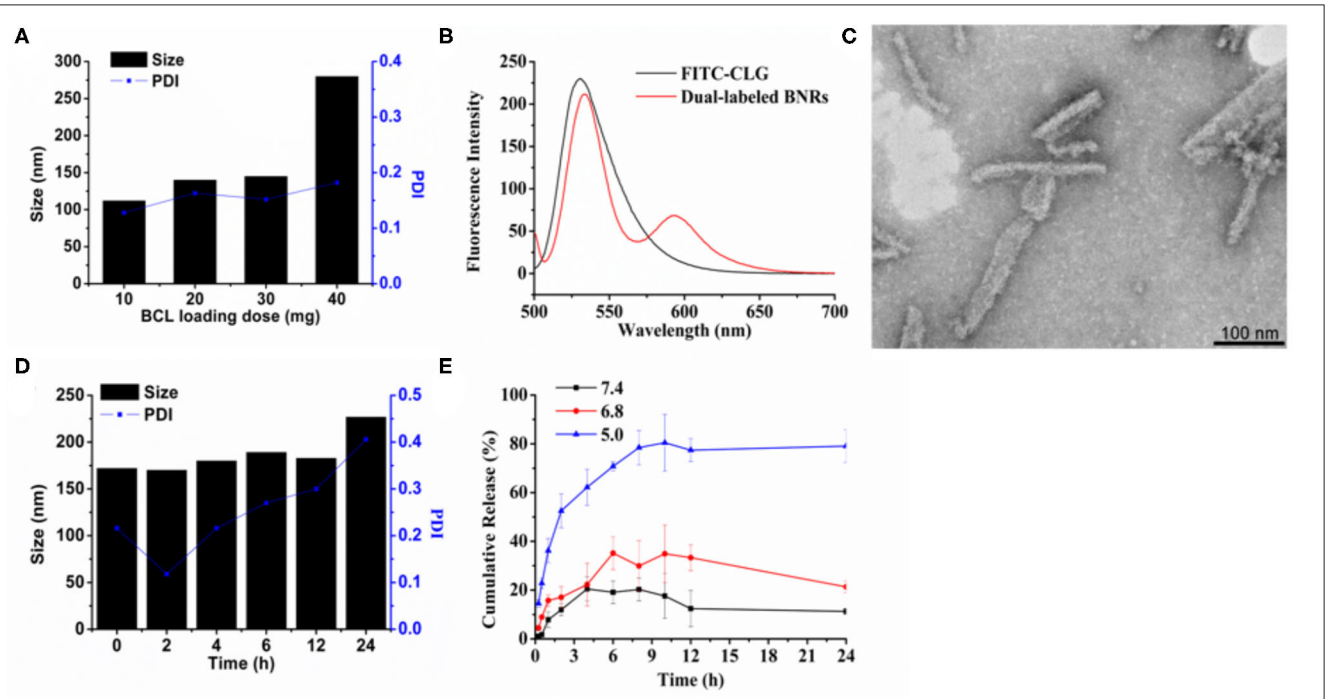

FIGURE 1 | Preparation and characterization. **(A)** Effect of baicalein loading on the particle size of BNRs. **(B)** Fluorescence emission spectra for FRET assay. FITC and RITC were used to label CLG and the drug crystals, respectively. Dual-labeled BNRs were prepared by coating the RITC-labeled drug crystals with FITC-CLG. Excitation wavelength: 492 nm. **(C)** TEM image of optimized formulation (scale bar = 100 nm). **(D)** Particle-size change of BNRs in 10% serum at 37°C for 12 h. **(E)** *in vitro* release of baicalein from BNRs in buffer solution at pH of 5.0, 6.8, and 7.4 at 37°C for 24 h.

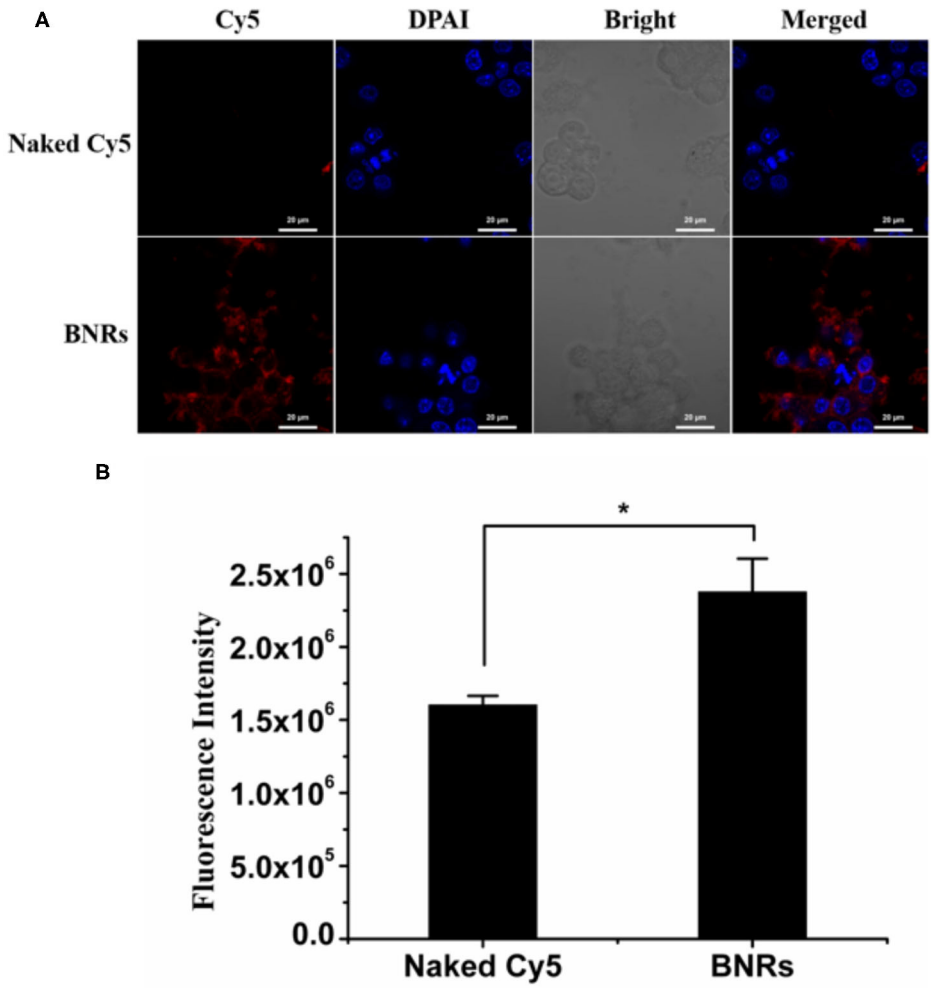

FIGURE 2 | Uptake in macrophages. Uptake of Cy5-labeled BNRs in RAW 264.7 cells was tested by **(A)** CLSM and **(B)** flow cytometry, following incubation at a dye concentration of 100 nM at 37°C for 4 h (mean ± SD, $n = 3$, $^*P < 0.05$). The scale bar is 10 μm.

Preparation and Characterization of Baicalein Nanocrystals

The BCL nanocrystals (BNRs) were prepared by the precipitation–ultrasonication method with a cationic beta-lactoglobulin (CLG) as a stabilizer (He et al., 2013; Xin et al., 2019). Briefly, BCL dissolved in 1 mL dimethyl sulfoxide (DMSO) was mixed with 10 mL CLG solution (1 mg/mL) under stirring and treated with an ultrasonic probe (20–25 kHz, Scientz Biotechnology Co., Ltd., Ningbo, China) at 300 W for 10 min in an ice bath. Dye-labeled nanoparticles were prepared by a similar method except for dissolving the dye and the drug in DMSO together in advance for the mixing.

Serum stability of nanoparticles was performed by incubation in PBS containing 10% FBS at 37°C. At specific time points, the particle size was tested by using a 90Plus Particle Size Analyzer (Brookhaven Instruments, Holtsville, NY) at 25°C.

The nanoparticles' shape was tested by a transmission electron microscope (TEM, JEM-1230, Tokyo, Japan) under an acceleration voltage of 200 kV. In brief, one drop of diluted sample was placed onto the copper mesh, and then the mesh was dried, stained with 2% (w/w) phosphotungstic acid for 30 s, and finally dried at 25°C for 5 min.

The coating of the stabilizer on the nanoparticles was studied by fluorescence resonance energy transfer (FRET) in a fluorescence spectrometer (SHIMADZU RF-5301PC, Japan), in which FITC and RITC were utilized as the energy donors and acceptors. The scanning was performed at an excitation wavelength of 492 nm. The split width was 5 nm for the excitation and 15 nm for the emission.

In vitro Drug Release

The drug release was investigated by a dialysis method. In brief, the samples were added into a dialysis bag (3,500 Da) and immersed in a shaking incubator (SHA-C, Jintan, China) with a speed of 100 rpm/min at 37°C. At pre-determined time intervals, samples were collected and purified with a 0.2 μm

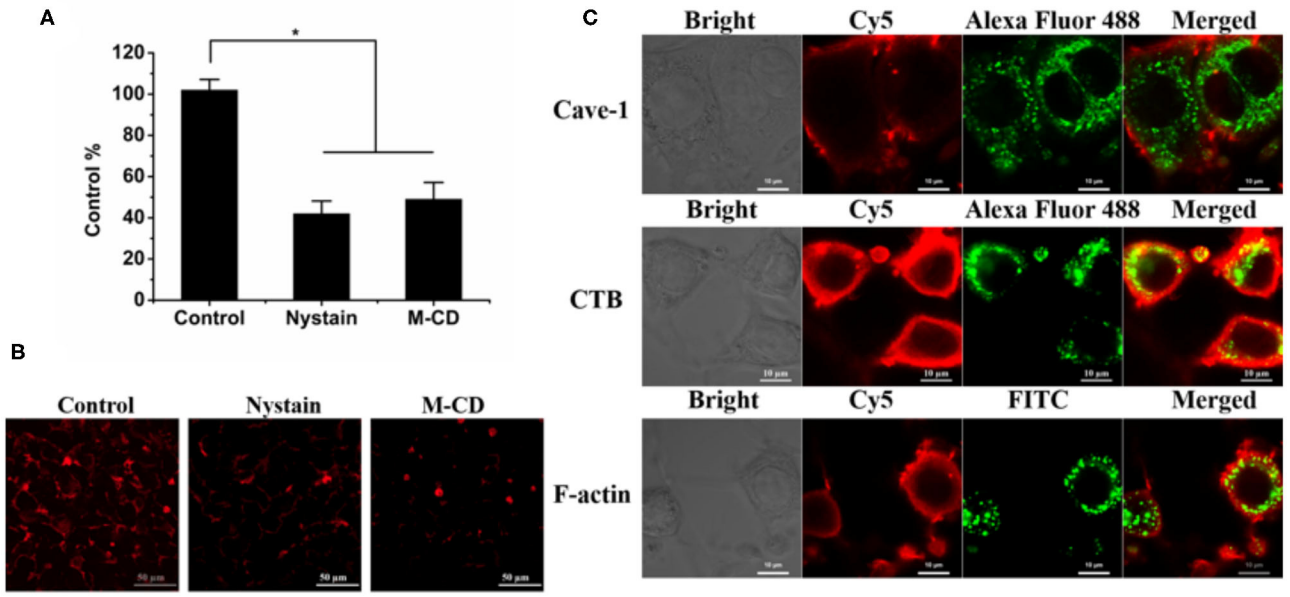

FIGURE 3 | Internalization pathway. **(A,B)** Cellular uptake of Cy5-labeled BNRs in RAW 264.7 cells pre-treated with different inhibitors for 0.5 h was determined by **(A)** flow cytometry (mean ± SD, $n = 3$, $^*P < 0.01$) and **(B)** CLSM observation after a 4 h incubation at 37°C (Scale bar, 50 μm). **(C)** Colocalization of Cy5-labeled BNRs with caveolae-trafficking proteins, Alexa Fluor 488-labeled CTB (green), Alexa Fluor 488-labeled Cave-1 (green), and FITC-labeled F-actin (green). The scale bar is 10 μm.

filter. The drug content was assayed in a high-performance liquid chromatography system equipped with an ultraviolet detector (SHIMAZU LC-10AT, Kyoto, Japan). The separation was performed on the ODS C18 column (250 mm × 4.6 mm, Diamonsil, Beijing, China) at 30°C at 276 nm. The mobile phase consisted of methanol and 0.05% phosphoric acid (70/30, v/v) and was pumped at a flow rate of 1 mL/min (Teng et al., 2020).

Cell Experiments

Cells cultured on the 6-well plates (1×10^5 cells/well) were incubated with the samples for 4 h and then were subjected to determination by flow cytometry (BD FACS Calibur, San Jose, CA, USA) and observation by using confocal laser scanning microscopy (CLSM, LSM700, Carl Zeiss, Germany). To study the internalization pathway, the cells were pre-incubated with inhibitors, nystatin (10 mM), or M-CD (2.5 mM), for 0.5 h. The colocalization was examined by confocal microscopy after incubation with the nanoparticles and staining with Alexa Fluor® 488-Cave-1, -F-actin, or -CTB for 3 h.

The polarization of RAW 264.7 cells were assayed by CLSM and flow cytometry. Briefly, the cells (1×10^5 cells/well) were cultured with the preparations for 12 h, incubated with a primary and secondary antibody for 2 and 24 h at 4°C, respectively, and stained with DAPI for 15 min. The anti-inflammation *in vitro* was tested by detecting IL-12 with ELISA kits after a 12 h incubation with various preparations. Cell viability was studied by MTT assay after incubation with preparations for 24 h.

Biocompatibility Study

Hemolytic activity was studied by incubating the formulations with erythrocytes. In brief, erythrocytes were collected from mouse blood by centrifugation at 1,500 × g for 15 min, wash, and resuspension with PBS. Then, CLG or PEI was incubated with the erythrocytes at 37°C for 1 h, followed by centrifugation at 1,500 × g for 15 min, collection of the supernatant, and comparison of hemolytic activity.

The immunogenicity was assessed by detecting IL-12 and INF-α in the plasma with ELISA kits at pre-determined time intervals after intravenous injection of various preparations at specific doses according to the body weight of mouse.

Statistical Analysis

One-way analysis of variance was performed to assess the statistical significance of the differences between samples. The results are expressed as the mean ± standard deviation (SD). $P < 0.05$ indicated significant differences.

RESULTS AND DISCUSSION

Preparation and Characterization of BNRs

CLG is a safe biopolymer and potent to stabilize drug crystals (He et al., 2013; Teng et al., 2020). Herein, BNRs were prepared *via* a precipitation–ultrasonication method by using CLG as a stabilizer. First, the influence of drug loading on the diameter of BNRs was investigated. As displayed in **Figure 1A**, increasing the drug loading from 10 to 40 mg in a 10 mL CLG solution containing 10 mg CLG resulted in an increase of particle size from 125 to 280 nm. Nonetheless, the diameter was <150 nm as the added drug was <30 mg, and all PDI values are smaller than 0.3, indicating a homogeneous dispersion with narrow size

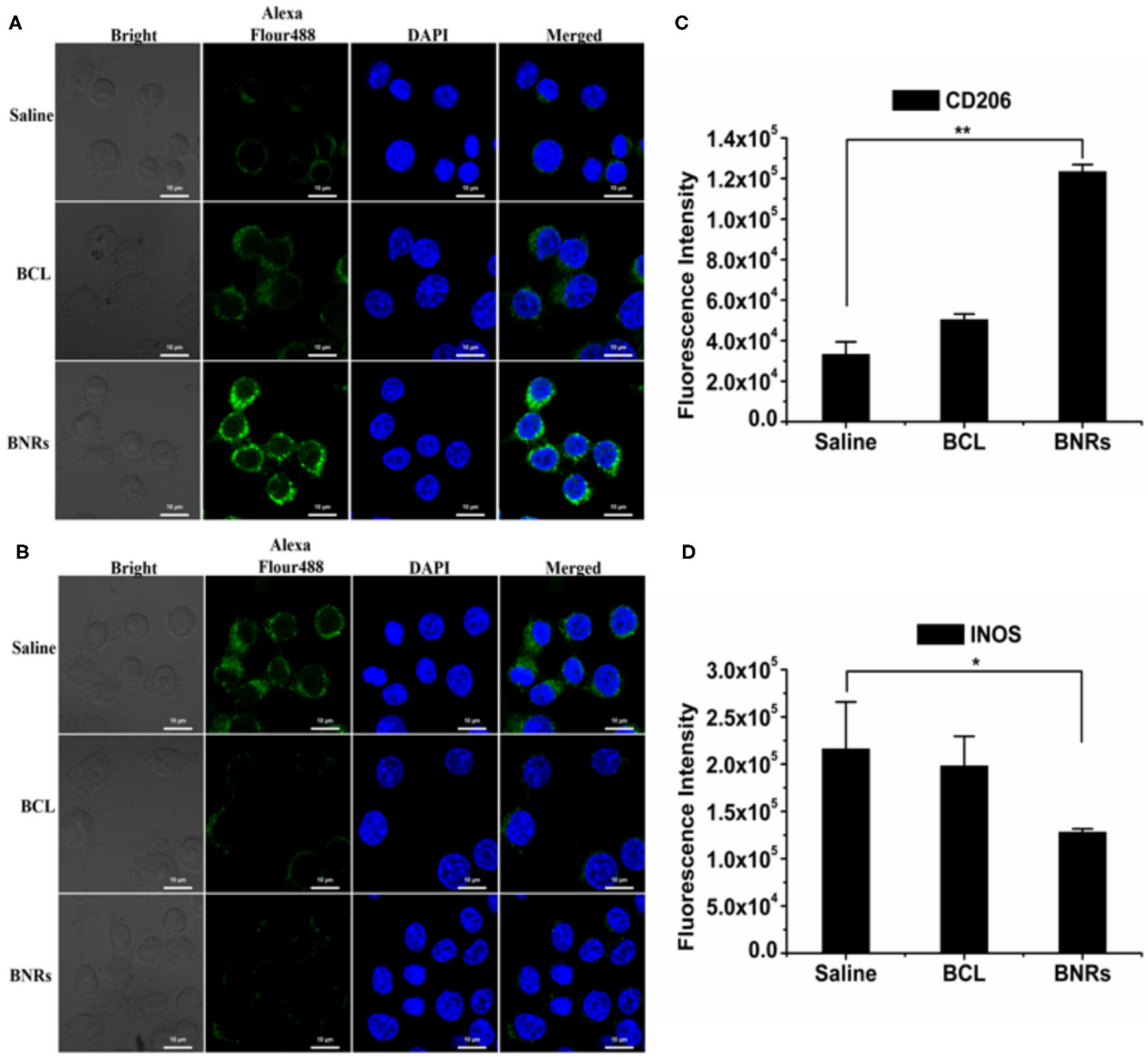

FIGURE 4 | Phenotypic shift study *in vitro*. Immunofluorescence and quantitative analysis of CD206 **(A,C)** and INOS **(B,D)** expression on RAW 264.7 cells after treatment ($n = 3$, $^{*}P < 0.05$, and $^{**}P < 0.01$). The nuclei were stained with DAPI (blue) and CD206 and INOS were stained with Alexa Fluor 488-conjugated antibody (green). The scale bar is 10 μm.

distribution of the nanoparticles. The results demonstrated that the stabilizer CLG is potent to stabilize the drug nanocrystals. To identify the interaction between the drug crystals and CLG, FRET was utilized, in which FITC and RITC were used as the energy donors and acceptors, respectively. FRET effect is displayed *via* the reduction fluorescence intensity of donor at 520 nm with increased fluorescence of the acceptor at 590 nm (**Figure 1B**), an indicator of the interplay between the stabilizer and the crystals. TEM examination demonstrated that BNRs has a rod shape and diameter of 100–150 nm in length (**Figure 1C**). The test of serum stability performed *via* incubation in 10% FBS displayed little alternation in the diameter of the nanoparticles at 12 h post-incubation and, as a result, demonstrated the potential stability in physiological conditions (**Figure 1D**).

The drug release profiles were studied at three pH conditions, pH 5, 6.8, and 7.4, through a dialysis method. The drug release at pHs of 6.8 and 7.4 was <40 and 20% in a 24 h period, respectively, whereas the release at pH 5 was up to 80% (**Figure 1E**). The results indicated that the drug release from BNRs was pH-dependent due to that BCL is a weak basic drug that has higher solubility in low pH conditions.

Cellular Uptake *via* Caveolar Pathway

First, the uptake in macrophages was evaluated. After a 4 h incubation, strong red fluorescent spots around the nucleic were displayed (**Figure 2A**), confirmed by the determination by flow cytometry (**Figure 2B**). Second, previous reports demonstrated that rod-like particles with a diameter of <200 nm in length always obtained cellular entry *via* the caveolar pathway, bypassing the endo-lysosomal systems (Xin et al., 2017, 2018, 2019). As depicted in **Figure 3A**, the internalization of BNRs decreased by ∼60% in the cells pre-treated with inhibitors of caveolar pathway, nystatin, or M-CD, compared with the control pre-treated with saline. The reduced uptake was verified by the examination by fluorescence microscopy (**Figure 3B**). In order to confirm the participation of the caveolar pathway in the uptake, co-localization of Cy5-labeled BNRs with caveolae-trafficking proteins, Cav-1, CTB, and F-actin, was studied using CLSM. Yellow fluorescent spots that appeared in the merged pictures demonstrated the colocalization of the nanoparticles with the three proteins (**Figure 3C**). These results indicated that 150 nm BNRs entered cells mainly *via* the caveolar pathway.

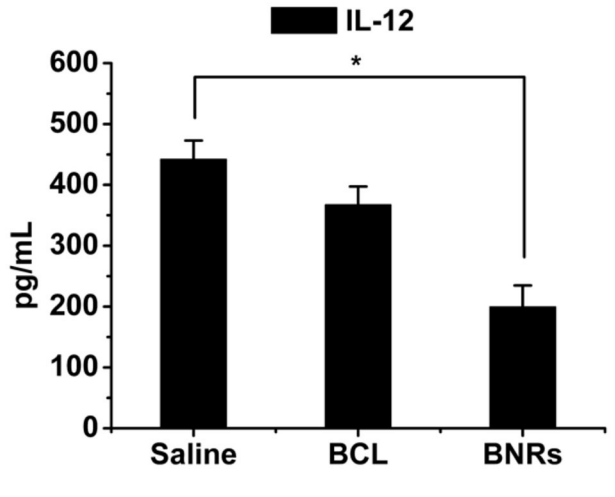

FIGURE 5 | Anti-inflammation *in vitro*. Quantitative analysis of IL-12 expression on RAW 264.7 cells after treatment for 12 h ($n = 3$, $^*P < 0.05$).

Enhanced Phenotype Switch From M1 to M2 and Anti-inflammation

BCL is potent to alleviate anti-inflammation effects. In this study, we hypothesized that BNRs allowed for reduced inflammation activities *via* promoting the phenotypic switch of macrophages from proinflammatory phenotype (M1) to anti-inflammatory phenotype (M2). To characterize the polarization of macrophages, two markers, CD206 and INOS, that highly express on phenotypic M2 and M1, respectively (He W. et al., 2019), were detected by immunofluorescence assay. Treatment with free BCL or BNRs upregulated CD206 compared with saline (**Figure 4A**), confirmed by the quantified results assayed by flow cytometry (**Figure 4B**). Importantly, BNRs enabled an ∼2-fold increase in the expression of CD206 over free BCL. Also, treatment with BNRs reduced the expression of INOS significantly (**Figures 4C,D**). Next, the anti-inflammatory effect was assessed in macrophages after incubation with various formulations. As expected, dosing BNRs significantly reduced the secretion of inflammatory factor, IL-12, along with a >50% decrease with that from BCL (**Figure 5**). The results demonstrated that BNRs polarized M1 into M2 with high efficacy and leased the inflammation effectively.

The enhanced anti-inflammation effect *in vitro* resulted from the benefits of BNRs, high drug-loading capacity, and sustained drug release. To react to the surrounding situations, macrophages tend to alter their polarization, implying that the polarization may be changed once the drug's simulation disappears (He W. et al., 2019). As is well-known, most of drug delivery systems (DDS) release their drugs rapidly in cells after uptake due to the decomposition by the endo-lysosomes (He et al., 2020), always discounting the inflammatory activity of drugs. Previous reports indicated that the drug crystals in cells could

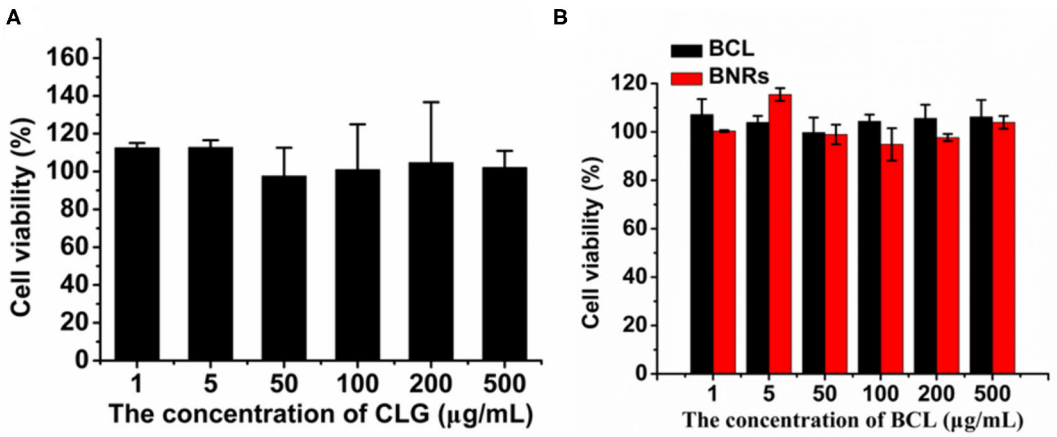

FIGURE 6 | Cell viability. Cytotoxicity of **(A)** stabilizer CLG and **(B)** formulations to RAW 264.7 cells post 48 h incubation.

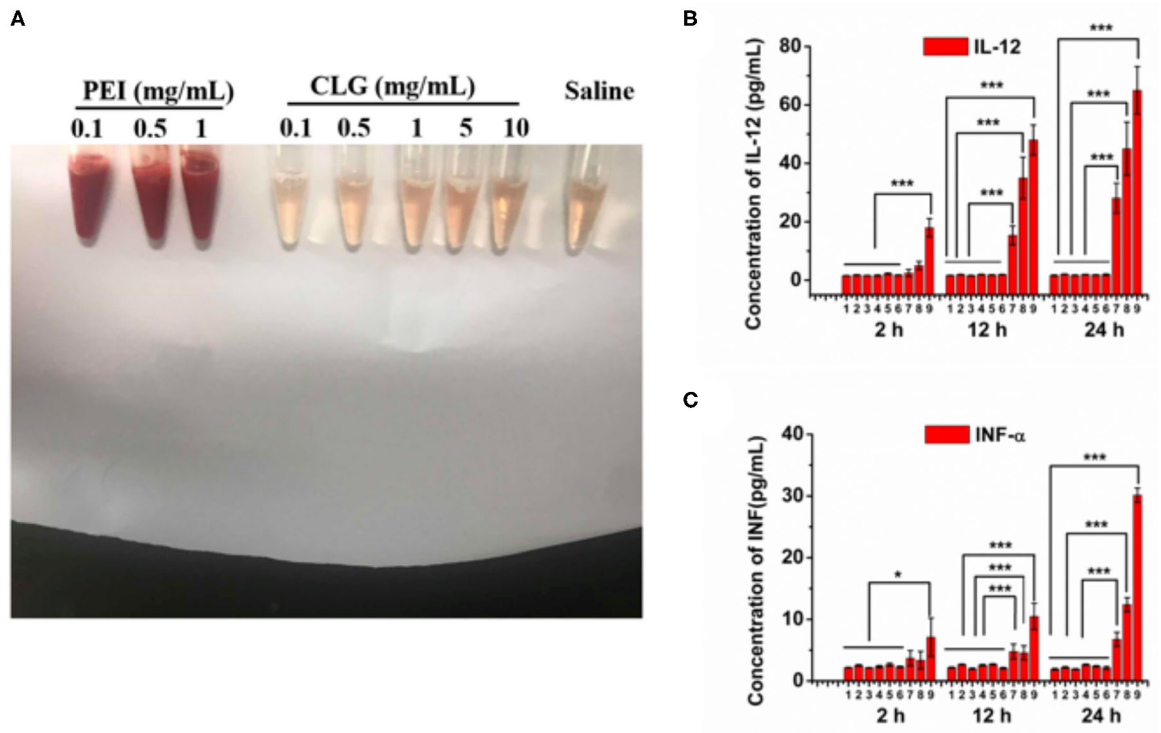

FIGURE 7 | Biocompatibility. **(A)** Hemolytic activity of CLG (0.1–10 mg/mL). A cationic vector, PEI, was used as a positive control. Inflammatory factors, **(B)** IL-12, and **(C)** INF-α, in the mouse plasma after injection of CLG or PEI for 2, 12, and 24 h, respectively. The formulations and administration doses based on the body weight are as follows: 1, saline; 2, CLG, 1 mg/kg; 3, CLG, 5 mg/kg; 4, CLG, 10 mg/kg; 5, CLG, 50 mg/kg; 6, CLG, 100 mg/kg; 7, PEI, 1 mg/kg; 8, PEI, 2.5 mg/kg; 9, PEI, 5 mg/kg. $n = 3$, $^{*}P < 0.05$ and $^{***}P < 0.001$.

keep their integrity up to 7–10 h (Lu et al., 2017; Qi et al., 2019). In this study, the BNRs with a payload capacity of 7–10-fold increase over conventional DDS entered cells *via* bypassing the endo-lysosomes and, as a result, maintained their integrity in the cytosol. These profiles allowed BNRs to sustain release of BCL over time after uptake. Indeed, as displayed in **Figure 1E,** BNRs released the drug in a slow pattern. Overall, the nanocrystal approach is promising to improve the efficacy of anti-inflammatory drugs against inflammatory diseases such as myocarditis, atherosclerosis, pulmonary hypertension, stroke, and cardiac disease.

Biocompatibility Study

First, the cell viability of the stabilizer CLG used in the formulations and BNRs was determined by the MTT assay. CLG and BNRs have little cytotoxicity to macrophages in the tested concentrations (**Figure 6**). Then, hemolytic activity was investigated by using PEI, a cationic vector, as positive control. Incubation with PEI resulted in profound hemolysis. In contrast, treatment with CLG at pre-determined concentrations showed ignored hemolytic toxicity (**Figure 7A**). In addition, the immunogenicity was evaluated by determination of inflammatory factors, IL-12 and INF-α, in the plasma after intravenous injection of CLG or PEI at specific doses. The levels of the two factors from the groups dosed with PEI went up markedly at 12 or 24 h post-injection compared with that from the saline-treated group (**Figures 7B,C**), whereas the injection of CLG did not increase the concentration of the factors. The results indicated that CLG is safe for intravenous injection.

CONCLUSIONS

In this study, BCL nanocrystals were prepared and characterized. The nanocrystals have a diameter of ∼150 nm with a rod-like structure. *Via* internalization through the caveolar pathway, the drug nanocrystals are potent to promote the phenotypic switch from proinflammatory M1 to anti-inflammatory M2 and, as a result, alleviate the inflammation activity *in vitro*. In conclusion, crystallization is a promising strategy to improve the activity of insoluble anti-inflammatory agents.

DATA AVAILABILITY STATEMENT

All datasets presented in this study are included in the article.

ETHICS STATEMENT

The animal study was reviewed and approved by The China Pharmaceutical University Institutional Animal Care and Use

Committee. Written informed consent was obtained from the owners for the participation of their animals in this study.

AUTHOR CONTRIBUTIONS

WH conceived and designed the research work. JZ, CT, and CL performed the experiments. All of the authors discussed the results and commented on the manuscript. All of the authors have read and approved the final manuscript.

FUNDING

This study was supported by the National Natural Science Foundation of China (No. 81872823), the Double First-Class (CPU2018PZQ13) of the CPU, the Shanghai Science and Technology Committee (19430741500), and the Key Laboratory of Modern Chinese Medicine Preparation of Ministry of Education of Jiangxi University of traditional Chinese Medicine.

REFERENCES

Anselmo, A. C., and Mitragotri, S. (2016). Nanoparticles in the clinic. *Bioeng. Transl. Med.* 1, 10–29. doi: 10.1002/btm2.10003

Anselmo, A. C., and Mitragotri, S. (2019). Nanoparticles in the clinic: an update. *Bioeng. Transl. Med.* 4:e10143. doi: 10.1002/btm2.10143

He, H., Lu, Y., Qi, J., Zhu, Q., Chen, Z., and Wu, W. (2019). Adapting liposomes for oral drug delivery. *Acta Pharm. Sin. B* 1, 36–48. doi: 10.1016/j.apsb.2018.06.005

He, W., Lu, Y., Qi, J., Chen, L., Hu, F., and Wu, W. (2013). Food proteins as novel nanosuspension stabilizers for poorly water-soluble drugs. *Int. J. Pharm.* 441, 269–278. doi: 10.1016/j.ijpharm.2012.11.033

He, W., Lv, Y., Xiao, Q., Ye, L., Cai, B., Qin, C., et al. (2016). Denatured protein stabilized drug nanoparticles: tunable drug state and penetration across the intestinal barrier. *J. Mater. Chem. B* 5, 1081–1097. doi: 10.1039/C6TB02577C

He, W., Kapate, N., Shields C. W. IV, and Mitragotri, S. (2019). Drug delivery to macrophages: a review of targeting drugs and drug carriers to macrophages for inflammatory diseases. *Adv. Drug Deliv. Rev*. doi: 10.1016/j.addr.2019.12.001. [Epub ahead of print].

He, W., Xing, X., Wang, X., Wu, D., Wu, W., Guo, J., et al. (2020). Nanocarrier-mediated cytosolic delivery of biopharmaceuticals. *Adv. Funct. Mater*. doi: 10.1002/adfm.201910566. [Epub ahead of print].

Leitinger, N., and Schulman, I. G. (2013). Phenotypic polarization of macrophages in atherosclerosis. *Arterioscler. Thromb. Vasc. Biol.* 33, 1120–1126. doi: 10.1161/ATVBAHA.112.300173

Li, B. Q., Fu, T., Gong, W. H., Dunlop, N., Kung, H., Yan, Y., et al. (2000). The flavonoid baicalin exhibits anti-inflammatory activity by binding to chemokines. *Immunopharmacology* 49, 295–306. doi: 10.1016/S0162-3109(00)00244-7

Lu, Y., Lv, Y., and Li, T. (2019). Hybrid drug nanocrystals. *Adv. Drug Deliv. Rev.* 143, 115–133. doi: 10.1016/j.addr.2019.06.006

Lu, Y., Qi, J., Dong, X., Zhao, W., and Wu, W. (2017). The *in vivo* fate of nanocrystals. *Drug Discov. Today* 22, 744–750. doi: 10.1016/j.drudis.2017.01.003

Lv, Y., Xu, C., Zhao, X., Lin, C., Yang, X., Xin, X., et al. (2018). Nanoplatform assembled from a CD44-targeted prodrug and smart liposomes for dual targeting of tumor microenvironment and cancer cells. *ACS Nano* 12, 1519–1536. doi: 10.1021/acsnano.7b08051

Qi, J., Hu, X., Dong, X., Lu, Y., Lu, H., Zhao, W., et al. (2019). Towards more accurate bioimaging of drug nanocarriers: turning aggregation-caused quenching into a useful tool. *Adv. Drug Deliv. Rev.* 143, 206–225. doi: 10.1016/j.addr.2019.05.009

Teng, C., Lin, C., Huang, F., Xing, X., Chen, S., Ye, L., et al. (2020). Intracellular codelivery of anti-inflammatory drug and anti-miR 155 to treat inflammatory disease. *Acta Pharm. Sin. B*. doi: 10.1016/j.apsb.2020.06.005. [Epub ahead of print].

Xin, X., Du, X., Xiao, Q., Azevedo, H. S., He, W., and Yin, L. (2019). Drug nanorod-mediated intracellular delivery of microRNA-101 for self-sensitization *via* autophagy inhibition. *Nano Micro Lett.* 11:82. doi: 10.1007/s40820-019-0310-0

Xin, X., Pei, X., Yang, X., Lv, Y., Zhang, L., He, W., et al. (2017). Rod-shaped active drug particles enable efficient and safe gene delivery. *Adv. Sci.* 4:1700324. doi: 10.1002/advs.201700324

Xin, X., Teng, C., Du, X., Lv, Y., Xiao, Q., Wu, Y., et al. (2018). Drug-delivering-drug platform-mediated potent protein therapeutics *via* a non-endo-lysosomal route. *Theranostics* 8, 3474–3489. doi: 10.7150/thno.23804

Yu, W., Shevtsov, M., Chen, X., and Gao, H. (2020). Advances in aggregatable nanoparticles for tumor-targeted drug delivery. *Chin. Chem. Lett.* 31, 1366–1374. doi: 10.1016/j.cclet.2020.02.036

Zhang, X., Tian, H., Wu, C., Ye, Q., Jiang, X., Chen, L., et al. (2009). Effect of baicalin on inflammatory mediator levels and microcirculation disturbance in rats with severe acute pancreatitis. *Pancreas* 38, 732–738. doi: 10.1097/MPA.0b013e3181ad9735

Zhao, Z., Ukidve, A., Krishnan, V., and Mitragotri, S. (2019). Effect of physicochemical and surface properties on *in vivo* fate of drug nanocarriers. *Adv. Drug Deliv. Rev.* 143, 3–21. doi: 10.1016/j.addr.2019.01.002

Zhou, X., Hao, Y., Yuan, L., Pradhan, S., Shrestha, K., Pradhan, O., et al. (2018). Nano-formulations for transdermal drug delivery: a review. *Chin. Chem. Lett.* 29, 1713–1724. doi: 10.1016/j.cclet.2018.10.037

Zhu, W., Jin, Z., Yu, J., Liang, J., Yang, Q., Li, F., et al. (2016). Baicalin ameliorates experimental inflammatory bowel disease through polarization of macrophages to an M2 phenotype. *Int. Immunopharmacol.* 35, 119–126. doi: 10.1016/j.intimp.2016.03.030

Conflict of Interest: The authors declare that the research was conducted in the absence of any commercial or financial relationships that could be construed as a potential conflict of interest.

frontiers in Chemistry

ORIGINAL RESEARCH
published: 29 September 2020
doi: 10.3389/fchem.2020.00762

Novel Polymeric Hybrid Nanocarrier for Curcumin and Survivin shRNA Co-delivery Augments Tumor Penetration and Promotes Synergistic Tumor Suppression

Bei Xu[1,2,3†], Wen Zhou[2†], Lizhi Cheng[1,4†], Yang Zhou[4], Aiping Fang[4], Chaohui Jin[4], Jun Zeng[4], Xiangrong Song[4] and Xia Guo[1]*

[1] Department of Pediatric Hematology/Oncology, Key Laboratory of Birth Defect and Related Disorders of Women and Children (Sichuan University), Ministry of Education, West China Second University Hospital, Sichuan University, Chengdu, China, [2] Department of Otolaryngology, Tongji Medical College, Union Hospital, Huazhong University of Science and Technology, Wuhan, China, [3] Department of Clinical Laboratory, Mianyang Central Hospital, Mianyang, China, [4] State Key Laboratory of Biotherapy and Cancer Center, West China Hospital, Sichuan University, Chengdu, China

OPEN ACCESS

Edited by:
Huaimin Wang,
Westlake University, China

Reviewed by:
Wei Tao,
Harvard Medical School,
United States
Ruibing Wang,
University of Macau, China

***Correspondence:**
Xia Guo
guoxkl@163.com

†These authors have contributed equally to this work

Specialty section:
This article was submitted to Supramolecular Chemistry, a section of the journal Frontiers in Chemistry

Received: 15 June 2020
Accepted: 22 July 2020
Published: 29 September 2020

Citation:
Xu B, Zhou W, Cheng L, Zhou Y, Fang A, Jin C, Zeng J, Song X and Guo X (2020) Novel Polymeric Hybrid Nanocarrier for Curcumin and Survivin shRNA Co-delivery Augments Tumor Penetration and Promotes Synergistic Tumor Suppression. Front. Chem. 8:762. doi: 10.3389/fchem.2020.00762

A major barrier for co-delivery of gene medicine with small molecular chemotherapeutic drugs in solid tumors is the inadequate tumor penetration and transfection. In this study, a novel polymeric nanocarrier with integrated properties of tumor penetration, nuclear targeting, and pH-responsive features was designed, and further used to achieve the synergistic anti-tumor effect of curcumin (CUR) and survivin shRNA (pSUR). The polymeric hybrid nanocarrier was constructed from the FDA-approved polymer PLGA and a novel conjugated triblock polymer W5R4K-PEG_{2K}-PHIS (WPH). CUR and pSUR were simultaneously encapsulated in the dual-drug-loaded nanoparticles (CUR/pSUR-NPs) by a modified double-emulsion solvent evaporation (W/O/W) method. The obtained nanoparticles exhibited better pharmaceutical properties with a uniform spherical morphology and sustained release manners of CUR and pSUR. Excellent features including preferable cellular uptake, efficient endosomal escape, enhanced tumor penetration, and elevated transfection efficiency were further proven. Additionally, a markedly enhanced anti-tumor efficacy for CUR/shRNA-NPs was achieved on SKOV-3 and Hela cells. The synergistic anti-tumor effect involved the inhibition of tumor cell proliferation, induction of cell apoptosis, and the activation of caspase-3 pathways. This work sets up an innovative co-delivery nanosystem to suppress tumor growth, contributing to the development of a comprehensive nanoparticulate strategy for future clinical applications.

Keywords: curcumin, survivin shRNA, co-delivery, tumor penetration, nuclear targeting

INTRODUCTION

A combination of multiple different therapeutic strategies with synergistic effects have been common practice for cancer therapy. Particularly, the co-administration of chemotherapy and gene therapy has shown great promise in achieving higher efficacy and potency with reduced toxicity (Chen et al., 2019; Meng et al., 2020). Curcumin, one of most commonly used chemotherapeutic

drugs, suppresses the initiation, progression, and metastasis of many kinds of cancers. In addition, it appears to inhibit carcinogenesis, affecting angiogenesis, and tumor growth (Hamzehzadeh et al., 2018). Survivin is a member of the family of inhibitors of apoptosis proteins. It is selectively overexpressed in tumors, but not in normal tissues (Peery et al., 2017). Survivin expression is essential for cancer cell survival and survivin targeting has been envisaged as a novel therapeutic strategy (Shamsabadi et al., 2016; Khan et al., 2017; Frassanito et al., 2019). Inhibiting survivin's function or downregulating its expression results in spontaneous apoptosis (Peery et al., 2017). Herein, a new combination consisting of survivin short hairpin RNA (pSUR) and CUR was designed. We hypothesized that the combination of CUR and pSUR would achieve a synergistic or combining effect in the treatment of solid cancer.

Nanomedicine has been extensively engineered to enhance the anti-tumor efficacy of therapeutic agents (Afsharzadeh et al., 2018; Islam et al., 2018; Kong et al., 2019; Tao et al., 2019; Tang et al., 2020), especially for the gene/chemo-therapy combination. Unfortunately, due to inadequate penetration and gene transfection in solid tumors, it only achieves modest therapeutic efficacy. Many strategies have been utilized to improve the nanomedicines' tumor penetration, mainly by optimizing nanoparticle properties (sizes, shapes, and charges) and modulating tumor microenvironments (Shi et al., 2017; Sun et al., 2017). However, due to the unchanged passive diffusion of bulky nanomedicines against the interstitial fluid pressure gradient, the efficiency usually remains unsatisfactory (Ding et al., 2019). Transcellular transport that actively transports nanoparticles through cells by cell-penetrating peptides might be a universal approach for tumor penetration enhancement (Ding et al., 2019). For instance, iRGD exhibiting increased penetration ability and improved tumors' accumulation, has been broadly applied in various nanoparticles (Wu et al., 2019). However, its application might be limited by the expression of integrin and NRP-1/2 on endothelial cells and/or specific tumor cells, and it has no potential for nuclear targeting delivery, probably leading to inefficient gene expression.

Cyclic peptides containing arginine (W) and tryptophan (R) are found to be appropriate for cell-penetrating and have nuclear targeting properties (Mandal et al., 2011). For instance, synthetic cyclic peptides [WR]4 and [WR]5 had been applied to enhance the cellular uptake of phosphopeptides, doxorubicin, and anti-HIV drugs, with the potential of intracellular nuclear targeting delivery (Oh et al., 2014). The rigidity in these peptides can enhance the cell penetrating property (Nguyen et al., 2010; Lättig-Tünnemann et al., 2011). Additionally, because the cyclization improves resistance to proteolytic degradation, these peptides are expected to be more stable toward human serum than linear peptides (Nguyen et al., 2010). Despite these advantages, the application of these cyclic peptides in drug/gene delivery polymeric nanosystems still remains unexplored. Considering this, the cyclic peptides [W5R4]K (tryptophan, K) were selected in this work, and their potential of tumor penetration and nuclear targeting conjugated to nanoparticulate formulation were first evaluated.

To enhance the anti-cancer efficacy of current nanosystems, another greatly indispensable factor is to achieve a fast drug/gene release at tumor sites. The design of pH-sensitive nanoformulations has been regarded as a potent strategy for drug/gene selective release, owing to the typical pH in the interstitium of solid tumors (pH 5.7–7.8) and in the endo/lysosome of tumor cells (pH 5.0–6.0) (Li et al., 2015; Gao et al., 2017; Zhu et al., 2018). Otherwise, the utilization of pH-dependent mechanisms can also facilitate the nanosystems' escape from endo/lysosomal trafficking pathways into cytosol (Wilson et al., 2013). Among various pH-sensitive biomaterials, Poly (L-histidine) (PHIS) has been harnessed as an excellent candidate. Its imidazole ring (pKa 6.0–7.0) has lone pairs of electrons on the unsaturated nitrogen, which endow it with pH-dependent amphoteric properties (Lee et al., 2007; Radovic-Moreno et al., 2012; Qiu et al., 2014). Moreover, the protonated PHIS can interact with anionic phospholipids composing the endosomal compartments and result in appreciable endolysosomal membrane disruption (Lee et al., 2005). Thus, PHIS was selected in our work to establish the perfect pH-sensitive polymeric carriers.

Herein, we aimed to synthesize an amphiphilic copolymer that consisted of [W5R4]K, poly(ethylene glycol), and poly(L-histidine) (WRK-PEG-PHIS, WPH), then used it to generated mixed nanoparticles with poly(lactic-co-glycolic acid) (PLGA). PLGA has been approved by the US Food and Drug Administration (FDA) for certain human applications, and its various advantages of non-toxicity, biodegradability, biocompatibility, and controlled-/sustained-release efficacy have been proven. Due to the integrated properties of this novel system, namely tumor penetration, nuclear targeting, and pH-responsive features, we hypothesized that this system could be promising in the co-delivery of CUR and pSUR, and be effective in the treatment of cancers (**Figure 1**).

MATERIALS AND METHODS

Materials

PLGA (LA/GA = 75:25; MW = 15 Kd) was obtained from the Jinan Daigang Biomaterial Co., Ltd. (Jinan, China). CBZ-L-HIS(DNP)-OH was purchased from the Jill Biochemical Co., Ltd. (Shanghai, China). [W5R4]K was received from the Phtdpeptides Pharmaceutical Co., Ltd (Zhengzhou, China). Survivin shRNA plasmid (pSUR) was constructed by the TsingKe Biological Technology Co., Ltd. (Chengdu, China). Curcumin (CUR), polyethylene glycol (PEG, MW =2 kD), polyvinyl alcohol (PVA, MW = 30–70 Kd, HD: 80%), Hochest 33258, poly-L-lysine (PLL, MW = 15–30 Kd), and 3-(4,5-dimethylthiazol-2-yl)-2,5-diphenyltetrazoliumbromide (MTT) were procured from the Sigma-Aldrich Chemical Co. (St. Louis, MO, USA). All other reagents were of analytical grade and were used without further purification. Anti-survivin and anti-cleaved caspase-3 antibodies were produced from the Abcam Trading (Shanghai) Co., Ltd. (China).

Cell Culture

Human embryonic kidney 293 (HEK293), SKOV-3, and Hela cells were all obtained from the American Type Culture Collection (ATCC). All cells were cultured in an incubator with a humidified atmosphere containing 5% CO_2 at 37°C

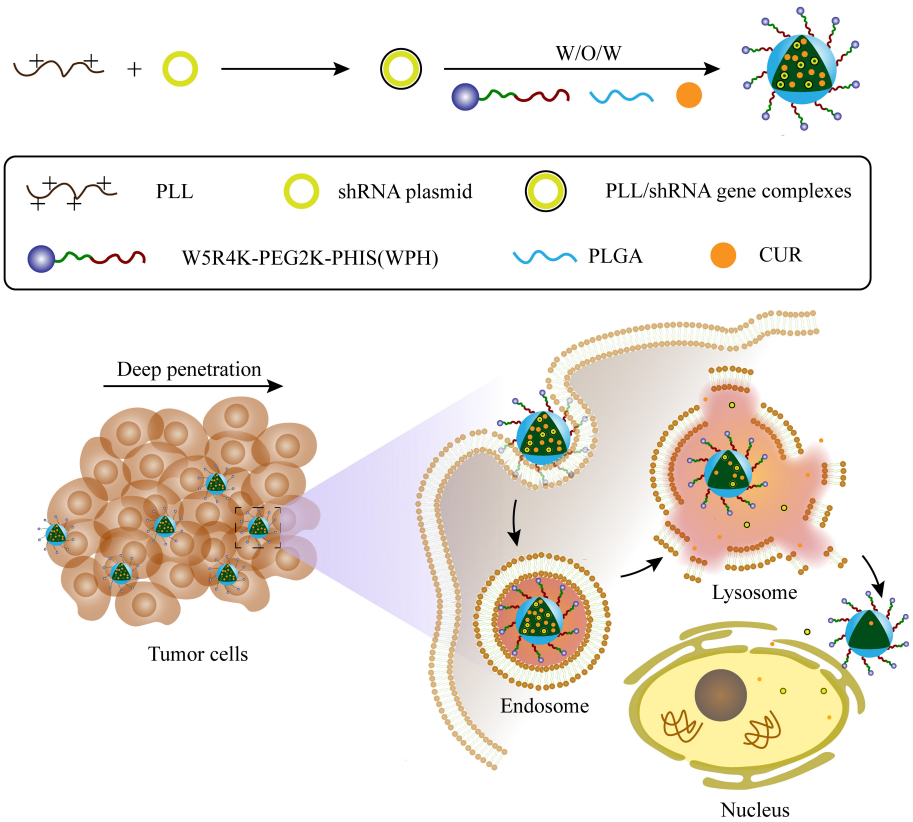

FIGURE 1 | Schematic illustration of the preparation for CUR/pSUR-NPs and the proposed mechanism of CUR/pSUR-NPs including superior tumor penetration, pH-responsive features, as well as the properties of nuclear targeting.

and were maintained in DMEM supplemented with 10% fetal bovine serum.

Anti-tumor Effect of CUR and pSUR *in vitro*

Cell Viability Assay by MTT

SKOV-3 and Hela cells were seeded and cultured in 96-well plates and transfected with pRNA (0.1 μg) using Lipofectamine® 3,000 for 24 h. Then, the medium was replaced by fresh medium containing various concentrations (2.5, 5, 10, and 20 μg/mL) CUR. After 48 h, MTT solution (20 μL, 5 mg/mL) was added, and the cells continued to be incubated for 4 h. The formazan crystals formed by the living cells were dissolved in DMSO (150 μL). The absorbances at 570 nm were read using a Spectra MAX M5 microplate spectrophotometer (Molecular Devices), and the inhibition rates were calculated.

RT-qPCR

SKOV-3 and Hela cells were seeded and cultured in 6-well plates and then transfected with pSUR (2.5 μg) using Lipofectamine® 3000. After 4 h, the transfection mixture was replaced by a fresh medium containing CUR (10 μg/mL), and cells continued to be cultured for another 24 h. Total RNA was extracted from the treated SKOV-3 and Hela cells using a TRIZOL reagent (Hung et al., 2012). After being purified through a genomic DNA elimination reaction, the extracted RNA was subsequently reversed-transcribed into cDNA. Real-time RT-PCR was performed using the IQ™ SYBR Green PCR Supermix PCR kit (BIO-RAD, USA) with the Bio-Rad iCycler apparatus system. The reaction conditions were: 95°C for 3 min, 95°C for 15 s, and 60°C for 1 min (44 cycles). The pair of primers for target genes are designed as: Survivin (forward, 5′-AGATGACGA CCCCATAGAGG-3′; reverse, 5′-ATTGTTGGTTTCCTTTGCA ATTTTG-3′); GAPDH (forward, 5′-GCACCGTCAAGGCTGA GAAC-3′; reverse, 5′-TGGTGAAGACGCCAGTGGA-3′).

Western Blot Analysis

SKOV-3 and Hela cells were cultured and treated as described in section Syntheses of [W5R4]K-PEG2K-PHIS. Total proteins were harvested and analyzed by western blot. The protein was separated on a SDS-PAGE, transferred onto a PVDF membrane, and blocked and incubated with the primary antibody at 4°C overnight. The proteins were detected by incubating membranes with a horseradish peroxidase (HRP)-conjugated secondary antibody. The binds were visualized using an enhanced chemiluminescence detection kit (Pierce, Rockford, IL, USA). The membranes were re-probed with a β-actin antibody to confirm equal protein loading.

Polymer Synthesis

Syntheses of PEG_{2K}-PHIS

N^{α}-CBZ-N^{im}-DNP-L-histidine was first dissolved in anhydrous THF followed by the addition of thionyl chloride under stirring. The reaction was performing for 12 h at room temperature. Then an excess of anhydrous diethyl ether was added to obtain the crystals of N^{im}-DNP-L-histidine carboxyanhydride hydrochloride (N^{im}-DNP-L-histidine NCA·HCl). The powder was subsequently washed, filtered, and dried under vacuum. Next, poly(N^{im}-DNP-L-histidine) [PHIS(DNP)] was synthesized by ring-opening polymerization (ROP) of protected N^{im}-DNP-L-histidine NCA·HCl with a predetermined amount of isopropylamine initiator, to obtain different polymerization degrees and molecular weights (Lee et al., 2003).

Meanwhile, COOH-PEG_{2K}-COOH (CPC) was synthesized according to our previous paper (Yu et al., 2016). Briefly, PEG_{2K}, succinic anhydride, and 4-dimethylaminopyridine (DMAP) were dissolved in dichloromethane (DCM) solution and stirred at room temperature (RT) over 24 h. Thereafter the solvent was evaporated, and the crude product CPC was purified by the recrystallization process from isopropyl alcohol. CPC was collected via vacuum filtration.

Finally, CPC was hydrophobically modified by chemical conjugation of PHIS(DNP) through amide formation to obtain a PEG_{2K}-PHIS(DNP) diblock copolymer. Briefly, CPC was dissolved in anhydrous N,N-dimethylformamide (DMF). Then, EDCI, NHS, and PHIS(DNP) were added, respectively, under stirring. After reacting for 72 h, the solution was dialyzed (MWCO 3,500 Da) to remove small fragments. The product PEG_{2K}-PHIS(DNP) was obtained by freeze-drying, and was then deprotected to yield PEG_{2K}-PHIS (PH) by thiolysis with 2-mercaptoethanol. The chemical structure of the intermediates and PH were analyzed by using ^{1}H-NMR.

Syntheses of [W5R4]K-PEG_{2K}-PHIS

The diblock copolymer PH was dissolved in anhydrous DMF, followed by the addition of EDCI and NHS under stirring. The mixture was continuously stirred for an additional 12 h under a nitrogen atmosphere, and then cycle peptide [W5R4]K dissolved in anhydrous DMF was added dropwise. The reaction was continued at room temperature for 72 h. The product [W5R4]K-PEG2K-PHIS (WPH) was purified by dialyzing (MWCO 3,500 Da), followed by lyophilization. The chemical structure of WPH was confirmed by ^{1}H-NMR.

Preparation of CUR/pSUR-NPs

CUR/pSUR-NPs were constructed by using the W/O/W double emulsification technique as reported previously (Xu et al., 2016a). Briefly, CUR, PLGA, and WPH were dissolved in DCM as the organic phase, and then emulsified with the internal aqueous phase (containing the pSUR gene) by sonication at 45 W for 20 s in an ice bath. PVA solution (1%, 4 mL) was added into the primary emulsion and emulsified by sonication (75 W for 2 min) to produce the multiple emulsion (W/O/W). PVA (1%, 2 mL) was further added and the final W/O/W emulsion was obtained by sonication at 40 W for 20 s. The organic solvent was immediately evaporated under vacuum at 37°C. The obtained colloidal solution was centrifuged (13,300 rpm, 40 min) at 4°C to remove PVA and the unencapsulated drug/gene. The precipitate was re-dispersed in PBS (pH 7.4) to get CUR/pSUR-NPs. This process was also used to prepare the contrast agents including the single drug or gene loaded CUR-NPs and pSUR-NPs.

Characterization of CUR/pSUR-NPs

Entrapment Efficiency and Drug Loading

Entrapment efficiency (EE%) and drug loading capacity (DL%) of CUR/pSUR-NPs were calculated as previously described (Xu et al., 2016b; Feng et al., 2020). Firstly, the supernatant and sediment were collected after centrifuging the CUR/pSUR-NPs colloidal solution. Then the supernatant was incubated with Hoechst 33258 (0.15 μg/mL), followed by a measurement of the fluorescence intensity by a spectrometer (Perkin Elmer, USA) at a 358 nm excitation wavelength and a 457 nm emission wavelength, which was used to calculate the amount of pSUR gene unentrapped into NPs. Meanwhile, the sediment was dissolved in methanol, and the content of CUR entrapped into CUR/pSUR-NPs was measured by UV-vis spectrophotometer (UV-2550, Shimadzu, Japan) with the detection wavelength at 420 nm. EE% and DL% of pSUR and CUR were monitored by using the following formulae:

$$\text{EE\% (pSUR)} = \left(\frac{\text{initial pSUR gene content content of pSUR gene unentrapped}}{\text{initial pSUR gene content}}\right) \times 100$$

$$\text{DL\% (pSUR)} = \left(\frac{\text{initial pSUR gene content content of pSUR gene unentrapped}}{\text{weight of nanoparticles}}\right) \times 100$$

$$\text{EE\% (CUR)} = \left(\frac{\text{content of CUR entrapped in nanoparticles}}{\text{initial CUR content}}\right) \times 100$$

$$\text{DL\% (CUR)} = \left(\frac{\text{content of CUR entrapped in nanoparticles}}{\text{weight of nanoparticles}}\right) \times 100$$

Particle Size and Zeta Potential

The mean diameter and zeta-potential of CUR/pSUR-NPs were determined by a Zetasizer Nano ZS (Malvern Instruments, Ltd., Malvern, Worcestershire, U.K.) at 25°C. Additionally, to investigate the influence of pH, CUR/pSUR-NPs were re-dispersed in PBS pH 4.5 and PBS pH 7.4, respectively, and the particle size and zeta-potential were further measured after shaking at 37°C at a gentle rate of 100 rpm for 24 h. A total of 3 parallel runs were carried out for each measurement, and all data were expressed as the mean ± SD.

Transmission Electron Microscopy (TEM)

For morphological observations, a small drop of the CUR/pSUR-NPs dispersion was placed on a copper grid and then negatively stained with a 2% (w/v) phosphotungstic acid solution for 2 min. Excess fluid was removed using a piece of filter paper. Morphology was examined on a transmission electron microscope (H-600, Hitachi, Ltd., Japan).

Differential Scanning Calorimetry (DSC)

Differential scanning calorimetry (DSC, 200PC, Netzsch, Karlsruhe, Germany) was used to perform the physical property of CUR loaded in CUR/pSUR-NPs. Freeze-dried

CUR/pSUR-NPs, free CUR, blank nanoparticle, and the physical mixture of the latter two with the same mass ratios as those in CUR/pSUR-NPs were heated from 20 to 400°C at a speed of 10°C/min.

In vitro CUR and pSUR Release

The release profiles of CUR and pSUR in CUR/pSUR-NPs were evaluated in phosphate buffer (PBS) containing 1 % (w/v) Tween 80 at pH 7.4 and 4.5, respectively. CUR/pSUR-NPs dispersed in PBS were divided into 20 parts and shaken at 37°C at a gentle rate of 100 rpm. One part was taken out at a definite time interval, and then treated with centrifugation. The amount of released pSUR in the supernatant and CUR remained in the sediment were investigated by the same methods as described at section Entrapment Efficiency and Drug Loading.

Hemolysis Assay

We first obtained 2% erythrocyte dispersion and then treated it with various amounts of formulations. Deionized water and normal saline (NS) were, respectively, employed as the positive and negative control. After incubation at 37°C for 3 h, all the samples were centrifuged. The absorbance (A) of the obtained supernatant was monitored by UV-Vis spectrophotometer (Perkin-Elmer Lambda35, USA) at 545 nm. The percentage of the samples-induced hemolysis was measured as follows:

$$\text{Hemolysis (\%)} = \frac{\text{A of sample} - \text{A of negative control}}{\text{A of positive control} - \text{A of negative control}} \times 100$$

In vitro Experiments

Cellular Uptake of Nanoparticles

SKOV-3 and Hela cells were seeded and cultured in 24-well plates overnight. The original medium was replaced by a fresh medium containing CUR/pSUR-NPs (shRNA labeled with red fluorescence). After incubation for 4h, the supernatant was removed and the cells were washed twice with cold PBS (pH 7.4). Cells were fixed in 4 % paraformaldehyde for 10 min at room temperature, and nuclei were stained using Hoechst 33258 (2.5 μg/mL) for 15 min in the dark. Finally, cells were visualized and imaged using a fluorescence microscopy.

Lysosomal Escape and Nuclear Targeting

In order to investigate the lysosomal escape and nuclear targeting properties of nanocarriers, a fluorescent lipophilic dye DiI was incorporated into the nanoparticles by the same W/O/W method as described in the section Preparation of CUR/pSUR-NPs. After overnight culturing, the medium was removed and replaced by a fresh medium containing DiI-NPs. After a 4 h incubation, the cells were washed, and stained by LysoTracker Green probe (Life technologies, USA) and Hoechst 33258. After being fixed with 4% paraformaldehyde, finally, the subcellular localization was observed using a fluorescence microscope. Meanwhile, to investigate the role of the PHIS and [W5R4]K segments, different nanoparticles, namely PLGA-NPs (P-NPs) and PLGA/PH-NPs (P/PH-NPs) were used as the contrast.

Penetration in Multicellular Tumor Spheroids

SKOV-3 and Hela tumor spheroids *in vitro* were first prepared. Low melting point agarose (2%, w/v) was added into the flat bottom of a 96-well plate, and 3,000 cells were seeded on it. Cells were cultured until uniform spheroids formed, then DiI-NPs were added. After further incubation for 12 h, the spheroids were rinsed, and their fluorescence intensity was observed with a confocal microscopy (Zeiss LSM 800 Airyscan).

Transfection of Nanoparticles

Gene transfection efficiency was tested using pGFP as reporter gene in HEK293 cells. pGFP-NPs (namely pGFP-P/WPH-NPs here) were prepared by the W/O/W method as described in the section Preparation of CUR/pSUR-NPs. Cells were seeded into 24-well plates. After 24 h, the old media were replaced by a fresh medium with the pGFP-NPs (4 μg of pDNA per well). The NPs containing a medium was replaced with a fresh medium at 4 h. After 48 h incubation, cells were imaged under fluorescence microscopy. Meanwhile, the transfection efficiency of contrast agents were also investigated, including pGFP-P-NPs which were conducted by PLGA polymer only, and pGFP-P/PH-NPs which were conducted by PLGA and PEG-PHIS polymers.

To investigate the influence of serum components, transfection efficiency of pGFP-NPs were further tested in a serum-free and serum-contained medium. After incubating the cells for 24 h, the old media were replaced by a fresh serum-free or serum-contained medium with the pGFP-NPs (4 μg pDNA per well). This medium was replaced with a fresh serum-contained medium at 4 h. After 48 h, cells were imaged using fluorescence microscopy. After that, the cell lysates were harvested and the transfection efficiency was evaluated by a FACS Calibur flow cytometer (FACS Canto II, BD Biosciences, San Jose, CA). Lipofectamine® 2000 was used as control.

Transfection efficiencies of P/WPH-NPs on SKOV-3 and Hela cells were also investigated, according to the same procedure on HEK 293.

Cell Viability Assay by MTT

SKOV-3 and Hela cells were seeded and cultured in 96-well plates. The cells were incubated with CUR-NPs, pSUR-NPs, physical mixture of two formers (namely Mixture-NPs), CUR/pSUR-NPs, and free CUR for 24 h. The concentrations of pSUR were 0.5 and 1 μg/mL, and corresponding concentrations of CUR were 1 and 10 μg/mL, respectively. Subsequent experimental steps were the same as described in section Syntheses of PEG_{2K}-PHIS.

Cell Apoptosis Analysis

The apoptosis of SKOV-3 and Hela cells was determined by an Annexin V-FITC/PI apoptosis detection kit. Briefly, after treatment with CUR, CUR-NPs, pSUR-NPs, Mixture-NPs, and CUR/pSUR-NPs at 37°C for 12 h, cells were trypsinized and collected by centrifugation. The cells were washed and resuspended in binding buffer. The cells were, respectively, stained with Annexin V-FITC and PI, followed by flow cytometry analysis (Becton-Dickinson, USA).

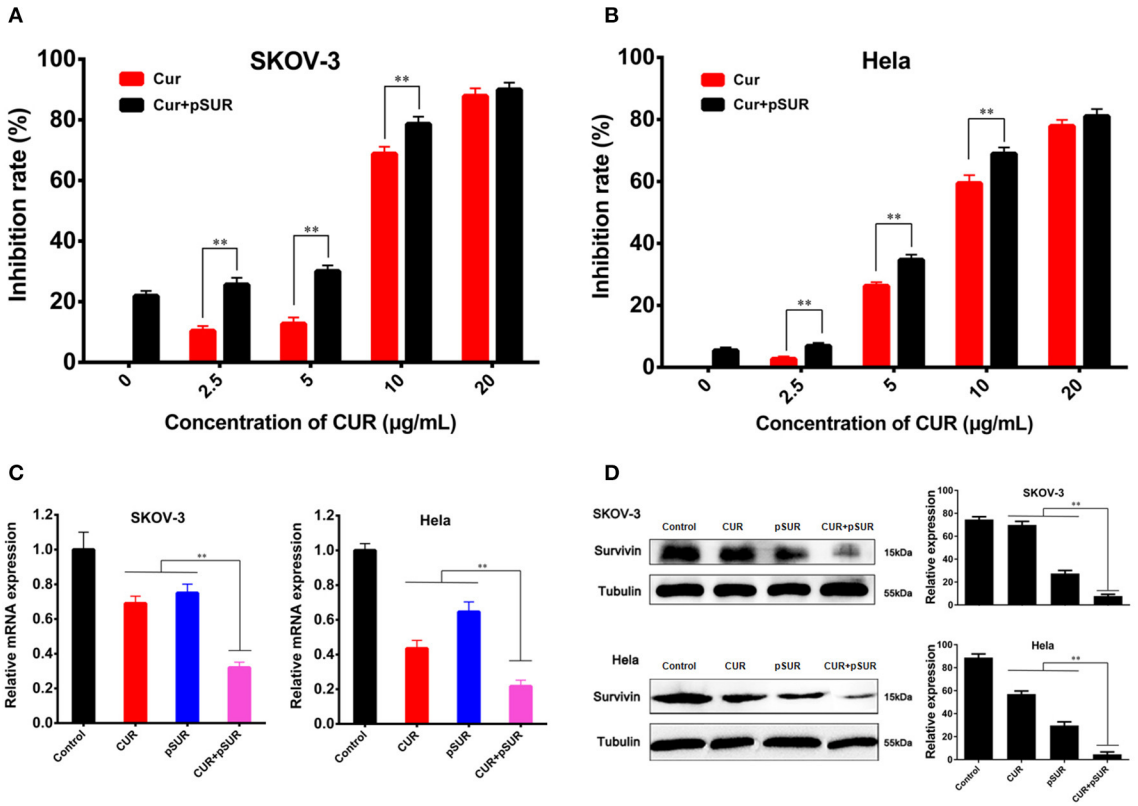

FIGURE 2 | Combined treatment of CUR and pSUR enhanced anti-tumor effects *in vitro*. Growth inhibition of SKOV-3 **(A)** and Hela **(B)** cells after treatment with varying concentrations of CUR or the combination of CUR and pSUR. Relative survivin mRNA **(C)** and protein **(D)** expression determined by RT-PCR and western blotting on SKOV-3 and Hela cells after treatment with CUR, pSUR, and their combination. $^{**}P < 0.01$.

Immunofluorescence Staining of Cleaved Caspase-3

SKOV-3 and Hela cells were seeded and cultured in 24-well plates. CUR, CUR-NPs, pSUR-NPs, Mixture-NPs, and CUR/pSUR-NPs were incubated for 24 h. Cells were fixed with paraformaldehyde, permeabilized with 0.1% Triton X-100, blocked with bovine serum albumin (BSA), and incubated with a cleaved caspase-3 antibody. Next, the immunocomplexes were incubated with a Alexa 488 anti-mouse secondary antibody and stained by Hoechst 33258. The signals and colocalization were assessed by fluorescence microscopy. The fluorescence intensity was measured by Image J software.

Nuclear Morphological Analysis

Apoptotic morphological changes were evaluated using Hoechst 33258 staining. After 48 h of CUR, CUR-NPs, pSUR-NPs, Mixture-NPs, and CUR/pSUR-NPs incubation, the cells were fixed with paraformaldehyde and stained with Hoechst 33258. Then the nuclear morphology of cells was observed by fluorescence microscopy.

Statistical Analysis

All quantitative data were presented as mean ± standard deviation (SD). Statistical comparisons between two groups were analyzed using an unpaired student *t*-test, and comparisons between multiple groups were assessed by one-way ANOVA. A value of $P < 0.05$ was considered significant and $P < 0.01$ was considered highly significant.

RESULTS AND DISCUSSION

Anti-tumor Effects of Free CUR and pSUR *in vitro*

The inhibitory effects on the proliferation of pSUR combined with various concentrations of free CUR were primarily evaluated by the MTT assay in SKOV-3 and Hela tumor cell lines. As shown in **Figures 2A,B**, both cells lines were inhibited with varying concentrations (2.5–20 μg/mL) of CUR. Additionally, the combined therapy displayed concentration-dependent cell growth inhibition activities. Notably, co-administration significantly elevated the inhibitory effects compared with the single use of CUR, revealing the synergistic effect arising from the co-delivery of CUR and pSUR.

The suppression of survivin expression was further evaluated using RT-PCR and western blot (**Figures 2C,D**). pSUR showed significant downregulation effects of the survivin mRNA/protein on both SKOV-3 and Hela cell lines, confirming that pSUR conducted in this work was indeed able to knock down the survivin expression. CUR also showed a strong inhibitory effect.

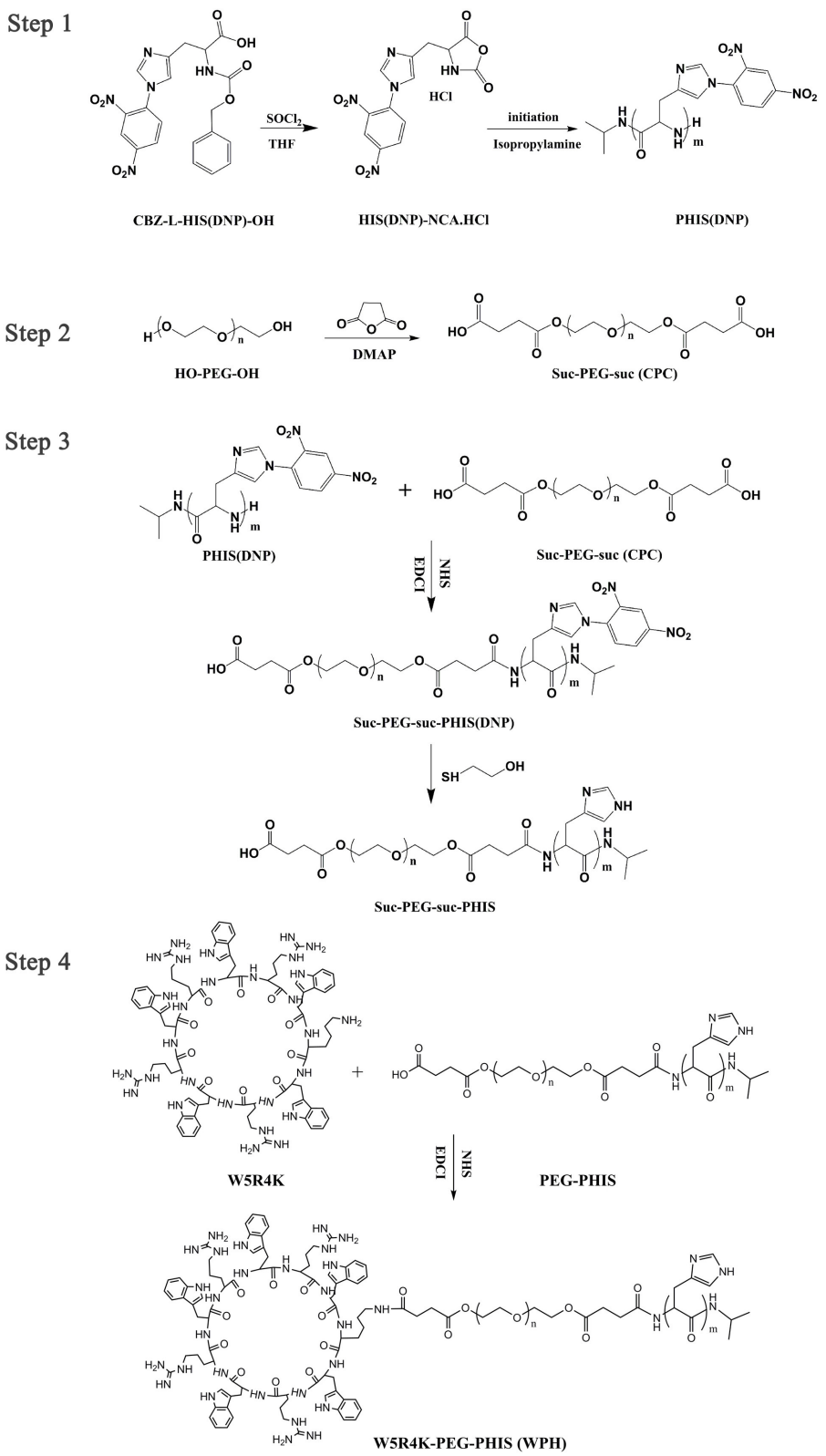

FIGURE 3 | Overall scheme for the synthesis of WPH.

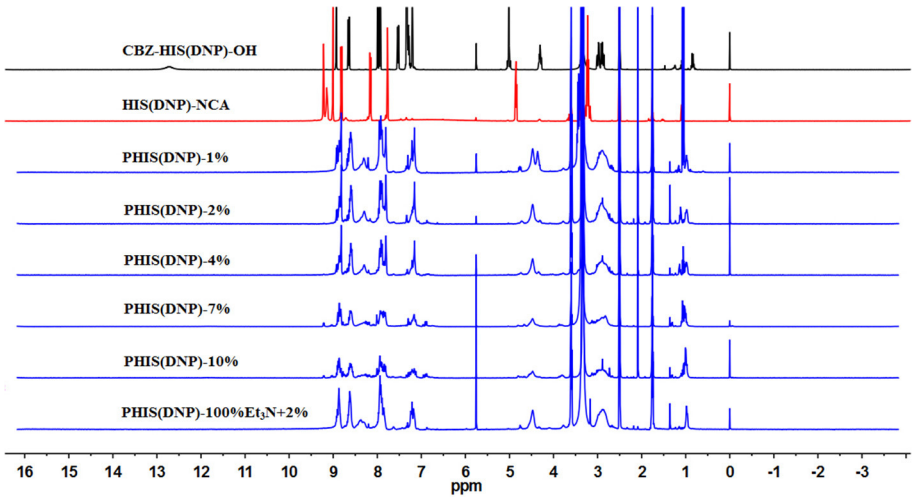

FIGURE 4 | ^{1}HNMR spectrum of PHIS(DNP) with different polymerization degrees (P.D.). The P.D. of polyhistidine was calculated by comparing the integrations of hydrogen protons on isopropylamine methyl and hydrogen protons of the DNP group on PHIS(DNP).

The results were in agreement with the earlier studies, in which most of the cell types displayed a decreased expression of survivin following curcumin treatment (Watson et al., 2010; Khaw et al., 2013). More importantly, pSUR and CUR co-administration exhibited the strongest inhibition, ascribed to the synergistic effect of the gene and drug.

Synthesis and Characterization of Polymer Conjugates

An overall synthetic route for preparation of [W5R4]K-PEG$_{2K}$-PHIS (WPH) was present in **Figure 3**. The structure of N^{im}-DNP-L-histidine NCA·HCl was confirmed by ^{1}H NMR [400 MHz, d6-DMSO trimethylsilyl (TMS)]: 8.25–9.26 (2,4-dinitrophenyl protons, DNP), 8.80 (-NH-), 8.25 (-N-CH=C-), 7.84 (-N=CH-), 4.88 (-CH-), and 3.25 (-CH$_2$-) (**Figure 4**). The ring opening polymerization of N^{im}-DNP-L-histidine NCA·HCl was then performed using different molar ratios of the initiator to monomer (I/M ratio). The polymerization degree (P.D.) of polyhistidine was calculated by comparing the integrations of hydrogen protons on isopropylamine methyl and hydrogen protons of DNP group on PHIS(DNP) (**Table 1**). ^{1}H NMR [400 MHz, d6-DMSO trimethylsilyl (TMS)] for PHIS(DNP) with various P.D.: 8.21–9.00 (2,4-dinitrophenyl protons, DNP), 7.98 (-N-CH=C-), 7.26 (-N=CH-), 4.41 (-CH-), 3.35 (-CH$_2$-), and 1.00 (-(CH$_3$)$_2$) (**Figure 4**). Results showed that P.D. of PHIS(DNP) decreased with the increasing I/M ratios from 1 to 7%, which was consistent with the previous study (Lee et al., 2003). Although when the I/M ratios further increased to 10%, P.D. no longer changed. The high I/M ratios of 7 and 10% produced rather low-molecular-weight polymers, likely due to the excessive initiators and faster propagation rates. Additionally, the P.D. of PHIS(DNP) initiated by (100% triethylamine + 2% isopropylamine) was lower than that by 2% isopropylamine only. This observation is not well-understood, but could be related to the incomplete neutralization of hydrochloride from N^{im}-DNP-L-histidine NCA·HCl. The residual salts might influence the following initiation by isopropylamine.

TABLE 1 | Polymerization degrees (P.D.) of PHIS(DNP) with various I/M molar radios.

Initiator with different I/M molar radios	P.D. of PHIS(DNP)
1% isopropylamine	22–24
2% isopropylamine	18–20
4% isopropylamine	17–18
7% isopropylamine	5–6
10% isopropylamine	5–6
100% triethylamine + 2% isopropylamine	12–14

PHIS(DNP) with P.D. of 6, 12, and 18, namely PHIS(DNP)$_{6U}$, PHIS(DNP)$_{12U,}$ and PHIS(DNP)$_{18U}$ were then selected to prepare PEG-PHIS(DNP)$_{6U}$, PEG-PHIS(DNP)$_{12U,}$ and PEG-PHIS(DNP)$_{18U,}$ respectively. The structures of these DNP-protected diblock polymers were confirmed by ^{1}H NMR [400 MHz, d6-DMSO trimethylsilyl (TMS)]: 7.93–8.88 (2, 4-dinitrophenyl protons, DNP), 7.64 (-N-CH=C-), 3.65 (-CH$_2$CH$_2$- in PEG group), 3.35 (-CH$_2$- in PHIS group), 2.65–2.68 (-COCH$_2$CH$_2$CO-), and 1.00 (-(CH$_3$)$_2$) (**Figures 5–7**). Otherwise, removal of the benzyloxylcarbonyl group was proven by the disappearance of the peak of 7.93–8.88 (DNP). ^{1}H NMR [400 MHz, d6-DMSO trimethylsilyl (TMS)] for PEG-PHIS (PH) with different P.D.: 8.21 (-N=CH-), 7.54 (-NH-C=O), 6.75 (-N-CH=C-), 3.65 (-CH$_2$CH$_2$- in PEG group), 3.35 (-CH$_2$- in PHIS group), 2.65–2.68 (-COCH$_2$CH$_2$CO-), and 1.00 (-(CH$_3$)$_2$) (**Figures 5–7**). Interestingly, peaks of 6.8 and 7.5 were observed, indicating that an active carboxylic terminal was provided in PH, which could be used to synthesize WPH in the next reaction step.

Finally, the purified PH diblock copolymers were coupled with [W5R4]K to yield triblock copolymers with different P.D. of PHIS. ^{1}H NMR [400 MHz, d6-DMSO trimethylsilyl (TMS)]

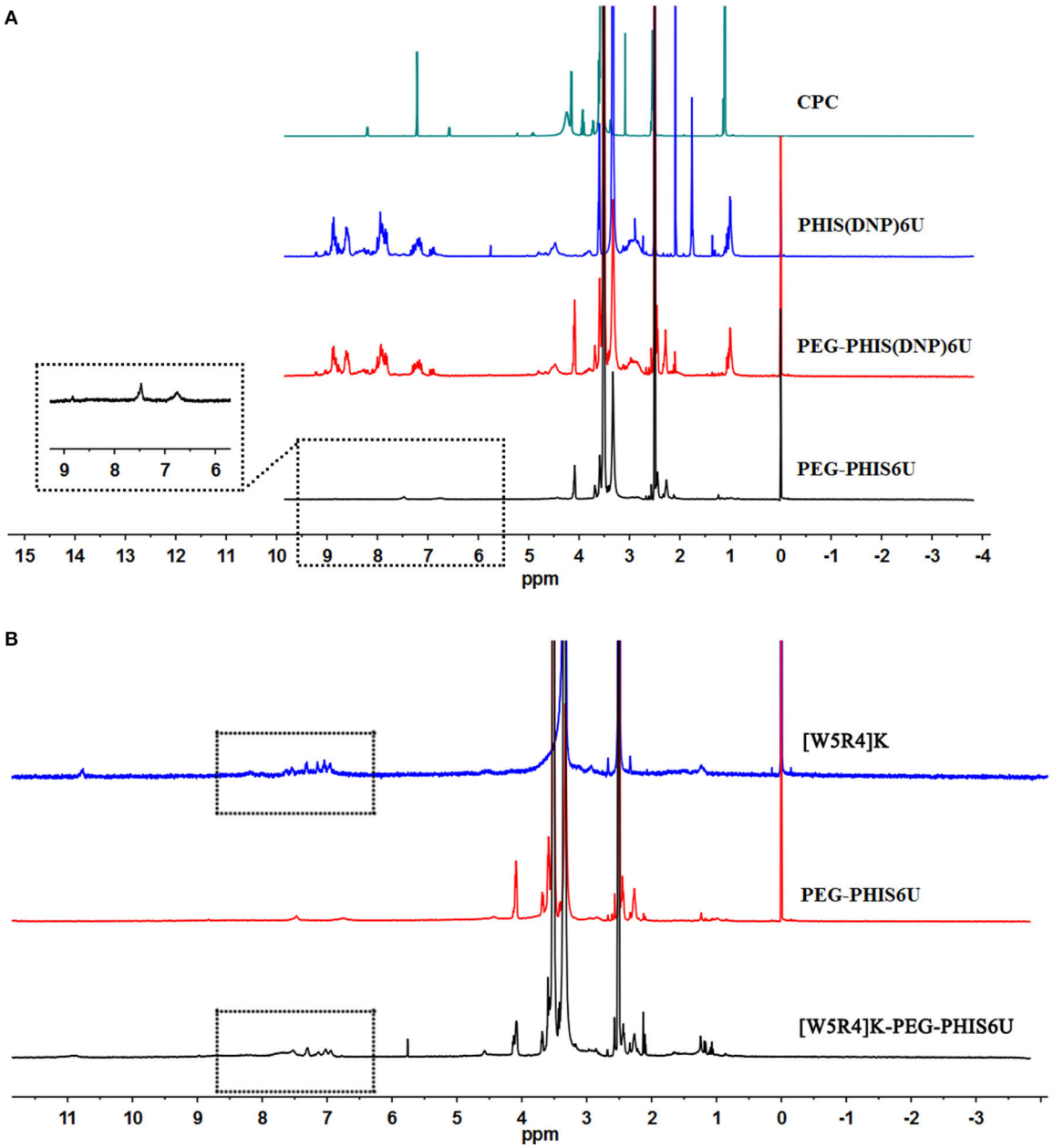

FIGURE 5 | ^{1}H-NMR spectrum of CPC, PEG-PHIS(DNP)$_{6U}$, PEG-PHIS$_{6U,}$ and WPH$_{6U}$. **(A)** PEG-PHIS$_{6U}$ was successfully synthesized by the removal of the benzyloxylcarbonyl group. **(B)** WPH$_{6U}$ was successfully synthesized for containing the principal proton peaks related to the [W5R4]K, PEG, and PHIS moieties.

for WPH: 6.96–8.22 (tryptophan indole ring proton), 3.65 (-CH_2CH_2- in PEG group), 3.35 (-CH_2- in PHIS group), 3.30 (cyclic peptide proton), 2.65–2.68 (-$COCH_2CH_2CO$-), and 1.00 (-$(CH_3)_2$). The principal peaks related to the [W5R4]K, PEG, and PHIS moieties in the ^{1}H-NMR spectrum of the final product indicated the successful synthesis of WPH (**Figures 5**–**7**).

Preparation and Characterization of CUR/pSUR-NPs

The preparation of the CUR/pSUR-NPs was depicted in **Figure 1**. The mass ratios of PLGA/WPH and the different P.D. of HIS in WPH triblock copolymer that might affect the particle size, EE%, and DL% were screened. As shown in **Figure 8**, all CUR/pSUR-NPs exhibited good size distribution and high EE% and DL% of both CUR and pSUR, indicating NPs had good properties for co-loading chemical drugs and genes. All NPs were characterized with nearly neutral surface potential. As the PLGA/WPH mass ratio elevated from 1/1 to 3/1, the particle sizes significantly increased, while the EE and DL showed no remarkable significant change. The increased particle size was likely due to the increased oil droplets in the emulsifying process with the increased PLGA concentration (Hou et al., 2017). Otherwise, as the P.D. of

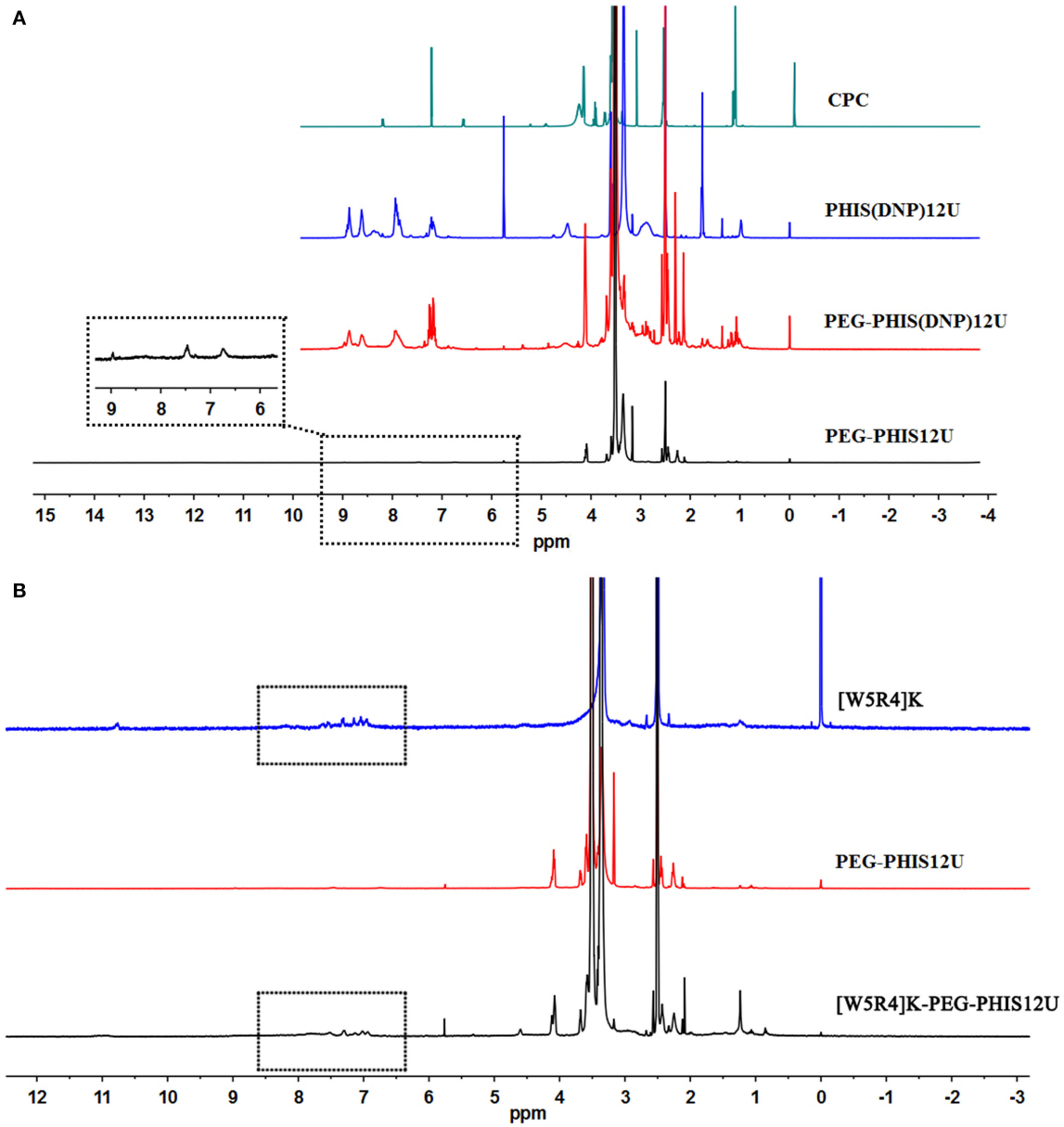

FIGURE 6 | ^{1}H-NMR spectrum of CPC, PEG-PHIS(DNP)$_{12U}$, PEG-PHIS$_{12U,}$ and WPH$_{12U}$. **(A)** PEG-PHIS$_{12U}$ was successfully synthesized by the removal of the benzyloxylcarbonyl group. **(B)** WPH$_{12U}$ was successfully synthesized for containing the principal proton peaks related to the [W5R4]K, PEG, and PHIS moieties.

HIS increased from 6 to 12, the particle sizes, EE and DL did not change significantly. Whereas, when the units further elevated to 18, the particle sizes markedly increased along with downward trends of EE and DL. The phenomenon was probably caused by the longer hydrophobic chain segment of PHIS, which could make the structure of NPs unstable during the solvent evaporation process. The pH-sensitive property of CUR/pSUR-NPs was further investigated. No obvious size changes were observed in pH 7.4, indicating the good stability of NPs in a normal physiological environment. However, in pH 4.5, the hydrated particle sizes were significantly increased, especially when the P.D. of HIS increased from 6 to 18, and the PLGA/WPH mass ratio was decreased from 3/1 to 1/1. This phenomenon might be related to the protonated PHIS blocks, which were positively charged in the acidic environment and caused the swelling of the core (Sun et al., 2015). The zeta potential was still neutral (data not shown), probably due to the PEG coating. Taking the parameters of sizes, EE, and DL into consideration, the optimal formulation with 1/1 PLGA/WPH mass ratio and 12 P.D. of HIS was selected and then its pharmaceutical properties were investigated.

The optimal NPs were uniformly distributed (PDI < 0.3, data not shown) with particles size around 180 nm. Otherwise, they had a good capacity for drug and gene incorporation with an

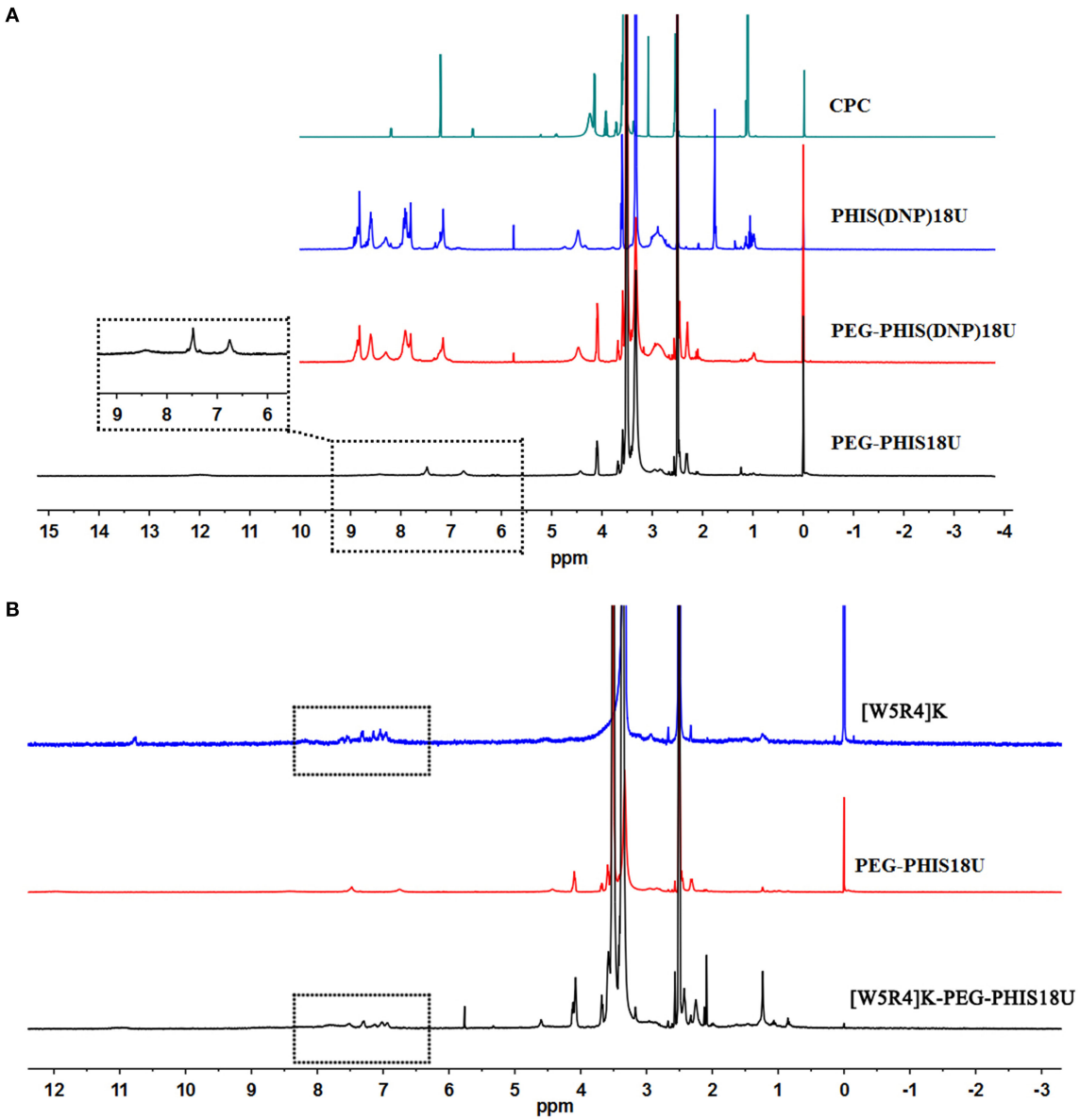

FIGURE 7 | ^{1}H-NMR spectrum of CPC, PEG-PHIS(DNP)$_{18U}$, PEG-PHIS$_{18U,}$ and WPH$_{18U}$. **(A)** PEG-PHIS$_{18U}$ was successfully synthesized by the removal of the benzyloxylcarbonyl group. **(B)** WPH$_{18U}$ was successfully synthesized for containing the principal proton peaks related to the [W5R4]K, PEG, and PHIS moieties.

EE% of 81.22 ± 1.56% and 93.41 ± 1.64%, and a DL% of 3.93 ± 0.12% and 0.46 ± 0.01%, respectively. TEM results certified that CUR/pSUR-NPs were homogeneous and spherical, being in good agreement with the narrow particle size distribution (**Figure 9A**).

In vitro release profiles of CUR and pSUR from CUR/pSUR-NPs were presented in **Figure 9B**. The CUR and pSUR loaded in NPs were progressively released in both of the release media with no obvious burst release. Moreover, typical pH-dependent releasing properties of CUR and pSUR were observed. At pH 7.4, 59.2 and 80.5% of CUR and pSUR were released at 72 h, while 93.7 and 73.5% were released at pH 4.5. The increased cumulative release might be caused by the protonated PHIS blocks in the acidic environment, that led to the swelling of core due to the same positive electrical charge (Sun et al., 2015). These release profiles can minimize the premature drug release during prolonged systemic circulation. In contrast, they can specifically enhance intracellular drug release, being beneficial to effective cancer treatment (Johnson et al., 2015). The pSUR gene displayed faster release rates than CUR. One reason might be that high hydrophilicity of the pSUR gene caused a relatively weaker interaction with hydrophobic polymer molecules than CUR. The observation was similar to our previous study (Xu et al., 2016b).

The DSC thermograms are shown in **Figure 9C**. An endothermic peak at 175.0°C was observed in the curve of

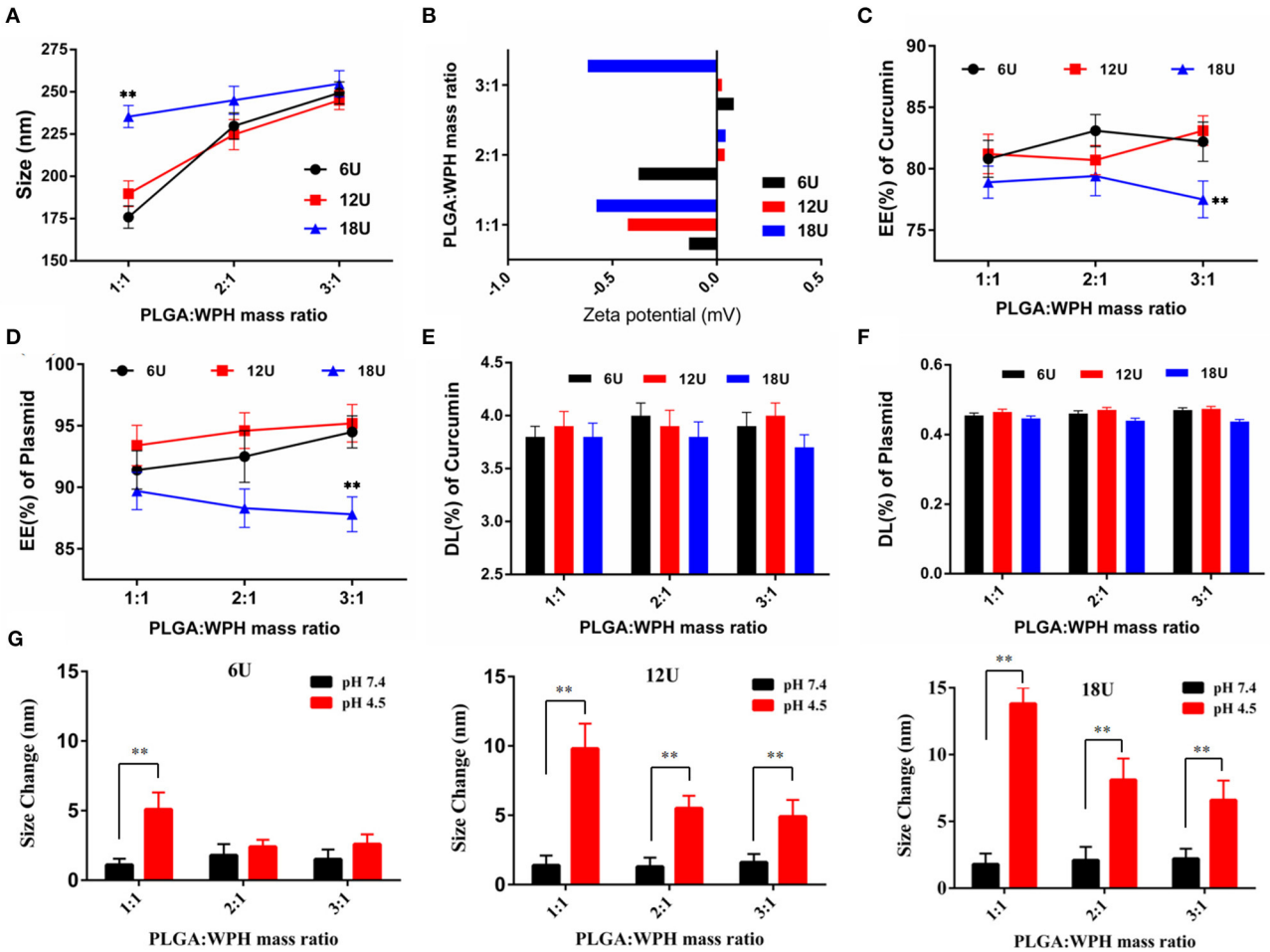

FIGURE 8 | The effects of mass ratios of PLGA/WPH and P.D. of HIS in WPH triblock copolymer on diameter **(A)**, zeta potential **(B)**, EE% **(C,D)**, and DL% **(E,F)** of CUR and pSUR of CUR/pSUR-NPs. **(G)** Size changes of P/WPH-NPs in PBS pH 7.4 and pH 4.5 with different mass ratios of PLGA/WPH and P.D. of HIS. $^{**}P < 0.01$.

free CUR powder. However, in the CUR/pSUR-NP group, the peak disappeared, and only two endothermic peaks at 118.2 and 193.6°C were presented, which corresponded to the PLGA and PVA's glass transition temperatures (Tg), respectively. Expectedly, the physical mixture presented all the three endothermic peaks, corresponding to the free CUR and the Tg of the PLGA and PVA. These results revealed that CUR had been successfully encapsulated into CUR/pSUR-NPs.

A hemolysis assay was conducted to evaluate CUR/pSUR-NPs' blood compatibility. All NPs treated groups had no visible hemolytic effect (**Figure 9D**). The percentage of erythrocyte hemolysis by all formulations was below 5%. The results suggested that CUR/pSUR-NPs had good blood compatibility and would be safe for i.v. injection.

Cellular Uptake and Intracellular Distribution of P/WPH-NPs

CUR (green autofluorescence) and red fluorescence labeled pSUR were used to investigate the co-uptake of the drug and plasmid in SKOV-3 and Hela cells. As **Figure 10A** showed, the green, red, and blue colors represent the CUR, pSUR, and the nucleus, respectively. The results showed that CUR and pSUR could be up-taken by the tumor cells simultaneously. Transporting the drug with the gene in the same carrier would be more advantageous for that they could be delivered to the same cells for combined actions and synergistic effects (Wang et al., 2006). Moreover, a great majority of CUR/pSUR-NPs subsequently targeted the nucleus, suggesting this nanovesicle is an excellent carrier that is suitable for the nuclear targeted delivery. The property might be related to the nuclear targeting profile of the [W5R4]K cell-penetrating peptide.

Additionally, the endosomal disruption of NPs in cells was further tested. To avoid an overlapped fluorescence signal between CUR and the Lysotracker (Green), we conducted DiI encapsulated PLGA/WPH-NPs (P/WPH-NPs) instead of CUR/pSUR-NPs. PLGA-NPs (P-NPs) and PLGA/PH-NPs (P/PH-NPs) label by DiI were used as the contrast. At 2 h, scattered green fluorescence inside of the cells was observed in the DiI-P/WPH-NPs and DiI-P/PH-NPs groups, indicating quick endosomal escape of the nanoparticles (**Figure 10B**).

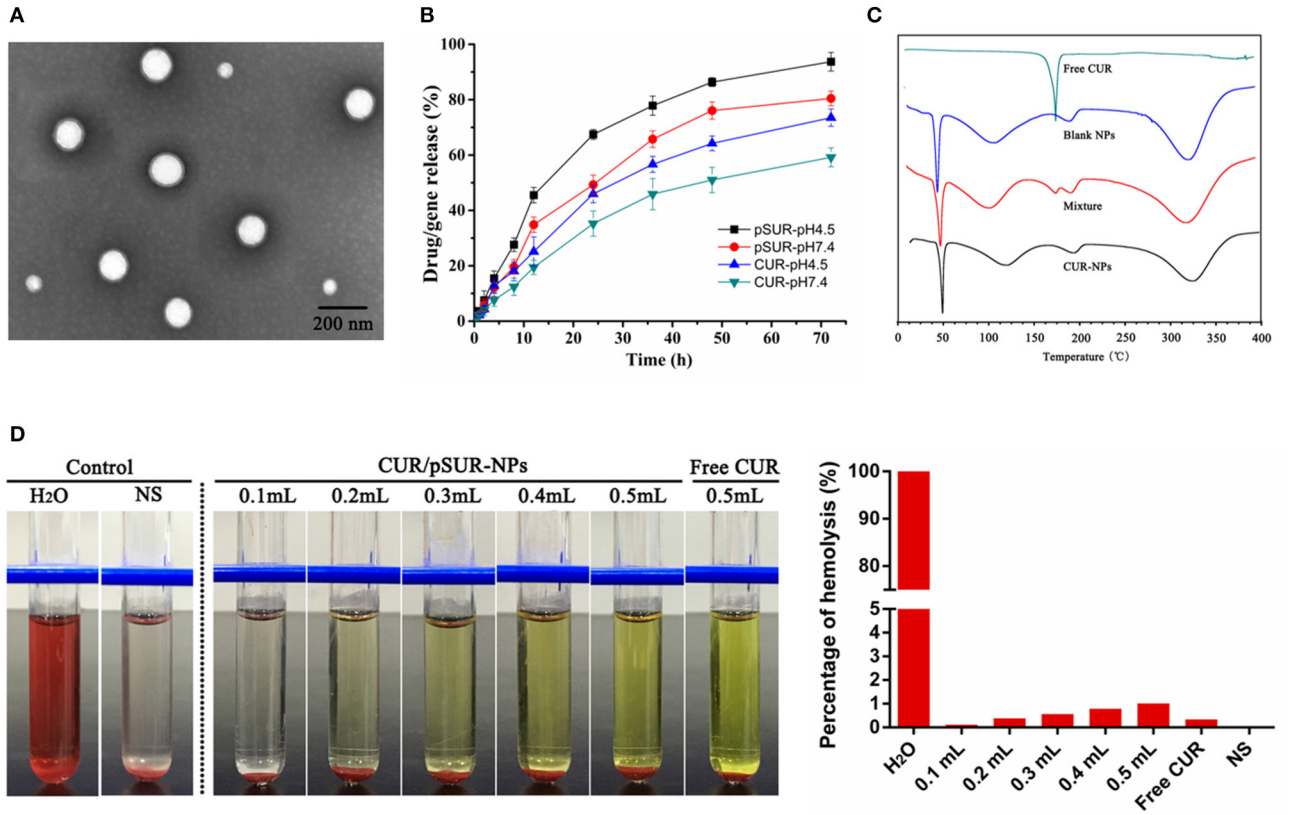

FIGURE 9 | Pharmaceutical properties of CUR/pSUR-NPs. **(A)** Representative TEM image of CUR/pSUR-NPs. **(B)** *In vitro* drug release profiles of CUR and pSUR from CUR/pSUR-NPs at pH 4.5 and pH 7.4. **(C)** DSC curves of free CUR, Blank NPs, physical mixture of CUR and Blank NPs, and CUR/pSUR-NPs. **(D)** Images of hemolysis and the percentages of hemolysis after treatment with various volumes of CUR/pSUR-NPs.

This phenomenon was probably attributed to the protonation of PHIS in the acidic tumor cells (Zhang et al., 2014). At 6 h, compared with the P-NPs and P/PH-NPs groups, a stronger superposition were seen as a pink color, implying lots of nanoparticles had escaped the endosome and entered the nucleus. The results confirmed our hypothesis of [W5R4]K for its potential of intracellular nuclear targeting delivery when utilized in drug/gene delivery polymeric nanosystems.

Enhanced Penetration in Multicellular Tumor Spheroids

To obtain initial evidence of the nanoparticle tissue-penetrating ability, three-dimensional tumor spheroids were used (Wang et al., 2017). *In vitro* tumor spheroids could imitate the *in vivo* status of solid tumors, due to the characterizations of altered enzyme activity, poor drug penetration, and a viable rim with gradients of oxygen tension (Ruan et al., 2015). The distribution of various formulations in superficial sections of both the SKOV-3 and Hela tumor spheroid was observed (**Figure 11**). The fluorescent intensity of DiI encapsulated P-NPs and P/PH-NPs decreased dramatically along with the increase of section depths. The two-kind particles were difficult in penetrating into the deep region of the tumor spheroid probably due to their large size. Nevertheless, DiI-P/WPH-NPs exhibited the strongest internalization within the spheroids, indicating that [W5R4]K conjugation could enhance the nanomedicines' uptake in tumor spheroids and improve their drug delivery efficiency. This property is highly promising for increased NPs' accumulation in tumors interstitium after extravasation from the blood vessels.

Transfection of P/WPH-NPs

The *in vitro* transfection activity of nanoparticles was shown in **Figure 12.** As present in **Figures 12A,C**, pGFP-P/WPH-NPs displayed the highest transfection efficiency on all the three cell lines compared with pGFP-P-NPs and pGFP-P/PH-NPs, likely because of the increased cellular uptake, fast endo/lysosome escape, elevated gene release rate, as well as the nucleus targeting property, which were surprisingly induced by the combination of the PHIS and [W5R4]K segments. Otherwise, the transfection efficiency on HEK 293 of Lipofectamine® 2000 dramatically decreases from 70.16 to 21.96% in a serum-contained medium (**Figure 12B**). The cause might be that the serum components especially the negatively charged proteins exhibited non-specific interactions with the cationic vector, which would largely affect the stability of the polyplex (Luan et al., 2016). However, pGFP-PLGA/WPH-NPs maintained the good transfection efficiency (22.06 vs. 21.17%) in the presence of serum, indicating that

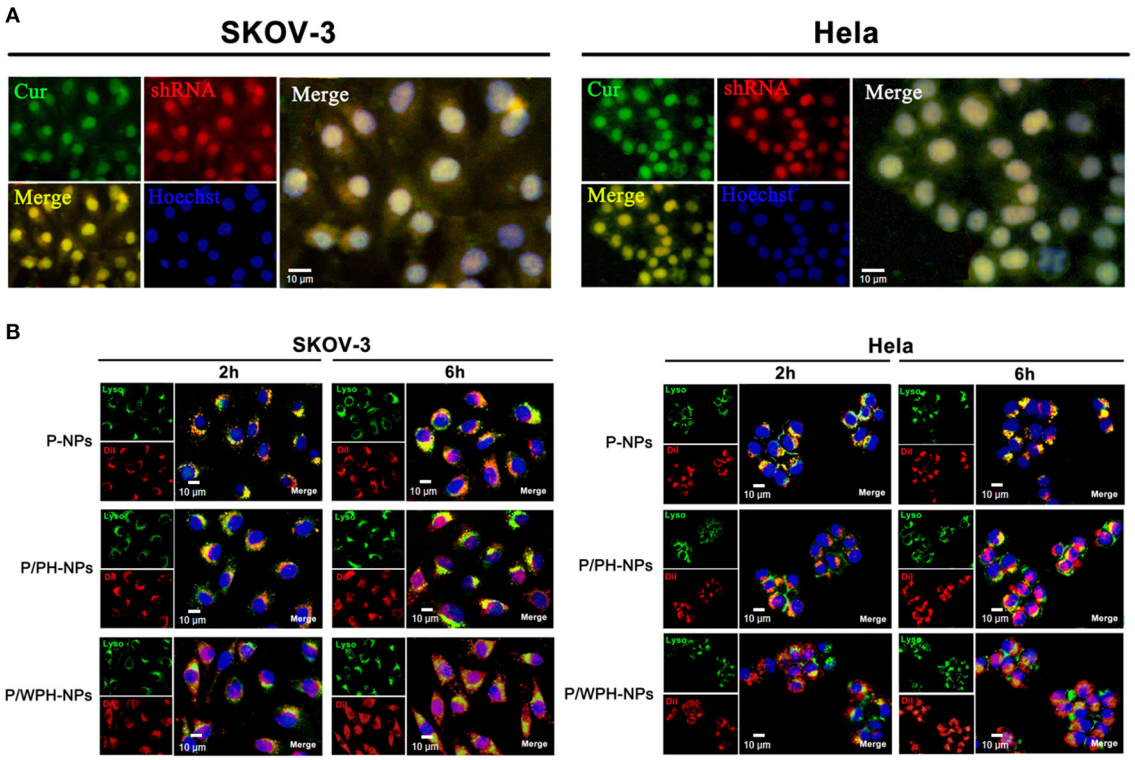

FIGURE 10 | Cellular uptake and intracellular distribution of P/WPH-NPs (with 3 replicates). **(A)** Simultaneous cellular uptake of CUR and red fluorescence labeled pSUR on SKOV-3 and Hela tumor cells. The green, red, and blue colors represent the CUR, pSUR, and the nucleus, respectively. **(B)** Endosomal disruption and intracellular nuclear targeting of P/WPH-NPs on SKOV-3 and Hela cells. DiI (red fluorescence dye) was encapsulated in various nanocarriers. Endosome (Green) stained by Lysotracker® Green.

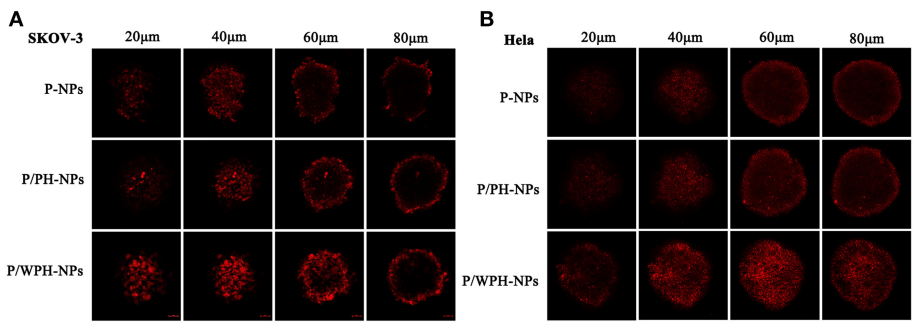

FIGURE 11 | Confocal images of the uptake of DiI-labeled P-NPs, P/PH-NPs, and P/WPH-NPs on SKOV-3 **(A)** and Hela **(B)** tumor spheroids with different depths.

the P/WPH-NPs were quite stable and are seldom affected by the serum.

Proliferation Inhibition of Tumor Cells of CUR/pSUR-NPs

As shown in **Figure 13**, concentration-dependent cell growth inhibition activities on SKOV-3 and Hela cells of all the formulations were present. Compared to single drug- or gene-loaded nanoparticles (CUR-NPs and pSUR-NPs), CUR/pSUR-NPs, and Mixture-NPs displayed higher proliferation inhibition activity ($P < 0.05$), indicating that the anti-tumor activity could be enhanced by a combination of CUR and pSUR. Intriguingly, CUR/pSUR-NPs presented a stronger cytotoxic effect compared with Mixture-NPs ($P < 0.05$). The reason might be that Mixture-NPs would disperse their firepower against the target inevitably, because it might be difficult for Mixture-NPs to ensure the simultaneous internalization of CUR and pSUR into the same cells. Hence, encapsulating CUR/pSUR into the one nanoparticle was crucial to exert higher anti-tumor activity.

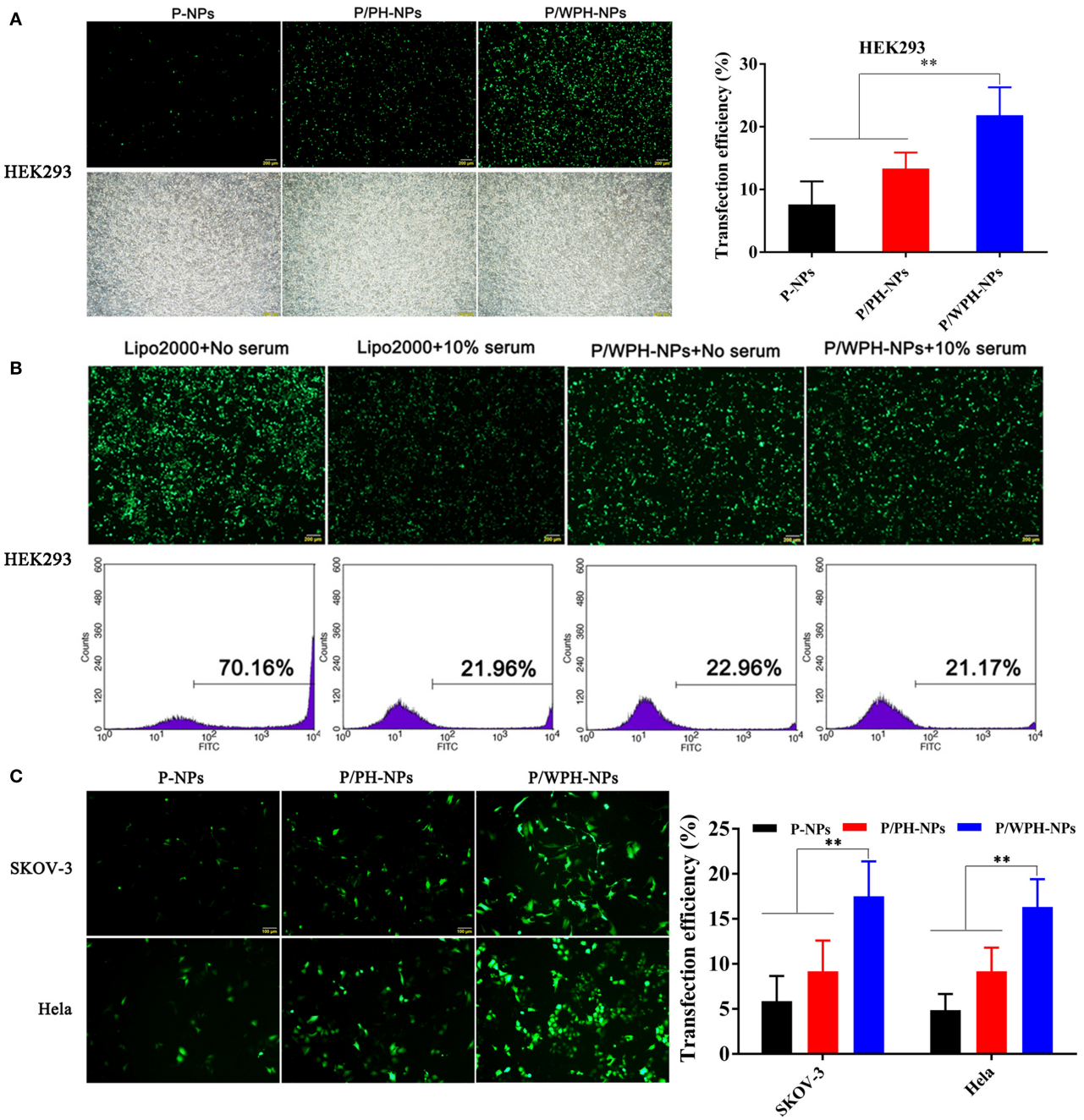

FIGURE 12 | (A) Transfection efficiency in HEK 293 cells mediated by P-NPs, P/PH-NPs, and P/WPH-NPs. Up column: GFP fluorescence microscopy photographs; Down column: light microscopy photographs. **(B)** Effects of serum on transfection of Lipofectamine® 2000 and P/WPH-NPs on HEK 293 cells. Up column: GFP fluorescence microscopy photographs; Down column: flow cytometry graphs. **(C)** Transfection efficiency in SKOV-3 and Hela cells mediated by P-NPs, P/PH-NPs, and P/WPH-NPs. $^{**}P < 0.01$.

In vitro Cell Apoptosis Analysis After Treatment of CUR/pSUR-NPs

Cell apoptosis induction of co-delivery and mono-delivery formulations was evaluated against SKOV-3 and Hela cells. As shown in **Figure 14A**, shRNA incubation increased the percentage of both early and late apoptotic SKOV-3 cells, indicating that pSUR caused apoptosis induction likely due to the downregulation of survivin protein expression. CUR/pSUR-NPs markedly increased the early apoptotic, late apoptotic, and necrotic percentages compared to the free CUR, CUR-NPs, and Mixture-NPs groups, demonstrating the synergetic anti-tumor effect of CUR and pSUR in one single nanocarrier. Additionally,

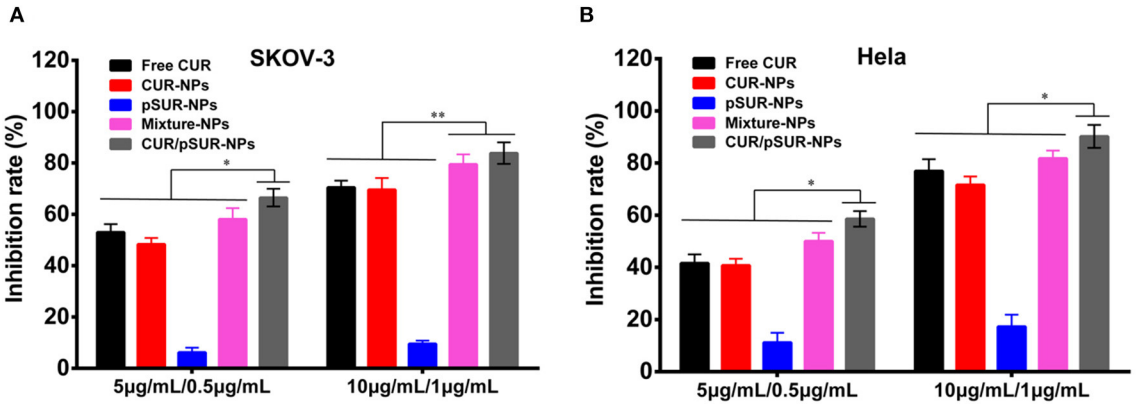

FIGURE 13 | Growth inhibition of SKOV-3 **(A)** and Hela **(B)** cells after treatment with free CUR, CUR-NPs, pSUR-NPs, Mixture-NPs, and CUR/pSUR-NPs, respectively. $^{**}P < 0.01$, $^{*}P < 0.05$.

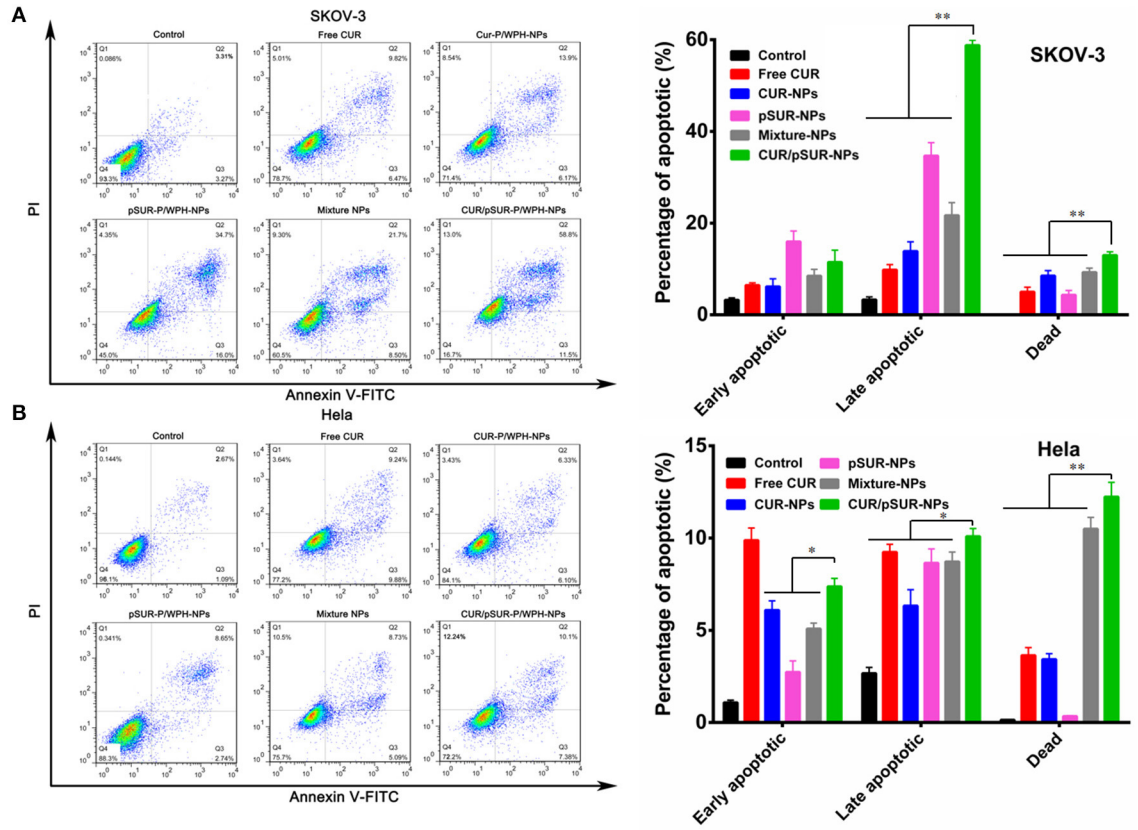

FIGURE 14 | Cell apoptosis of SKOV-3 **(A)** and Hela **(B)** cells at 12 h induced by free CUR, CUR-NPs, pSUR-NPs, Mixture-NPs, and CUR/pSUR-NPs tested by flow cytometric analysis. $^{*}P < 0.05$ and $^{**}P < 0.01$.

the combination groups induced more necrotic cells than single drug- or gene-loaded nanoparticles (CUR-NPs and pSUR-NPs) on Hela cells (**Figure 14B**), implying combined therapy could induce stronger cell apoptosis effect than mono-therapy groups. Compared to the other nanoparticle formulations, CUR/pSUR-NPs had the highest proportion of early apoptotic, late apoptotic, and necrotic cells, revealing again that drug/gene co-delivery could achieve the synergistic apoptosis-inducing effects.

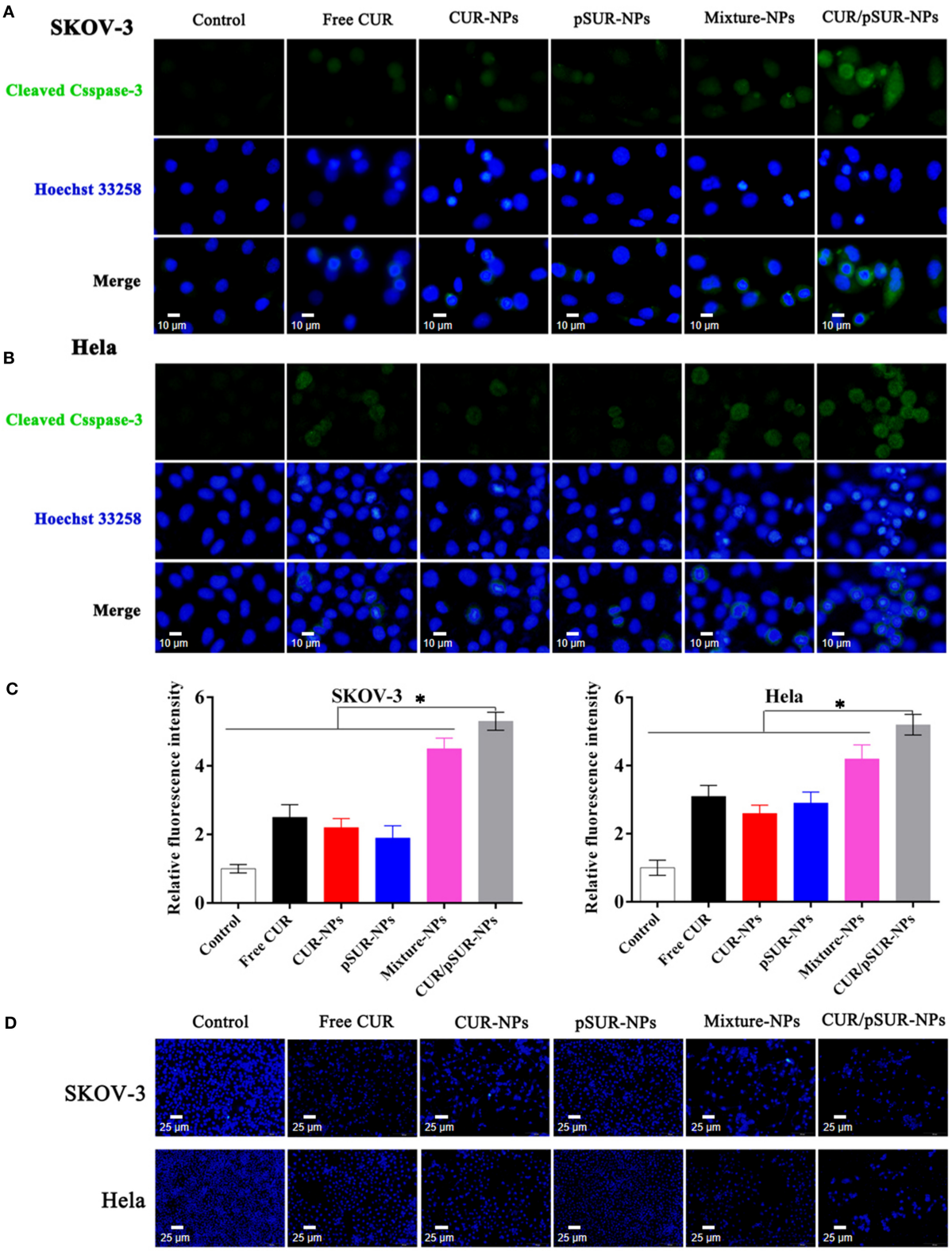

FIGURE 15 | Immunofluorescence staining analysis (with 3 replicates) of cleaved caspase-3 in SKOV-3 **(A)** and Hela **(B)** cells after free CUR, CUR-NPs, pSUR-NPs, Mixture-NPs, and CUR/pSUR-NPs treatment. **(C)** Relative fluorescence intensity of cleaved caspase-3 in SKOV-3 and Hela after various formulations' treatments. **(D)** Fluorescence microscopic appearance (with 3 replicates) of Hoechst-stained nuclei of SKOV-3 and Hela cells with the treatment of free CUR, CUR-NPs, pSUR-NPs, Mixture-NPs, and CUR/pSUR-NPs. *$P < 0.05$.

Cleaved Caspase-3 Immunofluorescence Staining and Nucleus Morphology Staining

The cysteinyl aspartate specific protease (caspase) family, which is involved in apoptotic signal transduction, plays an important role in regulating apoptosis. Caspase-3 is the final performer (Wang and Wang, 2014). Herein, to investigate caspase-3 expression after CUR/pSUR-NPs treatment, immunofluorescence staining was performed. **Figures 15A,B** showed that treatment of CUR, CUR-NPs, pSUR-NPs, Mixture-NPs, and CUR/pSUR-NPs significantly upregulated the expression of caspase-3 to increase apoptosis. Although caspase-3 activation was induced more strongly in the Mixture-NPs and CUR/pSUR-NPs groups, implying that the combination of CUR and pSUR was advantageous. Moreover, CUR/pSUR-NPs performed the highest fluorescence intensity, revealing transporting CUR/pSUR into the one nanoparticle was essential to exert enhanced anti-tumor activity.

Otherwise, the apoptotic rates were determined by the morphology of cancer cell nuclei which was assessed by Hoechst 33258 staining. Apoptotic or necrotic cells usually undergo chromatin margination, chromatin condensation, fragmentation, and eventual disruption (Tang et al., 2014; Hou et al., 2017). In this study, the nuclei of SKOV-3 and Hela cells treated with CUR, CUR-NPs, Mixture-NPs, and CUR/pSUR-NPs were all damaged (**Figure 15C**). This suggested that CUR-induced morphological changes were associated with apoptosis. CUR/pSUR-NPs treatment was the severest and many nuclei disappeared completely, pointing to the crucial need of encapsulating CUR/pSUR into one nanoparticle, which could exert a higher apoptosis rate.

CONCLUSION

In summary, the newly designed copolymer WPH was synthesized for the first time, and the novel nanovector P/WPH-NPs co-encapsulating hydrophobic chemotherapy drugs (CUR) and hydrophilic therapeutic genes (pSUR) was successfully prepared (CUR/pSUR-NPs). The optimized P/WPH-NPs achieved excellent features including preferable cellular uptake, efficient endosomal escape, nuclei targeting, elevated transfection efficiency, and enhanced tumor penetration, mediated by the combined effects of PHIS and [W5R4]K. To the best of our knowledge, the tumor penetration and nuclear targeting properties of [W5R4]K conjugated to nanoparticulate formulation were first proven in our study. Moreover, CUR/pSUR-NPs exhibited a more superior anti-tumor effect than the cocktail combination of CUR-NPs and pSUR-NPs, revealing that encapsulating CUR and pSUR into the same nanoparticle and transporting them to the same tumor cell was crucial in exerting higher synergistic therapeutic efficacy. These encouraging results suggested that the P/WPH-NPs based CUR/pSUR co-delivery system would be a promising strategy for clinical application in cancer therapy.

DATA AVAILABILITY STATEMENT

The raw data supporting the conclusions of this article will be made available by the authors, without undue reservation.

AUTHOR CONTRIBUTIONS

This project was conceptually designed by XS and XG. BX, WZ, and LC prepared materials and carried out the majority of the experiments. Data analysis and interpretation were carried out by YZ and AF. The manuscript was prepared by BX and CJ and edited by JZ. All authors discussed the results and implications and commented on the manuscript.

FUNDING

This work was financially supported by the National Natural Science Foundation of China (No. 81600122), Sichuan Province Science and Technology Support Program (2019YFH0155, 2019YFG0268, and 2018JY0582) and Sichuan Health and Health Committee Support Program (20PJ255).

REFERENCES

Afsharzadeh, M., Hashemi, M., Mokhtarzadeh, A., Abnous, K., and Ramezani, M. (2018). Recent advances in co-delivery systems based on polymeric nanoparticle for cancer treatment. *Artif. Cells Nanomed. Biotechnol.* 46, 1095–1110. doi: 10.1080/21691401.2017.1376675

Chen, W., Zhang, M., Shen, W., Du, B., Yang, J., and Zhang, Q. (2019). A polycationic brush mediated co-delivery of doxorubicin and gene for combination therapy. *Polymers* 11:60. doi: 10.3390/polym11010060

Ding, J. X., Chen, J. J., Gao, L. Q., Jiang, Z. Y., and Zhang, Y. (2019). Engineered nanomedicines with enhanced tumor penetration. *Nanotoday* 29:100800. doi: 10.1016/j.nantod.2019.100800

Feng, C., Ouyang, J., Tang, Z., Kong, N., Liu, Y., Fu, L., et al. (2020). Germanene-based theranostic materials for surgical adjuvant treatment: Inhibiting tumor recurrence and wound infection. *Matter* 3, 127–144. doi: 10.1016/j.matt.2020.04.022

Frassanito, M. A., Saltarella, I., Vinella, A., Muzio, L. L., Pannone, G., Fumarulo, R., et al. (2019). Survivin overexpression in head and neck squamous cell carcinomas as a new therapeutic target. *Oncol. Rep.* 41, 2615–2624. doi: 10.3892/or.2019.7082

Gao, C., Tang, F., Gong, G., Zhang, J., Hoi, M. P. M., Lee, S. M. Y., et al. (2017). pH-Responsive prodrug nanoparticles based on a sodium alginate derivative for selective co-release of doxorubicin and curcumin into tumor cells. *Nanoscale* 9, 12533–12542. doi: 10.1039/C7NR03611F

Hamzehzadeh, L., Atkin, S. L., Majeed, M., Butler, A. E., and Sahebkar, A. (2018). The versatile role of curcumin in cancer prevention and treatment: a focus on PI3K/AKT pathway. *J. Cell Physiol.* 233, 6530–6537. doi: 10.1002/jcp.26620

Hou, X., Yang, C., Zhang, L., Hu, T., Sun, D., Cao, H., et al. (2017). Killing colon cancer cells through PCD pathways by a novel hyaluronic acid-modified shell-core nanoparticle loaded with RIP3 in combination with chloroquine. *Biomaterials* 124, 195–210. doi: 10.1016/j.biomaterials.2016.12.032

Hung, C. S., Liu, H. H., Huang, M. T., Cheng, C. W., Kuo, L. J., Ho, Y. S., et al. (2012). Knockdown survivin expression reduces the efficacy of curcumin treatment in hepatocellular carcinoma cells. *Ann. Surg. Oncol.* 19, 3547–3555. doi: 10.1245/s10434-012-2393-4

Islam, M. A., Xu, Y., Tao, W., Ubellacker, J. M., Lim, M., Aum, D., et al. (2018). Restoration of tumour-growth suppression *in vivo* via systemic

nanoparticle-mediated delivery of PTEN mRNA. *Nat. Biomed. Eng.* 2, 850–864. doi: 10.1038/s41551-018-0284-0

Johnson, R. P., Uthaman, S., John, J. V., Lee, H. R., Lee, S. J., Park, H., et al. (2015). Poly(PEGA)-b-poly(L-lysine)-b-poly(L-histidine) hybrid vesicles for tumoral ph-triggered intracellular delivery of doxorubicin hydrochloride. *ACS Appl. Mater. Interfaces* 7, 21770–21779. doi: 10.1021/acsami.5b05338

Khan, Z., Khan, A. A., Yadav, H., Prasad, G. B. K. S., and Bisen, P. S. (2017). Survivin, a molecular target for therapeutic interventions in squamous cell carcinoma. *Cell Mol. Biol. Lett.* 22:8. doi: 10.1186/s11658-017-0038-0

Khaw, A. K., Hande, M. P., Kalthur, G., and Hande, M. P. (2013). Curcumin inhibits telomerase and induces telomere shortening and apoptosis in brain tumour cells. *J. Cell Biochem.* 114, 1257–1270. doi: 10.1002/jcb.24466

Kong, N., Tao, W., Ling, X., Wang, J., Xiao, Y., Shi, S., et al. (2019). Synthetic mRNA nanoparticle-mediated restoration of p53 tumor suppressor sensitizes p53-deficient cancers to mTOR inhibition. *Sci. Transl. Med.* 11:eaaw1565. doi: 10.1126/scitranslmed.aaw1565

Lättig-Tünnemann, G., Prinz, M., Hoffmann, D., Behlke, J., Palm-Apergi, C., Morano, I., et al. (2011). Backbone rigidity and static presentation of guanidinium groups increases cellular uptake of arginine-rich cell-penetrating peptides. *Nat. Commun.* 2:453. doi: 10.1038/ncomms1459

Lee, E. S., Na, K., and Bae, Y. H. (2005). Super pH-sensitive multifunctional polymeric micelle. *Nano Lett.* 5, 325–329. doi: 10.1021/nl0479987

Lee, E. S., Oh, K. T., Kim, D., Youn, Y. S., and Bae, Y. H. (2007). Tumor pH-responsive flower-like micelles of poly(L-lactic acid)-b-poly(ethylene glycol)-b-poly(L-histidine). *J. Control Release* 123, 19–26. doi: 10.1016/j.jconrel.2007.08.006

Lee, E. S., Shin, H. J., Na, K., and Bae, Y. H. (2003). Poly(L-histidine)-PEG block copolymer micelles and pH-induced destabilization. *J. Control Release* 90, 363–374. doi: 10.1016/S0168-3659(03)00205-0

Li, Z., Qiu, L., Chen, Q., Hao, T., Qiao, M., Zhao, H., et al. (2015). pH-sensitive nanoparticles of poly(L-histidine)-poly(lactide-co-glycolide)-tocopheryl polyethylene glycol succinate for anti-tumor drug delivery. *Acta Biomater.* 11, 137–150. doi: 10.1016/j.actbio.2014.09.014

Luan, C. R., Liu, Y. H., Zhang, J., Yu, Q. Y., Huang, Z., Wang, B., et al. (2016). Low molecular weight oligomers with aromatic backbone as efficient nonviral gene vectors. *ACS Appl. Mater Interfaces* 8, 10743–10751. doi: 10.1021/acsami.6b01561

Mandal, D., Nasrolahi Shirazi, A., and Parang, K. (2011). Cell-penetrating homochiral cyclic peptides as nuclear-targeting molecular transporters. *Angew. Chem. Int. Ed. Engl.* 50, 9633–9637. doi: 10.1002/anie.201102572

Meng, Q. Y., Cong, H. L., Hu, H., and Xu, F. J. (2020). Rational design and latest advances of codelivery systems for cancer therapy. *Mater. Today Bio.* 7:100056. doi: 10.1016/j.mtbio.2020.100056

Nguyen, L. T., Chau, J. K., Perry, N. A., de Boer, L., Zaat, S. A., and Vogel, H. J. (2010). Serum stabilities of short tryptophan- and arginine-rich antimicrobial peptide analogs. *PLoS ONE* 5:e12684. doi: 10.1371/journal.pone.0012684

Oh, D., Sun, J., Nasrolahi Shirazi, A., LaPlante, K. L., Rowley, D. C., and Parang, K. (2014). Antibacterial activities of amphiphilic cyclic cell-penetrating peptides against multidrug-resistant pathogens. *Mol. Pharm.* 11, 3528–3536. doi: 10.1021/mp5003027

Peery, R. C., Liu, J. Y., and Zhang, J. T. (2017). Targeting survivin for therapeutic discovery: past, present, and future promises. *Drug Discov. Today* 22, 1466–1477. doi: 10.1016/j.drudis.2017.05.009

Qiu, L., Li, Z., Qiao, M., Long, M., Wang, M., Zhang, X., et al. (2014). Self-assembled pH-responsive hyaluronic acid-g-poly((L)-histidine) copolymer micelles for targeted intracellular delivery of doxorubicin. *Acta Biomater.* 10, 2024–2035. doi: 10.1016/j.actbio.2013.12.025

Radovic-Moreno, A. F., Lu, T. K., Puscasu, V. A., Yoon, C. J., Langer, R., and Farokhzad, O. C. (2012). Surface charge-switching polymeric nanoparticles for bacterial cell wall-targeted delivery of antibiotics. *ACS Nano* 6, 4279–4287. doi: 10.1021/nn3008383

Ruan, S., Cao, X., Cun, X., Hu, G., Zhou, Y., Zhang, Y., et al. (2015). Matrix metalloproteinase-sensitive size-shrinkable nanoparticles for deep tumor penetration and pH triggered doxorubicin release. *Biomaterials* 60, 100–110. doi: 10.1016/j.biomaterials.2015.05.006

Shamsabadi, F. T., Eidgahi, M. R., Mehrbod, P., Daneshvar, N., Allaudin, Z. N., Yamchi, A., et al. (2016). Survivin, a promising gene for targeted cancer treatment. *Asian Pac. J. Cancer Prev.* 17, 3711–3719. doi: 10.14456/apjcp.2016.159/APJCP.2016.17.8.3711

Shi, J., Kantoff, P. W., Wooster, R., and Farokhzad, O. C. (2017). Cancer nanomedicine: progress, challenges and opportunities. *Nat. Rev. Cancer* 17, 20–37. doi: 10.1038/nrc.2016.108

Sun, W., Hu, Q., Ji, W., Wright, G., and Gu, Z. (2017). Leveraging physiology for precision drug delivery. *Physiol. Rev.* 97, 189–225. doi: 10.1152/physrev.00015.2016

Sun, Y., Li, Y., Nan, S., Zhang, L., Huang, H., and Wang, J. (2015). Synthesis and characterization of pH-sensitive poly(itaconic acid)-poly(ethylene glycol)-folate-poly(l-histidine) micelles for enhancing tumor therapy and tunable drug release. *J. Colloid Interface Sci.* 458, 119–129. doi: 10.1016/j.jcis.2015.07.008

Tang, J., He, J. F., Yang, C. L., Mao, Y., Hu, T. T., Zhang, L., et al. (2014). Antitumor effects of MsurvivinT34A-CaPi complex embedded PLGA nanoparticles in combination with Doxil in mice. *J. Nanoparticle Res.* 16:2682. doi: 10.1007/s11051-014-2682-x

Tang, Z., Kong, N., Ouyang, J., Feng, C., Kim, N. Y., Ji, X., et al. (2020). Phosphorus science-oriented design and synthesis of multifunctional nanomaterials for biomedical applications. *Matter* 2, 297–322. doi: 10.1016/j.matt.2019.12.007

Tao, W., Kong, N., Ji, X., Zhang, Y., Sharma, A., Ouyang, J., et al. (2019). Emerging two-dimensional monoelemental materials (Xenes) for biomedical applications. *Chem. Soc. Rev.* 48, 2891–2912. doi: 10.1039/C8CS00823J

Wang, X. F., and Wang, J. (2014). Icaritin suppresses the proliferation of human osteosarcoma cells *in vitro* by increasing apoptosis and decreasing MMP expression. *Acta Pharmacol. Sin.* 35, 531–539. doi: 10.1038/aps.2013.178

Wang, Y., Gao, S., Ye, W. H., Yoon, H. S., and Yang, Y. Y. (2006). Co-delivery of drugs and DNA from cationic core-shell nanoparticles self-assembled from a biodegradable copolymer. *Nat. Mater.* 5, 791–796. doi: 10.1038/nmat1737

Wang, Y. Z., Xie, Y., Li, J., Peng, Z. H., Sheinin, Y., Zhou, J., et al. (2017). Tumor-penetrating nanoparticles for enhanced anticancer activity of combined photodynamic and hypoxia-activated therapy. *ACS Nano* 11, 2227–2238. doi: 10.1021/acsnano.6b08731

Watson, J. L., Greenshields, A., Hill, R., Hilchie, A., Lee, P. W., Giacomantonio, C. A., et al. (2010). Curcumin-induced apoptosis in ovarian carcinoma cells is p53-independent and involves p38 mitogen-activated protein kinase activation and downregulation of Bcl-2 and survivin expression and Akt signaling. *Mol. Carcinog.* 49, 13–24. doi: 10.1002/mc.20571

Wilson, J. T., Keller, S., Manganiello, M. J., Cheng, C., Lee, C. C., Opara, C., et al. (2013). pH-Responsive nanoparticle vaccines for dual-delivery of antigens and immunostimulatory oligonucleotides. *ACS Nano* 7, 3912–3925. doi: 10.1021/nn305466z

Wu, P. H., Opadele, A. E., Onodera, Y., and Nam, J. M. (2019). Targeting integrins in cancer nanomedicine: applications in cancer diagnosis and therapy. *Cancers* 11:1783. doi: 10.3390/cancers11111783

Xu, B., Jin, Q., Zeng, J., Yu, T., Chen, Y., Li, S., et al. (2016a). Combined tumor- and neovascular- "dual targeting" gene/chemo-therapy suppresses tumor growth and angiogenesis. *ACS Appl. Mater. Interfaces* 8, 25753–25769. doi: 10.1021/acsami.6b08603

Xu, B., Xia, S., Wang, F., Jin, Q., Yu, T., He, L., et al. (2016b). Polymeric nanomedicine for combined gene/chemotherapy elicits enhanced tumor suppression. *Mol Pharm* 13, 663–676. doi: 10.1021/acs.molpharmaceut.5b00922

Yu, T., Xu, B., He, L., Xia, S., Chen, Y., Zeng, J., et al. (2016). Pigment epithelial-derived factor gene loaded novel COOH-PEG-PLGA-COOH nanoparticles promoted tumor suppression by systemic administration. *Int. J. Nanomed.* 11, 743–759. doi: 10.2147/IJN.S97223

Zhang, X., Chen, D., Ba, S., Zhu, J., Zhang, J., Hong, W., et al. (2014). Poly(l-histidine) based triblock copolymers: pH induced reassembly of copolymer micelles and mechanism underlying endolysosomal escape for intracellular delivery. *Biomacromolecules* 15, 4032–4045. doi: 10.1021/bm5010756

Zhu, J., Kim, Y., Lin, H., Wang, S., and Mirkin, C. A. (2018). pH-Responsive nanoparticle superlattices with tunable DNA bonds. *J. Am. Chem. Soc.* 140, 5061–5064. doi: 10.1021/jacs.8b02793

Conflict of Interest: The authors declare that the research was conducted in the absence of any commercial or financial relationships that could be construed as a potential conflict of interest.

frontiers in Chemistry

MINI REVIEW
published: 28 October 2020
doi: 10.3389/fchem.2020.00824

Peptide-Decorated Supramolecules for Subcellular Targeted Cancer Therapy: Recent Advances

Hua Jin†, *Xiao Lin*†, *Mengyue Gao*, *Liao Cui** and *Yun Liu**

Guangdong Key Laboratory for Research and Development of Natural Drugs, Guangdong Medical University, Zhanjiang, China

Binding small molecules through non-covalent molecular forces affords supramolecules, such as hydrogen bonds, with electrostatic, π-π interactions, van der Waals forces, and hydrophobic effects. Due to their good biocompatibility, low immunogenicity, and biodegradability, supramolecules have been intensely studied as multifunctional drug delivery platforms in targeted cancer therapy. In consideration of the defective therapeutic efficacy induced by simply transporting the therapeutic agents into tumor tissues or cancer cells instead of subcellular organelles, research is progressing toward the development of subcellular targeted cancer therapy (STCT) strategies. STCT is one of the most recent developments in the field of cancer nanomedicine. It is defined as the specific transportation of therapeutic agents to the target organelles for cancer treatment, which makes therapeutic agents accumulate in the target organelles at higher concentrations than other subcellular compartments. Compared with tumor-targeted and cancer-cell-targeted therapies, STCT exhibits dramatically improved specificity and precision, diminished adverse effects, and enhanced capacity to reverse multidrug resistance (MDR). Over the past few decades, peptides have played increasingly essential roles in multi-types of tumor-targeted drug delivery systems. Moreover, peptide-mediated STCT is becoming an emerging approach for precision cancer therapy and has been used in various cancer treatments, such as photothermal therapy (PTT), photodynamic therapy (PDT), chemotherapy, gene therapy, and non-drug-loaded nanoassemblies. In this review, we will focus on recent innovations in the variety of peptides used in designing peptide-decorated supramolecules for cell-membrane-, mitochondria-, and nucleus-localized STCT.

Keywords: supramolecules, functional peptides, subcellular targeted, cancer therapy, supramolecular cancer nanomedicine

OPEN ACCESS

Edited by:
Tianjiao Ji,
Boston Children's Hospital and Harvard Medical School, United States

Reviewed by:
Lin Hou,
Zhengzhou University, China
Jia Liu,
Huazhong University of Science and Technology, China

***Correspondence:**
Liao Cui
cuiliao@163.com
Yun Liu
liuyun_2017@hotmail.com

†*These authors have contributed equally to this work*

Specialty section:
This article was submitted to Supramolecular Chemistry, a section of the journal Frontiers in Chemistry

Received: *14 July 2020*
Accepted: *05 August 2020*
Published: *28 October 2020*

Citation:
Jin H, Lin X, Gao M, Cui L and Liu Y (2020) Peptide-Decorated Supramolecules for Subcellular Targeted Cancer Therapy: Recent Advances. Front. Chem. 8:824. doi: 10.3389/fchem.2020.00824

INTRODUCTION

In the past few decades, the rapid development of cancer nanomedicine has been focusing on overcoming challenges encountered by conventional medicines, such as low therapeutic efficacy, poor targetability, adverse side effects, and MDR (Sun et al., 2014). The employment of supramolecules in cancer treatment gives the definition of supramolecular cancer nanomedicine (Cui and Xu, 2017; Feng et al., 2017). Supramolecules are generated by the well-ordered self-assembly of small molecules through non-covalent molecular forces, such

as hydrogen bonds, enabling them to have electrostatic, π-π interactions, van der Waals forces, and hydrophobic effects (Webber et al., 2016). In terms of their good biocompatibility, low immunogenicity, and biodegradability, supramolecules have been widely developed as multifunctional drug delivery platforms in the field of supramolecular cancer nanomedicine (Yao et al., 2018; Chen R. et al., 2019). Moreover, tremendous progress has been made in developing various therapeutic strategies over the past two decades, including chemotherapy, gene therapy, PDT, PTT, and non-drug-loaded nanoassemblies (Dong et al., 2018; Kim et al., 2018; Cheng H. et al., 2019c; He H. et al., 2019; Zou et al., 2020). Hence, significant advancements in supramolecular cancer nanomedicine and therapeutic strategies have facilitated the development of novel therapeutic nanoplatforms to resolve challenging issues of conventional medicines.

In cancer cells, all types of subcellular organelles are indispensable, which play fundamental roles in critical cellular functions. Recently, supramolecules have been applied for STCT (Gao et al., 2019; Nurunnabi et al., 2019; Guo et al., 2020). Studies indicate that the specific transportation of therapeutic agents to the target subcellular compartments, for instance, cell membrane, mitochondria, and nucleus, can be achieved through using supramolecular nanoplatforms (Song et al., 2015; Zhong et al., 2015; Deng et al., 2020). In contrast to conventional cancer nanomedicines, supramolecule-mediated STCTs exhibit some unique merits (Chen et al., 2018). Firstly, the organelle-specific delivery of therapeutics to the sites of action in cancer cells is capable of affording an optimal dose administration. Consequently, the adverse side effects caused by off-target drug delivery and high dose can be dramatically relieved. In addition, it could provide a greatly promising approach to circumvent MDR via the inhibition of drug efflux through the physical barriers of certain organelles. Namely, it exhibits dramatically improved specificity, enhanced therapeutic efficacy, and better precision over conventional cancer nanomedicines. Due to their small sizes, good biocompatibility, low cost, and various functions, functional peptides are particularly appropriate for supramolecules-mediated STCT. In this mini review, we summarize the latest development of functional peptide-decorated supramolecules for STCT in the last 5 years, with an emphasis on their outstanding performance for modulating various therapeutic strategies.

FUNCTIONAL PEPTIDE-BASED SUPRAMOLECULES FOR STCT

According to their functions in supramolecules-mediated STCT, functional peptides can be classified into three categories: tumor targeting peptides, tumor-environment-responsive peptides, and other functional peptides (Rong et al., 2020). In accordance with the specific localization sites, tumor targeting peptides can be grouped into three main types, including tumor-environment targeting peptides, cancer cells targeting peptides, and subcellular targeting peptides. Through the employment of tumor-environment-responsive peptides, the supramolecular nanoplatforms could respond to the characteristic stimuli of the tumor microenvironment for improved cellular internalization or controlled drug release, for instance, mild acidity, elevated temperature, high enzyme concentration, hypoxia, and imbalanced redox status. To enhance the therapeutic efficacy, other functional peptides can be employed to construct the supramolecular nanoplatforms, such as cell penetrating peptides (CPP) and therapeutic peptides. In summary, the utilization of functional peptides is able to greatly enhance their therapeutic efficacy to the subcellular locations in the course of cell membrane-, mitochondria-, and nucleus-targeted cancer therapy.

Cell Membrane-Targeted Cancer Therapy

The cell membrane defines the borders of cells, and plays an essential role in maintaining cell integrity, cell internalization, and protecting living cells (Tani et al., 1978). Undoubtedly, damage of the cell membrane could dramatically increase the permeability. Consequently, it can lead to enhanced cellular uptake of therapeutic agents for improved therapeutic efficacy, or even cell death (see **Figure 1**). Hence, cell membrane-localized PTT (Chen P. et al., 2020), PDT (Ma et al., 2019), chemotherapy (Zhang C. et al., 2018; Wang et al., 2019), and non-drug-loaded supramolecular nanoassemblies (Hu et al., 2017) can be used to address MDR, avoid cell barriers, and enhance therapeutic efficacy in STCT.

As a type of noninvasive therapeutic approach, cell death in cancer cells could be efficiently triggered by PTT at a recommended target temperature range of 41–48°C (Fernandes et al., 2020), which can be generated by the activation of photothermal agents via near infrared (NIR) laser irradiation. Compared with other targeted PTTs, cell membrane-targeted PTT can avoid the inducible heat resistance of cancer cells caused by heat shock protein 70. In a recent study, Chen et al. designed the chimeric peptide-based dual-usage NIR fluorescence probe C_{16}-CARK, which was used both for cell membrane-targeted fluorescence imaging and PTT (Chen P. et al., 2020). The Arg-Arg-Lys (RRK) segment endows the system with a cell membrane-targeting property, while the alkyl chain C_{16} facilitates C_{16}-CARK to insert into the cell membrane with a long retention time (>4 h). Subsequently, the Cy5.5 moiety produced heat upon NIR laser irradiation to destroy the cell membrane *in situ*, and lead to cell death without the occurrence of heat resistance.

Nowadays, PDT has attracted a massive amount of research attention due to its minimal invasiveness, tunability, targetability, and few side effects (Dai et al., 2019; Chen J. et al., 2020). Upon the laser irradiation of photosensitizers (PSs) in the presence of the molecule oxygen, the produced reactive oxygen species (ROS) result in the apoptosis of cancer cells. In reality, PDT drugs were approved for bladder cancer, skin cancer, esophagus cancer, and lung cancer (Chilakamarthi and Giribabu, 2017; Kessel, 2019). However, it is still a challenging task to fulfill long-term anchoring of PSs onto cell membranes for cell membrane-targeted PDT, due to cellular uptake and endocytosis. Zhang's group pioneered in this field by using chimeric peptides as a cell membrane anchoring strategy (Liu et al., 2017). Their

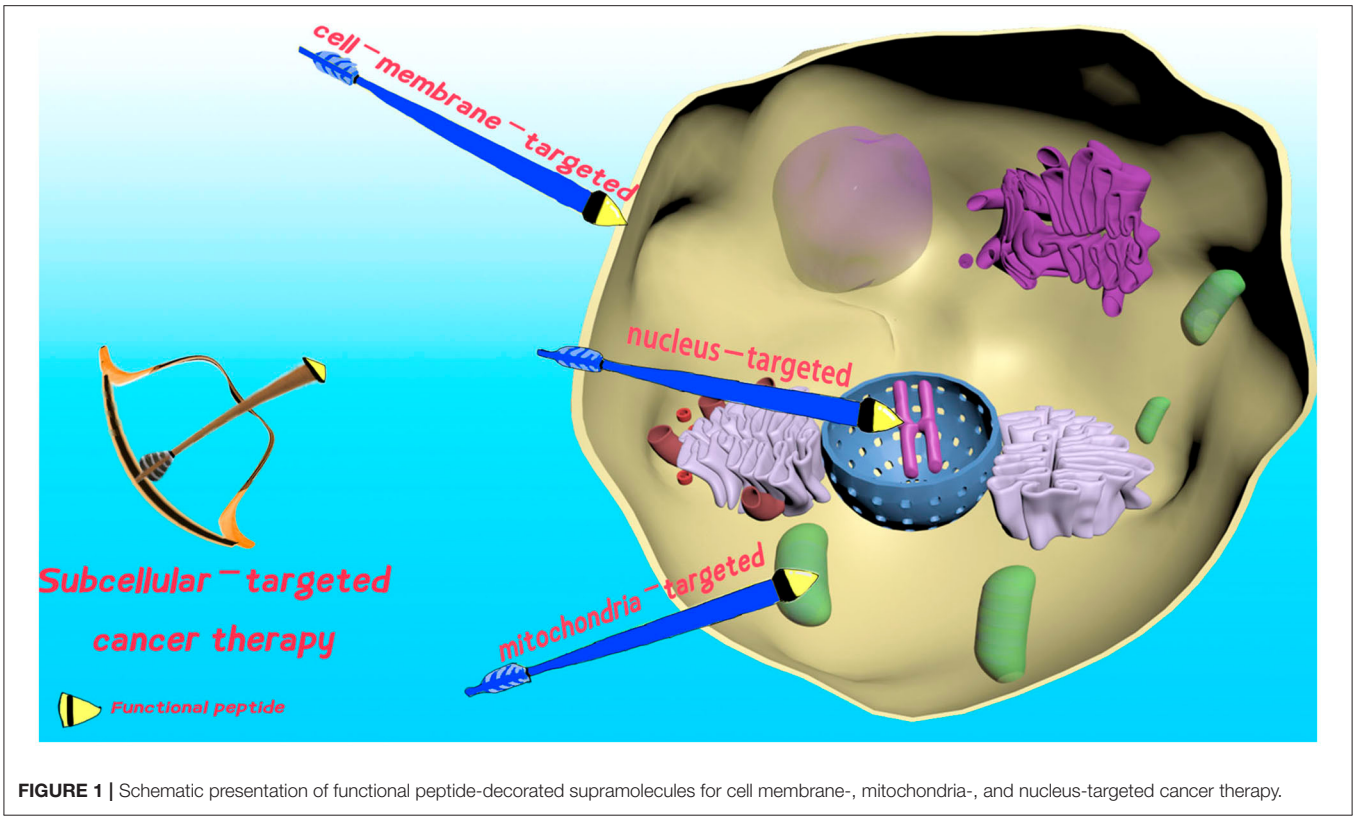

FIGURE 1 | Schematic presentation of functional peptide-decorated supramolecules for cell membrane-, mitochondria-, and nucleus-targeted cancer therapy.

early research employed the chimeric peptide-modified C_{16}-PRP-DMA, which can undergo charge reversal in a mildly acidic tumor environment. After the insertion onto the cell membrane through the C_{16} chain and chimeric peptide, *in situ* PDT took place upon the lase irradiation of PS protoporphyrinIX (PpIX). In their following research, the chimeric peptide strategy was further expanded to engineer cracked cancer cell membranes (CCCM) and exosomes, respectively (Qiu et al., 2018; Cheng H. et al., 2019b). Accordingly, the cell membranes were seriously damaged by the *in situ* occurred ROS, which induced apoptosis of cancer cells.

Despite of new therapeutic options, chemotherapy remains a cornerstone in cancer treatment. To overcome drug efflux induced MDR through the perturbation of the tumor membrane, cell membrane-targeted chemotherapy has recently drawn intensive research attention (Zhang X. et al., 2018). Zhang's group further used the chimeric peptide concept mentioned above for chemotherapy (Zhang C. et al., 2018). The therapeutic system loaded with doxorubicin (DOX) was denoted as CTGP. Upon arriving at tumor sites, the chimeric peptides anchored onto the cell membrane and generated self-assembled networks *in situ*, which strictly limited DOX efflux to obtain 49-fold greater anti-MDR ability than free DOX. Similarly but different, Xu's group perturbed the cell membrane to cause permeability enhancement of DOX through the recognition-reaction-aggregation (RRA) strategy (Wang et al., 2019).

Non-drug-loaded peptide nanoassemblies for cancer targeted therapy have been clearly proven by recent research (Hu et al., 2014). Particularly, it is not the therapeutic agents, the peptide supramolecular nanoassemblies, themselves that eliminate the cancer cells through physical disturbance (Lu et al., 2016). Non-drug-loaded peptide nanoassemblies for cell membrane-targeted cancer therapy can be conducted by the formation of an artificial extracellular matrix (AECM), which severely restricted cancer invasion and metastasis. For example, Wang's group developed a laminin-mimic peptide BP-KLVFFK-GGDGR-YIGSR, which specifically targeted cell membranes, transformed them into a supramolecular network, and formed AECM for the inhibition of cancer migration and metastasis (Hu et al., 2017).

Mitochondria-Targeted Cancer Therapy

Mitochondria have become the hottest subcellular target for precise cancer therapy (Wu et al., 2018; Lee and Cho, 2019). Mitochondrion take charge of ATP production and mitochondrial apoptosis. In consideration of its remarkably significant biological importance, mitochondria-targeted transportation of therapeutics to efficiently modulate its biological function can provide new strategies for STCT (see **Figure 1**). However, the efficiently specific transportation of therapeutic agents to mitochondria is still a challenging task, due to the extremely high negative transmembrane potential (∼-180 mV, Milane et al., 2015). Thus, cancer therapy is often mediated by the use of mitochondria-targeting moieties, including mitochondria-targeting signal peptides (MTSs), Szeto–Schiller (SS) peptides, mitochondria-penetrating peptides, (MPPs), and cationic triphenylphosphonium (TPP, Jean et al., 2016).

In consideration of the fact that mitochondria are the major organelles for ROS generation, the overexpression of mitochondrial ROS by mitochondria-targeted PDT could result in severe mitochondrial dysfunction. Therefore, mitochondria-targeted transportation of PSs via supramolecules has drawn considerable research efforts (Peng et al., 2020). Among the mitochondria-targeting molecules mentioned above, the pro-apoptosis peptide $(KLAKLAK)_2$ is the most utilized ligand for mitochondria-targeted PSs delivery (Han et al., 2016b; Cheng H. et al., 2019a). Plenty of evidence indicates that $(KLAKLAK)_2$ not only localizes therapeutics to mitochondria but also functions as a bio-drug itself, which could destroy the mitochondrial membrane and initiate apoptosis (Agemy et al., 2011). Zhang's group designed an effective drug self-delivery system PpIX-PEG-$(KLAKLAK)_2$ to conduct mitochondria-targeted PDT (Han K. et al., 2015). Here, $(KLAKLAK)_2$ acts both as the targeting segment and therapeutic agent to synergistically enhance PDT. Consequently, chemo/photodynamic synergistic therapy is realized in this system.

According to their mechanisms of action, almost all of the chemical drugs need to localize to specific organelles to elicit their pharmacological activities, including DOX, paclitaxel (PTX), camptothecin (CPT), cisplatin, and peptides. For this reason, mitochondria localization would achieve an optimal therapeutic efficiency and diminished side effects (Laws et al., 2018; Zhang et al., 2019; Zhu et al., 2019). As an ideal mitochondria-targeting cytotoxic drug, $(KLAKLAK)_2$ has been widely used for mitochondria-targeted chemotherapy (Chen S. et al., 2019; Cong et al., 2019). In 2019, Wang's group developed an ROS-responsive polymer-peptide conjugate (PPC) with $(KLAKLAK)_2$ for tumor therapy (Cheng D. et al., 2019). The comparatively high ROS concentration in mitochondria resulted in the transformation of PPCs from nanoparticles to fibrous nanoarchitectures. Consequently, the exposure of $(KLAKLAK)_2$ to mitochondria lead to high mitochondria-targeted therapeutic efficiency without the occurrence of MDR. Interestingly, the specific delivery of drugs into mitochondria also affords a novel strategy to relief MDR.

As one of the most essential organelles, the implementation of non-drug-loaded peptide nanoassemblies for mitochondria-targeted therapy has attracted increasing attention (Jeena et al., 2017; Du et al., 2018; Li et al., 2018; Liu et al., 2018; He P. et al., 2019). Given that the elimination of cancer cells was conducted by the nanoassemblies themselves without using drugs, it undoubtedly avoids MDR. In 2016, Xu's group exploited the rationally designed peptide precursors with TPP, which targeted cancer cells and generated nanostructures *in situ* because of enzyme-instructed self-assembly (EISA, Wang et al., 2016). The cell uptake and TPP-mediated specific transportation of resulting nanostructures to mitochondria triggered the mitochondrial pathway of apoptosis without the occurrence of MDR. In another study, Ryu's team designed tripeptides by utilizing the cationic TPP as a mitochondria-targeting segment, which was denoted as Mito-FF (Jeena et al., 2019). Under the direction of TPP, Mito-FFs preferably accumulated inside mitochondria and allowed for self-assembly to activate apoptosis without the generation of MDR.

Nucleus-Targeted Cancer Therapy

As the most essential subcellular compartment, the nucleus functions in the process of gene expression and proliferation. Given that the malignant proliferation of cells induced by gene mutation is believed to be the major cause of cancer, nucleus-targeted therapeutic supramolecular systems to hinder cellular proliferation have been intensively developed (Pan et al., 2018, see **Figure 1**). Up to now, various types of nuclear localization signal (NLS) peptides have been popularly employed for the specific conveyance of therapeutics to the nucleus for precise cancer treatment, containing SV40 T antigen, HIV-1 TAT peptide, and adenoviral (Pan et al., 2018).

Nucleus-targeted gene therapy by peptide-based supramolecules has long been used as one of the major approaches for cancer treatment via the nucleus-targeted transportation of therapeutic genes (Thapa and Sullivan, 2018; Cheng Y. et al., 2019; Muhammad et al., 2019). With reference to nucleus-targeted gene therapy, the major challenge is to exploit the optimal nanocarriers that are able to endure various intracellular obstacles and convey enough therapeutic genes into the nucleus. In 2018, Zhang's group generated a targeting peptide-based nanovehicle by coupling CPP cationic non-Arg (R_9) with the tumor-targeting peptide cyclic (Arg-Gly-Asp-Phe-Lys) c(RGDfK) via click chemistry. The resulting bioconjugates could form nanocomplexes with microRNA (miRNA) and transport therapeutic genes with high specificity and efficiency (Xiao et al., 2018).

A large amount of marketed drugs are DNA-replication-related toxins, including 10-hydroxycamptothecine (HCPT), DOX, and cisplatin. In order to elicit their pharmacological activities, these drugs should be efficiently delivered into the nucleus (Han S. et al., 2015; Li et al., 2015). Considering that it is extremely hard to convey negatively charged drugs to the nucleus, Yang's group developed a nucleus-localized dual drug delivery system by the utilization of co-assembly of the positively charged cisplatin and negatively charged drug-peptide conjugate, HCPT-FFERGD (Cai et al., 2017). Using a tumor-targeted RGD peptide moiety, the negatively charged HCPT was efficiently transported to the nucleus to exert its activity. In another piece of work for HCPT delivery, Zhou's group constructed a multifunctional micellar nanoplatform, namely PECL/DA-TAT, for TAT peptide-mediated nucleus-localization of HCPT (Jing et al., 2018). As a consequence, the treatment obtained satisfying therapeutic efficiency both *in vitro* and *in vivo*.

PTT and PDT are both effective therapeutic treatments for nucleus-targeted cancer therapy due to their unique merits, including minimal drug resistance and excellent spatial selectivity. The exploitation of novel peptide-mediated supramolecular nanovehicles for nucleus-targeted PSs delivery has drawn increasing attention (Han et al., 2016a). The TAT peptide is a commonly used CPP for nucleus localization. Given that nucleus-targeted PTT can "burn" cancer cell nuclei more efficiently and afford higher therapeutic efficiency compared to other organelle-targeted PTTs, Wang's group designed a conjugate TAT-IR780 modified with the TAT peptide (Wan et al., 2020). IR780 is a NIR fluorescence for both PTT and PDT. Upon laser

irradiation, TAT-IR780 efficiently destroyed genes in nucleus and induced apoptosis through both PTT and PDT. Speaking of nucleus-targeted PDT, ROS, generated by photoexcitation of nucleus-localized PS, could destroy nuclear DNA and proteins efficiently to induce cell death. In 2019, Li's team developed a self-delivery chimeric peptide, denoted as C_{16}-K(PpIX)PKKKRKV-PEG_8, for cell membrane and nucleus synergetic dual targeted PDT (Cheng H. et al., 2019d), which exhibited an improved therapeutic efficiency. The chimeric peptide consists of a hydrophobic alkyl chain (C_{16}) for cell membrane targeting and an NLS peptide (PKKKRKV) for nucleus targeting.

CONCLUSIONS AND OUTLOOKS

In this mini-review, we summarized recent advances in the field of functional peptide-decorated supramolecules for STCT, containing cell membrane-, mitochondria-, and nucleus-targeted cancer therapy. In each section, various therapeutic techniques currently used for STCT were introduced, including PTT, PDT, gene therapy, chemotherapy, and non-drug-loaded nanoassemblies. Compared with conventional targeted cancer therapy, STCT shows higher selectivity, improved sensitivity, lower dosage, and minimal adverse effects.

Due to the fact that the targeting mechanisms remain unclear, the development of lysosome-, Golgi apparatus-, and endoplasmic-reticulum (ER)-targeted nanoformulations is still challenging. Consequently, the related approaches have not received as much interest as cell-membrane-, nucleus-, and mitochondria-targeted therapies, especially for peptide-based supramolecular nanoformulations. Therefore, more research efforts should be paid in this field in the future. We believe that the discovery of new targets for lysosome, Golgi apparatus, and ER will open a new paradigm for lysosome-, Golgi apparatus- and ER-targeted therapy. STCT is still in an early stage of the development process. Despite the advantages mentioned above, there are still challenges that must be addressed for future development: (a) there is a lack of therapeutic nanoplatforms to visualize the process of STCT; (b) single therapeutic technique or single-organelle-targeted therapy often results in an insufficient therapy effect; (c) compared with cell membrane, mitochondrion, and nucleus, fewer research efforts were focused on other organelles. In view of these challenges, we propose that further research should concentrate on the following directions: (a) exploiting imaging-guided theranostic nanoplatforms for STCT; (b) developing combination/synergistic nanoplatforms for STCT; (c) concentrating more attention on the development of lysosome-, Golgi apparatus-, and endoplasmic reticulum-targeted cancer therapy. To conclude, we believe this mini review will afford helpful knowledge and new points of view in the field of functional peptide-decorated supramolecules for STCT. Under the united endeavor of researchers, clinical translation could be realized in the future.

AUTHOR CONTRIBUTIONS

YL and LC contributed conception and directed the work. HJ and XL contributed equally to the writing process of the first draft of the manuscript. MG revised the manuscript. All authors contributed to manuscript revision.

FUNDING

We acknowledge support from the Science and Technology Planning Project of Guangdong Province of China (2016B030309002). YL received funding from the National Natural Science Foundation of Guangdong, China (2019B1515120006, 2020A1515011244).

REFERENCES

Agemy, L., Friedmann-Morvinski, D., Kotamraju, V. R., Roth, L., Sugahara, K. N., Girard, O. M., et al. (2011). Targeted nanoparticle enhanced proapoptotic peptide as potential therapy for glioblastoma. *Proc. Natl. Acad. Sci. USA*. 108, 17450–17455. doi: 10.1073/pnas.1114518108

Cai, Y., Shen, H., Zhan, J., Lin, M., Dai, L., Ren, C., et al. (2017). Supramolecular "trojan horse" for nuclear delivery of dual anticancer drugs. *J. Am. Chem. Soc.* 139, 2876–2879. doi: 10.1021/jacs.6b12322

Chen, J., Fan, T., Xie, Z., Zeng, Q., Xue, P., Zheng, T., et al. (2020). Advances in nanomaterials for photodynamic therapy applications: status and challenges. *Biomaterials* 237, 119827. doi: 10.1016/j.biomaterials.2020.119827

Chen, P., Shi, Q., Chen, T., Wang, P., Liu, Y., Liu, L.-H., et al. (2020). A dual-usage near-infrared (NIR) cell membrane targeting chimeric peptide for cancer cell membrane imaging and photothermal ablation. *J. Mater. Sci.* 55, 7843–7856. doi: 10.1007/s10853-020-04546-1

Chen, R., Wang, J., Qian, C., Ji, Y., Zhu, C., Wu, L., et al. (2019). From nanofibers to nanorods: Nanostructure of Peptide-Drug conjugates regulated by Polypeptide-PEG derivative and enhanced antitumor effect. *Adv. Funct. Mater.* 29, 1806058. doi: 10.1002/adfm.201806058

Chen, S., Fan, J., Liu, X., Zhang, M., Liu, F., Zeng, X., et al. (2019). A self-delivery system based on an amphiphilic proapoptotic peptide for tumor targeting therapy. *J. Mater. Chem. B Mater. Biol. Med.* 7, 778–785. doi: 10.1039/C8TB02945H

Chen, W. H., Luo, G. F., and Zhang, X. Z. (2018). Recent advances in subcellular targeted cancer therapy based on functional materials. *Adv. Mater.* 31, 1802725. doi: 10.1002/adma.201802725

Cheng, D., Zhang, X., Gao, Y., Ji, L., Hou, D., Wang, Z., et al. (2019). Endogenous reactive oxygen Species-Triggered morphology transformation for enhanced cooperative interaction with mitochondria. *J. Am. Chem. Soc.* 141, 7235–7239. doi: 10.1021/jacs.8b07727

Cheng, H., Fan, J. H., Zhao, L. P., Fan, G. L., Zheng, R. R, and Qiu, X. Z., et al. (2019b). Chimeric peptide engineered exosomes for dual-stage light guided plasma membrane and nucleus targeted photodynamic therapy. *Biomaterials* 211, 14–24. doi: 10.1016/j.biomaterials.2019.05.004

Cheng, H., Jiang, X., Zheng, R., Zuo, S., Zhao, L., Fan, G.-L., et al. (2019c). A biomimetic cascade nanoreactor for tumor targeted starvation therapy-amplified chemotherapy. *Biomaterials* 195, 75–85. doi: 10.1016/j.biomaterials.2019.01.003

Cheng, H., Yuan, P., Fan, G., Zhao, L., Zheng, R., Yang, B., et al. (2019d). Chimeric peptide nanorods for plasma membrane and nuclear targeted photosensitizer delivery and enhanced photodynamic therapy. *Appl Mater Today* 16, 120–131. doi: 10.1016/j.apmt.2019.04.017

Cheng, H., Zheng, R., Fan, G., Fan, J., Zhao, L., Jiang, X.-Y., et al. (2019a). Mitochondria and plasma membrane dual-targeted chimeric peptide for single-agent synergistic photodynamic therapy. *Biomaterials* 188, 1–11. doi: 10.1016/j.biomaterials.2018.10.005

Cheng, Y., Sun, C., Liu, R., Yang, J., Dai, J., Zhai, T., et al. (2019). A multifunctional peptide-conjugated AIEgen for efficient and sequential targeted gene delivery into the nucleus. *Angew. Chem. Int. Ed.* 58, 5049–5053. doi: 10.1002/anie.201901527

Chilakamarthi, U., and Giribabu, L. (2017). Photodynamic therapy: past, present and future. *Chem. Rec.* 17, 775–802. doi: 10.1002/tcr.201600121

Cong, Y., Ji, L., Gao, Y. J., Liu, F. H., Cheng, D. B., Hu, Z., et al. (2019). Microenvironment-induced in situ self-assembly of polymer-peptide conjugates that attack solid tumors deeply. *Angew. Chem. Int. Ed.* 58, 4632–4637. doi: 10.1002/anie.201900135

Cui, H., and Xu, B. (2017). Supramolecular medicine. *Chem. Soc. Rev* 46, 6430–6432. doi: 10.1039/C7CS90102J

Dai, X., Du, T., and Han, K. (2019). Engineering nanoparticles for optimized photodynamic therapy. *ACS Biomater. Sci. Eng.* 5, 6342–6354. doi: 10.1021/acsbiomaterials.9b01251

Deng, Y., Jia, F., Chen, X., Jin, Q., and Ji, J. (2020). ATP suppression by pH-activated mitochondria-targeted delivery of nitric oxide nanoplatform for drug resistance reversal and metastasis inhibition. *Small* 16, 2001747. doi: 10.1002/smll.202001747

Dong, Y., Yu, T., Ding, L., Laurini, E., Huang, Y., Zhang, M., et al. (2018). A dual targeting dendrimer-mediated siRNA delivery system for effective gene silencing in cancer therapy. *J. Am. Chem. Soc.* 140, 16264–16274. doi: 10.1021/jacs.8b10021

Du, W., Hu, X., Wei, W., and Liang, G. (2018). Intracellular peptide self-assembly: a biomimetic approach for *in situ* nanodrug preparation. *Bioconjug. Chem.* 29, 826–837. doi: 10.1021/acs.bioconjchem.7b00798

Feng, Z., Zhang, T., Wang, H., and Xu, B. (2017). Supramolecular catalysis and dynamic assemblies for medicine. *Chem. Soc. Rev.* 46, 6470–6479. doi: 10.1039/C7CS00472A

Fernandes, N., Rodrigues, C. F., Moreira, A. F., and Correia, I. J. (2020). Overview of the application of inorganic nanomaterials in cancer photothermal therapy. *Biomater. Sci.* 8, 2990–3020. doi: 10.1039/D0BM00222D

Gao, P., Pan, W., Li, N., and Tang, B. (2019). Boosting cancer therapy with Organelle-Targeted nanomaterials. *ACS Appl. Mater. Interfaces* 11, 26529–26558. doi: 10.1021/acsami.9b01370

Guo, X., Wei, X., Chen, Z., Zhang, X., Yang, G., Zhou, S., et al. (2020). Multifunctional nanoplatforms for subcellular delivery of drugs in cancer therapy. *Prog. Mater. Sci.* 107, 100599. doi: 10.1016/j.pmatsci.2019.100599

Han, K., Lei, Q., Wang, S.-B., Hu, J.-J., Qiu, W.-X., Zhu, J.-Y., et al. (2015). Dual-stage-light-guided tumor inhibition by mitochondria-targeted photodynamic therapy. *Adv. Funct. Mater.* 25, 2961–2971. doi: 10.1002/adfm.201500590

Han, K., Zhang, W., Zhang, J., Lei, Q., Wang, S., Liu, J., et al. (2016a). Acidity-triggered tumor-targeted chimeric peptide for enhanced intra-nuclear photodynamic therapy. *Adv. Funct. Mater.* 26, 4351–4361. doi: 10.1002/adfm.201600170

Han, K., Zhu, J., Jia, H., Wang, S., Li, S., Zhang, X., et al. (2016b). Mitochondria-Targeted chimeric peptide for trinitarian overcoming of drug resistance. *ACS Appl. Mater. Interfaces* 8, 25060–25068. doi: 10.1021/acsami.6b06522

Han, S., Li, Z., Zhu, J., Han, K., Zeng, Z., Hong, W., et al. (2015). Dual-pH sensitive Charge-Reversal polypeptide micelles for Tumor-Triggered targeting uptake and nuclear drug delivery. *Small* 11, 2543–2554. doi: 10.1002/smll.201402865

He, H., Nieminen, A., and Xu, P. (2019). A bioactivatable self-quenched nanogel for targeted photodynamic therapy. *Biomater. Sci.* 7, 5143–5149. doi: 10.1039/C9BM01237K

He, P., Li, X., Wang, L., and Wang, H. (2019). Bispyrene-based self-assembled nanomaterials: *in vivo* self-assembly, transformation, and biomedical effects. *Acc. Chem. Res.* 52, 367–378. doi: 10.1021/acs.accounts.8b00398

Hu, Q., Gao, M., Feng, G., and Liu, B. (2014). Mitochondria-targeted cancer therapy using a light-up probe with aggregation-induced-emission characteristics. *Angew. Chem. Int. Ed.* 53, 14225–14229. doi: 10.1002/anie.201408897

Hu, X., He, P., Qi, G., Gao, Y., Lin, Y., Yang, C., et al. (2017). Transformable nanomaterials as an artificial extracellular matrix for inhibiting tumor invasion and metastasis. *ACS Nano* 11, 4086–4096. doi: 10.1021/acsnano.7b00781

Jean, S. R., Ahmed, M., Lei, E. K., Wisnovsky, S. P., and Kelley, S. O. (2016). Peptide-mediated delivery of chemical probes and therapeutics to mitochondria. *Acc. Chem. Res.* 49, 1893–1902. doi: 10.1021/acs.accounts.6b00277

Jeena, M. T., Jeong, K., Go, E. M., Cho, Y., Lee, S., Jin, S., et al. (2019). Heterochiral assembly of amphiphilic peptides inside the mitochondria for supramolecular cancer therapeutics. *ACS Nano* 13, 11022–11033. doi: 10.1021/acsnano.9b02522

Jeena, M. T., Palanikumar, L., Go, E. M., Kim, I., Kang, M. G., Lee, S., et al. (2017). Mitochondria localization induced self-assembly of peptide amphiphiles for cellular dysfunction. *Nat. Commun.* 8, 26. doi: 10.1038/s41467-017-00047-z

Jing, Y., Xiong, X., Ming, Y., Zhao, J., Guo, X., Yang, G., et al. (2018). A multifunctional micellar nanoplatform with pH-Triggered cell penetration and nuclear targeting for effective cancer therapy and inhibition to lung metastasis. *Adv. Healthc. Mater.* 7, 1700974. doi: 10.1002/adhm.201700974

Kessel, D. (2019). Photodynamic therapy: a brief history. *J. Clin. Med.* 8, 1581. doi: 10.3390/jcm8101581

Kim, S., Palanikumar, L., Choi, H., Jeena, M. T., Kim, C., and Ryu, J. H. (2018). Intra-mitochondrial biomineralization for inducing apoptosis of cancer cells. *Chem. Sci.* 9, 2474–2479. doi: 10.1039/C7SC05189A

Laws, K., Bineva-Todd, G., Eskandari, A., Lu, C., O'Reilly, N., and Suntharalingam, K. (2018). A Copper(II) phenanthroline metallopeptide that targets and disrupts mitochondrial function in breast cancer stem cells. *Angew. Chem. Int. Ed.* 57, 287–291. doi: 10.1002/anie.201710910

Lee, S. Y., and Cho, H. (2019). Mitochondria targeting and destabilizing hyaluronic acid Derivative-Based nanoparticles for the delivery of lapatinib to Triple-Negative breast cancer. *Biomacromolecules* 20, 835–845. doi: 10.1021/acs.biomac.8b01449

Li, L., Sun, W., Zhong, J., Yang, Q., Zhu, X., Zhou, Z., et al. (2015). Multistage nanovehicle delivery system based on stepwise size reduction and charge reversal for programmed nuclear targeting of systemically administered anticancer drugs. *Adv. Funct. Mater.* 25, 4101–4113. doi: 10.1002/adfm.201501248

Li, L. L., Qiao, Z. Y., Wang, L., and Wang, H. (2018). Programmable construction of peptide-based materials in living subjects: from modular design and morphological control to theranostics. *Adv. Mater.* 31, 1804971. doi: 10.1002/adma.201804971

Liu, F., Cong, Y., Qi, G., Ji, L., Qiao, Z., and Wang, H. (2018). Near-infrared laser-driven *in situ* Self-Assembly as a general strategy for deep tumor therapy. *Nano Lett.* 18, 6577–6584. doi: 10.1021/acs.nanolett.8b03174

Liu, L., Qiu, W., Zhang, Y., Li, B., Zhang, C., Gao, F., et al. (2017). A charge reversible Self-Delivery chimeric peptide with cell Membrane-Targeting properties for enhanced photodynamic therapy. *Adv. Funct. Mater.* 27, 1700220. doi: 10.1002/adfm.201700220

Lu, P., Bruno, B. J., Rabenau, M., and Lim, C. S. (2016). Delivery of drugs and macromolecules to the mitochondria for cancer therapy. *J. Controll. Release* 240, 38–51. doi: 10.1016/j.jconrel.2015.10.023

Ma, W., Sha, S. N., Chen, P. L., Yu, M., Chen, J. J., Huang, C. B., et al. (2019). A cell membrane-targeting self-delivery chimeric peptide for enhanced photodynamic therapy and in situ therapeutic feedback. *Adv. Healthc. Mater.* 9, 1901100. doi: 10.1002/adhm.201901100

Milane, L., Trivedi, M., Singh, A., Talekar, M., and Amiji, M. (2015). Mitochondrial biology, targets, and drug delivery. *J. Controll. Release* 207, 40–58. doi: 10.1016/j.jconrel.2015.03.036

Muhammad, K., Zhao, J., Ullah, I., Guo, J., Ren, X. K., and Feng, Y. (2019). Ligand targeting and peptide functionalized polymers as non-viral carriers for gene therapy. *Biomater. Sci.* 8, 64–83. doi: 10.1039/C9BM01112A

Nurunnabi, M., Khatun, Z., Badruddoza, A. Z. M., McCarthy, J. R., Lee, Y., and Huh, K. M. (2019). Biomaterials and bioengineering approaches for mitochondria and nuclear targeting drug delivery. *ACS Biomater. Sci. Eng.* 5, 1645–1660. doi: 10.1021/acsbiomaterials.8b01615

Pan, L., Liu, J., and Shi, J. (2018). Cancer cell nucleus-targeting nanocomposites for advanced tumor therapeutics. *Chem. Soc. Rev.* 47, 6930–6946. doi: 10.1039/C8CS00081F

Peng, N., Yu, H., Yu, W., Yang, M., Chen, H., Zou, T., et al. (2020). Sequential-targeting nanocarriers with pH-controlled charge reversal for enhanced mitochondria-located photodynamic-immunotherapy of cancer. *Acta Biomater.* 105, 223–238. doi: 10.1016/j.actbio.2020.01.005

Qiu, W., Zhang, M., Liu, L., Gao, F., Zhang, L., Li, S., et al. (2018). A self-delivery membrane system for enhanced anti-tumor therapy. *Biomaterials* 161, 81–94. doi: 10.1016/j.biomaterials.2018.01.037

Rong, L. F., Lei, Q., and Zhang, X. Z. (2020). Recent advances on peptide-based theranostic nanomaterials. *View*. doi: 10.1002/VIW.20200050. [Epub ahead of print].

Song, J., Zhang, Y., Zhang, W., Chen, J., Yang, X., Ma, P., et al. (2015). Cell penetrating peptide TAT can kill cancer cells via membrane disruption after attachment of camptothecin. *Peptides* 63, 143–149. doi: 10.1016/j.peptides.2014.12.001

Sun, T., Zhang, Y. S., Pang, B., Hyun, D. C., Yang, M., Xia, Y., et al. (2014). Engineered nanoparticles for drug delivery in cancer therapy. *Angew. Chem. Int. Ed.* 53, 12320–12364. doi: 10.1002/anie.201403036

Tani, E., Nakano, M., Itagaki, T., and Fukumori, T. (1978). Cell membrane structure of human giant-celled glioblastoma. *Acta Neuropathol.* 41, 61–65. doi: 10.1007/BF00689558

Thapa, R. K., and Sullivan, M. O. (2018). Gene delivery by peptide-assisted transport. *Curr. Opin. Biomed. Eng.* 7, 71–82. doi: 10.1016/j.cobme.2018.10.002

Wan, G., Cheng, Y., Song, J., Chen, Q., Chen, B., Liu, Y., et al. (2020). Nucleus-targeting near-infrared nanoparticles based on TAT peptide-conjugated IR780 for photo-chemotherapy of breast cancer. *Chem. Eng. J.* 380, 122458. doi: 10.1016/j.cej.2019.122458

Wang, H., Feng, Z., Wang, Y., Zhou, R., Yang, Z., and Xu, B. (2016). Integrating enzymatic Self-Assembly and mitochondria targeting for selectively killing cancer cells without acquired drug resistance. *J. Am. Chem. Soc.* 138, 16046–16055. doi: 10.1021/jacs.6b09783

Wang, Z., An, H., Hou, D., Wang, M., Zeng, X., Zheng, R., et al. (2019). Addressable peptide Self-Assembly on the cancer cell membrane for sensitizing chemotherapy of renal cell carcinoma. *Adv. Mater.* 31, 1807175. doi: 10.1002/adma.201807175

Webber, M. J., Appel, E. A., Meijer, E. W., and Langer, R. (2016). Supramolecular biomaterials. *Nat. Mater.* 15, 13–26. doi: 10.1038/nmat4474

Wu, J., Li, J., Wang, H., and Liu, C. (2018). Mitochondrial-targeted penetrating peptide delivery for cancer therapy. *Expert Opin. Drug Deliv.* 15, 951–964. doi: 10.1080/17425247.2018.1517750

Xiao, X., Wang, X., Gao, H., Chen, X., Li, J., and Zhang, Y. (2018). Cell-Selective delivery of MicroRNA with a MicroRNA-Peptide conjugate nanocomplex. *Chem. Asian J.* 13, 3845–3849. doi: 10.1002/asia.201801396

Yao, Q., Huang, Z., Liu, D., Chen, J., and Gao, Y. (2018). Enzyme-instructed supramolecular self-assembly with anticancer activity. *Adv. Mater.* 31, 1804814. doi: 10.1002/adma.201804814

Zhang, C., Liu, L., Qiu, W., Zhang, Y., Song, W., Zhang, L., et al. (2018). A transformable chimeric peptide for cell encapsulation to overcome multidrug resistance. *Small* 14, 1703321. doi: 10.1002/smll.201703321

Zhang, W., Hu, X., Shen, Q., and Xing, D. (2019). Mitochondria-specific drug release and reactive oxygen species burst induced by polyprodrug nanoreactors can enhance chemotherapy. *Nat. Commun.* 10, 1704. doi: 10.1038/s41467-019-10186-0

Zhang, X., Li, Y., Hu, C., Wu, Y., Zhong, D., Xu, X., et al. (2018). Engineering anticancer amphipathic Peptide-Dendronized compounds for Highly-Efficient Plasma/Organelle membrane perturbation and multidrug resistance reversal. *ACS Appl. Mater. Interfaces* 10, 30952–30962. doi: 10.1021/acsami.8b07917

Zhong, J., Li, L., Zhu, X., Guan, S., Yang, Q., Zhou, Z., et al. (2015). A smart polymeric platform for multistage nucleus-targeted anticancer drug delivery. *Biomaterials* 65, 43–55. doi: 10.1016/j.biomaterials.2015.06.042

Zhu, Y., Huang, Y., Jin, Y., Gui, S., and Zhao, R. (2019). Peptide-Guided system with programmable subcellular translocation for targeted therapy and bypassing multidrug resistance. *Anal. Chem.* 91, 1880–1886. doi: 10.1021/acs.analchem.8b03598

Zou, Y., Li, M., Xiong, T., Zhao, X., Du, J., Fan, J., et al. (2020). A single molecule drug targeting photosensitizer for enhanced breast cancer photothermal therapy. *Small* 16, 1907677. doi: 10.1002/smll.201907677

Conflict of Interest: The authors declare that the research was conducted in the absence of any commercial or financial relationships that could be construed as a potential conflict of interest.

Advantages of publishing in Frontiers

OPEN ACCESS
Articles are free to read for greatest visibility and readership

FAST PUBLICATION
Around 90 days from submission to decision

HIGH QUALITY PEER-REVIEW
Rigorous, collaborative, and constructive peer-review

TRANSPARENT PEER-REVIEW
Editors and reviewers acknowledged by name on published articles

Frontiers
Avenue du Tribunal-Fédéral 34
1005 Lausanne | Switzerland

Visit us: www.frontiersin.org
Contact us: frontiersin.org/about/contact

REPRODUCIBILITY OF RESEARCH
Support open data and methods to enhance research reproducibility

DIGITAL PUBLISHING
Articles designed for optimal readership across devices

FOLLOW US
@frontiersin

IMPACT METRICS
Advanced article metrics track visibility across digital media

EXTENSIVE PROMOTION
Marketing and promotion of impactful research

LOOP RESEARCH NETWORK
Our network increases your article's readership